The petrogenesis of carbonatites:

Mineral variations and effects on the REE mineralization

Dissertation

der Mathematisch-Naturwissenschaftlichen Fakultät
der Eberhard Karls Universität Tübingen
zur Erlangung des Grades eines
Doktors der Naturwissenschaften
(Dr. rer. nat.)

vorgelegt von
Dipl.-Geol. R. Johannes Giebel
aus Brandenburg an der Havel

Tübingen
20.06.2019

Gedruckt mit Genehmigung der Mathematisch-Naturwissenschaftlichen Fakultät der Eberhard Karls Universität Tübingen.

Tag der mündlichen Qualifikation:

Dekan:	Prof. Dr. Wolfgang Rosenstiel
1. Berichterstatter:	Prof. Dr. Gregor Markl
2. Berichterstatter:	Prof. Dr. Christoph D.K. Gauert

ACKNOWLEDGEMENTS

First of all, I would like to thank Prof. Dr. Gregor Markl, Prof. Dr. Christoph D. K. Gauert and PD Dr. Michael A. W. Marks for the assignment and supervision of my dissertation. I am especially grateful to them for their constant constructive criticism and their fast processing of my manuscripts. Furthermore, I would like to thank PD Dr. Thomas Wenzel for his support on the microprobe. Since this analytical method was an important cornerstone of my work, Dr. Wenzel's analytical finesse and his conclusive advice were fundamental contributions to the success of my work. I would also like to thank the entire working group "Petrology and Mineral Resources" of the Eberhard Karls University (EKU) in Tübingen (Germany) around Prof. Gregor Markl for many discussions, advices and general support. Many thanks to Prof. Dr. Gregor Markl, PD Dr. Michael A. W. Marks, PD Dr. Thomas Wenzel, Dr. Benjamin F. Walter, Dr. Udo Neumann, Dr. Maximilian Keim, Dr. Stefan Kreißl, Dr. Sebastian Staude, MSc. Rainer Babiel, MSc. Simon Braunger, MSc. Christian A. F. Dietzel, MSc. Tatjana Epp, MSc. Tim Kristandt, MSc. Manuel Scharrer, Mrs. Beate Fritz and Ms. Claudia Jahn. My special thanks also go to Dr. Horst Hann, who always assisted me in general scientific questions.

I would like to thank the members of the Department of Geology of the University of the Free State (UFS) in Bloemfontein (South Africa) for the realization and support of this work. I want to thank in particular Prof. Dr. Christoph D. K. Gauert, Prof. Dr. Freddy Roelfse, Prof. Dr. Marian Tredoux, Mrs. Rina Immelmann, MSc. George du Plesis, MSc. Megan Purchase, Mr. Andries Felix, MSc. Adriaan Odendaal, MSc. Raimund Rentel, MSc. Jarlen Joycelin Beukes, Mrs. Petro Swart and Mrs. Justine Magson. Prof. Dr. Glen Taylor (UFS) is thanked for the financial support during my studies at the UFS.

The employees of the mining companies Phosphate Corperation (Foskor), in particular mining geologists MSc. Henny Coetzee, BSc. Cynthia Muvhango and BSc. Megan Sauer and employees of the Palabora Mining Company (PMC), in particular mining geologists MSc. Thabitha Moyana, MSc. Paulien Lourens, MSc. Hans-Dieter Paetzold and staff members BSc. Pontsho Tyira, BSc. Nyiko Makhubele, Mr. Bongani Mabunda, Mr. Tshepang Molloane I would like to thank for the excellent cooperation during the sampling campaigns and the constant contact and discussions.

For sample preparation I like to thank Mrs. Simone Schafflick (EKU) and Mr. Daniel Radikgomo (UFS).

I would like to thank co-authors of publications for their cooperation. Many thanks to Prof. Dr. Gregor Markl, PD Dr. Michael A. W. Marks, Prof. Dr. Christoph D. K. Gauert, PD Dr. Thomas Wenzel, Dr. Benjamin F. Walter, MSc. Simon Braunger, MSc. Christian A. F. Dietzel, MSc. Tim Kristandt, Dr. Anis Parsapoor (EKU), Dr. Gelu “Gabi” Costin (Rice University), Prof. Dr. Aleksandra Gaweda, Dr. Krzysztof Szopa, Dr. Anna Sałacińska (University of Silesia), Dr. David Chew (Trinity College Dublin), Dr. Ashley Gumsley (Lund University), Dr. Sven Dahlgren (University of Oslo) and Dr. Mathew Steele-MacInnes (University of Alberta) as well as many thanks to the colleagues Dr. Mathias Burisch, MSc. Petya Atanasova (TU Bergakademie Freiberg), Mrs. Maguerita Duchoslav, MSc. Tamara de Riese (EKU), Dr. Ute Gebhard, Prof. Dr. Eberhard "Dino" Frey, Mr. Tim Niggemeyer, Ms. Christiane Birnbaum, Dipl.-Geol. Dieter Schreiber, Mr. Wolfgang Munk (State Museum of Natural History Karlsruhe) and Dr. Tomas Magna (Czech Geological Survey) for helpful discussions and cooperation.

Furthermore, members of the European Union’s Horizon 2020 research project “HiTech AlkCarb” Dipl. Geol. Klaus Brauch, Dr. Claudia Pohl (terratec Geophysical Services), Dr. Samuel Weatherley, Dr. Graham Banks, Dr. Anouk M. Borst and Dr. Björn Heincke (Geological Survey of Denmark and Greenland), MSc. Pete Siegfried (Geo-Africa Prospecting Services cc), Dr. Kathryn Goodenough, Dr. Charlie Beard and MSc. Eimear Deady (British Geological Survey), Prof. Dr. Frances Wall, Dr. Kathryn Moore, Dr. Sam Broom-Fendley, Dr. Holly Elliott (University of Exeter) and Prof. Dr. Anatoly Zaitsev (University of St. Petersburg) are gratefully acknowledged for constructive and insightful discussions on various topics related to this study. Financial support for this study was granted by the Deutsche Forschungsgemeinschaft [grant MA 2563/10].

My special thanks go to my family. First of all, my wife Yvonne Giebel and our children Jonas, Rose-Marie and Madita should be mentioned here. They have supported me in every way and made it possible for me to complete this work. I thank my grandparents Kurt and Dagmar Lober, who made my study of geosciences possible. Further I thank my mother Barbara Jusab and her husband Firoz Ahmed Noormohamed Jusab, as well as my father Manfred Giebel and his wife Hannelore Hellfeier for their constant support. I would also like to thank my sister Jaqueline Giebel, my nephew Melvin Giebel and my two brothers Alexander Giebel and Jan Giebel. For their tireless motivation I also want to thank our friends Andreas and Janine Clemens, Andy Monte, Patric Thie, Marcel Lutteropp, Felix Baum, Christina and Karl-Heinz Wendelstein, Sabine Dietrich and Gerald Berthold, Robert Lutzens, Edgar Ledur and Anne and Dennis Gutenmorgen. Thanks for everything!

ABSTRACT

Carbonatites show great economic potential and are important sources for a range of commodities, including P, Fe, F, Cu and HFSE (e.g., Zr, Hf, Nb, U), but especially REE. About 10% of all known carbonatite occurrences (50 out of 550) are currently mined for those commodities and about 40% of all REE exploration projects target carbonatites and associated rock types. Despite their economic importance we have a limited understanding of carbonatite systems and their relationship with associated rock types. A range of processes result in strong variability in the mineralogy and mineral chemistry of carbonatites, and hence their economic viability. However, the scientific interest to understand the complex mineralizations and associations in carbonatitic systems has tremendously increased. Our studies focus on two carbonatite complexes, namely the Palabora Carbonatite Complex (South Africa) and the Kaiserstuhl Volcanic Complex (Germany), that reflect a variety of mineral assemblages and mineral chemistry. The Palabora carbonatite clearly indicate an insignificant orthomagmatic REE mineralization, a late-magmatic enrichment of REE mineral phases and an effective post-magmatic redistribution of the REE mineralization. The Kaiserstuhl carbonatites, on the other hand, show a greater diversity in their REE concentrations due to a greater variety of petrogenetic processes. Some of the carbonatite bodies at the Kaiserstuhl experienced a strong hydrothermal enrichment of REE. In contrast, one Kaiserstuhl carbonatite body, namely the Badberg, shows strong retention of REE by apatite during early orthomagmatic stages. This carbonatite body lacks a late-magmatic to hydrothermal REE enrichment. The enhanced incorporation of REE into orthomagmatic apatite is attributed to a coupled substitution that is promoted through host rock contamination. Since the REE mineral type (its abundance) and mineral associations are decisive if a carbonatite is economic or not, the understanding of effects on the REE mineralization is of crucial importance. We use the Palabora complex (and the Fen complex, Norway) to illustrate the individual evolutionary stages of carbonatites and we illustrate the influence of external silicate contamination on the economic potential of a carbonatite at the Kaiserstuhl complex. Furthermore, we present a new model that reconstructs the emplacement of, and relation between, carbonatites and associated rocks. This model predicts the ratio between carbonatites and associated rock types, and explains the origin of phoscorite magmas. An extension of the model further explains the generation of various carbonatitic fluids.

KURZZUSAMMENFASSUNG

Karbonatite zeichnen sich durch ihr hohes wirtschaftliches Potenzial als wichtige Quelle für Rohstoffe, wie P, Fe, F, Cu und HFSE (z.B. Zr, Hf, Nb, U), aber vor allem LREE, aus. Etwa 10% aller bekannten Karbonatite (50 von 550) werden derzeit abgebaut, wobei etwa 40% aller REE-Explorationsprojekte auf diese und die mit ihnen assoziierten Gesteinsvorkommen abzielen. Trotz ihrer wirtschaftlichen Bedeutung ist das Verständnis von karbonatitischen Systemen und ihre Beziehungen zu assoziierten Gesteinstypen noch unvollständig. Hierbei kann eine Reihe von verschiedenen Prozessen eine starke Variabilität in der Mineralogie und Mineralchemie von Karbonatiten verursachen, und eine starke Auswirkung auf ihre Wirtschaftlichkeit haben. Das Interesse, diese komplexen Systeme zu verstehen, ist deshalb enorm gestiegen. Unsere Studien konzentrieren sich auf zwei Karbonatitkomplexe, den Palabora Komplex (PCC, Südafrika) und den Kaiserstuhl Komplex (KVC, Deutschland). Die Komplexe weisen eine stark variable Mineralogie und Mineral-chemie auf. Der PCC Karbonatit zeigt eine unbedeutende orthomagmatische REE-Mineralisation, eine spätmagmatische REE Anreicherung und eine effektive post-magmatische Umverteilung der REE-Mineralisation. Die KVC Karbonatite sind in ihrer REE-Anreicherung deutlich abweichend. Einige der Karbonatitkörper weisen eine starke hydrothermale Anreicherung auf. Ein Karbonatitkörper jedoch, der Badberg, erfuhr einen frühzeitigen Entzug von REE aus dem System während der ortho-magmatischen Phase. Dieser Karbonatitkörper zeigt in Folge dessen keine REE Anreicherung während der spätmagmatischen bis hydrothermalen Phase. Der Entzug von REE erfolgte aufgrund eines kontaminationsbedingten, bevorzugten Einbaus in Apatit. Da die Art, die Häufigkeit und die Vergesellschaftung der REE-Minerale entscheidend sind, ob ein Karbonatit wirtschaftlich ist oder nicht, ist das Verständnis von Auswirkungen auf die REE-Mineralisation von entscheidender Bedeutung. Wir veranschaulichen am Beispiel vom PCC (und dem Fen Komplex, Norwegen) die einzelnen Entwicklungsstufen von Karbonatiten und zeigen den Einfluss einer Silikat-Kontamination auf ihr wirtschaftliches Potenzial am Beispiel vom KVC. Darüber hinaus stellen wir ein Modell zur Platznahme und Beziehung von Karbonatiten und asso-ziierten Gesteinen vor. Dieses Model erklärt das Verhältnis zwischen Karbonatiten und zugehörigen Gesteinsarten sowie den Ursprung von Phoskoriten. Eine Erweiterung dieses Models erklärt die genese verschiedene karbonatitischer Fluide.

LIST OF PUBLICATIONS IN THE THESIS

This thesis contains the results, discussion and interpretation aspects of the following individual studies:

Study A.

Giebel, R.J., Gauert, C.D.K., Marks, M.A.W., Costin, G. and Markl, G. (2017): The Multistage REE Mineralization of the Palabora Carbonatite Complex, South Africa. American Mineralogist. Vol. 102(6). P 1218-1233. DOI: http://dx.doi.org/10.2138/am-2017-6004

Study B.

Giebel, R.J., Marks, M.A.W., Gauert, C.D.K. and Markl, G. (2019a): A model for the formation of carbonatite-phoscorite assemblages based on the compositional variation of mica and apatite from the Palabora Carbonatite Complex, South Africa. Lithos. Vol. 324-325. P 89-104. DOI: https://doi.org/10.1016/j.lithos.2018.10.030

Study C.

Giebel, R.J., Parsapoor, A., Walter, B.F., Braunger, S., Marks, M.A.W., Wenzel, T. and Markl, G. (2019b): Evidence for magma – wall rock interaction in carbonatites from the Kaiserstuhl Volcanic Complex (Southwest Germany). Journal of Petrology. Published online. DOI: https://doi.org/10.1093/petrology/egz028

Study D.

Dietzel, C.A.F., Kristandt, T., Dahlgren, S., **Giebel, R.J.**, Marks, M.A.W. and Markl, G. (2019): Hydrothermal processes in the Fen carbonatite complex, southern Norway. Ore Geology Reviews. Vol. 111. Published online. DOI: https://doi.org/10.1016/j.oregeorev.2019.102969

DESCRIPTION OF PERSONAL CONTRIBUTION

In the following, authors' contributions on publications in the thesis are declared by corresponding tables.

Author	Author position	Scientific ideas %	Data generation %	Analysis and interpretation %	Paper writing %
Giebel, RJ	**1**	**75**	**90**	**83**	**66**
Gauert, CDK	2	5	0	2	5
Marks, MAW	3	10	0	10	22
Costin, G	4	0	10	0	2
Markl, G	5	10	0	5	5
Titel of paper:		The Multistage REE Mineralization of the Palabora Carbonatite Complex, South Africa.			
Status in publication process:		asccepted and published			

Author	Author position	Scientific ideas %	Data generation %	Analysis and interpretation %	Paper writing %
Giebel, RJ	**1**	**77**	**100**	**81**	**68**
Marks, MAW	2	10	0	10	22
Gauert, CDK	3	3	0	4	5
Markl, G	4	10	0	5	5
Titel of paper:		A model for the formation of carbonatite-phoscorite assemblages based on the compositional variation of mica and apatite from the Palabora Carbonatite Complex, South Africa.			
Status in publication process:		accepted and published			

Author	Author position	Scientific ideas %	Data generation %	Analysis and interpretation %	Paper writing %
Giebel, RJ	**1**	**24**	**0**	**34**	**44**
Parsapoor, A	2	0	50	2	0
Walter, BF	3	21	30	15	7
Braunger, S	4	22	0	24	12
Marks, MAW	5	23	0	20	32
Wenzel, T	6	0	20	0	0
Markl, G	7	10	0	5	5
Titel of paper:		Evidence for magma – wall rock interaction in carbonatites from the Kaiserstuhl Volcanic Complex (Southwest Germany).			
Status in publication process:		accepted and published			

Author	Author position	Scientific ideas %	Data generation %	Analysis and interpretation %	Paper writing %
Dietzel, CAF	1	15	45	35	35
Kristandt, T	2	15	45	35	35
Dahlgren, S	3	30	5	10	5
Giebel, RJ	**4**	**0**	**5**	**10**	**5**
Marks, MAW	5	10	0	5	15
Markl, G	6	30	0	5	5
Titel of paper:		Hydrothermal processes in the Fen carbonatite complex, southern Norway.			
Status in publication process:		accepted and published			

Table of content

1. INTRODUCTION

1.1 Genesis of carbonatites and associated rocks

Carbonatites are mantle-derived igneous rocks that contain ≥30 vol.% primary magmatic carbonate minerals (Mitchell, 2005). Worldwide, about 550 occurrences are known to date, most of them (80%) are associated with a, compositionally largely variable range of typically SiO_2 undersaturated silicate rocks (Mitchell, 2005; Woolley and Kjarsgaard, 2008). Carbonatites can be subdivided into calcio- (sövites and alvikites), magnesio- (beforsites) and ferro-carbonatites, depending on their predominant carbonate phase, with calico-carbonatites being the most frequent carbonatites (Woolley and Kempe, 1989). Less common are primary magmatic dolomitic and ankeritic carbonatites. Theorised petrogenetic models on the origin of carbonatites have been reviewed by e.g. Bell (1989), Lee and Wyllie (1994, 1997), Mitchell (2005), and Jones et al. (2013). Two formation processes are accepted:

(1) Derivation from a primary carbonatitic magma by low-degree partial melting of carbonate-bearing mantle (Bell and Simonetti, 2010; Dalton and Presnall, 1998). The primary melt composition, is however, still unclear and under debate.

(2) Derivation from a carbonate-bearing silicate magma by (2a) fractional crystallization (Lee and Wyllie, 1994) and (2b) separation of a carbonatitic magma from a carbonate-bearing silicate magma by liquid-liquid immiscibility (Veksler et al., 1998).

Some carbonatites (~4%) are additionally spatially and temporally associated and genetically related to phoscorites, which are defined as carbonate-bearing ultramafic rocks that mainly consist of magnetite, apatite and forsterite/diopside/phlogopite. Phoscorites almost exclusively occur in multiphase carbonatite complexes and are situated around or in carbonatite cores (Krasnova et al., 2004b). Phoscoritic small-scale structures are present in many carbonatites (Krasnova et al., 2004b), but most of these occurrences are poorly described. The genetic relationship between carbonatites and phoscorites has been discussed among petrologists for many years and two potential processes have been suggested for the generation of phoscorites:

(1) Derivation from an individual primary phoscoritic magma.

(2) Derivation from a carbonatitic magma by (2a) fractional crystallization and (2b) separation from a parental carbonatitic melt by liquid-liquid immiscibility (Krasnova et al., 2004b).

However, the formation from an individual magma is specified as unrealistic because of the instability of phoscoritic melts at plausible temperatures (Lindsley and Epler, 2017). Processes 2a and 2b on the other hand, may also explain the common geometric relations between carbonatites and phoscorites (Krasnova et al., 2004b). Spherulitic and orbicular textures of phoscorite portions in carbonatites and vice versa in numerous carbonatite complexes (e.g., Krasnova et al., 2004b; Lapin and Vartiainen, 1983) as well as mineral inclusions in apatite and olivine (Mikhailova et al., 2002) give evidences for phoscorite formation by liquid immiscibility. In addition, melt inclusions show an Fe and P enrichment in parental magmas of some carbonatites (e.g., Chen et al., 2013; Guzmics et al., 2008; Krasnova et al., 2004b). Phoscorites, however, contain carbonate-dominated melt inclusions (e.g., Veksler et al., 1998; Zaitsev and Kamenetsky, 2013). Even though liquid immiscibility plays an important role in the phoscorite genesis, the role of fractional crystallization is still under debate for some complexes (e.g., Rimskaya-Korsakova and Krasnova, 2002). The formation of many carbonatite occurrences and their relationship to associated rocks remains unclear, but detailed mineralogical and mineral chemical investigations may reveal relevant formation processes (see above).

1.2 Mineralogical and mineral chemical variations in carbonatites/phoscorites

The most common non-carbonate minerals in carbonatites and phoscorites are apatite, magnetite and phlogopite, with apatite and phlogopite in particular, varying largely in composition (e.g., Andersen, 1988; Brod et al., 2001; Chakhmouradian et al., 2017; Chakrabarty et al., 2009; Hogarth, 1989; Mitchell et al., 2017). Therefore, they are used as monitors for the magmatic and hydrothermal evolution of carbonatitic systems (e.g., Brigatti et al., 1996; Chakhmouradian et al., 2017). Apatites from carbonatites (and phoscorites) may usually contain higher concentrations of Sr, rare-earth elements (REE) as well as Na and Si relative to most other magmatic rocks. The halogen-site is primarily occupied by OH and F, whereas Cl distribution is typically very low (Teiber et al., 2015 and references therein). Micas from carbonatites (and phoscorites) can be distinguished into four main groups: (1) The phlogopite-annite, (2) phlogopite-eastonite, (3) phlogopite-kinoshitalite, and (4) phlogopite-tetraferriphlogopite series (e.g., Reguir et al., 2009 and references therein). These micas are very Mg-rich (phlogopite) and typically evolve towards an Al-rich composition (eastonite and kinoshitalite; e.g., Brod et al., 2001; Lee et al., 2003) or an $^{IV}Fe^{3+}$-rich composition

(tetraferriphlogopite; e.g., Brod et al., 2001; Gaspar and Wyllie, 1987). In contrast, micas of associated silicate rocks typically contain a significant annite ($^{VI}Fe^{2+}$) component >20% and are thus classified as biotites.

In addition, a number of other silicate minerals (e.g. monticellite, forsterite, clinopyroxene, foid, alkali feldspar, etc.) have been described (Barker, 2001), but it is difficult to distinguish primary carbonatitic mineral phases from xenocrysts (Barker, 2001). In this context, a mineral chemical comparison of silicates from carbonatites and cogenetic silicate rocks, country rocks and mantle rocks, can provide insights on their provenance. However, relevant studies are rare (e.g., Vuorinen and Skelton, 2004). Furthermore, various HFSE-rich minerals and sulphides (pyrrhotite, pyrite, chalcopyrite, etc.) are commonly present (e.g., Bell et al., 2015; Chakhmouradian, 2006; Farrell et al., 2010; Gomide et al., 2013). A detailed understanding of mineral variability and their process-related character is crucial to understand how carbonatitic complexes emplace and how their mineralizations develop. This understanding, in turn, is critical to mineral exploration and future development of these important resources (Moore et al., 2015).

1.3 REE mineralization in carbonatites and phoscorites

Both, carbonatites and phoscorites are of high economic interest and are currently mined for their HFSE mineral-bearing phases (e.g., Nb in pyrochlore; Zr in baddeleyite; REE in monazite and REE-fluorocarbonates, etc.; e.g., Niobec, Canada; Kovdor, Russia; Mount Weld, Australia; Bayan Obo, China; Gendron et al., 1984; Ivanyuk et al., 2002; Kanazawa and Kamitani, 2006; Krasnova et al., 2004a; Yang et al., 2011). Additionally, they can represent important sources for Fe (in magnetite) and P (in apatite; e.g., Palabora, South Africa; Kovdor, Russia; e.g., Hanekom et al., 1965; Ivanyuk et al., 2002) and other minor commodities. About 45 REE-minerals and REE-bearing minerals have been reported from carbonatites worldwide (Chakhmouradian and Zaitsev, 2012; Wall and Zaitsev, 2004; Zaitsev et al., 2015). Two general types of REE mineralization can be distinguished in carbonatites: (1) those with “true” REE-minerals where REE are major constituents and (2) those where independent REE-minerals are absent and the significant amounts of REE are hosted in minerals such as calcite and apatite (Wall and Zaitsev, 2004). A variety of those minerals may be found in a single carbonatite. The most common REE-minerals in carbonatites are ancylite, bastnäsite-group minerals (known as REE-fluorocarbonates), britholite, and

monazite (Mariano, 1989; Zaitsev et al., 1998; Zaitsev et al., 2014), which are interpreted to be either of magmatic (relatively rare, mostly bastnäsite/parisite; Chakhmouradian and Zaitsev, 2012; Moore et al., 2015), hydrothermal (mostly bastnäsite and monazite; Williams-Jones et al., 2012) or supergene origin (e.g., crandallite-group minerals in carbonatite-derived laterites; Kynicky et al., 2012). Numerous carbonatite complexes experienced a multi-stage evolution (e.g., Brigatti et al., 1996; Lee et al., 2003; Moore et al., 2015), with processes potentially responsible for REE enrichment including fractional crystallization of carbonatitic magma, enrichment of REE in magmatic fluids and subsequent precipitation, breakdown of primary carbonatitic minerals with sequestration of REE in secondary minerals, and subsolidus redistribution of REE (e.g., Verplanck et al., 2016). But in general, several studies pointed out that hydrothermal processes usually are the most important parameter to form a major REE mineralization (e.g., Barra do Itapirapua, Bear Lodge, Tundulu and Kangankunde, Khibina; Andrade et al., 1999; Moore et al., 2015; Wall and Mariano, 1996; Zaitsev, 1996).

1.4 Case studies of carbonatite deposits

Some of the best studied REE-rich carbonatite complexes are those of the Kola Province (Finland and Russia). Phoscorites and early-stage carbonatites of most of these complexes are relatively REE-poor (≥2000 µg/g). The REE is generally hosted in major rock-forming minerals such as calcite and apatite, whereas REE-minerals are mostly absent. Late-stage carbonatites, however, show high REE contents (up to 5 wt.%) and incorporating distinct REE-minerals (e.g., bastnäsite; Lee et al., 2004; Zaitsev et al., 2015). Additionally, a primary (crystallized from a melt or carbo-hydrothermal fluid) and a secondary (formed during metasomatic replacement) REE mineralization are distinguished (Zaitsev et al., 2015).

A good example for the complexity of multi-stage REE mineralizations is the Bear Lodge carbonatite (USA), where five distinct REE-mineral assemblages can be texturally distinguished and record multiple stages of hydrothermal deposition involving compositionally distinct fluids followed by supergene oxidation (Moore et al., 2015). Similar processes were documented from several other carbonatite complexes in Russia, China, Finland, Malawi and Siberia (Al Ani and Sarapää, 2009; Bulakh et al., 1998; Chakhmouradian and Zaitsev, 2012; Wall and Mariano, 1996; Xu et al., 2010; Zaitsev et al., 2002; Zaitsev et al., 1998). In several of these cases, changes in

temperature and in activities of CO_2, HF and HCl in such fluids (caused e.g., by the dissolution of primary minerals such as carbonates, apatite or phlogopite) are assumed to be responsible for the variability of the observed REE mineralizations (Andersen and Austrheim, 1991; Downes et al., 2014).

The formation of the currently largest producing REE deposit Bayan Obo (China) was also explained by carbonatite-derived multistage hydrothermal metasomatism, in this case of sedimentary carbonate rocks (e.g., Chao, 1997). The Bayan Obo deposit contains several distinct REE mineralizations. The dominant REE-minerals are bastnäsite and monazite, which are assumed to have precipitated from CO_2-rich fluids (Kanazawa and Kamitani, 2006). The major variation in fluid composition (as indicated by fluid inclusion data) points to a multistage deposition and remobilization of the REE. In the second largest producing REE deposit, Mountain Pass (USA), three distinct REE-mineral assemblages include magmatic bastnäsite, parisite and monazite, late-stage bastnäsite and secondary synchisite, sahamalite and ancylite (Castor, 2008). Interestingly, textural observations in these rocks indicate an upward streaming of REE- and Ca-rich fluids. In this case, fluids of distinct compositions have the potential to precipitate REE-minerals and to modify pre-existing REE mineralizations.

In summary, REE-deposits in carbonatites are divers and often show a multi-stage origin. The REE mineralizations in a single orebody can be highly variable and depend on temperature, pressure, pH and fluid composition (e.g., Cooper et al., 2015). REE mineralizations can be of primary magmatic origin, but many REE mineralizations in carbonatites are attributed to changes in REE speciation and complexation during the transition from magmatic to hydrothermal/carbothermal stages (Haas et al., 1995).

The present thesis deals with the Palabora Carbonatite Complex (South Africa) and the Kaiserstuhl Volcanic Complex. The former is one of the deepest emplaced carbonatite occurrences world-wide and is associated with a prominent phoscorite occurrence. The latter reflects a subvolcanic emplacement including several geometrically distinct carbonatite bodies, but no phoscorite association. Due to extensive sampling campaigns and the provision of available drill core material, the investigation of the Palabora and Kaiserstuhl Complexes, which will be described in more detail below, is a unique opportunity for a systematic study on mineral variations in carbonatitic systems. This study will further advance the knowledge and understanding concerning the emplacement and evolution of carbonatites and their associated REE mineralization.

1.5 Regional geology of the studied complexes

1.5.1 Palabora Carbonatite Complex (PCC)

Palabora represents a kidney-shaped, pipe-like complex of Proterozoic age (2060 Ma; Reischmann, 1995), which intruded the Archean granite-gneiss basement of the north-eastern Kaapvaal craton (Wu et al., 2011). The complex covers an area of about 12 km² next to the city of Phalaborwa (Limpopo province, South Africa). The tripartite intrusion is dominated by different types of pyroxenite and is divided into a northern and southern pyroxenite, and the central Loolekop pipe. Only the latter comprises a 1.3 x 0.8 km sized circular structure consisting of carbonatites and phoscorite.

Phoscorite (FOS), for which Palabora represents the type locality, is strongly interwoven with banded carbonatite (BCB). This association, in turn, is transected by a transgressive carbonatite (TCB). Newly discovered carbonatite veins of increasing frequency with increasing depth, indicate another (hidden) carbonatite body in the centre of the southern pyroxenite. Carbonatites of the Palabora complex are generally sövitic. Marginal zones of the pyroxenite intrusion (dominantly micaceous pyroxenite, MPY) experienced an interaction with the basement during emplacement that resulted in the formation of a feldspathic pyroxenite (FPY). The surrounding basement was fenitized (Fenite - FEN). Within the immediate vicinity of the complex syenites intruded as satellite bodies and dolerite dykes (mostly Proterozoic; Wu et al., 2011) crosscut the entire region. Correlations to the extrapolated sediment cover yielded an emplacement depth of about 15 km (Eriksson, 1982), which defines Palabora one of the deepest known carbonatite complexes world-wide. Furthermore, it is suggested that the primary magma that formed the carbonatite complex was derived from an enriched mantle source and that the magma was generated by the same mantle plume activity that caused the formation of the Bushveld Complex (Wu et al., 2011).

The Palabora carbonatite is the only carbonatite world-wide that is primarily mined for copper. Besides copper, the complex is mined for apatite and magnetite. Due to intensive mining over more than 50 years, the Palabora Mine represents one of the deepest open pit mines in the world. After reaching the economic level of the open pit (2003), an underground mine was constructed. As a result of an intensive drilling campaign, the complete sampling of a vertical profile of about 2000 m through the Loolekop pipe was possible. While those drillings verify a continuity of the complex to a depth of at least 2 km, gravity data expand the continuity to a depth of at least 5 km (Eriksson, 1982).

1.5.2 Kaiserstuhl Volcanic Complex (KVC)

The Kaiserstuhl represents a Miocene (18-15 Ma; e.g., Kraml et al., 2006) volcanic to subvolcanic complex, which is situated in the Upper Rhine Graben, an area that is characterized by lithospheric thinning (Bourgeois et al., 2007; Edel et al., 2006; Hüttner, 1996). Furthermore, the Upper Rhine Graben is featured by numerous partly deep-reaching listric and steep fault sets that are mostly subparallel to the graben geometry and typically form a horst and graben structure including variably sized tectonic blocks and relay ramps (e.g., Beccaletto et al., 2010).

The rocks of the KVC mainly consist of tephritic to phonolitic rocks, and minor nephelinitic, limburgitic, melilititic, haüynitic rock series (e.g., Baranyi et al., 1976; Braunger et al., 2018; Keller et al., 1990; Wimmenauer, 2003). Carbonatites emplaced in the centre of the complex (e.g., Schleicher et al., 1990; Wang et al., 2014), where they are exposed as four major carbonatite bodies (Badberg, Degenmatt, Haselschacher Buck, Orberg), spatially associated with polygenetic breccias. Additionally, two smaller occurrences (<10 m in diameter) are situated at the Katharinenberg and Kirchberg. All carbonatite bodies are sövitic with minor, alvikitic and beforsitic dykes (cm- to m thick) crosscutting all rock types (Katz-Lehnert, 1989; Sommerauer and Katz-Lehnert, 1985). Field observations and geophysical data (Brauch et al., 2018 and references therein) identified an intersection of the KVC by the regional Tuniberg normal fault, with a westwards down-throw of a vertical displacement between 1000 and 3000 m (Beccaletto et al., 2010; Groschopf et al., 1996), separating the Badberg from the other sövite bodies. While the pipe-like Badberg sövite (400 m thick, inclined ~60° towards NW) shows no evidence to continue at greater depth, a continuous pipe-like system is indicate below the Degenmatt and Haselschacher Buck (Brauch et al., 2018). Furthermore, the Badberg contains numerous cm- to m-sized rafts of calcite foidolites (xenoliths). Sövites at the Orberg display variable geometries including sills, sheet-like bodies and irregular cauliflower-like structures, that are strongly associated with polygenic breccias. These breccias probably promoted an intrusion into zones of weakness (Hubaux, 1964). At Henkenberg and Kirchberg alternating sequences of carbonatitic lavas, crystal tuffs and lapillistones (three 1 to 1.5 m thick layers, interbedded with silicate pyroclastics) are exposed (Keller, 1978; Keller, 1981; Keller, 1989). The KVC sövites only experienced a historical, small-scale mining on Nb during which, 4 boreholes with a depth between 100 to 500 m were drilled. Today the area is a protected natural habitat.

2. OBJECTIVES AND EXPECTED OUTPUTS

2.1 Studies on the main topic of this dissertation

Although carbonatites represent a high economic potential, their mode of emplacement and processes that cause variations in their mineralization are not yet fully understood. However, the interest to understand such processes has increased significantly during the last years. Thus, our studies on the Palabora (South Africa) and Kaiserstuhl Complex (Southwest Germany) contribute to a better understanding of carbonatitic systems, their emplacement and mineralization. Carbonatites from Palabora (e.g., Aldous, 1980; Eriksson, 1982; Hanekom et al., 1965; Palabora Mining Company, 1976; Wu et al., 2011) and the Kaiserstuhl (e.g., Braunger et al., 2018; Keller, 1981; Teiber et al., 2015; Walter et al., 2018; Wang et al., 2014; Wimmenauer, 2003) have been subject to previous investigations, but no detailed and systematic studies on their mineralogy and mineral chemistry were available to date. Therefore, a comprehensive data set of the mineralogical inventory and the compositional variation of major minerals in carbonatites of these complexes is generated. In addition to a detailed textural, mineralogical and mineral chemical characterization of the carbonatites (and phoscorite), this thesis focuses on the following aspects of the individual studies.

2.1.1 The orthomagmatic, late-magmatic and post-magmatic REE mineralization, and its significance in carbonatites

Title of publication:
The Multistage REE Mineralization of the Palabora Carbonatite Complex, South Africa.
(Study A)

This study is driven by the following major questions:

- How does the mineralogy, and especially the paragenetic sequence of REE minerals, change between the carbonatites and phoscorite?
- What are the different stages and related formation processes that caused a distinct REE mineralization?
- Which processes caused a REE mineralization how effectively?
- How do different processes affect an existing REE mineralization?
- Which mechanisms lead to an effective REE mineral alteration and REE redistribution?

2.1.2 The relationship of carbonatites and phoscorites based on phlogopite and apatite composition including a new emplacement model

Title of publication:

A model for the formation of carbonatite-phoscorite assemblages based on the compositional variation of mica and apatite from the Palabora Carbonatite Complex, South Africa. (Study B)

This study is driven by the following major questions:

- How are carbonatites (BCB and TCB), phoscorite and silicate rocks genetically related to each other?
- Why did carbonatites and phoscorites emplace late into silicate rock-dominated complexes?
- How do phoscorites form?
- Why do some carbonatite complexes lack any associated silicate rocks?
- Is it possible to create a petrogenetic model which explains the volumetric relationship between carbonatites, phoscorites and silicate rocks?

2.1.3 Mineralogical and mineral chemical variations in carbonatites due to magma-wall rock interactions

Title of publication:

Evidence for magma – wall rock interaction in carbonatites from the Kaiserstuhl Volcanic Complex (Southwest Germany). (Study C)

This study is driven by the following major questions:

- How does the mineralogy of the different sövite bodies of the KVC vary?
- Which features can be used to track contamination in carbonatites?
- How can we identify whether a silicate mineral in a carbonatite formed by (I) a pristine sufficiently high silica activity or (II) a change in silica activity by contamination, or whether (III) it is entrained as a xenocryst?
- Are uncontaminated carbonatites capable of crystallizing higher amounts of silicates, especially mica?
- What effects does contamination by silicate-rich wall rocks have on the REE mineralization of carbonatites?

2.2 Further co-authored publication on the petrogenetic significance of interactions with carbonatite-derived fluids

A further study contributes to the main topic of the thesis. These study are supposed to provide comparisons and additions to the above described publications (especially study A) in order to highlight the previous results and bring them into a broader context.

Title of publication:
Hydrothermal processes in the Fen carbonatite complex, southern Norway. (Study D)

This study is driven by the following major questions:

- Which processes formed the mineralization of the Fen carbonatites?
- How do the different processes affect each other with respect to their mineralization?

3. RESULTS AND DISCUSSION

3.1 The orthomagmatic, late-magmatic and post-magmatic REE mineralization, and its significance in carbonatites

Title of publication:
The Multistage REE Mineralization of the Palabora Carbonatite Complex, South Africa. (Study A)

This study is based on a collection of about 400 drill core samples from 6 drill holes that combine to a vertical profile of about 2000 m. For analytical work 45 representative samples (20 TCB, 15 BCB, 10 FOS) have been chosen from the sample set. The samples were texturally investigated in much detail and all (10) relevant REE minerals and their different generations were analysed by electron micro probe (341 analyses). The analytical data was primarily used to identify the different REE minerals and to distinguish different mineral generations by mineral composition. This distinction is based on a comparison of texturally characterized mineral phases and their mineral composition. Furthermore, this compositional distinction was especially important for mineral assemblages, where a clear textural distinction was not possible.

Our study has proven that phoscorites, and both carbonatite types (BCB and TCB) generally contain the almost same mineral assemblages in the same crystallization sequence, only modal abundances and textural features are variable. While phoscorites are dominated by early orthomagmatic minerals (e.g., olivine, apatite, phlogopite and magnetite), carbonatites commonly contain larger amounts of later orthomagmatic minerals (e.g., carbonates). The frequency of very early magmatic minerals (e.g., olivine and thorianite) and in general silicates (olivine and phlogopite) is higher in BCB than in TCB. A detailed investigation of the individual mineral generations and mineral assemblages has shown that the Loolekop has experienced four different evolutionary stages. This includes an orthomagmatic, a late-magmatic (hydrothermal), sulphide and post-magmatic (hydrothermal) stage, which can be observed in phoscorites as well as both carbonatites with a particularly strong late-magmatic effect on TCBs.

A combination of orthomagmatic and subsequent late-magmatic hydrothermal stages is typically observed in carbonatites of various complexes (e.g., Bear Lodge and Wicheeda; Moore et al., 2015; Trofanenko et al., 2016). Later hydrothermal post-magmatic stages are also common (e.g., Amba Dongar; Doroshkevich et al., 2009). Therefore, the individual evolutionary stages of carbonatites of the Palabora complex can be used as a generalized example for a typical formation and redistribution of REE minerals in carbonatitic systems, while, of course, compositional variation of the original magma and involved fluids can initiate relevant mineralogical differences. For this purpose, the different stages are first characterized and then compared with respect to their significance for the REE mineralizations.

The orthomagmatic stage is characterized by an early formation of forsteritic olivine, apatite, baddeleyite and thorianite, and first REE minerals (fergusonite and REE-Ti-betafite). However, the REE minerals are rare and form only small crystals. This mineral association is followed by the formation of phlogopite and the beginning of titanomagnetite crystallization coprecipitating with minor amounts of spinel and ilmenite. Additional spinel and ilmenite exsolved from titanomagnetite during cooling. The precipitation of Mg-rich calcite, which later exsolved wormlike dolomite, already started during the final stages of apatite formation, but its main crystallization stage took place relatively late in the crystallization sequence. Discrete dolomite crystallized during the intermediate stage of calcite formation. Contemporaneously to the main calcite crystallization, REE-, Ba- and Sr-carbonates such as bastnäsite, strontianite

and barytocalcite formed. Furthermore, there are indications (see below) that carbocernaite and/or burbankite formed at this late orthomagmatic stage as is typical for other carbonatite complexes, but these phases were commonly replaced by later REE minerals (Wall et al., 1997; Zaitsev et al., 1998).

The late-magmatic stage is interweaved with the orthomagmatic stage and probably represents the result of an interaction of orthomagmatic minerals with a residual aqueous-carbonic fluid that was released by the carbonatite itself. This stage is characterized by a serpentinization of olivine and a replacement of olivine by chondrodite. The formation of serpentine or chondrodite certainly depends on the enrichment of F in the late-magmatic fluid, which in turn is most likely dependent on the mobilization of F by apatite dissolution. Furthermore, chloritization of orthomagmatic phlogopite, formation of secondary apatite and precipitation of tetraferriphlogopite (see study B) as well as monazite and britholite is observed. Monazite replaced apatite as thin rims or occasionally even completely by dissolution-reprecipitation reactions. Although orthomagmatic apatites incorporated significant concentrations of REE (Ø 8000 ppm), mass balance considerations demonstrate that these concentrations are not sufficient to provide enough REE for monazite precipitation. Therefore, an additional introduction of REE was essential for the formation of monazite. Britholite, in contrast, crystallized either at the expense of olivine, where it usually formed rims around olivine- serpentine/chondrodite assemblages, or less frequently in contact with phlogopite-chlorite assemblages.

Britholite was only rarely found as a discrete crystal in vein-like structures, where it occurs together with tetraferriphlogopite (see Study B). Usually, britholite occurrences worldwide indicate a primarily hydrothermal origin, replacing apatite or monazite and obtaining Si from the fluid itself (Budzyń et al., 2011; Uher et al., 2015). However, since britholite in Palabora was formed only after the provision of Si by the alteration of orthomagmatic silicates (olivine and phlogopite), it can be assumed that the mineralization fluid was originally low in Si and was only enriched during the alteration of silicates. The Si-enriched fluid might later form the discrete britholite crystals together with tetraferriphlogopite. As britholite mainly represents fluorbritholite-(Ce), it can also be assumed that the involved fluid must have been sufficiently enriched in F. Finally, the formation of a particular type of REE mineral was locally dependent on the availability of P or Si, provided by the alteration of orthomagmatic silicates or

phosphates. Monazite is the dominant REE phase of this stage due to the high abundance of apatite and minor abundance of olivine.

Between the late-magmatic and the post-magmatic stage, a sulphide stage occurs. This sulphide stage is characterized by an injection of a sulphide-rich liquid which causes the extensive Fe-Cu sulphide mineralization of the Palabora complex. But, since this stage does not lead to an REE mineral formation or redistribution, it is not further discussed in this study. However, it should be mentioned that a corresponding inclusion of previous REE minerals (e.g., late-magmatic monazites and orthomagmatic REE-fluorocarbonates) in sulphide phases prevents alteration of these minerals by subsequent processes of the post-magmatic stage.

The post-magmatic stage caused a strong alteration of previously formed minerals (e.g., valleriitization of sulphides, recrystallization of carbonates) and a significant redistribution of certain elements (e.g., Sr and Th, but especially REE). Carbocernaite and/or burbankite are completely replaced by post-magmatic cordylite and ancylite, which are strongly associated with strontianite and baryte. Orthomagmatic bastnäsite is either replaced by a mixture of parisite, synchysite, strontianite and occasionally fluorite, or strongly dissolved with only few relicts that witness a former presence of bastnäsite. The alteration of late-magmatic REE minerals (dominantly represented by monazite) is also characterized by strong dissolution and (only for monazite) an additional replacement by a REE-poor apatite (mobilization of REE). Occasionally the formation of post-magmatic apatite at the expense of monazite is associated with the simultaneous formation of bastnäsite needles. It is suggested that this feature is caused by a REE oversaturation of the fluid during the remobilization of REE by alteration, and hence, indicates the fertility of the fluid. The remobilized element budget finally precipitates as a range of different REE minerals in carbonate veins due to fluid cooling. While the alteration of former REE phases can be seen as a proximal mineralization of the post-magmatic fluid, the recrystallization of the remobilized element budget in veins can be described as the corresponding distal mineralization. This distal mineralization is dominated by bastnäsite and ancylite, which are often associated with further secondary magnetite, strontianite (in absence of ancylite) and thorianite or thorite.

The formation of secondary Th minerals (thorianite and thorite) is typical for those hydrothermal low temperature mineralizations. Since Th was mobilized during the alteration of REE minerals (with certain amounts of Th), but also of primary Th minerals

(e.g., orthomagmatic thorianite), and Th cannot easily be incorporated into secondary REE minerals at significantly lower temperatures (Budzyń et al., 2010; Doroshkevich et al., 2008; Read et al., 2002), Th precipitates as discrete Th minerals. This is evidenced by a comparison of mineral compositions of the different REE mineral generations and represents an important indicator to distinguish those mineral generations.

Finally, an important post-magmatic mineral of both proximal and distal mineralization is anzaite. The identification of anzaite in Palabora represents the second occurrence of anzaite [$REE_4FeTi_6O_{18}(OH)_2$] world-wide, with the type locality being the Afrikanda complex (Russia; Chakhmouradian et al., 2015). The formation of anzaite is dependent on the availability of Ti, which is obtained by the alteration of ilmenite. If REE are already sufficiently enriched in the fluid, ilmenite is simply replaced by anzaite (proximal mineralization). Otherwise, ilmenite is dissolved by the fluid and Ti is remobilized. Such a remobilization of Ti is usually ascribed to very low pH fluids containing sufficient F as complexing agent (e.g., Van Baalen, 1993). But those conditions are considered to be unlikely for the post-magmatic fluid. Alternatively, Manning (2004) pointed out that Ti can be transported by complexing agents of polymerized silicate molecules (e.g., Ti-aluminosilicate complexes; Beitter et al., 2008; Tropper and Manning, 2005). Since the post-magmatic fluid causes a strong valleriitization of sulphides and precipitation of serpentine (independent on the presence of silicate minerals), which both require a certain concentration of mobilized Al and Si, respectively, it can be concluded that adequate amounts of these complexing agents are available. A direct indication is the rapid sequential formation of valleriite (consumption of Al), serpentine (consumption of Si) and subsequent precipitation of anzaite by the loss of complexing agents.

Since the post-magmatic fluid did not cause an intensive alteration of pre-existing silicate phases, but caused a significant formation of serpentine and tetraferriphlogopite, it can be assumed that this fluid was, in contrast to the late-magmatic fluid, already enriched in Si. On the other hand, the strong alteration and dissolution of orthomagmatic and late-magmatic REE minerals, and remobilization of REE instead of precipitation, indicates that the involved fluid was originally low in REE and was only enriched during the alteration of REE minerals. A comparison of the late-magmatic and post-magmatic fluid further reveals the importance of the late-magmatic fluid to initiate the REE mineralization of Palabora. The post-magmatic fluid, in contrast,

caused an effective alteration of pre-existing mineral phases and redistribution of REE minerals due to remobilization and reprecipitation processes.

The lack of REE in olivine and low/insufficient REE content in apatite (see above) reflects the necessity to import REE into the system during the late-magmatic stage to precipitate REE minerals (britholite and monazite). While not only late-magmatic, but also late orthomagmatic REE minerals were altered during the post-magmatic stage, early orthomagmatic REE minerals were frequently preserved in subsequently formed mineral phases (e.g., magnetite), similar to REE minerals enclosed in sulphides (see above). Nevertheless, it should be noted that, very similar to what is observed in other carbonatite complexes, due to its high modal content, apatite represents the main REE host at the PCC (Dawson and Hinton, 2003). However, the economic character of a carbonatite is dependent on the occurrence of discrete REE minerals (e.g., bastnäsite and monazite) due to the processability of these mineral phases.

3.2 The relationship of carbonatite and phoscorite magmas during emplacement based on phlogopite and apatite mineral chemistry including a new emplacement model

Title of publication:

A model for the formation of carbonatite-phoscorite assemblages based on the compositional variation of mica and apatite from the Palabora Carbonatite Complex, South Africa. (Study B)

This study is based on the same sample set that was used in study A and the same selected samples were analysed in this study. In addition, we added three samples of associated silicate rocks (2 MPY, 1 FEN). As mica and apatite occur as major constituents in all rock types of the Loolekop deposit, textural and mineral chemical variations in these minerals are used to shed light into the relations between the different lithologies. For this approach about 450 mica and 550 apatite electron micro probe analyses were acquired.

Mineral chemical analyses have shown that 5 different types of mica can be distinguished in the carbonatites (TCB and BCB), phoscorite and silicate rocks at Palabora. These types include common phlogopite (Fe^{2+}-poor; type I), mica of the phlogopite-kinoshitalite ($K^{+}+Si^{4+}\leftrightarrow Ba^{2+}+{}^{IV}Al^{3+}$; type II), phlogopite-eastonite

($Mg^{2+}+Si^{4+}\leftrightarrow {}^{VI}Al^{3+}+{}^{IV}Al^{3+}$; type III), phlogopite-annite series / biotite ($Mg^{2+}\leftrightarrow Fe^{2+}$; annite component >20%; type IV), and tetraferriphlogopite ($^{IV}Al^{3+}\leftrightarrow {}^{IV}Fe^{3+}$; type V). Mica of type I-IV are interpreted to be of magmatic origin, whereas tetraferriphlogopites (type V) indicate a late-magmatic hydrothermal origin. Our study pointed out that the different types of mica are limited to specific rock types (except tetraferriphlogopite). Type I mica occur exclusively in BCB and FOS. Type II mica exclusively occur in TCB. Mica type III is limited to sections of BCB and FOS that are in contact or close to a contact to TCB and were interpreted as a product of an interaction with TCB melt. Mica type IV (biotites) exclusively occur in pyroxenites. This is in accordance to mica composition of other carbonatite complexes, where silicate rocks are associated with carbonatitic rocks and biotite exclusively occur in the silicate rocks (e.g., Brod et al., 2001). Tetraferriphlogopites (mica type V) typically occur in late-stage rocks, crystallizing at lower temperatures (Fleet, 2003; Lee et al., 2003), forming rims with sharp compositional changes to pre-existing phlogopite cores (e.g., Brod et al., 2001) or completely new individual crystals (e.g., Lee et al., 2003). Tetraferriphlogopite from Palabora crystallized as new individual crystals in veins, where it is occasionally associated with aggregates of (rarely euhedral) britholite and apatite-monazite dissolution structures (see study A) that are both aligned parallel to the vein-like orientation of tetraferriphlogopites. Hence, it is assumed that tetraferriphlogopite, britholite and monazite formed contemporaneously during the late-magmatic stage (characterized in study A) in TCB, BCB and FOS, decoupled from the orthomagmatic mica formation.

The majority of apatites (in FOS, BCB and TCB) depicts a large compositional overlap with generally low concentrations of REE, Si, Sr and Na (all <0.05 apfu) and are interpreted to be orthomagmatic. In contrast, there are a few outliers exhibiting higher REE concentrations (up to 0.15 apfu), which are suggested to represent late-stage apatites. The REE enrichment results from different coupled substitution mechanisms, namely britholite substitution ($P^{5+}+Ca^{2+}\leftrightarrow Si^{4+}+REE^{3+}$ in FOS and few BCB) and belovite substitution ($5Ca^{2+} \leftrightarrow Na^{+}+3Sr^{2+}+REE^{3+}$ in BCB and TCB), which probably dependent on the availability of Si and Sr in late-stage fluids. Interestingly, these outliers occur in samples which are characterized by the occurrence of late-stage mica type V (tetraferriphlogopite) and hence confirm the assumption of study A that late-magmatic fluids introduced a REE mineralization.

In this terms, the compositional variations of both, phlogopite and apatite reflect the multistage evolution of the Loolekop deposit, with the availability of Al being a prominent factor controlling the mica composition. However, neither phlogopite nor apatite show systematic compositional changes with depth (over a profile of >2000 m), which evidences the absence of a vertical zonation. Furthermore, the obtained data point out that compositional variations in mica are much more useful to reconstruct magmatic differentiation processes than apatite at Palabora. Magmatic apatites plot unsystematically in a defined cloud without clear indications, with respect to composition. Additionally, the distinct mica compositions provide information about the relations between the different rock types at Palabora.

The nearly identical mica mineral chemistry of BCB and FOS, their identical mineralogy but different modal composition (see study A) and strong structural relations (strongly intercalated into each other) indicate a genetic dependence of these rock types. While fractional crystallization cannot explain an analogous compositional development of mica in BCB and FOS, liquid immiscibility seems to be the most likely process that might have formed the phoscorite. This has also been described from other carbonatite-phoscorite associations (e.g., Catalão I+II, Sokli; Brod et al., 2001; Lee et al., 2003). Further observations on other carbonatite-phoscorite complexes strengthens the assumption that liquid immiscibility plays a key role for phoscorite formation. Those observations include orbicular and spherulitic phoscorite fractions in carbonatites and vice versa (e.g., Krasnova et al., 2004b; Lapin and Vartiainen, 1983) and studies of mineral inclusions in olivine and apatite (Mikhailova et al., 2002). Melt inclusions evidence that the parental magma of some carbonatites was enriched in Fe and/or P (e.g., Chen et al., 2013; Guzmics et al., 2008; Krasnova et al., 2004b). Phoscorites, in turn, contain melt inclusions dominated by various carbonates (Veksler et al., 1998; Zaitsev and Kamenetsky, 2013). In contrast, TCB as well as associated silicate rocks (MPY, FEN) reflect a completely different mica composition, which indicates a separate evolution of these lithologies with TCBs representing a higher evolved carbonatite magma compared to BCB.

Anyhow, the assumption that carbonatite-phoscorite associations are formed by liquid immiscibility raises the question of a parental magma, its origin and mode of intrusion. Furthermore, it is of utmost interest to compare the variable ratios of carbonatites and phoscorites between different complexes in order to point out dependencies, e.g. with depth. Interestingly, a few studies have shown that there is a depth dependency

between the proportions of carbonatites and silicate rocks (Arzamastsev et al., 2000) as well as certain mineralogical variations (Frolov, 1971). But individual mechanisms are only unsatisfactorily known. This has driven us to develop a model based on the existence of a parental melt for carbonatites and phoscorites, which explains the rock associations in carbonatite complexes. For this purpose it must be considered that previous isotope studies indicate that neither fractional crystallization nor liquid immiscibility can be attributed to the formation of associated silicate rocks and carbonatites/phoscorites at Palabora (Eriksson, 1982). Accordingly, we suggest a contemporaneous emplacement of both lithologies but no genetic link between them. Such genetic independence of spatially associated carbonatites and silicate rocks in alkaline complexes is frequently suspected (Gittins and Harmer, 2001).

We suppose that carbonate-rich melts that are generated in the lithospheric metasomatized mantle at depths >70 km (e.g., Wyllie and Lee, 1998) by low degree partial melting (<5%; e.g., Dasgupta et al., 2007; Gudfinnsson and Presnall, 2005) are enriched in Fe and especially in P (in the upper mantle) due to the preferred partition of these elements into carbonatites (Jones et al., 1995; Lindsley and Epler, 2017; Naslund, 1983). A remixing with silicate melt is prohibited by the liquid immiscibility, which further supports the separation of these two melts. The enrichment of Fe and P finally forms carbonate-phosphate/iron-oxide-rich (CPIO) melts, which can be considered as the required parental melts for carbonatites and phoscorites. The pristine carbonatite melt provides a buoyancy due to its low densities (typically 2.2-2.6 g/cm³; e.g., Dobson et al., 1996; Genge et al., 1995; Kono et al., 2014; Wolff, 1994) within the much more voluminous silicate melt accumulation. But by the enrichment of Fe and P the CPIO melt becomes increasingly denser, resulting in a loss of buoyancy and a state of density equalization. As a result of a depressurization-related magma ascent, the CPIO melt is dragged together with the silicate melt into an ascending channel (activated weakness zones) and introduced into crustal levels. The introduction timing (relative to the first introduction of silicate melt) is dependent on the distance between the CPIO melt body and the ascending channel. Therefore, these channels were commonly already passed by silicate magma prior to the intrusion of the CPIO melt. Due to decreases in temperature and pressure during ascent, a Fe and P-rich melt (phoscorite) and carbonate-rich melt (carbonatite) finally segregates from the CPIO melt. This segregation can additionally be supported by the presence of larger quantities of F in the parental melt (Hou et al., 2017). Lindsley and Epler (2017)

pointed out that discrete iron-oxide melts (low in Ti) are not stable below 1000 °C even in the presence of fluxes such as P, F and C. It must, therefore, be assumed that the phoscorite melts starts to crystallize very soon after segregation, which is additionally supported by the fact that C is generally the most important flux (Lindsley and Epler, 2017) and remains in large quantities in the carbonatite magma during segregation. Hence, it can be assumed, that larger quantities of phoscorite only occur in relatively deep emplacement depth, where segregation took place. Medium to shallow emplacement depth of carbonatite complexes may consequently be characterized by rather low amounts or complete absence of phoscorites, which is confirmed by the absence of any extrusive phoscorites (Krasnova et al., 2004b). The simultaneous/directly subsequent crystallization of early carbonatite (e.g., BCB) causes the typical intercalation with phoscorite, while crystal fractionation produces higher evolved carbonatite magmas (e.g., TCB). The segregation and differentiation processes initiate a substantial density contrast between the high density phoscorite and low density carbonatite melts, which may cause a “jet-like” ascent of the residual carbonatite melt. Since silicate melts have relatively high viscosities and higher solidus temperatures in contrast to carbonatitic melts, their magma activity may already have ebbed in certain crustal levels. Rapidly ascending extremely low viscose carbonatites (Treiman and Schedl, 1983) may pass through those silicate magma fronts ascending to higher emplacement levels, where the intruding carbonatite magma forms carbonatite complexes without a silicate rock association. About 20% of carbonatite occurrences reflect such silicate rock-free complexes and, confirmatively, most of them (where an emplacement depth is known) represent rather shallow intruded carbonatites (Woolley and Kjarsgaard, 2008). However, it must be noted that the sequence of characteristic carbonate-phoscorite-silicate rock ratios in certain emplacement depths can be variable. These ratios strongly dependent on factors such as crustal thickness, geological setting (e.g., inter-cratonic or rift zone) and the timing of silicate magma chamber formation within the crust. The typical sequences of rock associations in carbonatite complexes are thus controlled by the source-emplacement-distance (ΔS-E).

In this context, it can be assumed from our generalized model that deeper crustal regions, relatively close to the melt source (low ΔS-E), are characterized by higher volumetric proportions of ultramafic silicate rocks and lower amounts of carbonatitic rocks. Additionally, these complexes display a relatively high phoscorite-carbonatite

ratio. Conclusively, an increase of the ΔS-E entails a decrease in phoscorite-carbonatite ratios, and a decrease in silicate-carbonatite ratios, until the carbonatite proportion of a complex exceeds the silicate proportion and finally pure carbonatite complexes occur.

3.3 Mineralogical and mineral chemical variations in carbonatites due to magma – wall rock interactions

Title of publication:

Evidence for magma – wall rock interaction in carbonatites from the Kaiserstuhl Volcanic Complex (Southwest Germany). (Study C)

This study is based on a collection of about 400 surface outcrop and drill core samples (2 historic drill holes). For analytical work 48 representative samples have been chosen from the sample set. A detailed textural investigated was carried out and all major minerals and relevant minor minerals were analysed by electron micro probe (apatite [N≈520], mica [N≈620], magnetite [N≈260], carbonates [N≈380], clinopyroxene [N≈130], garnet [N≈200], olivine [N≈36], monticellite [N≈19]). The selected samples represent the four major (Badberg, Degenmatt, Haselschacher Buck and Orberg) and one minor (Katharinenberg) intrusive carbonatite bodies, as well as two extrusive carbonatite occurrences (Henkenberg and Kirchberg). The analytical data was used to identify compositional variation in minerals of the different carbonatite bodies.

Since mica and apatite are typically used to indicate different processes within carbonatitic systems (e.g., see study B) we used these minerals to reveal processes that are in relation to the mineralogical variations between the carbonatite bodies of the KVC. Macroscopically, the Badberg sövites differ from the other KVC carbonatites due to the presence of cm- to m-sized silicate rock inclusions (xenoliths), which can be best described as calcite foidolites. Furthermore, the Badberg is the only sövite body of the Kaiserstuhl that contains clinopyroxene. In general, besides calcite, sövites of the Kaiserstuhl contain, apatite, mica, variable amounts of spinel group minerals of the magnesioferrite-magnetite series, pyrochlore, occasionally olivine (Katharinenberg and Haselschacher Buck only), monticellite (Orberg only), zirconolite (Haselschacher Buck only) and a range of sulphides (trace minerals).

Similar to the Badberg, also some extrusive carbonatites (crystal tuffs) of the Henkenberg location include xenolitic calcite foidolites. Other extrusive carbonatites

contain xenocrysts of nepheline (lava from Kirchberg), garnet (lava from Kirchberg, lapillistones and crystal tuffs from Henkenberg) and clinopyroxenes (lapillistones and crystal tuffs from Henkenberg).

Calcite foidolite (xenolith) itself contains large amounts of a mixture of various zeolite minerals, calcite, mica and other minerals that have almost completely replaced (post-magmatically) former foid minerals (nosean or haüyne). In addition, relicts of alkali feldspar can rarely be observed. Relictic garnet cores occur enclosed in anhedral masses of recrystallized garnet, while clinopyroxenes have been completely recrystallized as subhedral and interstitial grains. Since most minerals of the calcite foidolite are completely replaced or recrystallized, it is difficult to identify its protolith. However, a comparison of relicts of the original garnet with the garnet composition of other KVC rock types indicates that nosean syenite represents the most probable candidate. The occurrence of alkali feldspar relicts, foids and clinopyroxene confirm this suggestion. Furthermore, those nosean syenites directly underlay the tilted Badberg body.

The contact between sövite and the enclosed calcite foidolites is characterized by a black-wall-like seam of coarse-grained khaki to olive-green mica. This mica seam occasionally surrounds a transition zone (outer rim of calcite foidolites) that is characterized by strongly altered clinopyroxene and garnet and high proportions of calcite, which typically intruded as carbonatitic veins into the xenoliths. This contact indicates at least a marginal resorption of the calcite foidolites by the carbonatitic magma, which is accompanied by a metasomatic alteration of the remaining xenoliths and has caused the recrystallization of corresponding minerals (see above). A resorption of xenoliths is further indicated by an increasing disaggregation of xenoliths in a margin-centre profile of the pipe-like structure of the Badberg carbonatite. This feature could be assigned to a longer persisting heat flow in the central area and an earlier cooling in the marginal zones of the carbonatite pipe.

In addition to the stubby coarse-grained black wall mica, which occasionally covers large portions of the carbonatite around the xenoliths, the Badberg sövite also contains large-sized bundles of mica laths that occur independently of the presence of silicate rock xenoliths. Although these two types of mica in the Badberg sövite differ slightly in their composition, they are, as a whole, clearly separated texturally and compositionally from micas of the other carbonatite occurrences of the KVC. While the Badberg is commonly very mica-rich, with mica up to a size of 2 cm, the other locations

are generally mica-poor and contain significantly smaller mica crystals (<2 mm). Compositionally, mica of the Badberg differs from mica of the other KVC carbonatites mainly by a considerably higher Fe^{2+} and increased Mn content. In general, mica of the Kaiserstuhl is characterized by a combination of the kinoshitalite ($K^{+} + Si^{4+} \leftrightarrow Ba^{2+} + {}^{IV}Al^{3+}$) and eastonite substitution ($Mg^{2+} + Si^{4+} \leftrightarrow {}^{IV}Al^{3+} + {}^{VI}Al^{3+}$). Most micas (with exception of the Badberg) are dominated by the kinoshitalite substitution. Badberg mica, in contrast, is dominated by the eastonite substitution. This indicates an excess of Al over Ba in the Badberg carbonatite.

Apatites also depict a strong variability between carbonatites of the Badberg and other KVC localities. The composition of Badberg apatite cores is very similar to the apatite composition of the other carbonatite localities and differs only by an increased Sr content (with few Orberg apatites also have an increased Sr content). In contrast, the composition of Badberg apatite rims differs strongly from those of the other apatites. These rims experienced a strong britholite substitution ($Ca^{2+} + P^{5+} \leftrightarrow REE^{3+} + Si^{4+}$) and thus an enrichment of REE. This enrichment increases further from the margin to the centre of the pipe-like structure of the Badberg carbonatite. In contrast, some Orberg apatites show an increased concentration of Na and a subordinate belovite substitution ($2Ca^{2+} + \textit{(3Ca}^{2+}\textit{)} \leftrightarrow REE^{3+} + Na^{+} + \textit{(3Sr}^{2+}\textit{)}$). This belovite substitution is also responsible for the above-mentioned enrichment of Sr in Orberg apatites. However, since magmatic processes shall be discussed and a belovite substitution in apatites is predominantly assigned to hydrothermal processes (e.g., de Toledo et al., 2004; Doroshkevich et al., 2009), this should not be considered for now. A pronounced britholite substitution (0.3-0.5 REE+Si pfu) in apatite, in contrast, is not possible in hydrothermal stages (Anenburg et al., 2018; Anenburg and Mavrogenes, 2018) and is attributed to a magmatic phase (>600 °C). A hydrothermal overprint at these high REE contents (4-6 wt.% REE_2O_3) would have led to the formation of REE-poor apatites and discrete REE minerals. In the presence of sufficient Si e.g. cerite (e.g., Anenburg et al., 2018; Anenburg and Mavrogenes, 2018) and in the absence of Si e.g. monazite would have formed (e.g., study A).

In contrast to the enrichment of Sr in apatite, which indicates a higher magmatic evolution (by magmatic differentiation; of the Badberg with respect to the other localities), the sharp contact between core and compositionally variable rim argues against magmatic differentiation as a mechanism for Si and REE enrichment in the rim, for which a continuous transition in mineral chemistry would be expected. Likewise,

the increased occurrence of mica and the exclusive occurrence of clinopyroxene in the Badberg carbonatite cannot be explained by magmatic differentiation, since silicates crystallize in carbonatites quite early and accordingly deplete the magma in SiO_2 by fractionation. All available evidence suggests that the variability of Badberg mineralogy and mineral chemistry depends on the inclusion of calcite foidolites, and the more these calcite foidolites are resorbed and metasomatized, the larger the variability.

A comparison of mineral compositions of the calcite foidolite with mineral composition of the KVC nosean syenite (protolith) demonstrates that certain amounts of Si, Al, K, Fe and Ti must have been released during the replacement of alkali feldspar by foids and the recrystallization of clinopyroxene and garnet. On the other hand, certain amounts of Ca and Mg as well as smaller amounts of Nb and Zr are consumed. This indicates an interaction between the xenoliths and the carbonatitic melt and may explain an abrupt availability of elements that cause corresponding mineral chemical variations in mica (observed at the Badberg). Nevertheless, it remains the question if mineralogical variations were also caused by contamination and thus the increased occurrence of mica and clinopyroxenes in Badberg can be explained.

In general, different silicates are described in carbonatites worldwide (e.g., Reguir et al., 2012), while their presence is strongly dependent on silica activity, which is generally very low in carbonatites (Barker, 2001; Massuyeau et al., 2015). Three main types of silicates are distinguished in carbonatites (modified after Barker, 2001): (1) primary crystallized silicates, which are (a) either formed by sufficient Si in the original melt or (b) by a supply of Si (e.g., by contamination), (2) xenocrysts and (3) subsolidus phases. According to experimental constrains, which suggest a low solubility of Si and Al in carbonatites (<2.9 wt.% SiO_2, <1 wt.% Al_2O_3; Brooker and Kjarsgaard, 2011; Weidendorfer et al., 2017), mass balance calculations based on carbonatite melt densities (2.2-2.6 g/cm³; e.g., Dobson et al., 1996; Genge et al., 1995; Kono et al., 2014; Wolff, 1994) and typical Al and Si contents of mica indicate that a maximum modal amount of about 7 % can be expected to crystallize from a carbonatite without additional Si influx.

Textural features of mica (black wall seams around xenoliths and bundles of long, occasionally filigree laths) indicate an in-situ formation. Compositional overlaps with clinopyroxene from calcite foidolites and structural evidence that clinopyroxene in sövite is not a xenocryst of the calcite foidolite (euhedral in sövite, anhedral in calcite foidolites), as well as the absence of small-scale compositional changes (zoning)

further indicate an in-situ formation of clinopyroxene in the carbonatite. Therefore, neither mica nor clinopyroxene are xenocrysts, but both are crystallized by Si-contamination (silicate type 1b, see above).

This contamination also had a strong effect on apatite. The higher the silica input, the higher the incorporation of Si into apatite and thus the consumption of REE based on britholite substitution (e.g., Hammouda et al., 2010). Furthermore, experimental data (Klemme and Dalpé, 2003) confirm a pronounced partitioning of REE into apatite with increasing SiO_2 content in the melt.

A comparison of main REE-bearing minerals (apatite and pyrochlore) between the Badberg and other KVC sövites has shown that the contamination process has significantly influenced the REE distribution at the Badberg. Most pyrochlore of the KVC sövites (with exception of the Badberg) experienced a late-stage hydrothermal overprint, which strongly enriched this pyrochlore in REE (Walter et al., 2018), whereas the pyrochlore of the Badberg is largely unaffected. This phenomenon may be attributed to an early consumption of REE by the contamination-induced britholite substitution in apatite and thus to a limited availability of REE in late stages. This is in accordance with the occurrence of relatively REE-poor apatite in the sövites, where pyrochlore was hydrothermally enriched in REE.

3.4 Further co-authored publication on the petrogenetic significance of interactions with carbonatite-derived fluids

Title of publication:
Hydrothermal processes in the Fen carbonatite complex, southern Norway. (Study D)

The Fen carbonatite complex experienced at least three different hydrothermal alteration events. Besides a sulphide-rich fluid (fluid 1) that was most likely derived from associated mafic silicate rocks, a REE-rich fluid (fluid 2) and a Si-rich fluid (fluid 3) modified the original mineralogy of the Fen complex. The REE-rich fluid was most likely derived from the carbonatites and represents an autometasomatic fluid. The Si-rich fluid represents most probably an oxidizing meteoric fluid that was in equilibrium with the basement. An interaction of the REE-rich and Si-rich fluids caused an intense alteration of the carbonatites and the formation of the famous rødberg.

Fluid 1 induced a widespread pyrite formation that can be found in all lithologies. Occasionally massive pyrite veins cross-cut the carbonatites. Fluid 2 caused a remobilization and redistribution of Fe and Al and formation of discrete REE minerals dominated by REE-fluorocarbonates. Minor amounts of allanite, monazite, samarskite and aeschynite can be identified. Fluid 3 induced a partial silicification of the carbonatite and an unusual mobilization of phosphorus by the replacement of apatite by quartz, resulting in the formation of apatite and monazite veins. A mixing of fluid 2 and 3 finally caused the formation of iron ores (hematite). A remobilization of preferentially LREE by fluid 3 from pre-existing minerals (formed by fluid 2) resulted in the relative enrichment of HREE in some altered portions of the complex. There are evidences that Nb and Ti were transported together with REE in the evolved carbonatitic fluid. Furthermore, mineral associations and enrichment of Th together with HREE indicate similar behaviour of this elements during the hydrothermal alteration of the carbonatites.

4. SUMMARY, CONCLUSION AND IMPLICATION

Our studies have demonstrated that carbonatites may experience a variety of different processes that may result in distinct variability in both mineralogy and mineral chemistry. The REE mineralization of carbonatites may strongly vary as a function of the absence or involvement of relevant processes as well as their intensity. In fact, orthomagmatic processes within a carbonatite body cause the weakest variations and a subordinate formation of REE minerals. Early orthomagmatic REE mineralizations typically consist predominantly of REE-Ti/Nb oxides (e.g., pyrochlore group minerals; study A & C). Minor REE-Zr phases (e.g., zirconolite; study C) can be detected. Frequently, those early (small sized) mineral phases are included in later crystallizing (much larger) mineral phases and thus often protected from later alteration (study A). Furthermore, REEs are incorporated in apatites and despite a low REE content, apatites may significantly contribute to a whole rock REE enrichment due to their high modal proportions. Late orthomagmatic phases mainly occur as REE carbonates (e.g., bastnäsite, synchisite, parisite, burbankite and carbocernaite; study A). Additionally monazite is rarely described as orthomagmatic phase (e.g., at Mountain Pass; Castor, 2008). Besides, REE may be incorporated in carbonates (e.g., calcite, dolomite). Even

if these carbonates contain rather lower contents of REE, the REE budget of a carbonatite may, similar to apatite, be strongly affected by carbonates due to their high modal content.

Carbonatites are typically associated with phoscorites in several complexes and a genetic relation can be traced by mineral compositional variations, especially in mica (study B). Apatites, on the other hand, are rather poor indicators for such relations, at least at Palabora, as they do not reveal systematic variations. Instead apatites indicate hydrothermal variations (see below). Neither mica nor apatite depict depth-dependent systematic variations over a vertical profile of 2000 m, which reflects a lacking zonation over this range. This is confirmed by a depth profile of 1550 m at Kovdor (Krasnova et al., 2004a). Nevertheless, mica composition emphasizes that the carbonatite-phoscorite association must have been formed by liquid immiscibility, due to the segregation of a parenteral mantle melt (study B). Consequently, phoscorites are mainly present in deeply intruded carbonatite complexes. Carbonatites and phoscorites show a nearly identical mineralogy, which differs only in the modal composition. This is also valid for the REE mineralization. Similarly, mineral composition differs only negligibly. However, due to the very high apatite modal content in phoscorites, REE are primarily incorporated in apatite, with a subordinate occurrence of later formed discrete REE mineral phases.

In general, the orthomagmatic REE mineralization of carbonatites (as well as phoscorites) is not economically relevant with exception of the Mountain Pass carbonatite (e.g., Castor, 2008). In contrast, hydrothermal late-magmatic and post-magmatic processes play a much more important role in the enrichment of REE in carbonatites. In particular, hydrothermal late-magmatic processes are responsible for an enhanced introduction of REE and corresponding REE mineralization. At Palabora, this results in a precipitation of discrete REE minerals at the expense of pre-existing non-REE phases. Additionally, these processes occasionally lead to a modification of apatite (REE enrichment) and to the formation of Al-poor mica. The mineralizing late-magmatic fluid probably originates from the carbonatite itself. Those fluids represent most likely the most common sources for a deposit-quality enrichment of REE-minerals in carbonatites (e.g., Wall and Mariano, 1996). The most common REE minerals are monazite and britholite (study A). Allanite and occasionally REE-carbonates are also known from other carbonatite complexes (e.g., Fen, study D).

Another hydrothermal stage represents the post-magmatic stage, which induced a strong alteration of the pre-existing mineral content and a redistribution especially of the REE. Both orthomagmatic and late-magmatic REE minerals are affected by this alteration and redistribution processes, which form a proximal and distal mineralization. While the proximal mineralization involves alteration or direct replacement of pre-existing minerals, distal mineralization depends on effective mobilization of relevant elements and a subsequent reprecipitation. The most frequent REE minerals of this stage are REE-carbonates (bastnäsite, synchisite, parisite, ancylite, cordylite; study A), as a special feature for the Palabora complex additionally anzaite occurs. According to the strong dependence on the pre-existing mineralogy, an enhanced mobilization, enrichment and redistribution of REE minerals within variable local chemical (micro) environments only occurs if the previous stages have formed appropriate REE phases. On the other hand, the late-magmatic stage can only provide an adequate REE mineralization if enough REE has been enriched in the related fluid. This is of course dependent on the partition of REE (and other relevant elements) between the residual melt and the fluid. An enrichment of REE in a carbonatite melt of the late orthomagmatic stage, in turn, depends on the consumption of REE by early orthomagmatic minerals. In this context, particularly apatite may play an important role (see above).

Similar to the Palabora complex (study A), carbonatites of the Fen complex (study D) also experienced an intense hydrothermal overprint. Involved fluids of both complexes are in some aspects very similar. Both complexes contain REE-rich carbonatite-derived fluids that formed the main REE mineralization. Both complexes contain a Si-rich fluid that caused a significant alteration of pre-existing minerals, and a mobilization and redistribution of their element budget. Although no information could be provided about the origin (certainly not a meteoric) of the post-magmatic fluid of Palabora, an external origin and an equilibrium with the basement could be possible (similar to the Fen complex). Nevertheless, the intense hydrothermal overprint of the carbonatites made Fen to the biggest carbonatite-related REE and Th deposit in Europe.

The Kaiserstuhl, in contrast, shows an almost missing REE mineralization in the late-magmatic stage of the Badberg, but a significant REE enrichment in apatite (study C). In contrast, other carbonatite bodies of the KVC (Orberg, Degenmatt, Haselschacher Buck) lack an enhanced REE enrichment in apatite, but reveal a late magmatic hydrothermal modification (incl. REE enrichment) of pyrochlore (Walter et al., 2018).

We assign this variation to a contamination of the Badberg by silicate rocks, where a britholite substitution and related REE enrichment in the apatite was promoted during the orthomagmatic stage. This further inhibited later enrichment of REE in residual liquids/fluids and emphasizes the potential importance of contamination of carbonatitic magmas for REE mineralizations.

In general, contamination in carbonatites is typically very poorly identifiable by means of radiogenic isotope (e.g. Sr, Nd) data, as their isotope systems are "buffered" (due to high concentrations) against contamination with silicate rocks (usually much lower concentrations of these elements; e.g., Bell and Tilton, 2002). Furthermore, it is assumed that carbonatites are not specifically prone to contamination by crustal or cogenetic intrusive rocks, as low densities and extremely low viscosities of carbonate melts allow a rapid ascent (e.g., Jones et al., 2013; Treiman and Schedl, 1983) without a notable melt-rock interaction. However, based on textural observations and compositional variations of mica and apatite, we were able to verify a related contamination of the Badberg. This points out, as Study B has already shown, that especially mica, but also apatite (under certain conditions), can be effectively used as geochemical indicators in carbonatitic systems. In addition, it also demonstrates the basically sensitive behaviour of REEs.

In conclusion, it can be assumed that one important candidate for an ideal REE enrichment of high economic significance is a carbonatite which has not experienced any contamination, contains only minor amounts of apatite, experienced a strong enrichment of REE by a late magmatic fluid, and finally completed a redistribution and enrichment of REE by external fluids. Such characteristics may be most likely expected from highly differentiated carbonatites that intruded shallow crustal levels and consequently lack associated phoscorites, but did not intrude into tectonically active areas where entrainment of silicate wall rock fragments is promoted. As an absolute optimum, such carbonatites experienced a supergene enrichment as laterites. Further work on this topic should focus in particular on the potential fluid phases that induce the formation of discrete REE minerals. Especially for carbonatites, neither the influence of different natural fluid types on the REE mineralization nor the influence of different processes on the fluid composition is sufficiently known. Additionally, as contamination in carbonatitic systems reflects a previously unnoticed effect, it is necessary to investigate such processes and their influences in further case studies to determine differences due to variable rock compositions (e.g. BIF, gabbro, etc.).

5. REFERENCES

Al Ani, T., Sarapää, O., 2009. Rare earth elements and their mineral phases in Jammi carbonatite veins and fenites on the south side of Sokli carbonatite complex, NE Finland. Geological Survey of Finland, Report M 19.

Aldous, R.T.H., 1980. Ore genesis in copper bearing carbonatites: a geochemical, fluid inclusion and mineralogical study. Imperial College London (University of London), London, p. 365.

Andersen, T., 1988. Evolution of peralkaline calcite carbonatite magma in the Fen complex, southeast Norway. Lithos 22, 99-112.

Andersen, T., Austrheim, H., 1991. Temperature-HF fugacity trends during crystallization of calcite carbonatite magma in the Fen complex, Norway. Mineralogical Magazine 55, 81-94.

Andrade, F., Möller, P., Lüders, V., Dulski, P., Gilg, H., 1999. Hydrothermal rare earth elements mineralization in the Barra do Itapirapuã carbonatite, southern Brazil: behaviour of selected trace elements and stable isotopes (C, O). Chemical Geology 155, 91-113.

Anenburg, M., Burnham, A.D., Mavrogenes, J.A., 2018. Ree Redistribution Textures in Altered Fluorapatite: Symplectites, Veins, and Phosphate-Silicate-Carbonate Assemblages from the Nolans Bore P-REE-Th Deposit, Northern Territory, Australia. The Canadian Mineralogist 56, 331-354.

Anenburg, M., Mavrogenes, J.A., 2018. Carbonatitic versus hydrothermal origin for fluorapatite REE-Th deposits: Experimental study of REE transport and crustal “antiskarn” metasomatism. American Journal of Science 318, 335-366.

Arzamastsev, A., Glaznev, V., Raevsky, A., Arzamastseva, L., 2000. Morphology and internal structure of the Kola Alkaline intrusions, NE Fennoscandian Shield: 3D density modelling and geological implications. Journal of Asian Earth Sciences 18, 213-228.

Baranyi, I., Lippolt, H.J., Todt, W., 1976. K-Ar Altersbestimmungen an tertiaren Vulkaniten des Oberrheingraben-Gebietes: II Die Alterstraverse vom Hegau nach Lothringen. Oberrheinische Geologische Abhandlungen 25, 41-62.

Barker, D.S., 2001. Calculated silica activities in carbonatite liquids. Contributions to Mineralogy and Petrology 141, 704-709.

Beccaletto, L., Capar, L., Cruz-Mermy, D., Rupf, I., Nitsch, E., Oliviero, G., Elsass, P., Perrin, A., Marc, S., 2010. The GeORG project-Geological Potential of the Upper Rhine Graben-Situation, goals and first scientific results, 23ème Réunion des Sciences de la Terre (RST2010), Bordeaux.

Beitter, T., Wagner, T., Markl, G., 2008. Formation of kyanite–quartz veins of the Alpe Sponda, Central Alps, Switzerland: implications for Al transport during regional metamorphism. Contributions to Mineralogy and Petrology 156, 689-707.

Bell, K., 1989. Carbonatites: Genesis and Evolution. Unwin Hyman, London, UK.

Bell, K., Simonetti, A., 2010. Source of parental melts to carbonatites–critical isotopic constraints. Mineralogy and Petrology 98, 77-89.

Bell, K., Tilton, G.R., 2002. Probing the mantle: the story from carbonatites. Eos, Transactions American Geophysical Union 83, 273-277.

Bell, K., Zaitsev, A., Spratt, J., Fröjdö, S., Rukhlov, A., 2015. Elemental, lead and sulfur isotopic compositions of galena from Kola carbonatites, Russia–implications for melt and mantle evolution. Mineralogical Magazine 79, 219-241.

Bourgeois, O., Ford, M., Diraison, M., De Veslud, C.L.C., Gerbault, M., Pik, R., Ruby, N., Bonnet, S., 2007. Separation of rifting and lithospheric folding signatures in the NW-Alpine foreland. International Journal of Earth Sciences 96, 1003-1031.

Brauch, K.W., Pohl, C.M., Symons, G., Tauchnitz, M., 2018. Paper on instrument test and best practice for carbonatites and alkaline rocks. Terratec geoservices, p. 78.

Braunger, S., Marks, M., Walter, B.F., Neubauer, R., Reich, R., Wenzel, T., Parsapoor, A., Markl, G., 2018. The Petrology of the Kaiserstuhl Volcanic Complex, SW Germany: The Importance of Oxidized Lithosphere for Carbonatite Generation. Journal of Petrology, in press.

Brigatti, M.F., Medici, L., Saccani, E., Vaccaro, C., 1996. Crystal chemistry and petrologic significance of Fe^{3+}-rich phlogopite from the Tapira carbonatite complex, Brazil. American Mineralogist 81, 913-927.

Brod, J., Gaspar, J., De Araújo, D., Gibson, S., Thompson, R., Junqueira-Brod, T., 2001. Phlogopite and tetra-ferriphlogopite from Brazilian carbonatite complexes: petrogenetic constraints and implications for mineral-chemistry systematics. Journal of Asian Earth Sciences 19, 265-296.

Brooker, R., Kjarsgaard, B., 2011. Silicate-carbonate liquid immiscibility and phase relations in the system SiO_2–Na_2O–Al_2O_3–CaO–CO_2 at 0.1-2.5 GPa with applications to carbonatite genesis. Journal of Petrology 52, 1281-1305.

Budzyń, B., Harlov, D.E., Williams, M.L., Jercinovic, M.J., 2011. Experimental determination of stability relations between monazite, fluorapatite, allanite, and REE-epidote as a function of pressure, temperature, and fluid composition. American Mineralogist 96, 1547-1567.
Budzyń, B., Hetherington, C.J., Williams, M.L., Jercinovic, M.J., Michalik, M., 2010. Fluid− mineral interactions and constraints on monazite alteration during metamorphism. Mineralogical Magazine 74, 659-681.
Bulakh, A.G., Le Bas, M.J., Wall, F., Zaitsev, A.N., 1998. Ancylite-bearing carbonatites of the Seblyavr massif, Kola Peninsula, Russia. Neues Jahrbuch für Mineralogie Monatshefte, 171-192.
Castor, S.B., 2008. The Mountain Pass rare-earth carbonatite and associated ultrapotassic rocks, California. The Canadian Mineralogist 46, 779-806.
Chakhmouradian, A.R., 2006. High-field-strength elements in carbonatitic rocks: geochemistry, crystal chemistry and significance for constraining the sources of carbonatites. Chemical Geology 235, 138-160.
Chakhmouradian, A.R., Cooper, M.A., Medici, L., Abdu, Y.A., Shelukhina, Y.S., 2015. Anzaite-(Ce), a new rare-earth mineral and structure type from the Afrikanda silicocarbonatite, Kola Peninsula, Russia. Mineralogical Magazine 79, 1231-1244.
Chakhmouradian, A.R., Reguir, E.P., Zaitsev, A.N., Couëslan, C., Xu, C., Kynický, J., Mumin, A.H., Yang, P., 2017. Apatite in carbonatitic rocks: Compositional variation, zoning, element partitioning and petrogenetic significance. Lithos 274, 188-213.
Chakhmouradian, A.R., Zaitsev, A.N., 2012. Rare earth mineralization in igneous rocks: sources and processes. Elements 8, 347-353.
Chakrabarty, A., Sen, A.K., Ghosh, T.K., 2009. Amphibole—a key indicator mineral for petrogenesis of the Purulia carbonatite, West Bengal, India. Mineralogy and Petrology 95, 105-112.
Chao, E.C., 1997. The sedimentary carbonate-hosted giant Bayan Obo REE-Fe-Nb ore deposit of Inner Mongolia, China: a cornerstone example for giant polymetallic ore deposits of hydrothermal origin. US Government Printing Office.
Chen, W., Kamenetsky, V.S., Simonetti, A., 2013. Evidence for the alkaline nature of parental carbonatite melts at Oka complex in Canada. Nature communications 4, 2687.
Chew, D.M., Sylvester, P.J., Tubrett, M.N., 2011. U–Pb and Th–Pb dating of apatite by LA-ICPMS. Chemical Geology 280, 200-216.
Cooper, A.F., Collins, A.K., Palin, J.M., Spratt, J., 2015. Mineralogical evolution and REE mobility during crystallisation of ancylite-bearing ferrocarbonatite, Haast River, New Zealand. Lithos 216, 324-337.
Dalton, J.A., Presnall, D.C., 1998. Carbonatitic melts along the solidus of model lherzolite in the system CaO-MgO-Al_2O_3-SiO_2-CO_2 from 3 to 7 GPa. Contributions to Mineralogy and Petrology 131, 123-135.
Dasgupta, R., Hirschmann, M.M., Smith, N.D., 2007. Partial melting experiments of peridotite + CO_2 at 3 GPa and genesis of alkalic ocean island basalts. Journal of Petrology 48, 2093-2124.
Dawson, J.B., Hinton, R.W., 2003. Trace-element content and partitioning in calcite, dolomite and apatite in carbonatite, Phalaborwa, South Africa. Mineralogical Magazine 67, 921-930.
de Toledo, M.C.M., Lenharo, S.L., Ferrari, V.C., Fontan, F., de Parseval, P., Leroy, G., 2004. The compositional evolution of apatite in the weathering profile of the Catalão I alkaline-carbonatitic complex, Goiás, Brazil. The Canadian Mineralogist 42, 1139-1158.
Dobson, D.P., Jones, A.P., Rabe, R., Sekine, T., Kurita, K., Taniguchi, T., Kondo, T., Kato, T., Shimomura, O., Urakawa, S., 1996. In-situ measurement of viscosity and density of carbonate melts at high pressure. Earth and Planetary Science Letters 143, 207-215.
Doroshkevich, A.G., Ripp, G.S., Viladkar, S.G., Vladykin, N.V., 2008. The Arshan REE carbonatites, southwestern Transbaikalia, Russia: mineralogy, paragenesis and evolution. The Canadian Mineralogist 46, 807-823.
Doroshkevich, A.G., Viladkar, S.G., Ripp, G.S., Burtseva, M.V., 2009. Hydrothermal REE mineralization in the Amba Dongar carbonatite complex, Gujarat, India. The Canadian Mineralogist 47, 1105-1116.
Downes, P.J., Demény, A., Czuppon, G., Jaques, A.L., Verrall, M., Sweetapple, M., Adams, D., McNaughton, N.J., Gwalani, L.G., Griffin, B.J., 2014. Stable H–C–O isotope and trace element geochemistry of the Cummins Range Carbonatite Complex, Kimberley region, Western Australia: implications for hydrothermal REE mineralization, carbonatite evolution and mantle source regions. Mineralium Deposita 49, 905-932.
Edel, J.-B., Whitechurch, H., Diraison, M., 2006. Seismicity wedge beneath the Upper Rhine Graben due to backwards Alpine push? Tectonophysics 428, 49-64.
Eriksson, S.C., 1982. Aspects of the petrochemistry of the Phalaborwa Complex, northeastern Transvaal, South Africa. University of the Witwatersrand, Johannesburg, p. 496.
Farrell, S., Bell, K., Clark, I., 2010. Sulphur isotopes in carbonatites and associated silicate rocks from the Superior Province, Canada. Mineralogy and Petrology 98, 209-226.

Fleet, M.E., 2003. Sheet silicates: Micas, in: Deer, W.A., Howie, R.A., Zussman, J. (Eds.), Rock-Forming Minerals. Geological Society of London, p. 765.
Frolov, A.A., 1971. Vertical zonations in deposition of ore as in ultrabasic-alkaline rocks and carbonatites. International Geology Review 13, 685-695.
Gaspar, J.C., Wyllie, P.J., 1987. The phlogopites from the Jacupiranga carbonatite intrusions. Mineralogy and Petrology 36, 121-134.
Gendron, L., Bis, R., Rodrigue, M., 1984. Underground mining and pyrochlore ore processing at Niobec mine, Quebec, Canada, in: Stuart, H. (Ed.), Niobium, Proceedings of the International Symposium of the Metallurgical Society of AIME (American Institute of Mining, Metallurgical, and Petroleum Engineers), Warrendale, Pennsylvania, pp. 79-96.
Genge, M.J., Price, G.D., Jones, A.P., 1995. Molecular dynamics simulations of CaCO3 melts to mantle pressures and temperatures: implications for carbonatite magmas. Earth and Planetary Science Letters 131, 225-238.
Gittins, J., Harmer, R., 2001. The carbonatite-alkalic silicate igneous rock 'association': an unfortunate and misleading assumption. Journal of African Earth Sciences (and the Middle East) 32, A16-A16.
Gomide, C.S., Brod, J.A., Junqueira-Brod, T.C., Buhn, B.M., Santos, R.V., Barbosa, E.S.R., Cordeiro, P.F.O., Palmieri, M., Grasso, C.B., Torres, M.G., 2013. Sulfur isotopes from Brazilian alkaline carbonatite complexes. Chemical Geology 341, 38-49.
Groschopf, R., Kessler, G., Leiber, J., Maus, H., Ohmert, W., Schreiner, A., Wimmenauer, W., 1996. Erläuterungen zur Geologischen Karte von Baden-Württemberg Freiburg i. Br. und Umgebung. Geologische Landesamt Baden-Würrtemberg, Freiburg.
Gudfinnsson, G.H., Presnall, D.C., 2005. Continuous gradations among primary carbonatitic, kimberlitic, melilititic, basaltic, picritic, and komatiitic melts in equilibrium with garnet lherzolite at 3–8 GPa. Journal of Petrology 46, 1645-1659.
Guzmics, T., Zajacz, Z., Kodolányi, J., Halter, W., Szabó, C., 2008. LA-ICP-MS study of apatite-and K feldspar-hosted primary carbonatite melt inclusions in clinopyroxenite xenoliths from lamprophyres, Hungary: Implications for significance of carbonatite melts in the Earth's mantle. Geochimica et Cosmochimica Acta 72, 1864-1886.
Haas, J.R., Shock, E.L., Sassani, D.C., 1995. Rare earth elements in hydrothermal systems: estimates of standard partial molal thermodynamic properties of aqueous complexes of the rare earth elements at high pressures and temperatures. Geochimica et Cosmochimica Acta 59, 4329-4350.
Hammouda, T., Chantel, J., Devidal, J.-L., 2010. Apatite solubility in carbonatitic liquids and trace element partitioning between apatite and carbonatite at high pressure. Geochimica et Cosmochimica Acta 74, 7220-7235.
Hanekom, H.J., van Staden, C.M.v.H., Smit, P.J., Pike, D.R., 1965. The geology of the Palabora igneous complex. South African Geological Survey, Pretoria.
Hogarth, D., 1989. Pyrocholre, apatite and amphibole: distinctive minerals in carbonatite, in: Bell, K. (Ed.), Carbonatites: genesis and evolution. Unwin Hyman, London, pp. 105-148.
Hou, T., Charlier, B., Namur, O., Schütte, P., Schwarz-Schampera, U., Zhang, Z., Holtz, F., 2017. Experimental study of liquid immiscibility in the Kiruna-type Vergenoeg iron–fluorine deposit, South Africa. Geochimica et Cosmochimica Acta 203, 303-322.
Hubaux, A., 1964. Sructure des carbonatites de Schelingen, in: Van Wambeke, L. (Ed.), Les roches alcalines et les carbonatites du Kaiserstuhl. European Atomic Energy Community (EURATOM). Mineralogy Geochemistry Section, Brussels, pp. 31-46.
Hüttner, R., 1996, 1996. Tektonik im Grundgebirge, in: Groschopf, R., Kessler, G., Leiber, J., Maus, H., Ohmert, A., Schreiner, A., Wimmenauer, A. (Eds.), Geologische Karte von Baden-Württemberg 1:50000, Freiburg i.Br. und Umgebung. Landesamt für Geologie, Rohstoffe und Bergbau Baden-Württemberg, Freiburg im Breisgau, Germany, pp. 119-228.
Ivanyuk, G.Y., Yakovenchuk, V., Pakhomovsky, Y.A., 2002. Kovdor. Laplandia Minerals, Apatity, 326.
Jones, A.P., Genge, M., Carmody, L., 2013. Carbonate melts and carbonatites. Reviews in Mineralogy and Geochemistry 75, 289-322.
Jones, J.H., Walker, D., Pickett, D.A., Murrell, M.T., Beattie, P., 1995. Experimental investigations of the partitioning of Nb, Mo, Ba, Ce, Pb, Ra, Th, Pa, and U between immiscible carbonate and silicate liquids. Geochimica et Cosmochimica Acta 59, 1307-1320.
Kanazawa, Y., Kamitani, M., 2006. Rare earth minerals and resources in the world. Journal of alloys and compounds 408, 1339-1343.
Katz-Lehnert, K., 1989. Petrologie der Gangkarbonatite im Kaiserstuhl. Albert-Ludwig University, Freiburg, p. 290.
Keller, J., 1978. Karbonatitische Schmelzen im Oberflächenvulkanismus des Kaiserstuhls. Fortschritte der Mineralogie 56, 1-58.

Keller, J., 1981. Carbonatitic volcanism in the Kaiserstuhl alkaline complex: evidence for highly fluid carbonatitic melts at the Earth's surface. Journal of Volcanology and Geothermal Research 9, 423-431.
Keller, J., 1989. Extrusive carbonatites and their significance, in: Bell, K. (Ed.), Carbonatites: genesis and evolution. Unwin Hyman, London, pp. 70-88.
Keller, J., Brey, G., Lorenz, V., Sachs, P., Schleicher, H., 1990. Pre-conference Excursion 2A: Volcanism and Petrology of the Upper Rhinegraben (Urach-Hegau-Kaiserstuhl), IAVCEI International Volcanic Congress Mainz, p. 60.
Klemme, S., Dalpé, C., 2003. Trace-element partitioning between apatite and carbonatite melt. American Mineralogist 88, 639-646.
Kono, Y., Kenney-Benson, C., Hummer, D., Ohfuji, H., Park, C., Shen, G., Wang, Y., Kavner, A., Manning, C.E., 2014. Ultralow viscosity of carbonate melts at high pressures. Nature communications 5, 5091.
Kraml, M., Pik, R., Rahn, M., Selbekk, R., Carignan, J., Keller, J., 2006. A New Multi-Mineral Age Reference Material for 40Ar/39Ar,(U-Th)/He and Fission Track Dating Methods: The Limberg t3 Tuff. Geostandards and Geoanalytical Research 30, 73-86.
Krasnova, N., Balaganskaya, E., Garcia, D., 2004a. Kovdor - classic phoscorites and carbonatites, in: Wall , F., Zaitev, A.N. (Eds.), Phoscorites and Carbonatites from Mantle to Mine: the Key Example of the Kola Alkaline Province. Mineralogical Society of Great Britain and Ireland, London, UK, pp. 99-132.
Krasnova, N., Petrov, T., Balaganskaya, E., Garcia, D., Moutte, J., Zaitsev, A., Wall, F., 2004b. Introduction to phoscorites: occurrence, composition, nomenclature and petrogenesis, in: Wall , F., Zaitev, A.N. (Eds.), Phoscorites and Carbonatites from Mantle to Mine: the Key Example of the Kola Alkaline Province. The Mineralogical Society of Great Britain and Ireland, London, UK, pp. 45-74.
Kynicky, J., Smith, M.P., Xu, C., 2012. Diversity of rare earth deposits: the key example of China. Elements 8, 361-367.
Lapin, A., Vartiainen, H., 1983. Orbicular and spherulitic carbonatites from Sokli and Vuorijärvi. Lithos 16, 53-60.
Lee, M., Garcia, D., Moutte, J., Williams, C., Wall, F., 2004. Carbonatites and phoscorites from the Sokli complex, Finland, in: Wall , F., Zaitev, A.N. (Eds.), Phoscorites and carbonatites from mantle to mine: the key example of the Kola Alkaline Province. The Mineralogical Society of Great Britain and Ireland, London, UK, pp. 133-162.
Lee, M.J., Garcia, D., Moutte, J., Lee, J.I., 2003. Phlogopite and tetraferriphlogopite from phoscorite and carbonatite associations in the Sokli massif, Northern Finland. Geosciences Journal 7, 9-20.
Lee, W.-j., Wyllie, P.J., 1994. Experimental data bearing on liquid immiscibility, crystal fractionation, and the origin of calciocarbonatites and natrocarbonatites. International Geology Review 36, 797-819.
Lee, W.-j., Wyllie, P.J., 1997. Liquid immiscibility between nephelinite and carbonatite from 1.0 to 2.5 GPa compared with mantle melt compositions. Contributions to Mineralogy and Petrology 127, 1-16.
Lindsley, D.H., Epler, N., 2017. Do Fe–Ti oxide magmas exist? Probably not! American Mineralogist 102, 2157-2169.
Manning, C.E., 2004. Polymeric silicate complexing in aqueous fluids at high pressure and temperature, and its implications for water-rock interaction, in: Wanty, R.B., Seal II, R.R. (Eds.), Water-Rock Interactions. Balkema, New York, pp. 45-49.
Mariano, A.N., 1989. Nature of economic mineralization in carbonatites and related rocks, in: Bell, K. (Ed.), Carbonatites: genesis and evolution. Unwin Hyman, London, pp. 149-176.
Massuyeau, M., Gardès, E., Morizet, Y., Gaillard, F., 2015. A model for the activity of silica along the carbonatite–kimberlite–mellilitite–basanite melt compositional joint. Chemical Geology 418, 206-216.
Mikhailova, Y.A., Krasnova, N., Kretser, Y.L., Wall, F., Pakhomovsky, Y.A., 2002. Inclusions in minerals of the Kovdor intrusion of ultrabasic, alkaline rocks and carbonatites as indicators of the endogenic evolution processes, in: Vladykin, N.V. (Ed.), Deep-seated magmatism, magmatic sources and the problem of plumes. Siberian Branch of the Russian Academy of Sciences, Irkutsk–Vladivostok, Russia, pp. 296-320.
Mitchell, R., Chudy, T., McFarlane, C.R., Wu, F.-Y., 2017. Trace element and isotopic composition of apatite in carbonatites from the Blue River area (British Columbia, Canada) and mineralogy of associated silicate rocks. Lithos 286, 75-91.
Mitchell, R.H., 2005. Carbonatites and carbonatites and carbonatites. The Canadian Mineralogist 43, 2049-2068.
Moore, M., Chakhmouradian, A.R., Mariano, A.N., Sidhu, R., 2015. Evolution of rare-earth mineralization in the Bear Lodge carbonatite, Wyoming: Mineralogical and isotopic evidence. Ore Geology Reviews 64, 499-521.

Naslund, H., 1983. The effect of oxygen fugacity on liquid immiscibility in iron-bearing silicate melts. American Journal of Science 283, 1034-1059.
Palabora Mining Company, L.a.G.a.M.S., 1976. The geology and economic deposits of copper, iron and vermiculite in the Palabora Igneous Complex: A brief review. Economic Geology 71, 177-192.
Rankin, A., 2005. Carbonatite-associated rare metal deposits: composition and evolution of ore-forming fluids–the fluid inclusion evidence, in: Linnen, R., Samson, I. (Eds.), Rare Metal Geochemistry and Ore Deposits, Geological Association of Canada, Short Course Notes, pp. 299-314.
Read, D., Andreoli, M.A.G., Knoper, M., Williams, C.T., Jarvis, N., 2002. The degradation of monazite: Implications for the mobility of rare-earth and actinide elements during low-temperature alteration. European Journal of Mineralogy 14, 487-498.
Reguir, E., Chakhmouradian, A., Halden, N., Malkovets, V., Yang, P., 2009. Major-and trace-element compositional variation of phlogopite from kimberlites and carbonatites as a petrogenetic indicator. Lithos 112, 372-384.
Reguir, E.P., Chakhmouradian, A.R., Pisiak, L., Halden, N.M., Yang, P., Xu, C., Kynický, J., Couëslan, C.G., 2012. Trace-element composition and zoning in clinopyroxene-and amphibole-group minerals: implications for element partitioning and evolution of carbonatites. Lithos 128, 27-45.
Reischmann, T., 1995. Precise U/Pb age determination with baddeleyite (ZrO_2), a case study from the Phalaborwa igneous complex, South Africa. South African Journal of Geology 98, 1-4.
Rimskaya-Korsakova, O., Krasnova, N., 2002. Geology of the deposits of Kovdor massif. St. Petersburg State University, St. Petersburg, Russia.
Schleicher, H., Keller, J., Kramm, U., 1990. Isotope studies on alkaline volcanics and carbonatites from the Kaiserstuhl, Federal Republic of Germany. Lithos 26, 21-35.
Sommerauer, J., Katz-Lehnert, K., 1985. A new partial substitution mechanism of CO_3^{2-}/CO_3OH^{3-} and SiO_4^{4-} for the PO_4^{3-} group in hydroxyapatite from the Kaiserstuhl alkaline complex (SW-Germany). Contributions to Mineralogy and Petrology 91, 360-368.
Teiber, H., Marks, M.A., Arzamastsev, A.A., Wenzel, T., Markl, G., 2015. Compositional variation in apatite from various host rocks: clues with regards to source composition and crystallization conditions. Neues Jahrbuch für Mineralogie-Abhandlungen: Journal of Mineralogy and Geochemistry 192, 151-167.
Treiman, A.H., Schedl, A., 1983. Properties of carbonatite magma and processes in carbonatite magma chambers. The Journal of Geology 91, 437-447.
Trofanenko, J., Williams-Jones, A., Simandl, G., Migdisov, A., 2016. The Nature and Origin of the REE Mineralization in the Wicheeda Carbonatite, British Columbia, Canada. Economic Geology 111, 199-223.
Tropper, P., Manning, C.E., 2005. Letter: Very low solubility of rutile in H2O at high pressure and temperature, and its implications for Ti mobility in subduction zones. American Mineralogist 90, 502-505.
Uher, P., Ondrejka, M., Bačík, P., Broska, I., Konečný, P., 2015. Britholite, monazite, REE carbonates, and calcite: Products of hydrothermal alteration of allanite and apatite in A-type granite from Stupné, Western Carpathians, Slovakia. Lithos 236, 212-225.
Van Baalen, M.R., 1993. Titanium mobility in metamorphic systems: a review. Chemical Geology 110, 233-249.
Veksler, I., Nielsen, T., Sokolov, S., 1998. Mineralogy of crystallized melt inclusions from Gardiner and Kovdor ultramafic alkaline complexes: implications for carbonatite genesis. Journal of Petrology 39, 2015-2031.
Verplanck, P.L., Mariano, A.N., Mariano, A., Jr, 2016. Rare Earth Element Ore Geology of Carbonatites, in: Verplanck, P.L., Hitzman, M.W. (Eds.), Rare Earth and Critical Elements in Ore Deposits. Reviews in Economic Geology, Society of Economic Geologists, Littleton, CO, pp. 5-32.
Vuorinen, J.H., Skelton, A.D., 2004. Origin of silicate minerals in carbonatites from Alnö Island, Sweden: magmatic crystallization or wall rock assimilation? Terra Nova 16, 210-215.
Wall, F., Mariano, A.N., 1996. Rare earth minerals in carbonatites: a discussion centred on the Kangankunde Carbonatite, Malawi, in: Jones, A.P., Wall, F., Williams, C.T. (Eds.), Rare Earth Minerals: Chemestry, Origin and Ore Deposits. Mineralogical Society Series. Chapman and Hall, London, pp. 193-226.
Wall, F., Zaitsev, A., Jones, A.P., Mariano, A.N., 1997. Rare-earth rich carbonatites: a review and latest results. Journal of the Czech Geological Society 42, 49.
Wall, F., Zaitsev, A.N., 2004. Rare earth minerals in Kola carbonatites, in: Wall, F., Zaitsev, A.N. (Eds.), Phoscorites and carbonatites from mantle to mine: the key example of the Kola Alkaline Province. . Mineralogical Society Series, Mineralogical Society, London, UK, pp. 341-373.
Walter, B.F., Parsapoor, A., Braunger, S., Marks, M.A.W., Wenzel, T., Martin, M., Markl, G., 2018. Pyrochlore in carbonatites from the Kaiserstuhl volcanic complex, SW Germany – Monitor for

magmatic and hydrothermal processes and evidence for an exploration indicator? Chemical Geology, in press.
Walther, J., 1981. Fluide Einschlüsse im Apatite des Carbonatits vom Kaiserstuhl (Oberrheingraben): Ein Beitrag zur Interpretation der Carbonatitgenese. University of Karlsruhe, Karlsruhe, p. 136.
Wang, L.-X., Marks, M.A., Wenzel, T., Von Der Handt, A., Keller, J., Teiber, H., Markl, G., 2014. Apatites from the Kaiserstuhl Volcanic Complex, Germany: new constraints on the relationship between carbonatite and associated silicate rocks. European Journal of Mineralogy 26, 397-414.
Weidendorfer, D., Schmidt, M.W., Mattsson, H.B., 2017. A common origin of carbonatite magmas. Geology 45, 507-510.
Williams-Jones, A.E., Migdisov, A.A., Samson, I.M., 2012. Hydrothermal mobilisation of the rare earth elements–a tale of "ceria" and "yttria". Elements 8, 355-360.
Wimmenauer, W., 2003. Kaiserstuhl. Geologische Karte von Baden-Württemberg 1:25.000 mit Erläuterungen. Landesamt für Geologie, Rohstoffe und Bergbau Baden-Württemberg, Freiburg.
Wolff, J., 1994. Physical properties of carbonatite magmas inferred from molten salt data, and application to extraction patterns from carbonatite–silicate magma chambers. Geological Magazine 131, 145-153.
Woolley, A., Kempe, D., 1989. Carbonatites: nomenclature, average chemical composition, and element distribution, in: Bell, K. (Ed.), Carbonatites: genesis and evolution. Unwin Hyman, London, pp. 1-14.
Woolley, A.R., Kjarsgaard, B.A., 2008. Carbonatite occurrences of the world: map and database. Geological Survey of Canada.
Wu, F.-Y., Yang, Y.-H., Li, Q.-L., Mitchell, R.H., Dawson, J.B., Brandl, G., Yuhara, M., 2011. In situ determination of U–Pb ages and Sr–Nd–Hf isotopic constraints on the petrogenesis of the Phalaborwa carbonatite Complex, South Africa. Lithos 127, 309-322.
Wyllie, P.J., Lee, W.-J., 1998. Model system controls on conditions for formation of magnesiocarbonatite and calciocarbonatite magmas from the mantle. Journal of Petrology 39, 1885-1893.
Xu, C., Kynicky, J., Chakhmouradian, A.R., Campbell, I.H., Allen, C.M., 2010. Trace-element modeling of the magmatic evolution of rare-earth-rich carbonatite from the Miaoya deposit, Central China. Lithos 118, 145-155.
Yang, K.-F., Fan, H.-R., Santosh, M., Hu, F.-F., Wang, K.-Y., 2011. Mesoproterozoic carbonatitic magmatism in the Bayan Obo deposit, Inner Mongolia, North China: constraints for the mechanism of super accumulation of rare earth elements. Ore Geology Reviews 40, 122-131.
Zaitsev, A.N., 1996. Rhombohedral carbonates from carbonatites of the Khibina massif, Kola peninsula, Russia. The Canadian Mineralogist 34, 453-468.
Zaitsev, A.N., Demény, A., Sindern, S., Wall, F., 2002. Burbankite group minerals and their alteration in rare earth carbonatites—source of elements and fluids (evidence from C–O and Sr–Nd isotopic data). Lithos 62, 15-33.
Zaitsev, A.N., Kamenetsky, V., 2013. Magnetite-hosted melt inclusions from phoscorites and carbonatites (Kovdor, Kola): Ahydrous analog of Oldoinyo Lengai natrocarbonatites?, Goldschmidt, Florence, Italy, p. 2576.
Zaitsev, A.N., Wall, F., Le Bas, M.J., 1998. REE-Sr-Ba minerals from the Khibina carbonatites, Kola Peninsula, Russia: their mineralogy, paragenesis and evolution. Mineralogical Magazine 62, 225-250.
Zaitsev, A.N., Williams, C.T., Jeffries, T.E., Strekopytov, S., Moutte, J., Ivashchenkova, O.V., Spratt, J., Petrov, S.V., Wall, F., Seltmann, R., 2014. Rare earth elements in phoscorites and carbonatites of the Devonian Kola Alkaline Province, Russia: examples from Kovdor, Khibina, Vuoriyarvi and Turiy Mys complexes. Ore Geology Reviews 61, 204-225.
Zaitsev, A.N., Williams, C.T., Jeffries, T.E., Strekopytov, S., Moutte, J., Ivashchenkova, O.V., Spratt, J., Petrov, S.V., Wall, F., Seltmann, R., Borozdin, A.P., 2015. Reprint of "Rare earth elements in phoscorites and carbonatites of the Devonian Kola Alkaline Province, Russia: examples from Kovdor, Khibina, Vuoriyarvi and Turiy Mys complexes". Ore Geology Reviews 64, 477-498.

Appendix I

Accepted publication

Study A

Giebel, R.J., Gauert, C.D.K., Marks, M.A.W., Costin, G. and Markl, G. (2017): The Multistage REE Mineralization of the Palabora Carbonatite Complex, South Africa. *American Mineralogist*. Vol. **102(6).** P 1218-1233.

American Mineralogist, Volume 102, pages 1218–1233, 2017

Multi-stage formation of REE minerals in the Palabora Carbonatite Complex, South Africa

R. Johannes Giebel[1,2,*], Christoph D.K. Gauert[2,3], Michael A.W. Marks[1], Gelu Costin[4,5], and Gregor Markl[1]

[1]Department of Geoscience, Eberhard Karls University, Wilhelmstrasse 56, 72076 Tübingen, Germany
[2]Department of Geology, University of the Free State, 250 Nelson-Mandela-Drive, Bloemfontein 9300, South Africa
[3]Department of Applied Geology and Geohazards, Geological Survey of Saxony-Anhalt, Köthener Str. 38, 06118 Halle (Saale), Germany
[4]Department of Geology, Rhodes University, PO Box 94, Artillery Road, Grahamstown 6140, South Africa
[5]Department of Earth Science, Rice University, 6100 Main Street, Houston, Texas, 77005, U.S.A.

Abstract

The 2060 Ma old Palabora Carbonatite Complex (PCC), South Africa, comprises diverse REE mineral assemblages formed during different stages and reflects an outstanding instance to understand the evolution of a carbonatite-related REE mineralization from orthomagmatic to late-magmatic stages and their secondary post-magmatic overprint. The 10 rare earth element minerals monazite, REE-F-carbonates (bastnäsite, parisite, synchysite), ancylite, britholite, cordylite, fergusonite, REE-Ti-betafite, and anzaite are texturally described and related to the evolutionary stages of the PCC. The identification of the latter five REE minerals during this study represents their first described occurrences in the PCC as well as in a carbonatite complex in South Africa.

The variable REE mineral assemblages reflect a multi-stage origin: (1) fergusonite and REE-Ti-betafite occur as inclusions in primary magnetite. Bastnäsite is enclosed in primary calcite and dolomite. These three REE minerals are interpreted as orthomagmatic crystallization products. (2) The most common REE minerals are monazite replacing primary apatite, and britholite texturally related to the serpentinization of forsterite or the replacement of forsterite by chondrodite. Textural relationships suggest that these two REE-minerals precipitated from internally derived late-magmatic to hydrothermal fluids. Their presence seems to be locally controlled by favorable chemical conditions (e.g., presence of precursor minerals that contributed the necessary anions and/or cations for their formation). (3) Late-stage (post-magmatic) REE minerals include ancylite and cordylite replacing primary magmatic REE-Sr-carbonates, anzaite associated with the dissolution of ilmenite, and secondary REE-F-carbonates. The formation of these post-magmatic REE minerals depends on the local availability of a fluid, whose composition is at least partly controlled by the dissolution of primary minerals (e.g., REE-fluorocarbonates).

This multi-stage REE mineralization reflects the interplay of magmatic differentiation, destabilization of early magmatic minerals during subsequent evolutionary stages of the carbonatitic system, and late-stage fluid-induced remobilization and re-/precipitation of precursor REE minerals. Based on our findings, the Palabora Carbonatite Complex experienced at least two successive stages of intense fluid–rock interaction.

Keywords: Rare earth minerals, Loolekop, monazite, britholite, anzaite, fluoro-carbonates, ancylite, cordylite, fergusonite, REE-Ti-betafite

Introduction

Carbonatites are important exploration targets for rare earth elements (REE) and high field strength elements (HFSE, e.g., Mariano 1989; Wall and Mariano 1996; Verplanck et al. 2016). Since REE have become increasingly important for industrial use (Chakhmouradian and Wall 2012; Hatch 2012; Wall 2014) and were categorized as critical and strategic metals (European Commission 2014; Nassar et al. 2015), the scientific interest to understand the complex REE mineralizations found in carbonatitic systems has tremendously increased (e.g., Verplanck et al. 2016). Processes potentially responsible for REE enrichment in carbonatites include fractional crystallization of carbonatitic magma, enrichment of REE in magmatic fluids and subsequent precipitation, breakdown of primary carbonatitic minerals with sequestration of REE in secondary minerals, and subsolidus redistribution of REE (e.g., Verplanck et al. 2016). In all these processes, REE-bearing minerals (such as apatite, calcite, and dolomite) have to be distinguished from actual REE minerals with REE as major constituents. The most common REE minerals in carbonatites include REE-phosphates (mostly monazite) and various hydrous and anhydrous carbonates (e.g., ancylite, burbankite, and carbocernaite) and fluorocarbonates, such as bastnäsite, parisite, and synchysite (e.g., Wall and Zaitsev 2004b; Kanazawa and Kamitani 2006).

This study presents detailed textural observations on the vari-

* E-mail: r.j.giebel@gmx.de

0003-004X/17/0006–1218$05.00/DOI: http://dx.doi.org/10.2138/am-2017-6004

ous REE phases in the Loolekop pipe of the Palabora Complex (PCC, South Africa). These textural relations to both the carbonatitic minerals and among each other are used to distinguish between orthomagmatic, late-magmatic, and post-magmatic stages of formation and provide a better understanding for the importance of fluid-assisted mobilization and reprecipitation of these minerals. Understanding these typically late-stage processes is crucial for any economic judgement on REE in carbonatites (Wall and Zaitsev 2004a; Chakhmouradian and Zaitsev 2012; Zaitsev et al. 2015). Accordingly, the aim of this study is to present the crystallization and alteration history of the various REE minerals within the different evolutionary stages observed in the PCC as a prime example of REE-mineralized, large carbonatitic systems worldwide.

Geological background and previous work on the REE mineralization at Palabora

The Palabora Carbonatite Complex (PCC) is located close to the town of Phalaborwa (South Africa) and intruded at about 2060 Ma into Archaean basement rocks (Reischmann 1995; Wingate and Compston 2000; Heaman 2009; Wu et al. 2011). The complex represents an elongated tripartite pipe-like intrusion divided into a northern and southern pyroxenite and the central Loolekop pipe, with only the latter hosting carbonatites (Fig. 1; Hanekom et al. 1965; Yuhara et al. 2003; Verwoerd and Du Toit 2006).

The Loolekop pipe is composed of phoscorite (FOS) and banded carbonatite (BCB), which are intruded by transgressive carbonatite (TCB). Both the BCB and TCB are dolomite-bearing, but calcite-dominated with varying proportions of fluorapatite, phlogopite, magnetite, forsterite/chondrodite, and accessory phases (Fig. 2). Geochronological data indicate no significant age differences between these two rock types and Wu et al. (2011) suggest that they crystallized from different magma batches derived from a heterogeneous mantle source. Subsequent injection of a sulfide-rich liquid caused Fe-Cu-sulfide enrichment in the carbonatite pipe (Kavecsanszki et al. 2012). The carbonatite-phoscorite association is surrounded by micaceous pyroxenite (MPY, Lombaard et al. 1964; Hanekom et al. 1965; Eriksson 1989). Several syenite bodies were injected into the surrounding basement rocks in the vicinity of the complex (Eriksson 1989; Yuhara et al. 2003; Wu et al. 2011) and the basement rocks in the border zone toward the complex were fenitized (Verwoerd 1966). The entire complex was cross cut by dolerite dikes (DOL),

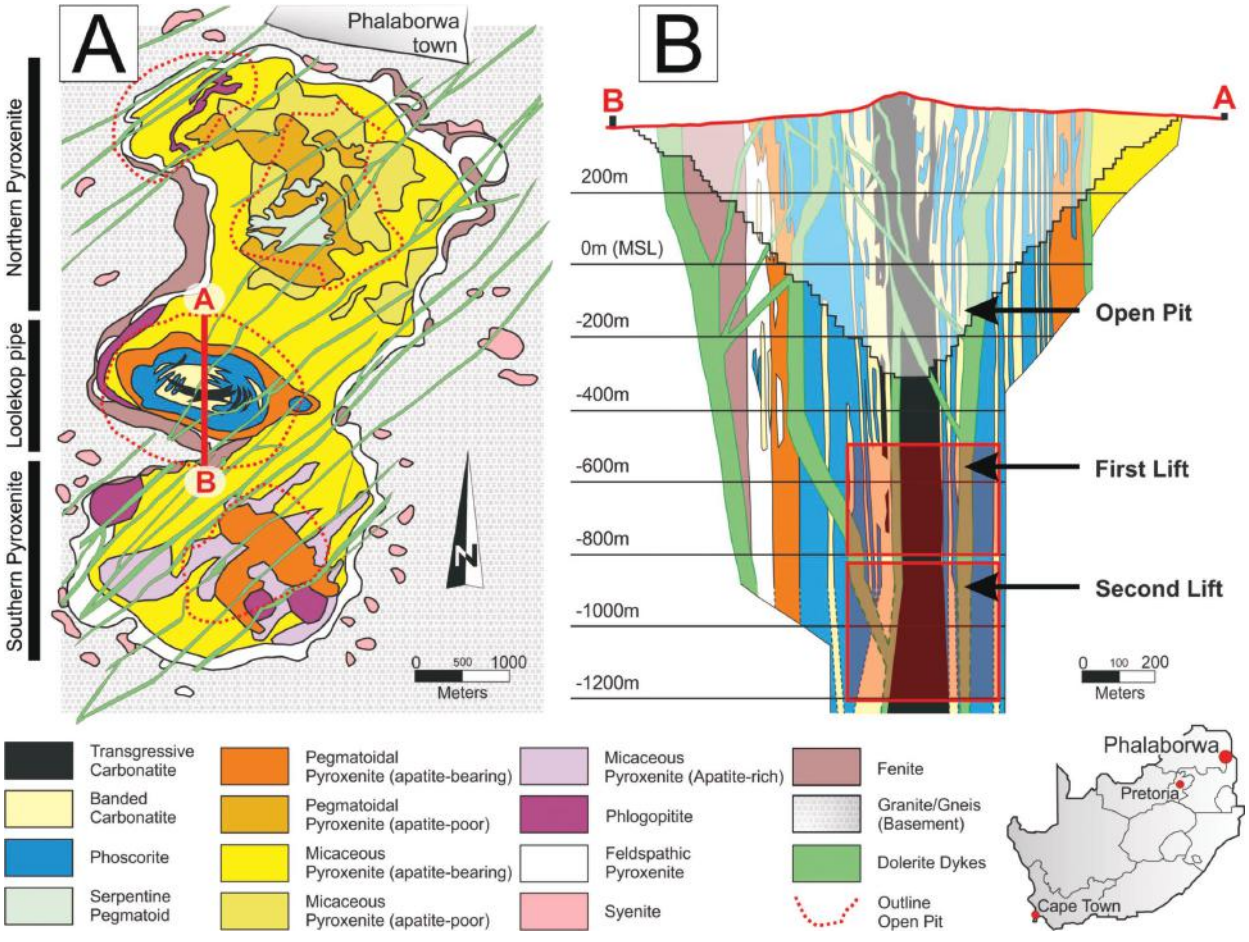

Figure 1. Generalized geological map of the Palabora Complex (modified after Hanekom et al. 1965; Fourie and De Jager 1986; Wilson 1998) and cross section of the Loolekop pipe in N-S direction showing the irregular ring structure of the pipe (modified and extended after Wilson 1998).

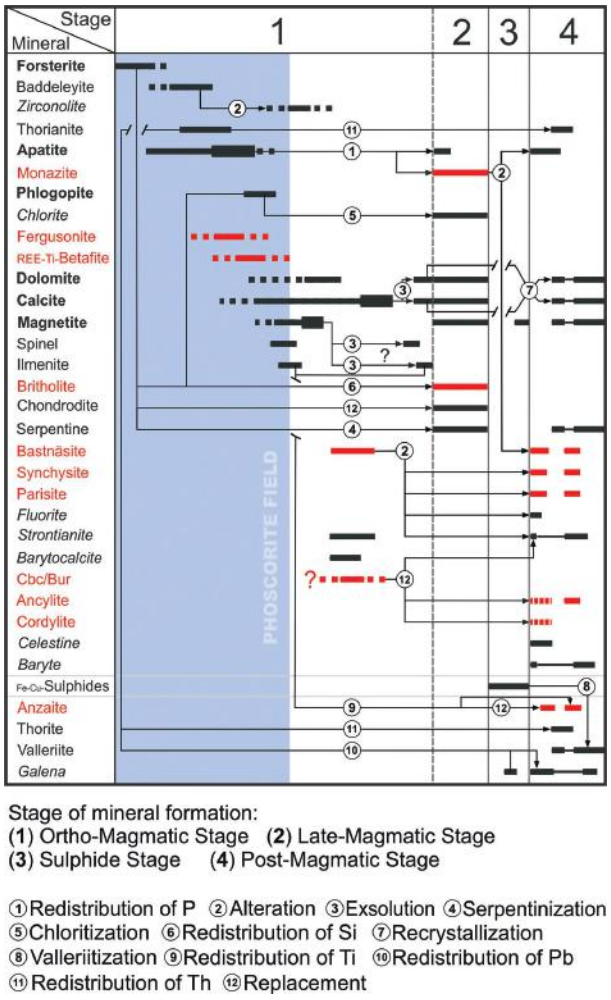

FIGURE 2. Paragenetic scheme for carbonatites and phoscorite (blue field) of the Loolekop deposit. Note: Main phases in bold, minor phases in plain style, accessory phases in italics, and REE phases in red.

which were interpreted as being Proterozoic (Briden 1976; Stettler et al. 1989; Wu et al. 2011) to Post-Karoo (<180 Ma) in age (Hanekom et al. 1965; Uken and Watkeys 1997).

Very similar to what is observed in other carbonatite complexes, apatite represents the main REE host in carbonatites from the PCC and is much higher in REE than calcite and dolomite (Dawson and Hinton 2003). Early investigations on the REE distribution in carbonatites of the PCC suggested the absence of REE minerals (Aldous 1980). Later, bastnäsite, parisite, synchysite, ancylite, monazite, Sr-REE apatite, and an unknown REE-silicate were described by Bulakh et al. (1998) and Karchevsky (2000). These studies used the same five samples from the open pit level (random sampling—upper 600 m of the deposit; Bulakh, personal communication) and provided only incomplete textural descriptions on their occurrence. Bastnäsite (and minor parisite) was identified as the most abundant REE mineral in the BCB, whereas ancylite (and minor synchysite) was described as the most abundant REE mineral in the TCB. Monazite was described as mainly forming rims around or veins in apatite and an unknown REE-silicate was mentioned to form rims around chondrodite.

SAMPLE MATERIAL AND ANALYTICAL METHODS

The Loolekop pipe is divided into three sections: the open pit level (uppermost part), the first lift level (upper underground level), and the second lift level (lowest part, Fig. 1), representing a vertical profile of >1500 m. We collected about 400 samples from 6 drill holes (LK-109, U-2, U-33, MT-1, SL-131, FS-14) and the observations reported in the following derive from 45 representative samples (20 TCB, 15 BCB, and 10 FOS) covering all three levels of the Loolekop pipe. All mineral formulas and abbreviations used are given in Table 1.

Polished thin sections were investigated using petrographic and reflected-light microscopes and were further examined using the backscattered electron (BSE) mode (focused beam) of a Hitachi Tabletop SEM (Tübingen), a JEOL JSM-6610 SEM (UFS, Bloemfontein), and the FE-SEM of the Centre for Microscopy (UFS, Bloemfontein).

Quantitative analyses of REE minerals were acquired using a JEOL JXA 8230 Superprobe at the Department of Geology, Rhodes University and a JEOL JXA 8900 Superprobe at the Department of Geosciences, Eberhard Karls University, Tübingen. Data acquisition was performed using four wavelength-dispersive spectrometers. Standardization was done using natural mineral standards, synthetic REE phosphates (SPI Supply), and REE1-4 glasses (Drake and Weill 1972). The ZAF matrix correction method (Bence and Albee 1968; Armstrong 1988) was employed for quantification, except for monazite, where a PRZ (JEOL) correction was used. For analyses of the different REE minerals, variable settings were used as detailed in the electronic appendix[1].

RESULTS

Crystallization sequence of the Palabora carbonatites and phoscorites

Here we provide an overview of the crystallization sequence for carbonatites and phoscorites of the Loolekop deposit. Detailed descriptions of REE minerals (marked red in Fig. 2) are given in the subsequent chapter. The PCC experienced at least four stages of crystallization, which were distinguished as (1) orthomagmatic, (2) late-magmatic, (3) sulfide-rich, and (4) post-magmatic. Phoscorites (blue field in Fig. 2) are dominated by orthomagmatic minerals, whereas in carbonatites later-magmatic minerals are more common. Although BCB and TCB were classified as two different carbonatites (e.g., Wu et al. 2011), they show some textural differences (from fine banding of mainly magnetite, apatite, and phlogopite in BCB to large patchy crystallization of the same minerals in TCB) but generally comprise the same mineral assemblages in the same crystallization sequence. This favors integration into a single paragenetic scheme together with the phoscorites (Fig. 2).

The orthomagmatic crystallization (stage 1) commenced by the formation of forsterite (with higher abundance in BCB), apatite, baddeleyite (later altered to zirconolite), and thorianite (Figs. 3a–3e). Subsequent formation of phlogopite (with higher abundance in BCB; Figs. 3d–3f) is followed by magnetite (with minor spinel and ilmenite; Figs. 3g and 3h), which exsolved further spinel (Figs. 3i and 3j) and ilmenite (Figs. 3i–3k) during later cooling. Precipitation of Mg-rich calcite started during the final stages of apatite formation with its main crystallization phase outlasting that of magnetite. A dolomite formation stage (Fig. 3l) existed contemporaneous with the intermediate stages of calcite formation, and during the main calcite stage,

[1]Deposit item AM-17-66004, Supplemental Material and Table 2. Deposit items are free to all readers and found on the MSA web site, via the specific issue's Table of Contents (go to http://www.minsocam.org/MSA/AmMin/TOC/2017/Jun2017_data/Jun2017_data.html).

TABLE 1. Chemical formulae of the minerals mentioned in the text and figures

Mineral	Abbr.	Formula	Mineral	Abbr.	Formula
SILICATES:			**CARBONATES:**		
chlorite	chl	$(Mg_4Al_2)Si_3Al)O_{10}(OH)_8$	ancylite-(Ce)	anc	$(Sr,Ca)(REE)(CO_3)_2(OH)\cdot H_2O$
chondrodite	chn	$(Mg,Fe)_5(SiO_4)_2(F,OH)_2$	bastnäsite-(Ce)	bsn	$(REE,Ca)(CO_3)_2F$
fluorbritholite-(Ce)	bri	$Ca_2(REE)_3(SiO_4)_3(F,OH)$	burbankite	bur	$(Ca,Na)_3(Sr,REE,Ba)_3(CO_3)_5$
olivine	ol	$(Mg,Fe)SiO_4$	calcite	cal	$CaCO_3$
phlogopite	phl	$KMg_3(Si_3Al)O_{10}(OH,F)_2$	carbocernaite	cbc	$(Ca,Na)(Sr,REE,Ba)(CO_3)_2$
serpentine	srp	$Mg_6Si_4O_{10}(OH)_8$	cordylite-(Ce)	cdy	$(Ca,Na)Ba(REE)_2(CO_3)_3F_2$
thorite	thr	$ThSiO_4$	dolomite	dol	$CaMg(CO_3)_2$
			parisite-(Ce)	pst	$Ca(REE)_2(CO_3)_3F_2$
OXIDES:			strontianite	str	$(Sr,Ca,Ba)CO_3$
anzaite-(Ce)	anz	$(REE)_4FeTi_6O_{18}(OH,F)_2$	synchysite-(Ce)	syn	$Ca(REE)(CO_3)_2F$
baddeleyite	bdl	ZrO_2	barytocalcite	bcl	$BaCa(CO_3)_2$
REE-Ti-betafite-(Ce)	btf	$(REE,Ca)_2Ti_2O_6(O,OH,F)$			
fergusonite-(Nd)-β	frg	$(REE)NbO_4$	**SULFATES:**		
ilmenite	ilm	$FeTiO_3$	baryte	brt	$BaSO_4$
magnetite	mgt	Fe_3O_4	celestine	cls	$SrSO_4$
spinel	spl	$MgAl_2O_4$			
thorianite	thn	ThO_2	**PHOSPHATES:**		
zirconolite	zrc	$CaZrTi_2O_7$	fluorapatite	ap	$Ca_5(PO_4)_3(F,OH)$
			monazite-(Ce)	mnz	$(REE,Ca)PO_4$
SULFIDES:					
bornite	bn	Cu_5FeS_4	**HALIDES:**		
chalcopyrite	cp	$CuFeS_2$	fluorite	fl	CaF_2
galena	gn	PbS			
valleriite	val	$2[(Fe,Cu)S]\cdot 1.53[(Mg,Al)(OH)_2]$			

additional Sr- and Ba-carbonates formed. Exsolution of dolomite and Mg-poor calcite from Mg-rich calcite (Fig. 3m) concludes the magmatic stage 1.

A late-magmatic stage (stage 2) is reflected by the serpentinization (and further magnetite formation) of forsterite (Figs. 4e and 4f) and replacement of forsterite by chondrodite (Fig. 4g), occasional chloritization of phlogopite (Figs. 4h), and the formation of secondary apatite (ap-II). Stage 2 interweaved with stage 1 and is probably the result of the action of aqueous-carbonic fluids (LM fluid in the following).

The subsequent injection of a sulfide-rich liquid (stage 3) resulted in extensive Fe-Cu sulfide mineralization (with minor magnetite). The interaction of a sulfide magma with the carbonatite magma is suspected during this stage (Kavecsanszki et al. 2012).

Subsequently, a post-magmatic fluid (stage 4; PM fluid in the following) caused a second serpentinization event (again associated with magnetite), valleriitization of the sulfide minerals (Figs. 4c, 4d, and 5e), recrystallization of carbonates (Fig. 6g; restricted to TCB), and the formation of thorianite, thorite (Figs. 6g and 6h; restricted to TCB), galena, baryte, celestine (Fig. 7f), and late-stage apatite (ap-III; Figs. 6f and 5f).

Textural appearance of REE minerals in the Palabora carbonatites and phoscorites

Ten REE minerals were identified during this study (marked red in Fig. 2; plus the suspected former occurrence of carbocernaite/burbankite), partly occurring in different generations. All REE minerals from the PCC are strongly LREE-enriched (Table[1] 2) and typically represent Ce-dominated members, which is displayed by the suffix-(Ce) after the nomenclature of Bayliss and Levinson (1988). The only exception is fergusonite, which reflects a Nd-rich end-member [fergusonite-(Nd)-β]. Even though the suffix use in the mineral nomenclature is recommended by the Commission on New Minerals, Nomenclature and Classification (CNMNC) of the International Mineralogical Association (IMA), for simplification we abstain from using the suffix in the following.

Fergusonite. The REE-niobate fergusonite (Table[1] 2) at the PCC belongs to the Ce-enriched, Nd-dominated end-member of this mineral group and is very rare compared to all other REE minerals found in the Palabora carbonatites. It mostly occurs as rounded to irregular inclusions (max. 80 µm) in magnetite, often associated with baddelyite and zirconolite (Figs. 8a and 8b).

REE-Ti-betafite (pyrochlore-group member). The REE-Ti-oxide REE-Ti-betafite (alternatively named ceriobetafite; not approved by IMA; Table[1] 2) seems to be restricted to TCB and represents, after fergusonite, the second rarest REE mineral in the PCC. Betafite requires Ti/(Nb+Ta+Ti) ratios above 1/3. Compositions with Ti > Nb+Ta (Ti-betafite) are very rare and normally exclusively known from granite pegmatites (Yaroshevskii and Bagdasarov 2008). REE-Ti-betafite in the PCC occurs as 25–75 µm sized needles and rods, mostly as inclusions in magnetite or, more rarely, in dolomite and calcite (Figs. 8c and 8d).

REE-F-carbonates. The REE-fluorocarbonates bastnäsite, parisite, and synchisite (Table[1] 2) are strongly associated with each other, with bastnäsite being by far the most abundant (>80% of all measured REE-F-carbonates). The following three associations can be distinguished.

The first type (REEFC-I) occurs mostly as 10–200 µm sized rods enclosed in magmatic calcite and dolomite (Figs. 6a–6c) and is associated with fluorite, strontianite (Fig. 6d), or ancylite (see below). These rods are often partly dissolved and form optically continuous single crystals (Figs. 6a–6d). REEFC-I needles partly included in sulfides show a higher resistance to dissolution for parts protected by the sulfide phase (Fig. 6b). The second type (REEFC-II a; restricted to TCB) forms as bastnäsite rods in the vicinity of monazite replacing apatite and is mostly associated with sulfides, valleriite, and ap-III (Figs. 6e and 6f). A third type (REEFC-II b; restricted to TCB) consists mainly of bastnäsite and generally occurs as irregularly shaped grains (5–100 µm) in late-stage carbonate veins (Figs. 6g and 6h). This type is frequently intergrown with magnetite or strontianite and contains inclusions of thorianite and rarely thorite (Figs. 6g and 6h). In few cases REEFC-II b is associated with anzaite (Fig. 6h).

Monazite. The REE-phosphate monazite (Table[1] 2) typically

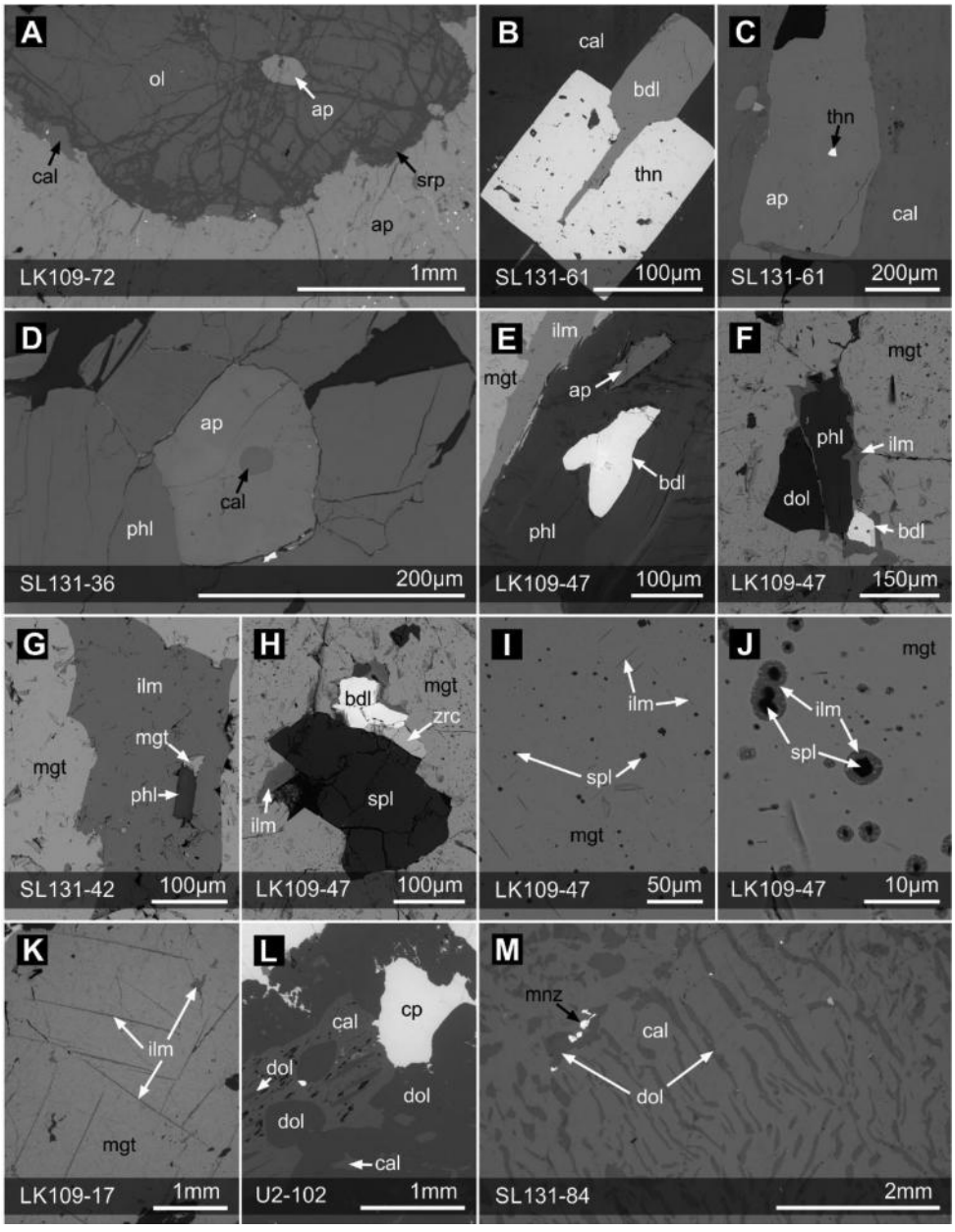

FIGURE 3. General orthomagmatic mineral assemblages observed in carbonatites and phoscorite from the Loolekop deposit. (**a**) Euhedral apatite inclusion in partly serpentinized forsterite. (**b**) Intergrowth of magmatic baddeleyite and thorianite. (**c**) Euhedral inclusion of thorianite in apatite. (**d**) Calcite inclusion in apatite, which again is enclosed in phlogopite. (**e**) Baddeleyite and apatite inclusions in phlogopite. (**f**) Dolomite and phlogopite surrounded by ilmenite in magnetite. Baddeleyite included in ilmenite. (**g**) Ilmenite with inclusions of phlogopite and magnetite, all included in magnetite. (**h**) Spinel with baddeleyite and zirconolite included in magnetite. (**i**) Exsolved spinel cubes (note the equality of orientation) associated with exsolved ilmenite lamellae in magnetite. (**j**) Slightly rounded spinel with a rim of ilmenite in magnetite. (**k**) Ilmenite exsolution lamellae in magnetite. (**l**) Distinct dolomite accumulations partly enclosed in calcite with dolomite exsolution (arrow). (**m**) Sub-graphic intergrowth of vermicular dolomite exsolutions with calcite.

represents La-enriched, Ce-dominated monazite [lanthanian monazite-(Ce) after the nomenclature of Bayliss and Levinson 1988]. Monazite is almost always replacing apatite, forming thin skins (≥3 µm) to massive rims (≤40 µm) around the latter (Fig. 4a). These textures can develop to a nearly complete replacement of apatite with lobate-like expansions up to 300 µm in diameter (Fig. 4a). In some cases relics of apatite are surrounded by thick rims of monazite (40–300 µm) in cases together with calcite (Fig. 4b). More uncommon appearances include monazite enclosed or in contact with sulfides, which may show reaction rims toward apatite in contact to the reaction of primary sulfide to valleriite (Figs. 4c and 4d).

Britholite. The Ca-REE-silicate britholite (Table[1] 2) is mainly present as fluorbritholite-(Ce). Britholite forms rims (≤60 µm thick) around forsterite-serpentine/chondrodite assemblages, where it usually precipitates at the outer rim of the serpentine (Figs. 4e and 4f) and chondrodite (Fig. 4g). In rare cases britholite (~20 µm thick) is also found in contact with phlogopite/chlorite (Fig. 4h).

Ancylite. The hydrous REE-Sr-carbonate ancylite (Table[1] 2) occurs in two textural varieties: The first type (ANC-I) forms 15–100 µm sized needles, rods, or irregular grains (Figs. 7a–7c) that may contain tiny inclusions of baryte (Figs. 7a and 7b) and are enclosed in calcite and dolomite (in cases associated with REEFC-I). ANC-I is often associated with strontianite and cordylite (see below). A second type (ANC-II) is restricted to TCB and forms 10–50 µm sized grains that are mostly associated with magnetite, thorite (Figs. 7d and 7e), strontianite, and baryte

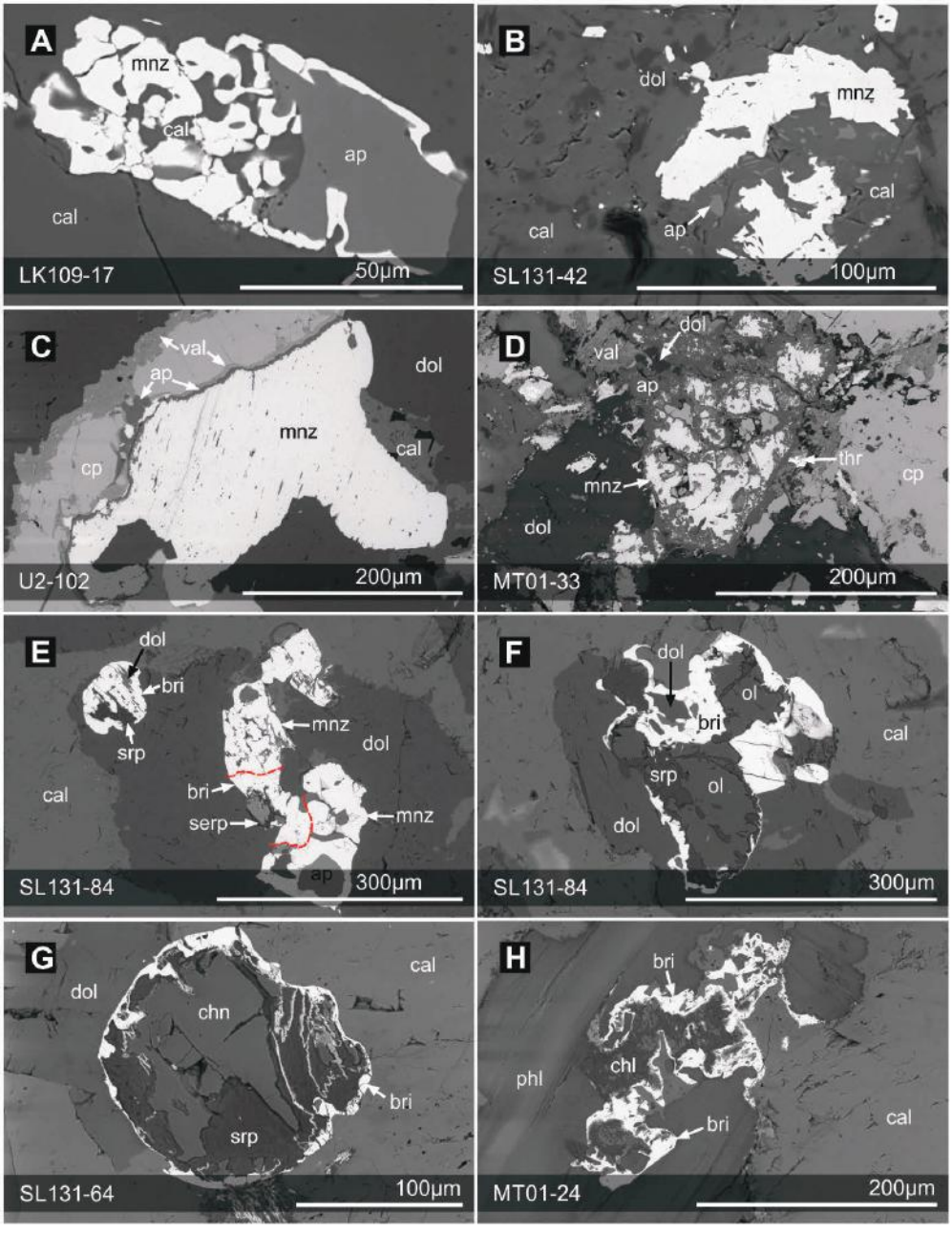

Figure 4. Textural appearances of monazite and britholite. (**a**) Lobate-like expansions of monazite rim around apatite. (**b**) Tiny relics of apatite enclosed by calcite with a thick rim and irregular precipitation of monazite. (**c**) Monazite partly enclosed by sulfides with apatite rim where sulfide shows valleriitization. Note the lack of apatite rim at monazite where no valleriitization took place. (**d**) Strongly altered monazite with formation of secondary apatite associated with valleriitization of sulfides. Note thorite inclusions in valleriite. (**e**) Monazite and britholite in equilibrium around serpentinized forsterite and apatite. The red dashed line marks the border between britholite and monazite. (**f**) Thick britholite rim around serpentinized forsterite. (**g**) Britholite around forsterite replaced by chondrodite and serpentine. (**h**) Britholite associated with phlogopite and chlorite.

and rarely occur as crack-fillings together with magnetite and celestine (Fig. 7f). Similar to REEFC-II b, this type occurs in late carbonate veins, but shows a higher affinity to serpentine, where REE-F-carbonates are usually absent (Figs. 7d and 7e).

Cordylite. Similar to ANC-I, the REE-Ba-carbonate cordylite (Table[1] 2) occurs as 10–100 µm sized needles or irregular grains enclosed in calcite and dolomite (Figs. 7g and 7h). Cordylite is often patchy (Fig. 7h) and may show tails filling tiny veins (Fig. 7g). It was only found in few samples mainly from the uppermost part of the Loolekop pipe, where baryte and celestine are relatively abundant. Importantly, cordylite in the direct vicinity of partly dissolved REEFC-I (see above)

shows no dissolution or alteration features.

Anzaite. A REE-Ti-oxide rarely found in the PCC is most likely anzaite (Table[1] 2), which up to now has only been described from the Afrikanda Complex (Russia; Chakhmouradian et al. 2015). To ultimately distinguish anzaite from a cation-deficient perovskite (which has to date not been described from a natural occurrence, though) XRD analyses would be needed (Chakhmouradian et al. 2015). In the investigated samples, anzaite occurs in two distinct associations: (1) In most cases 10–30 µm sized anzaite replaces ilmenite (Figs. 5a–5d) and often shows patchy zonation, reflecting variable REE/Ti ratios (Fig. 5a). (2) Mostly in medium to highly serpentinized samples (restricted to TCB), however, 5–30 µm sized irregular grains or schlieren of anzaite occur, which are commonly associated and mostly intergrown with valleriite, but not with ilmenite (Figs. 5e and 5f).

Discussion

The identification of fergusonite, REE-Ti-betafite, cordylite, and britholite during this study represents the first described occurrence of these REE minerals in the PCC and the first occurrence in a carbonatite complex of South Africa. Bulakh et al. (1998) mentioned a Ti-REE mineral and Karchevsky (2000) described a REE-silicate for the PCC, but both gave no further specifications on these minerals. The probable identification of anzaite represents its second occurrence worldwide.

Multistage formation of REE minerals in the Palabora carbonatites and phoscorites

Most REE mineralizations in carbonatites are believed to have crystallized from carbo- or hydrothermal fluids (e.g., Mariano 1989; Wall and Mariano 1996; Wyllie et al. 1996; Wall et al. 2001; Zaitsev et al. 2002; Williams-Jones et al. 2012; Nadeau et al. 2015). However, fluid inclusion studies show that REE do not preferentially fractionate into fluids, although they would be capable of transporting REE (Bühn and Rankin 1999). Experimental studies at high temperatures (Song et al. 2016) imply that carbonatite-related REE deposits may form by fractional crystallization of carbonatitic melts rather than from

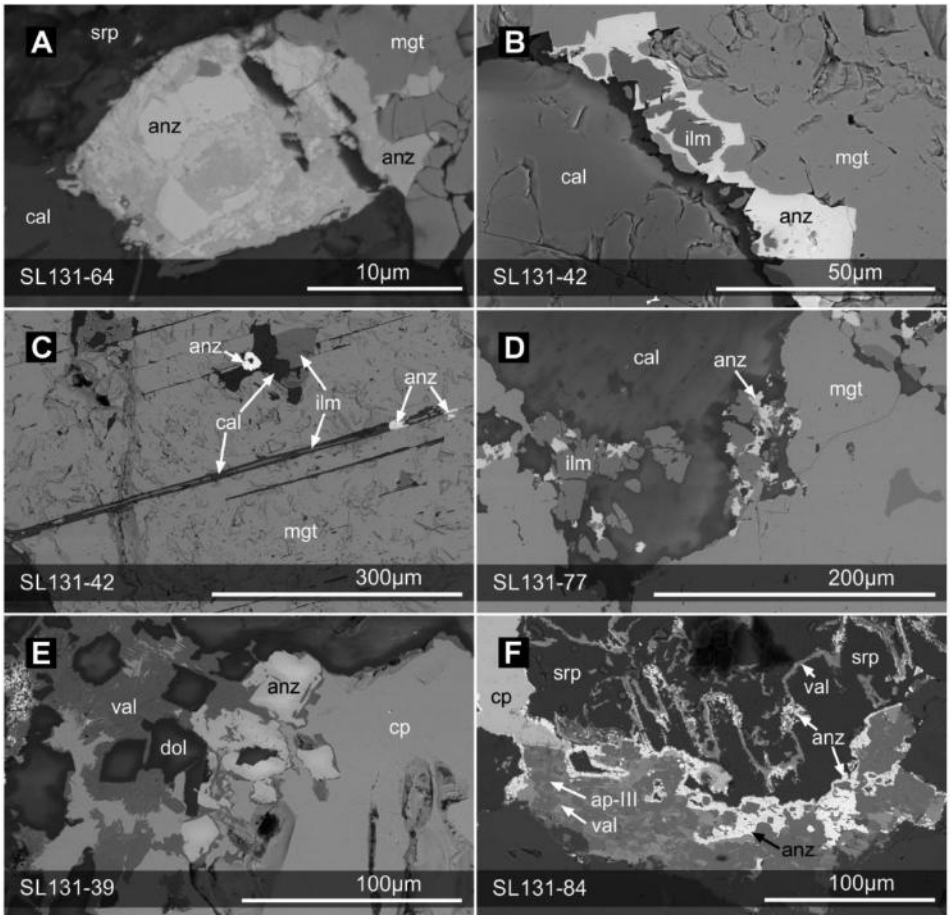

Figure 5. Textural appearances of anzaite. (**a**) Compositionally zoned anzaite completely replacing ilmenite in contact with magnetite. Anzaite shows mostly patchy zoning with the brightest areas having high REE/Ti ratios and the darker areas showing the opposite. (**b**) Anzaite replacing ilmenite with ilmenite relics enclosed by anzaite. (**c**) Dissolved ilmenite lamellae (partly filled with calcite) with relictic ilmenite in the center of the lamellae and precipitation of anzaite within the former lamellae. The upper part of the image displays the same phenomenon with a batch of ilmenite partly dissolved and filled by calcite and showing marginal precipitation of anzaite. (**d**) Part replacement of ilmenite by anzaite as well as precipitation of anzaite around ilmenite relicts. (**e**) Anzaite associated with valleriite replacing chalcopyrite. (**f**) Association of anzaite, valleriite, serpentine, and secondary apatite (ap-III). Note the intergrowth of valleriite, ap-III, and anzaite.

exsolved hydrothermal fluids. In rare cases only, a magmatic origin for REE mineralizations in carbonatites is assumed, based on textural (e.g., Mountain Pass, Mariano 1989) and isotopic data (e.g., Zaitsev et al. 2002) with alteration, replacement, and remobilization of preexisting REE minerals clearly linked to a late-stage process involving water-bearing fluids (e.g., Wall and Mariano 1996; Zaitsev et al. 1998, 2002; Wall et al. 2001; Moore et al. 2015). Some paragenetic studies on individual carbonatite complexes indicate multistage mineralization processes with significant overprint of the orthomagmatic mineralization by a

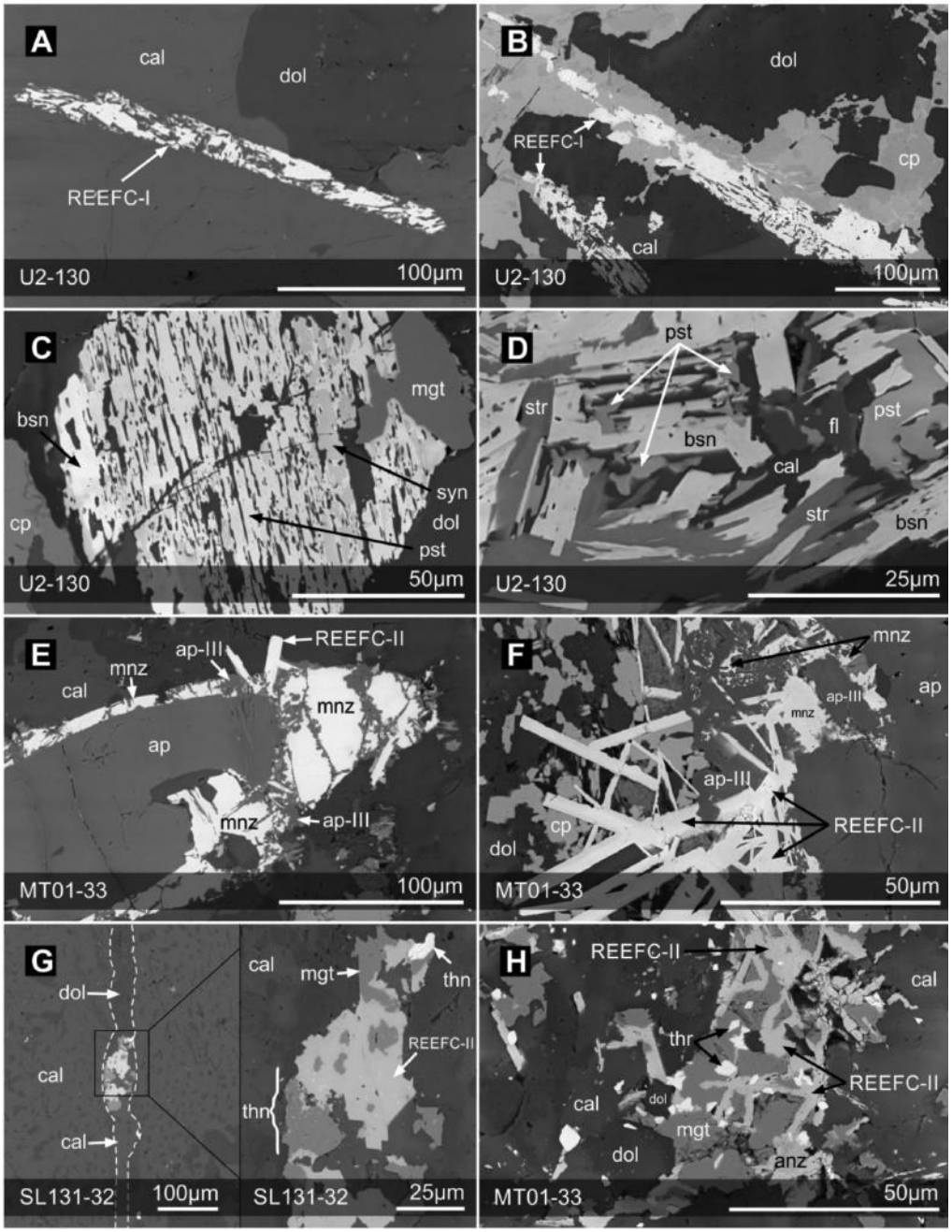

Figure 6. Textural appearances of REE-F-carbonates. (**a**) Partly dissolved REEFC-I needle. (**b**) REEFC-I partly included in chalcopyrite. Note the strong dissolved parts of REEFC-I outside the sulfide enclosure. (**c** and **d**) Partly dissolved REEFC-I with interdigitated parisite/synchysite and bastnäsite, and (**d**) the additional presence of strontianite and fluorite. (**e** and **f**) Relics of monazite around apatite with interlocked REEFC-II a. Monazite decomposed to secondary REEFC-II a needles and secondary apatite (ap-II). (**g**) Carbonate vein (marked with white dashed line) through calcite with exsolved dolomite and REEFC-II b. The enlargement shows the intergrowth with magnetite. Note the tiny secondary thorianite inclusions in magnetite and REEFC-II b. (**h**) REEFC-II b intergrown with magnetite and anzaite with inclusions of secondary "fusiform" thorite. Recrystallized zone is located next to a serpentinized area.

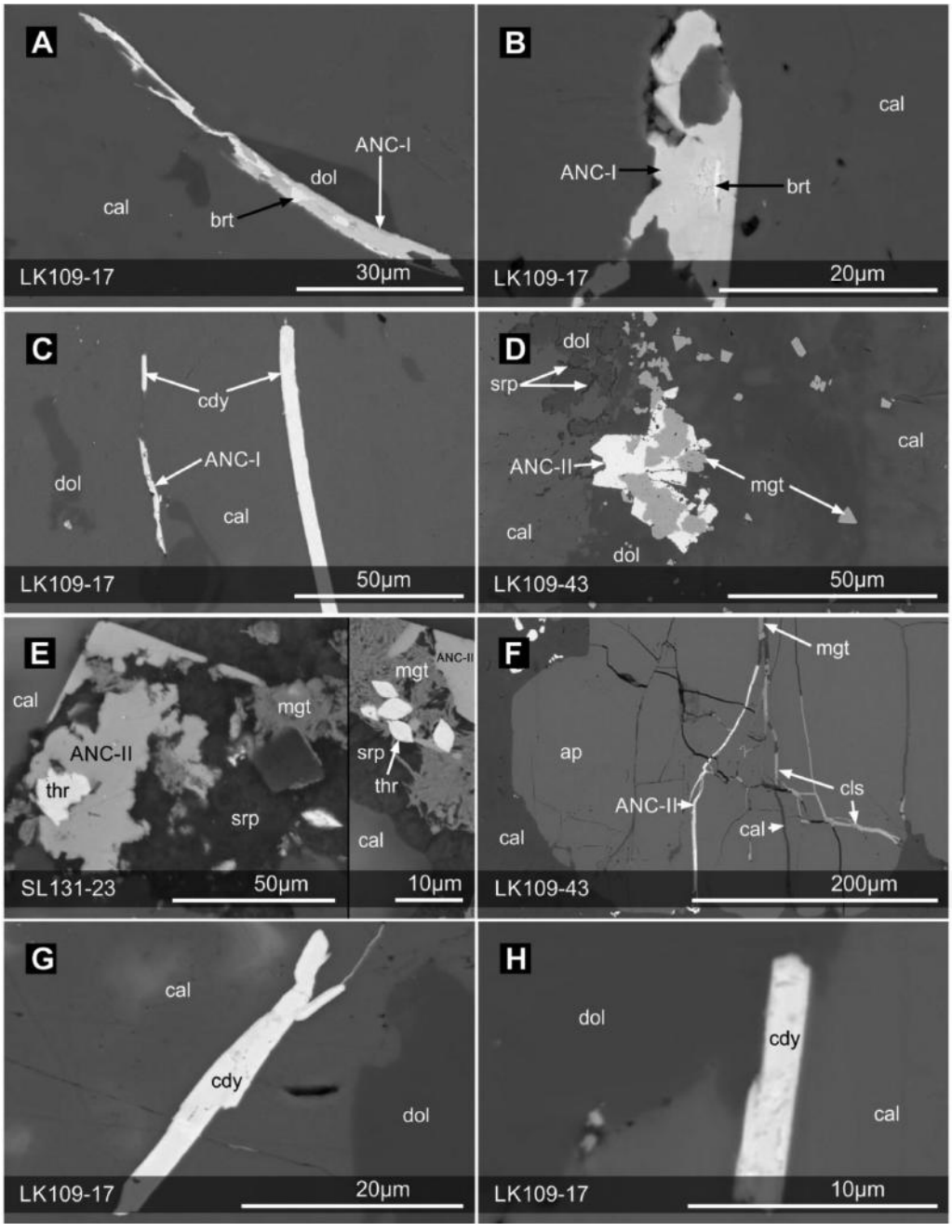

Figure 7. Textural appearances of ancylite and cordylite. (**a**) Heterogeneous ancylite needle with light parts reflecting intergrown baryte. The darkest parts reflect a high Ca, low Sr, and low REE contents and the medium light parts reflect a high Sr and low Ca content with a high concentration of REE. (**b**) Rod-like/partly irregular ancylite with an inclusion of baryte. (**c**) Ancylite associated with cordylite. (**d**) Ancylite intergrowth with magnetite in recrystallized carbonate vein. Dark rims around dolomite represent serpentine. (**e**) Ancylite pseudomorphed after completely dissolved primary thorianite, with a thorite inclusion enclosed in ancylite, serpentine, and magnetite, all associated with recrystallized calcite. (**f**) Cracks in apatite filled with ancylite, celestine, and magnetite. (**g**) Cordylite with a thin tail filling a crack in calcite. (**h**) Patchy zonation of cordylite shows the heterogeneity of this phase.

late-stage hydrothermal or carbothermal mineralization (Rankin 2005). Nevertheless, the controls on the REE mineralization in carbonatites are poorly understood (Trofanenko et al. 2016).

Based on the textures described above, the various REE mineral associations at Palabora formed during different stages (Figs. 2 and 9). While fergusonite, REE-Ti-betafite, and probably also REEFC-I crystallized during the orthomagmatic stage directly from a carbonatitic melt, monazite and britholite

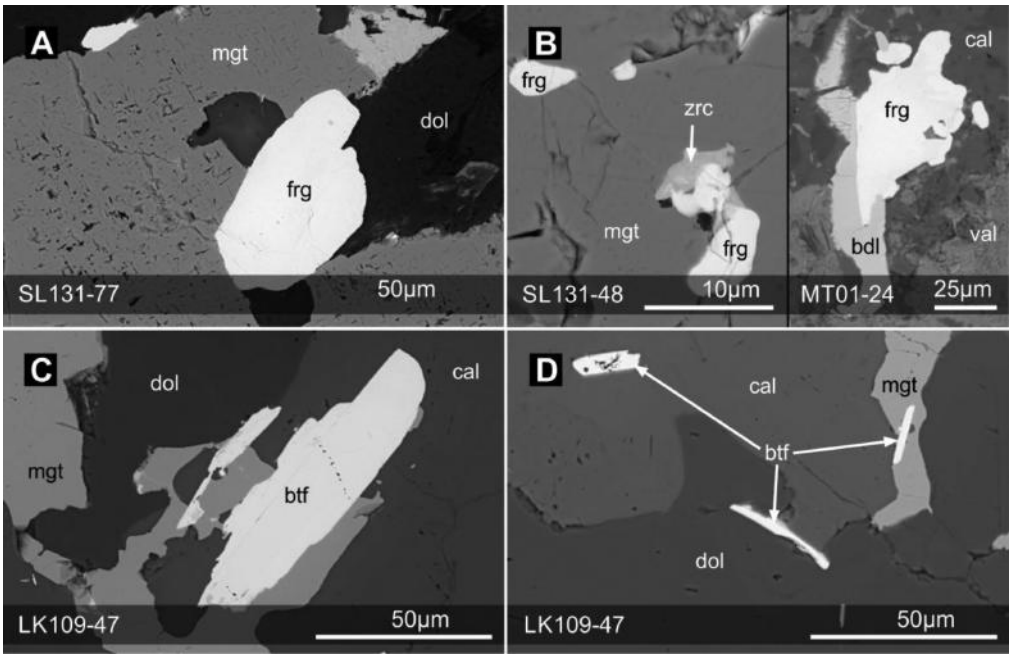

Figure 8. Textural appearances of fergusonite and REE-Ti-betafite. (**a**) Rounded fergusonite partly included in magnetite. (**b**) Rounded fergusonite associated with zirconolite included in magnetite and partly dissolved fergusonite with overgrown baddeleyite. Small baddelyite grain on the left side in contrast shows an overgrowth by fergusonite. (**c**) Rod-shaped REE-Ti-betafite partly included in magnetite. (**d**) Rod-shaped REE-Ti-betafites included in magnetite, calcite, and dolomite.

precipitated from late-magmatic fluids (LM fluid). Finally, the formation of anzaite, REEFC-II (a+b) and ANC-II and the alteration of monazite and REEFC-I is assigned to REE redistribution processes caused by post-magmatic fluids (PM fluid). Although the genetic position of ANC-I and cordylite is not entirely clear, the association with baryte, the integrity of ANC-I, and the presence of cordylite needles next to strongly dissolved REEFC-I needles favor a formation during stage 4 (Fig. 2).

The variability of types of REE mineralization in the PCC largely reflects the sensitive character of REE mineral formation during fluid-assisted processes. We suggest that late-magmatic and post-magmatic fluids show compositional variabilities, which are probably caused by local dissolution-reprecipitation processes. We distinguish the following fluid types: LM = late-magmatic fluid enriched in REE, LM′ = REE-depleted analog of LM that results from REE mineral precipitation from LM, PM = post-magmatic REE-poor or -free initial fluids, PM′ = fluids enriched in REE by remobilization, PM″ = REE- and cation-enriched fluids transporting the element content for distal precipitation, and PM‴ = REE-depleted fluids after REE mineral precipitation from PM′ and PM″.

Orthomagmatic crystallization of fergusonite, REE-Ti-betafite, and REE-F carbonates

Texturally, fergusonite and REE-Ti-betafite are interpreted as early magmatic REE phases, which probably crystallized more or less contemporaneously. Fergusonite represents the most important Nb-phase in the system (pyrochlore sensu stricto is lacking), but its very low abundance reflects a general depletion of Nb in the Palabora carbonatites. Hence, the PCC comprises a magmatic association of a Ti-poor Nb-oxide (fergusonite; <0.13 wt% TiO_2) and a Nb-poor Ti-oxide (REE-Ti-betafite; <0.11 wt% Nb_2O_5). Notably, Ti-bearing fergusonite (>1 wt% TiO_2) and Nb-bearing betafite (up to 20 wt% Nb_2O_5) have been described (e.g., Mitchell and Chakhmouradian 1998; Tomašić et al. 2006; Yaroshevskii and Bagdasarov 2008). At this stage it remains unclear why magmatic fergusonite and betafite in the PCC do not incorporate significant amounts of Ti and Nb, respectively. The enclosure of both mineral phases in magnetite isolates these minerals mostly from later fluid interactions and alteration (Fig. 9).

In general, REE-fluorocarbonates are among the most abundant REE minerals in carbonatites (Shunhua et al. 1986; Hsu 1992; Williams-Jones and Wood 1992). Although REE-F-carbonates (especially bastnäsite) are stable to temperatures above 600 °C (Wyllie et al. 1996 and references therein), most REE-fluorocarbonates precipitate at comparatively low temperatures (Williams-Jones and Wood 1992). Magmatic REE-F-carbonates (mainly represented by bastnäsite) from Mountain Pass were described as coarse-grained, hexagonal prismatic (strongly elongated), crystals in fine- to medium-grained calcite and baryte, while fine-grained, stubby, hexagonal, interstitial prisms of bastnäsite were formed by a late residual fluid (Castor 2008).

At Palabora REE-F-carbonates (REEFC-I) occur as small and elongated crystals that are partly dissolved and form optically continuous single crystals (Fig. 6a and 6b) and well-preserved REEFC-I needles are included in sulfides. Based on this and the similarities to REE-F-carbonates at Mountain Pass (except for crystal size), we assume a magmatic origin for

REEFC-I at Palabora.

Normally REE-F-carbonates contain minor amounts of Th (e.g., Armbrustmacher 1979; Smith et al. 2000; Humphries 2012). For example, bastnäsite typically contains 0.2–0.3 wt% Th (Wang et al. 2013) and can also occur as thorbastnäsite (Smith et al. 2000) with 47 wt% Th (Pavlenko et al. 1965). Uher et al. (2015) even report ThO_2 concentrations of 0.5 to 1.4 wt% for bastnäsite and 0.4 to 4.5 wt% for synchysite in a granite from Stupné, Slovakia. In our case, REEFC-I are Th-poor (<0.08 wt%), which is in contrast to REEFC-II (see below). We suggest that early magmatic precipitation of Th-minerals (mostly thorianite; Figs. 2 and 3b) caused an early depletion of Th in the magmatic system, which resulted in lower Th concentrations during the stage of REEFC-I precipitation. Furthermore, partly dissolved REEFC-I (Fig. 6a) indicates a later remobilization of REE and the patchy appearance of parisite and synchysite within the bastnäsite interdigitation indicates an alteration of bastnäsite to synchysite and parisite during the remobilization of REE (see below).

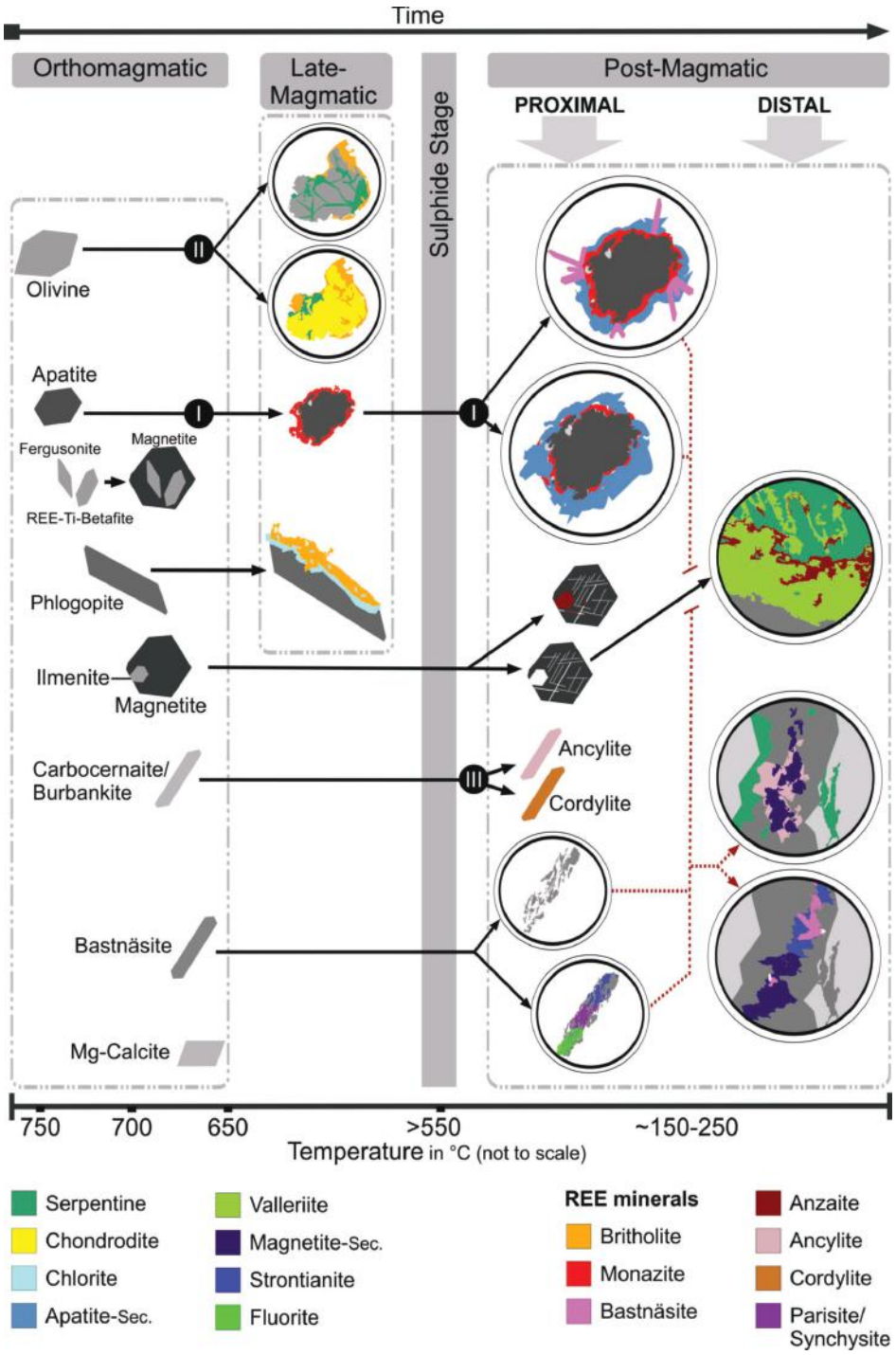

FIGURE 9. Scheme for REE mineral precipitation during different evolutionary stages of the Palabora carbonatites. Estimated temperatures after (Fernandez et al. 1977; Solovova et al. 1998; Fleet 2006; Sharygin et al. 2011; Chakhmouradian et al. 2015). Roman numbers (I–III) refer to diagrams in Figure 10.

Late-magmatic formation of monazite and britholite at the expense of apatite and forsterite

Monazite formation. The replacement of apatite by monazite has been described for some hydrothermal deposits (e.g., Pan et al. 1993a; Lieftink et al. 1994; Smith et al. 1999) as a late-stage alteration phenomenon (Wall and Mariano 1996). Monazite inclusions and rims around apatite are often explained by fluid-induced (metasomatic) alteration of apatite via coupled substitution and mass transfer (Harlov et al. 2002, 2005; Harlov and Förster 2003). As such, monazite may have originated from the REE budget available from the apatite itself, where Si and Na would be removed from the apatite without the concurrent removal of REE (Pan et al. 1993a; Harlov and Förster 2002; Harlov et al. 2002).

In the investigated samples there is no textural evidence to

suggest that monazite is the result of exsolution from precursor apatite during metasomatic alteration. Rather, apatite shows strong dissolution textures. Mass-balance considerations imply that the REE content of the apatite is not sufficient to allow for the precipitation of the observed amounts of monazite (Figs. 4a and 4b). We suggest that the precipitation of monazite (in cases associated with calcite) at the expense of apatite was caused by a REE-bearing fluid, according to the following schematic equation:

Apatite + LM Fluid = Monazite + Calcite + LM′ Fluid

$$Ca_5(PO_4)_3F + CO_3^{2-} + 3REE^{3+} = 3REE(PO_4) + CaCO_3 + F^- + 4Ca^{2+} \quad (1)$$

Due to the relative immobility of P (Smith et al. 1999; Poitrasson et al. 2004; Cetiner et al. 2005; Louvel et al. 2015), monazite mainly precipitates directly at the contact to apatite or within its immediate vicinity. The different appearances from surficial dissolution (thin rims of monazite around euhedral apatite; Fig. 4a) to nearly complete dissolution (larger masses of monazite with relict apatite; Fig. 4b) probably reflect variable degrees of apatite replacement by monazite linked to the degree of apatite dissolution by the fluid.

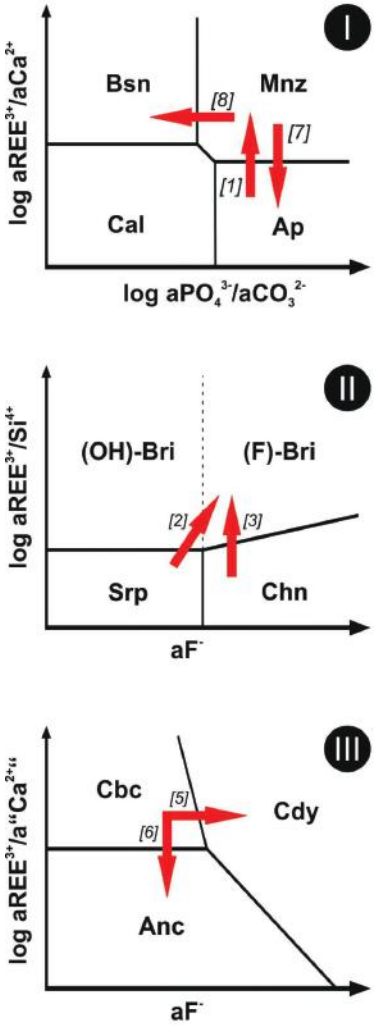

Figure 10. Qualitative activity diagrams illustrating the relative stabilities of different REE mineral phases. Numbers in parentheses refer to reactions mentioned in the text. Note the necessity of REE introduction for the formation of monazite and britholite during stage 2 (I and II) as well as the locally controlled variability of F in stage 2 and 4 fluids (II and III). The activity of "Ca^{2+}" in diagram III reflects the combination of the alkali- and alkaline earth metals Na^++Ca^{2+}+Sr^{2+}+Ba^{2+} for simplification.

Britholite formation. Britholite is mainly described from nepheline syenites and contact metasomatic deposits, where it generally forms during hydrothermal processes related to the replacement of apatite or monazite (Budzyń et al. 2011; Uher et al. 2015; Zirner et al. 2015). Britholite has also been described as a low-temperature phase in the Virulando carbonatite (Angola) where it formed during late-stage supergene alteration processes, associated with synchysite, cerite, goethite, hollandite, and baryte (Torró et al. 2012). In all, britholite is assumed to have a late stage to post-magmatic (subsolidus alteration of primary minerals) origin for most occurrences (Wall et al. 1993; Uher et al. 2015).

Typically, britholite obtains the necessary anions from Si-bearing hydrothermal fluids. However, because of a general lack of Si-rich fluids in carbonatitic systems, another Si source has to be considered. Based on textural evidence, we suggest that Si is provided by the serpentinization of forsterite and the replacement of forsterite by chondrodite to which britholite is largely bound (Fig. 4f, 4g, and 9). As forsterite is REE-poor, the britholite-forming fluid contained appreciable amounts of REE, in accordance with the assumptions made for monazite formation above:

Forsterite + LM Fluid = Serpentine + Dolomite + Britholite + LM′ Fluid

$$9Mg_2SiO_4 + 3½H_2O + 5½H^+ + ½F^- + 4Ca^{2+} + 4CO_3^{2-} + 3REE^{3+} = 3Mg_3Si_2O_5(OH)_4 + 2MgCa(CO_3)_2 + Ca_2(REE)_3(SiO_4)_3(F,OH) + 7Mg^{2+} \quad (2)$$

Forsterite + LM Fluid = Chondrodite + Britholite + LM′ Fluid

$$5Mg_2SiO_4 + ⅔Ca^{2+} + 4⅓F^- + REE^{3+} = 2Mg_5(SiO_4)_2F_2 + ⅓Ca_2(REE)_3(SiO_4)_3(F) \quad (3)$$

In a few cases britholite formation is associated with the chloritization of phlogopite:

Phlogopite + LM Fluid = Chlorite + Britholite + LM′ Fluid

$$2KMg_3(Si_3Al)O_{10}(F_2) + 10OH^- + 2Ca^{2+} + 3REE^{3+} = (Mg_5Al)(Si_3Al)O_{10}(OH)_8 + Ca_2(REE)_3(SiO_4)_3(F) + Mg^{2+} + 2K^+ + 3F^- + 2H^+ \quad (4)$$

Although britholite from Palabora is generally F-rich (fluorbritholite; Fig. 10 II), britholite associated with the replacement of forsterite by chondrodite and the chloritization of phlogopite is higher in F than the britholite associated with the serpentinization of forsterite. This shows that the LM fluid contains variable contents of F (Fig. 10 II).

Based on textural observations (Fig. 4e), we suggest that monazite and britholite formed contemporaneously from the same fluid (Fig. 9). Accordingly, the type of REE phase formed depends on the local presence of forsterite or apatite, which provide the necessary SiO_4^{4-} or PO_4^{3-}, respectively. The occasional presence of acicular ap-II in serpentine indicates that small amounts of P (released by monazite formation; confirmed by mass-balance calculations or dissolution of apatite) may cause precipitation of secondary apatite during serpentinization of forsterite. The absence of REE

in olivine and the too low concentrations in apatite indicates the necessity to import REE into the system to precipitate britholite and monazite (arrows labeled 1–3 in Fig. 10).

Post-magmatic redistribution of REE: Formation of cordylite, ancylite, REE-F carbonates, and anzaite

Cordylite and ancylite (ANC-I) formation. Whereas ancylite is a relatively common REE mineral in carbonatites, cordylite is extremely rare (Zaitsev et al. 1998). Ancylite has never been described as a primary magmatic mineral, instead it is specified as a useful indicator of hydrothermal/carbothermal processes (Wall and Zaitsev 2004a; Verplanck et al. 2016). Zaitsev et al. (1998) describe the association of cordylite and ancylite as resulting from the hydrothermal alteration of magmatic carbocernaite and burbankite. Based on this and our own textural observations (see above), we suggest that cordylite (Fig. 7g) and ANC-I (Figs. 7a–7c), together with baryte and strontianite with which it is tightly associated, may replace precursor REE-Ca-Sr-carbonates. Because of the absence of any relics it is not possible to identify the precursor mineral of cordylite and ANC-I. However, based on very similar textural descriptions in the literature (Pecora and Kerr 1953; Somina 1975; Kapustin 1980; Zaitsev et al. 1998; Moore et al. 2015), we assume the former presence of carbocernaite/burbankite (red question mark in Fig. 2). Burbankite and/or carbocernaite are important REE minerals in carbonatites that were probably present in many carbonatites but are typically replaced by ancylite, strontianite, synchysite, calcite, baryte, quartz, monazite, and apatite (e.g., Kangankunde, Malawi; Wigu Hill, Tanzania; Adiounedj, Mali; Bear Lodge, Wyoming, and Gem Park, U.S.A.; Wall et al. 1997). Supposing the precipitation of cordylite and ancylite during the early phase of stage 4 (Fig. 2 and 9), we suggest that dissolution of REEFC-II (see below) controls the activity of F in the fluid, which in turn controls the formation of ancylite and cordylite (Fig. 10 III). Ancylite and cordylite are depleted in Th, which suggest that the fluid from which they precipitated from was also Th-poor. The later precipitation of secondary thorianite and thorite, as well as slightly higher Th contents in later secondary REE minerals, suggest Th-enrichment of the fluid by dissolution of primary Th minerals.

Monazite alteration. Monazite in contact with or enclosed by sulfides is occasionally altered to ap-III associated with the valleriitization of the sulfide (Figs. 4c, 4d, and 9). This may be caused by the remobilization of REE from monazite (Fig. 10 I) by the same fluid that caused valleriitization of sulfides and can be explained by the following schematic equation:

Monazite + Chalcopyrite + PM Fluid = Apatite + Valleriite + PM′ Fluid

$$3REE(PO_4) + CuFeS_2 + 5Ca^{2+} + HF + Mg^{2+} + \tfrac{1}{2}Al^{3+} + 2OH^- = Ca_5(PO_4)_3F + 2[(Fe,Cu)S]\cdot 1.53(Mg,Al)(O,OH)_2 + 3REE^{3+} + 2\tfrac{1}{2}H^+ \quad (5)$$

Valleriitization in association with ap-III formation sometimes includes thorite (Fig. 4d), which is supposed to be formed by the remobilization of Th from primary Th minerals by a post-magmatic fluid.

REEFC-II formation. REEFC-II show two different types of occurrence, which may be distinguished into a proximally (REEFC-II a) and a distally precipitated (REEFC-II b) variety depending on the REE saturation of the fluid (Fig. 9). The proximal variety (Figs. 6e and 6f) indicates reaction of monazite, apatite, and a fluid, which is linked to reaction 5 with the exception of the availability of CO_3^{2-} by the dissolution of carbonate. The remobilization of REE during this reaction will be prevented by the formation of REEFC-II a (exclusively bastnäsite), similar to what was observed in the Bayan Obo deposit (Smith et al. 1999):

Monazite + Calcite + PM Fluid = Apatite + Bastnäsite + PM′ Fluid

$$3(REE)PO_4 + 5CaCO_3 + 4HF = Ca_5(PO_4)_3F + 3(REE)(CO_3)F + 2H_2O + 2CO_2 \quad (6)$$

Partial dissolution of REEFC-I (see above) may form strontianite, parisite/synchysite and fluorite in the interstices of the REEFC-I interdigitation (Figs. 6d and 9). This may cause additional remobilization of REE by the evacuation of dissolved components $[(REE)(CO_3)F \leftrightarrow REE^{3+} + CO_3^{2-} + F^-]$. The alteration of REEFC-I to parisite and synchysite may be caused by interaction with a Ca-rich fluid, while the presence of Sr promotes additional precipitation of strontianite and fluorite:

Bastnäsite + PM Fluid = Parisite

$$2(REE)(CO_3)F + Ca^{2+} + CO_3^{2-} = Ca(REE)_2(CO_3)_3F_2 \quad (7)$$

Bastnäsite + PM Fluid = Strontianite + Parisite + Fluorite + PM′ Fluid

$$4(REE)(CO_3)F + 2Ca^{2+} + Sr^{2+} = SrCO_3 + Ca(REE)_2(CO_3)_3F_2 + CaF_2 + 2REE^{3+} \quad (8)$$

The observation that REEFC-I needles, protected as inclusions in sulfide (Fig. 6b), do not show the described alteration, indicates that this process happens after the formation of sulfide minerals and during the post-magmatic stage.

The second variety (distal; REEFC-II b) precipitated in veinlike fluid paths together with secondary strontianite, magnetite, anzaite, valleriite, thorianite, and thorite (Figs. 6g, 6h, and 9). Thus, the fluid causing the precipitation of these secondary minerals was probably enriched in Th. Thorium can be remobilized by leaching and dissolution of primary Th-bearing minerals such as thorianite (Pan et al. 1993b). At high temperatures, Th can be incorporated into REE minerals (Harlov et al. 2011), whereas at low temperatures, Th incorporation into REE minerals is restricted (Read et al. 2002; Doroshkevich et al. 2008; Budzyń et al. 2010), which explains the coexistence of secondary Th minerals with REEFC-II b (Figs. 6g and 6h). In fact, Th contents in REEFC-II are higher than in REEFC-I, but the depletion of Th in REEFC-I depends on the depletion of Th in the melt during REEFC-I precipitation after the early crystallization of Th minerals (see above). At the same time, REEFC-II b formed concurrently with Th minerals due to the remobilization of Th from primary Th minerals. Formation of REEFC-II b may have occurred according to the following schematic reactions:

Dolomite A + Calcite A + PM′ Fluid =
REEFC-II b (Bastnäsite) + Calcite B + Dolomite B + PM‴ Fluid

$$2MgCa(CO_3)_2 + CaCO_3 + REE^{3+} + HF = REE(CO_3)F + 2CaCO_3 + MgCa(CO_3)_2 + Mg^{2+} + H^+ \quad (9)$$

The percolating fluid that caused the formation of REEFC-II b further induced dissolution (calcite A and dolomite A) and recrystallization (calcite B and dolomite B) of carbonates constituting a further generation of carbonates within veins (Fig. 6g).

Ancylite (ANC-II) formation. Similarly, ANC-II is bound to vein-like fluid paths with a secondary mineralization of carbonates (Fig. 7d). However, ANC-II was not observed to coexist with REEFC-II b. Rather, in cases where REEFC-II b are present, the dominant Sr phase is a REE-poor strontianite (ΣREE_2O_3 < 4 wt%; Karchevsky 2000) and the REE are mainly incorporated into REEFC-II b (Fig. 9). At presumably higher H_2O activities, the formation of serpentine and the absence of the REEFC-II b lead to the concentration of REE into the Sr phase ancylite. The necessary Sr was probably provided by the dissolution of strontianite and/or Sr-rich calcite (which occurs as secondary exsolutions in exsolved dolomite):

Dolomite A + Calcite A + Strontianite + PM′ Fluid =
ANC-II + Dolomite B + Calcite B + PM‴ Fluid

$$MgCa(CO_3)_2 + 2¼CaCO_3 + ¾SrCO_3 + 2H_2O + REE^{3+} = (Sr_{0.75}Ca_{0.25})(REE)(CO_3)_2(OH)\cdot H_2O + MgCa(CO_3)_2 + CaCO_3 + Ca^{2+} + H^+ \quad (10)$$

Dolomite A + Sr-Calcite + PM′ Fluid =
ANC-II + Dolomite B + Calcite + PM‴ Fluid

$$MgCa(CO_3)_2 + 3(Ca_{0.75}Sr_{0.25})CO_3 + 2H_2O + REE^{3+} = (Sr_{0.75}Ca_{0.25})(REE)(CO_3)_2(OH)\cdot H_2O + MgCa(CO_3)_2 + CaCO_3 + Ca^{2+} + H^+ \quad (11)$$

Anzaite formation. Anzaite-(Ce) was first described from Afrikanda (Russia) as a late hydrothermal alteration product where Ti and Fe were derived from primary Ti oxides such as ilmenite. This is reflected by a ubiquitous association of anzaite with ilmenite and/or Ti-rich magnetite (Chakhmouradian et al. 2015). The associated mineral assemblage precipitated at Afrikanda at 150–250 °C, $aH^+ \approx 10^{-5}$ and $aH_4SiO_4^0 > 10^{-4}$ (Chakhmouradian and Zaitsev 2004).

The close association of anzaite with valleriite (Figs. 5e and 5f) at Palabora confirms the assumption of a low-temperature origin. Anzaite is texturally bound to ilmenite (Figs. 5b and 5d). Therefore, the partial dissolution of ilmenite by a REE-bearing fluid seems to be essential for the local enrichment of Ti allowing for the formation of anzaite. Two different occurrences of anzaite can be distinguished, which might reflect a proximal and distal fluid transport (Fig. 9) of a Ti-enriched, REE-bearing fluid.

The common association includes anzaite with relics of ilmenite in direct contact or close vicinity with magnetite (Figs. 5a–5d). In this case, anzaite directly replaces ilmenite, which can be described by the following schematic equation:

Ilmenite + PM′ Fluid = Anzaite + PM‴ Fluid

$$6FeTiO_3 + 2OH^- + 4REE^{3+} = REE_4FeTi_6O_{18}(OH)_2 + 5Fe^{2+}. \quad (12)$$

The less common occurrence of anzaite is not directly bound to ilmenite but associated with valleriite and serpentine (Figs. 5e and 5f). This association requires small-scale hydrothermal transport of Ti, Al, and Si by a REE-bearing fluid. In general, very low pH fluids, combined with the availability of complexing ligands such as F, can enable Ti transport (van Baalen 1993). However, we consider such low pH values (<2) unlikely for Palabora. Alternatively, significant mass transfer of Ti has been explained by complexing agents of polymerized silicate molecules in solution (Manning 2004), most likely Ti-aluminosilicate complexes (Tropper and Manning 2005; Beitter et al. 2008). We favor this explanation as the assumption of the existence of Ti-transporting aluminosilicate complexes provides Al and Si for valleriite and serpentine formation, respectively (as observed; reaction 13b). The precipitation of this type of anzaite together with valleriite may be expressed by a two-step process. First, ilmenite is dissolved and Ti-aluminosilicate-complexes form:

Ilmenite + PM′ Fluid (incl. aluminosilicate-complex) = PM″ Fluid

$$FeTiO_3 + 6⅓OH^- + 3H_2O + 7Mg^{2+} + 2AlOSi(OH)_3^{2+} + ⅔REE^{3+} = 12⅓OH^- + 7Mg^{2+} + 2(Ti,Fe)\text{-}AlOSi(OH)_3^{5+} + ⅔REE^{3+} \quad (13a)$$

This Ti-enriched fluid may then precipitate anzaite together with valleriite and serpentine when coming into contact with sulfides:

PM″ Fluid + Cu-Fe Sulfide (e.g., Chalcopyrite) =
Anzaite + Valleriite + Serpentine + PM‴ Fluid

$$12⅓OH^- + 7Mg^{2+} + 2(Ti,Fe)\text{-}AlOSi(OH)_3^{5+} + ⅔REE^{3+} + 4CuFeS_2 = ⅙REE_4FeTi_6O_{18}(OH)_2 + 4\{2[(Fe,Cu)S]\cdot 1.53[(Mg,Al)(O,OH)_2]\} + ½Mg_6Si_4O_{10}(OH)_8 + {}^5/_6Fe^{2+} + 12H^+ \quad (13b)$$

The type of anzaite formation (proximal or distal; Fig. 9) depends on the availability of potential Ti-complexing ligands and is therefore locally controlled by the earlier enrichment of Si and Al.

Although Kavecsanszki et al. (2012) assume that the sulfide-bearing liquid (stage 3) released fenitizing fluids, the actual source of the PM fluid has not yet been demonstrated. Alternatively, external fluids, e.g., related to the cross-cutting dolerite dikes, may have caused post-magmatic alteration reactions within the carbonatites.

IMPLICATIONS

Our new data reveal a complex interplay between host minerals, fluid chemistry, and REE mineralogy after the orthomagmatic stage. This interplay leads to various local chemical (micro) environments reflected in different REE mineral assemblages. Our results suggest that hydrothermal processes during late-magmatic and post-magmatic stages are of greater importance with respect to the formation and variability of REE minerals than orthomagmatic crystallization. Hydrothermal overprint causes alteration and in some cases complete replacement of primary REE minerals. Our study on the Palabora carbonatites further implies that the REE contents of magmatic minerals (such as apatite and carbonates) are not high enough to account for the formation of late-magmatic REE minerals such as monazite, which suggests that a REE-enriched fluid was introduced into the observed sections of the complex during late-magmatic stages. The results of this study confirm (1) the significance of late-stage introduction of REE and their reaction with precursor mineral phases, and (2) the redistribution of REE during post-magmatic stages in natural carbonatitic systems.

ACKNOWLEDGMENTS

Anatoly N. Zaitsev is thanked for helpful comments on an earlier version of our manuscript. We thank Glen Taylor (Director of Research UFS) for providing funds for the visits in RSA as well as the stays at Phalaborwa and the DFG for general funding of this project (MA 2563/10-1). The Department of Geology at the University of the Free State is acknowledged for making the FE-SEM (Pieter van Wyk) and SEM available, to continuously facilitate contact to PMC (operating company at Palabora) and for several discussions. Furthermore we want to thank PMC (in particular Hans-Dieter Paetzold, Paulien Lourens, and Thabitha Moyana) for providing core material and the help during our different sampling campaigns.

In a special way, we remember Pavel I. Karchevsky (1976–2002) whose study about the rare earth mineralization of the PCC was a significant cornerstone for our work.

REFERENCES CITED

Aldous, R.T.H. (1980) Ore genesis in copper bearing carbonatites: a geochemical, fluid inclusion and mineralogical study, 365 p. Ph.D. thesis, Imperial College London (University of London), London.

Armbrustmacher, T.J. (1979) Replacement and primary magmatic carbonatites from the Wet Mountains area, Fremont and Custer counties, Colorado. Economic Geology, 74, 888–901.

Armstrong, J.T. (1988) Bence-Albee after 20 years: review of the accuracy of a-factor correction procedures for oxide and silicate minerals. Microbeam Analysis, Applications in Geology, 469–476.

Bayliss, P., and Levinson, A.A. (1988) A system of nomenclature for rare-earth mineral species: revision and extension. American Mineralogist, 73, 93–99.

Beitter, T., Wagner, T., and Markl, G. (2008) Formation of kyanite–quartz veins of the Alpe Sponda, Central Alps, Switzerland: implications for Al transport during regional metamorphism. Contributions to Mineralogy and Petrology, 156, 689–707.

Bence, A.E., and Albee, A.L. (1968) Empirical correction factors for the electron microanalysis of silicates and oxides. The Journal of Geology, 76, 382–403.

Briden, J.C. (1976) Application of palaeomagnetism to Proterozoic tectonics. Philosophical Transactions of the Royal Society of London A: Mathematical, Physical and Engineering Sciences, 280, 405–416.

Budzyń, B., Hetherington, C.J., Williams, M.L., Jercinovic, M.J., and Michalik, M. (2010) Fluid-mineral interactions and constraints on monazite alteration during metamorphism. Mineralogical Magazine, 74, 659–681.

Budzyń, B., Harlov, D.E., Williams, M.L., and Jercinovic, M.J. (2011) Experimental determination of stability relations between monazite, fluorapatite, allanite, and REE-epidote as a function of pressure, temperature, and fluid composition. American Mineralogist, 96, 1547–1567.

Bühn, B, and Rankin, A.H. (1999) Composition of natural, volatile-rich Na–Ca–REE−Sr carbonatitic fluids trapped in fluid inclusions. Geochimica et Cosmochimica Acta, 63, 3781–3797.

Bulakh, A.G., Rudashevsky, N.S., and Karchevsky, P.I. (1998) Native gold and silver, sulfides and REE minerals in carbonatites from Loolekop Deposit, South Africa. Zapiski Vserossijskogo Mineralogiceskogo Obscestva, 127, 45–54 (in Russian).

Castor, S.B. (2008) The Mountain Pass rare-earth carbonatite and associated ultrapotassic rocks, California. Canadian Mineralogist, 46, 779–806.

Cetiner, Z.S., Wood, S.A., and Gammons, C.H. (2005) The aqueous geochemistry of the rare earth elements. Part XIV. The solubility of rare earth element phosphates from 23 to 150 °C. Chemical Geology, 217, 147–169.

Chakhmouradian, A.R., and Wall, F. (2012) Rare earth elements: minerals, mines, magnets (and more). Elements, 8, 333–340.

Chakhmouradian, A.R., and Zaitsev, A.N. (2004) Afrikanda: An association of ultramafic, alkaline and alkali-silica-rich carbonatitic rocks from mantle-derived melts. Phoscorites and carbonatites from mantle to mine: the key example of the Kola Alkaline Province, Mineralogical Society (U.K.) Series, 10, 247–291.

——— (2012) Rare earth mineralization in igneous rocks: sources and processes. Elements, 8, 347–353.

Chakhmouradian, A.R., Cooper, M.A., Medici, L., Abdu, Y.A., and Shelukhina, Y.S. (2015) Anzaite-(Ce), a new rare-earth mineral and structure type from the Afrikanda silicocarbonatite, Kola Peninsula, Russia. Mineralogical Magazine, 79, 1231–1244.

Dawson, J.B., and Hinton, R.W. (2003) Trace-element content and partitioning in calcite, dolomite and apatite in carbonatite, Phalaborwa, South Africa. Mineralogical Magazine, 67, 921–930.

Doroshkevich, A.G., Ripp, G.S., Viladkar, S.G., and Vladykin, N.V. (2008) The Arshan REE carbonatites, southwestern Transbaikalia, Russia: mineralogy, paragenesis and evolution. Canadian Mineralogist, 46, 807–823.

Drake, M.J., and Weill, D.F. (1972) New rare earth element standards for electron microprobe analysis. Chemical Geology, 10, 179–181.

Eriksson, S.C. (1989) Phalaborwa: a saga of magmatism, metasomatism and miscibility. In K. Bell, Eds., Carbonatites: Genesis and Evolution, p. 221–254. Unwin Hyman, London.

European Commission (2014) Report on critical raw materials for the EU—report of the Ad hoc Working Group on defining critical raw materials.

Fernandez, A.L.I., Doval, M., and Lopez-Aguayo, F. (1977) Thermal behavior of valleriite. American Mineralogist, 62, 1030–1031.

Fleet, M.E. (2006) Phase equilibria at high temperatures. In D.J. Vaughan, Eds., Sulphide Mineralogy and Geochemistry, p. 365–419. Reviews in Mineralogy and Geochemistry, Mineralogical Society of America, Chantilly, Virginia.

Fourie, P.J., and De Jager, D.H. (1986) Phosphate in the Phalaborwa complex. Mineral Deposits of Southern Africa, 2, 2239–2253.

Hanekom, H.J., Van Staden, C.M.V.H., Smit, P.J., and Pike, D.R. (1965) The Geology of the Palabora Igneous Complex, 185 p. South African Geological Survey, Pretoria.

Harlov, D.E., and Förster, H.-J. (2002) High-grade fluid metasomatism on both a local and a regional scale: the Seward peninsula, Alaska, and the Val Strona di Omegna, Ivrea–Verbano Zone, Northern Italy. Part I: petrography and silicate mineral chemistry. Journal of Petrology, 43, 769–799.

——— (2003) Fluid-induced nucleation of (Y+ REE)-phosphate minerals within apatite: Nature and experiment. Part II. Fluorapatite. American Mineralogist, 88, 1209–1229.

Harlov, D.E., Förster, H.-J., and Nijland, T.G. (2002) Fluid-induced nucleation of (Y+REE)-phosphate minerals within apatite: Nature and experiment. Part I. Chlorapatite. American Mineralogist, 87, 245–261.

Harlov, D.E., Wirth, R., and Förster, H.-J. (2005) An experimental study of dissolution–reprecipitation in fluorapatite: fluid infiltration and the formation of monazite. Contributions to Mineralogy and Petrology, 150, 268–286.

Harlov, D.E., Wirth, R., and Hetherington, C.J. (2011) Fluid-mediated partial alteration in monazite: the role of coupled dissolution–reprecipitation in element redistribution and mass transfer. Contributions to Mineralogy and Petrology, 162, 329–348.

Hatch, G.P. (2012) Dynamics in the global market for rare earths. Elements, 8, 341–346.

Heaman, L.M. (2009) The application of U–Pb geochronology to mafic, ultramafic and alkaline rocks: an evaluation of three mineral standards. Chemical Geology, 261, 43–52.

Hsu, L.C. (1992) Synthesis and stability of bastnaesites in a part of the system (Ce, La)-F-H-C-O. Mineralogy and Petrology, 47, 87–101.

Humphries, M. (2012). Report R41347. Congressional Research Service.

Kanazawa, Y., and Kamitani, M. (2006) Rare earth minerals and resources in the world. Journal of Alloys and Compounds, 408, 1339–1343.

Kapustin, Y.L. (1980) Mineralogy of Carbonatites, 259 p. Amerind Publishing Company, New Delhi.

Karchevsky, P.I. (2000) Minerals of Sr and REE in carbonatites from Loolekop deposit (Palabora, RSA). Zapiski Vserossijskogo Mineralogiceskogo Obscestva, 129, 99–109 (in Russian).

Kavecsanszki, D., Moore, K.R., Rollinson, G.K., Wall, F., and Lusty, P.A.J. (2012) Magma mingling between sulphide-rich and carbonatite magmas to form a multi-commodity metal deposit: reconstruction using QUEMSCAN analysis. In E. Jonsson, Eds., Proceedings of the Conference Proceedings. 12th SGA Biennial Meeting: Mineral deposit research for a high tech world, p. 1024–1027. Uppsala, Sweden.

Lieftink, D.J., Nuland, T.G., and Maijer, C. (1994) The behavior of rare earth elements in high-temperature Cl-bearing aqueous fluids: Results from the Odegardens Verk Natural Laboratory. Canadian Mineralogist, 32, 149–158.

Lombaard, A F., Ward-Able, N.M., and Bruce, R.W. (1964) The exploration and main geological features of the copper deposit in carbonatite at Loolekop, Palabora complex. In The Geology of Some Ore Deposits in Southern Africa, p. 315–337. Geological Society of South Africa, Johannesburg.

Louvel, M., Bordage, A., Testemale, D., Zhou, L., and Mavrogenes, J. (2015) Hydrothermal controls on the genesis of REE deposits: Insights from an in situ XAS study of Yb solubility and speciation in high temperature fluids (T < 400° C). Chemical Geology, 417, 228–237.

Manning, C.E. (2004) Polymeric silicate complexing in aqueous fluids at high pressure and temperature, and its implications for water-rock interaction. In R.B. Wanty and R.R. Seal II, Eds., Water-Rock Interactions, p. 45–49. Balkema, New York.

Mariano, A.N. (1989) Nature of economic mineralization in carbonatites and related rocks. In K. Bell, Eds., Carbonatites: Genesis and evolution, p. 149–176. Unwin Hyman, London.

Mitchell, R.H., and Chakhmouradian, A.R. (1998) Th-rich loparite from the Khibina alkaline complex, Kola Peninsula: isomorphism and paragenesis. Mineralogical Magazine, 62, 341–353.

Moore, M., Chakhmouradian, A.R., Mariano, A.N., and Sidhu, R. (2015) Evolution of rare-earth mineralization in the Bear Lodge carbonatite, Wyoming: Mineralogical and isotopic evidence. Ore Geology Reviews, 64, 499–521.

Nadeau, O., Cayer, A., Pelletier, M., Stevenson, R., and Jébrak, M. (2015) The Paleoproterozoic Montviel carbonatite-hosted REE–Nb deposit, Abitibi, Canada: Geology, mineralogy, geochemistry and genesis. Ore Geology Reviews, 67, 314–335.

Nassar, N.T., Du, X., and Graedel, T. (2015) Criticality of the rare earth elements. Journal of Industrial Ecology, 19, 1044–1054.

Pan, Y., Fleet, M.E., and Macrae, N.D. (1993a) Oriented monazite inclusions in

apatite porphyroblasts from the Hemlo gold deposit, Ontario, Canada. Mineralogical Magazine, 57, 697–708.

——— (1993b) Late alteration in titanite ($CaTiSiO_5$): redistribution and remobilization of rare earth elements and implications for U/Pb and Th/Pb geochronology and nuclear waste disposal. Geochimica et Cosmochimica Acta, 57, 355–367.

Pavlenko, A.S., Orlova, L.P., Akhmanova, M.V., and Tobelko, K.I. (1965) A thorium fluorcarbonate–thorbastnäsite. Zapiski Vserossijskogo Mineralogiceskogo Obscestva, 94, 105–113 (in Russian).

Pecora, W.T., and Kerr, J.H. (1953) Burbankite and Calkinsite, 2 new Carbonate Minerals from Montana. American Mineralogist, 38, 1169–1183.

Poitrasson, F., Oelkers, E., Schott, J., and Montel, J.-M. (2004) Experimental determination of synthetic $NdPO_4$ monazite end-member solubility in water from 21 C to 300 C: Implications for rare earth element mobility in crustal fluids. Geochimica et Cosmochimica Acta, 68, 2207–2221.

Rankin, A. (2005) Carbonatite-associated rare metal deposits: composition and evolution of ore-forming fluids–the fluid inclusion evidence. In R. Linnen and I. Samson, Eds., Rare Metal Geochemistry and Ore Deposits, Geological Association of Canada, Short Course Notes, 299–314.

Read, D., Andreoli, M.a.G., Knoper, M., Williams, C.T., and Jarvis, N. (2002) The degradation of monazite: Implications for the mobility of rare-earth and actinide elements during low-temperature alteration. European Journal of Mineralogy, 14, 487–498.

Reischmann, T. (1995) Precise U/Pb age determination with baddeleyite (ZrO_2), a case study from the Phalaborwa igneous complex, South Africa. South African Journal of Geology, 98, 1–4.

Sharygin, V.V., Zhitova, L.M., and Nigmatulina, E.N. (2011) Fairchildite $K_2Ca(CO_3)_2$ in phoscorites from Phalaborwa, South Africa: the first occurrence in alkaline carbonatite complexes. Russian Geology and Geophysics, 52, 208–219.

Shunhua, H., Zonggang, W., Zhongnei, Z., and Songyu, H. (1986) An experimental study of the conditions of the formation of bastnaesite. Acta Mineralogica Sinica, 6, 155–170.

Smith, M.P., Henderson, P., and Peishan, Z. (1999) Reaction relationships in the Bayan Obo Fe-REE-Nb deposit Inner Mongolia, China: implications for the relative stability of rare-earth element phosphates and fluorocarbonates. Contributions to Mineralogy and Petrology, 134, 294–310.

Smith, M.P., Henderson, P., and Campbell, L.S. (2000) Fractionation of the REE during hydrothermal processes: constraints from the Bayan Obo Fe-REE-Nb deposit, Inner Mongolia, China. Geochimica et Cosmochimica Acta, 64, 3141–3160.

Solovova, I.P., Ryabchikov, I.D., Kogarko, L.N., and Konokova, N.N. (1998) Inclusions in minerals of the Phalaborwa carbonatite complex. South Africa. Geochimija, 5, 435–447 (in Russian).

Somina, M.Y. (1975) Dolomite and Ankerite Carbonatites from the East Siberia, 191 p. Nedra, Moscow.

Song, W., Xu, C., Veksler, I.V., and Kynicky, J. (2016) Experimental study of REE, Ba, Sr, Mo and W partitioning between carbonatitic melt and aqueous fluid with implications for rare metal mineralization. Contributions to Mineralogy and Petrology, 171, 1–12.

Stettler, E.H., De Beer, J.H., and Blom, M.P. (1989) Crustal domains in the northern Kaapvaal Craton as defined by magnetic lineaments. Precambrian Research, 45, 263–276.

Tomašić, N., Gajović, A., Bermanec, V., Su, D.S., Linarić, M.R., Ntaflos, T., and Schlögl, R. (2006) Recrystallization mechanisms of fergusonite from metamict mineral precursors. Physics and Chemistry of Minerals, 33, 145–159.

Torró, L., Villanova, C., Castillo, M., Campeny, M., Gonçalves, A.O., and Melgarejo, J.C. (2012) Niobium and rare earth minerals from the Virulundo carbonatite, Namibe, Angola. Mineralogical Magazine, 76, 393–409.

Trofanenko, J., Williams-Jones, A., Simandl, G., and Migdisov, A. (2016) The nature and origin of the REE mineralization in the Wicheeda carbonatite, British Columbia, Canada. Economic Geology, 111, 199–223.

Tropper, P., and Manning, C.E. (2005) Letter: Very low solubility of rutile in H_2O at high pressure and temperature, and its implications for Ti mobility in subduction zones. American Mineralogist, 90, 502–505.

Uher, P., Ondrejka, M., Bačík, P., Broska, I., and Konečný, P. (2015) Britholite, monazite, REE carbonates, and calcite: Products of hydrothermal alteration of allanite and apatite in A-type granite from Stupné, Western Carpathians, Slovakia. Lithos, 236, 212–225.

Uken, R., and Watkeys, M.K. (1997) An interpretation of mafic dyke swarms and their relationship with major mafic magmatic events on the Kaapvaal Craton and Limpopo Belt. South African Journal of Geology, 100, 341–348.

van Baalen, M.R. (1993) Titanium mobility in metamorphic systems: a review. Chemical Geology, 110, 233–249.

Verplanck, P.L., Mariano, A.N., and Mariano, A. Jr. (2016) Rare earth element ore geology of carbonatites. In P.L. Verplanck and M.W. Hitzman, Eds., Rare Earth and Critical Elements in Ore Deposits, p. 5–32. Reviews in Economic Geology, Society of Economic Geologists, Littleton, Colorado.

Verwoerd, W.J. (1966) South African carbonatites and their probable mode of origin. Annals of the University of Stellenbosch, 41(A2), 233 p. Stellenbosch University, Stellenbosch.

Verwoerd, W.J., and Du Toit, M.C. (2006) The Phalaborwa and Schiel complexes. In M.R. Johnson, C R. Anhaeusser and R.J. Thomas, Eds., The Geology of South Africa, 291–299. Council for Geoscience, Pretoria.

Wall, F. (2014) Rare earth elements. In G. Gunn, Eds., Critical Metals Handbook, p. 312–339. British Geological Survey, Nottingham, U.K.

Wall, F., and Mariano, A.N. (1996) Rare earth minerals in carbonatites: a discussion centred on the Kangankunde Carbonatite, Malawi. In A.P. Jones, F. Wall, and C.T. Williams, Eds., Rare Earth Minerals: Chemestry, Origin and Ore Deposits. Mineralogical Society Series, p. 193–226. Chapman and Hall, London.

Wall, F., and Zaitsev, A.N. (2004a) Phoscorites and carbonatites from mantle to mine: the key example of the Kola Alkaline Province, 503 p. The Mineralogical Society of Great Britain and Ireland, London.

——— (2004b) Rare earth minerals in Kola carbonatites. In F. Wall and A.N. Zaitsev, Eds., Phoscorites and Carbonatites from Mantle to Mine: The key example of the Kola Alkaline Province., p. 341–373. Mineralogical Society Series, Mineralogical Society, London, U.K.

Wall, F., Le Bas, M.J., and Srivastava, R.K. (1993) Calcite and carbocernaite exsolution and cotectic textures in a Sr, REE-rich carbonatite dyke from Rajasthan, India. Mineralogical Magazine, 57, 495–513.

Wall, F., Zaitsev, A.N., Jones, A.P., and Mariano, A.N. (1997) Rare-earth rich carbonatites: a review and latest results. Journal of the Czech Geological Society, 42, 49.

Wall, F., Zaitsev, A.N., and Mariano, A.N. (2001) Rare earth pegmatites in carbonatites. Journal of African Earth Sciences, 32, A35–A36.

Wang, L., Yu, Y., Huang, X., Long, Z., and Cui, D. (2013) Toward greener comprehensive utilization of bastnaesite: Simultaneous recovery of cerium, fluorine, and thorium from bastnaesite leach liquor using HEH (EHP). Chemical Engineering Journal, 215, 162–167.

Williams-Jones, A.E., and Wood, S.A. (1992) A preliminary petrogenetic grid for REE fluorocarbonates and associated minerals. Geochimica et Cosmochimica Acta, 56, 725–738.

Williams-Jones, A.E., Migdisov, A.A., and Samson, I.M. (2012) Hydrothermal mobilisation of the rare earth elements–a tale of "ceria" and "yttria". Elements, 8, 355–360.

Wilson, M.G.C. (1998) Copper. In M.G.C. Wilson and C.R. Anhaeusser, Eds., The mineral resources of South Africa, p. 209–217. Council for Geoscience, Pretoria.

Wingate, M.T.D., and Compston, W. (2000) Crystal orientation effects during ion microprobe U–Pb analysis of baddeleyite. Chemical Geology, 168, 75–97.

Wu, F.-Y., Yang, Y.-H., Li, Q.-L., Mitchell, R.H., Dawson, J.B., Brandl, G., and Yuhara, M. (2011) In situ determination of U–Pb ages and Sr–Nd–Hf isotopic constraints on the petrogenesis of the Phalaborwa carbonatite Complex, South Africa. Lithos, 127, 309–322.

Wyllie, P.J., Jones, A.P., and Deng, J. (1996) Rare earth elements in carbonate-rich melts from mantle to crust. In A.P. Jones, F. Wall, and C.T. Williams, Eds., Rare Earth Minerals: Chemestry, Origin and Ore Deposits. Mineralogical Society Series, p. 77–103. Chapman and Hall, London.

Yaroshevskii, A.A., and Bagdasarov, Y.A. (2008) Geochemical diversity of minerals of the pyrochlore group. Geochemistry International, 46, 1245–1266.

Yuhara, M., Kohno, M., Kagami, H., Hiroi, Y., and Tsuchiya, N. (2003) Geochemistry of syenite of the Phalaborwa carbonatite complex, South Africa. Polar Geoscience, 16, 176–195.

Zaitsev, A.N., Wall, F., and Le Bas, M.J. (1998) REE-Sr-Ba minerals from the Khibina carbonatites, Kola Peninsula, Russia: their mineralogy, paragenesis and evolution. Mineralogical Magazine, 62, 225–250.

Zaitsev, A.N., Demény, A., Sindern, S., and Wall, F. (2002) Burbankite group minerals and their alteration in rare earth carbonatites—source of elements and fluids (evidence from C–O and Sr–Nd isotopic data). Lithos, 62, 15–33.

Zaitsev, A.N., Williams, C.T., Jeffries, T.E., Strekopytov, S., Moutte, J., Ivashchenkova, O.V., Spratt, J., Petrov, S.V., Wall, F., Seltmann, R., and Borozdin, A.P. (2015) Reprint of "Rare earth elements in phoscorites and carbonatites of the Devonian Kola Alkaline Province, Russia: examples from Kovdor, Khibina, Vuoriyarvi and Turiy Mys complexes." Ore Geology Reviews, 64, 477–498.

Zirner, A.L.K., Marks, M.A.W., Wenzel, T., Jacob, D.E., and Markl, G. (2015) Rare Earth Elements in apatite as a monitor of magmatic and metasomatic processes: the Ilímaussaq complex, South Greenland. Lithos, 228, 12–22.

Manuscript received November 3, 2016
Manuscript accepted December 28, 2016
Manuscript handled by Daniel Harlov

Appendix II

Accepted publication

Study B

Giebel, R.J., Marks, M.A.W., Gauert, C.D.K. and Markl, G. (2019a): A model for the formation of carbonatite-phoscorite assemblages based on the compositional variation of mica and apatite from the Palabora Carbonatite Complex, South Africa. *Lithos*. Vol. **324-325**. P 89-104.

Lithos 324–325 (2019) 89–104

Contents lists available at ScienceDirect

Lithos

journal homepage: www.elsevier.com/locate/lithos

A model for the formation of carbonatite-phoscorite assemblages based on the compositional variations of mica and apatite from the Palabora Carbonatite Complex, South Africa

R. Johannes Giebel [a,b,*], Michael A.W. Marks [a], Christoph D.K. Gauert [b,c], Gregor Markl [a]

[a] Department of Geoscience, Eberhard Karls University, Wilhelmstr. 56, 72076 Tübingen, Germany
[b] Department of Geology, University of the Free State, 250 Nelson-Mandela-Drive, Bloemfontein 9300, South Africa
[c] Department of Applied Geology and Geohazards, Geological Survey of Saxony-Anhalt, Köthener Str. 38, 06118 Halle (Saale), Germany

ARTICLE INFO

Article history:
Received 4 April 2018
Accepted 27 October 2018
Available online 01 November 2018

Keywords:
Phlogopite and tetraferriphlogopite
Palabora Carbonatite Complex
Liquid immiscibility
Phoscorite
Formation model

ABSTRACT

A detailed electron microprobe study has been carried out on the compositional variations of mica and apatite from carbonatites, phoscorites and associated pyroxenites (and fenites) of the Loolekop deposit, Palabora Carbonatite Complex (South Africa). Mica in pyroxenites and fenites is Mg-rich biotite, whilst micas in carbonatites and phoscorites are compositionally diverse including phlogopite, Ba-rich phlogopite (up to 30% kinoshitalite component), ^{IV}Al-rich phlogopite (up to 30% eastonite component) and tetraferriphlogopite. The various types of phlogopites are interpreted as orthomagmatic phases, whereas tetraferriphlogopite precipitation was a late-magmatic to hydrothermal process that additionally introduced REE into the system. Orthomagmatic apatite is generally REE- and Sr-poor fluorapatite and does not show large compositional differences between rock types. Apatite associated with the late-stage tetraferriphlogopite mineralization reaches higher levels of REE (up to 4.9 wt%), Si (up to 1.5 wt% SiO_2), Sr (up to 2.6 wt% SrO) and Na (up to 1.0 wt% Na_2O).
The compositional variation of micas and apatites, which is affiliated with distinct rock types, reflects the multi-stage evolution of the Loolekop deposit and provides detailed insight into the relationships of the carbonatite-phoscorite assemblage. The obtained data support the separation of phoscorite and carbonatite by immiscibility from a common parental magma, which may happen due to a decrease of temperature and/or pressure during the ascent of the magma. This results in a density contrast between the carbonatitic and phoscoritic components that will lead to descending phoscorite accumulations at the outer zones of the magma channel and a jet-like ascent (further promoted by its extremely low viscosity) of the carbonatite magma. The genetic model deduced here explains the peculiar association of carbonatites, phoscorites and silicate rocks in many alkaline complexes worldwide.

1. Introduction

Apatite and mica are two of the most abundant non-carbonate minerals in carbonatites. They cover a large compositional range and are therefore ideal monitors for the magmatic and hydrothermal evolution of such systems (e.g., Brigatti et al., 1996b; Chakhmouradian et al., 2017). Apatites from carbonatites and phoscorites are known to reach elevated contents of rare-earth elements (REE), large ion lithophile elements (e.g., Sr) and higher concentrations of Na and Si compared to most other plutonic rocks, while the halogen-site is mainly occupied by F and OH, with normally negligible Cl (Teiber et al., 2015 and references therein). Micas from carbonatite/phoscorite – silicate rock associations world-wide generally comprise four main groups, namely the phlogopite-annite, phlogopite-eastonite, phlogopite-kinoshitalite, and the phlogopite-tetraferriphlogopite series (e.g., Reguir et al., 2009 and references therein; see Table 1 for end-member compositions). Commonly, micas with an annite component >20% (biotites) are restricted to the associated silicate rocks, whereas those from carbonatites and phoscorites are very Mg-rich (phlogopite) and may show some evolution towards eastonite (e.g. Sokli; Lee et al., 2003) and/or kinoshitalite (e.g. Jacupiranga; Brod et al., 2001).

Micas evolving towards tetraferriphlogopite composition were first described from Kovdor (Rimskaya-Korsakova and Sokolova, 1964), but in the meantime have been described from many alkaline rock-carbonatite complexes (e.g., Brigatti et al., 1996a; Brigatti et al., 1996b;

Abbreviations: BCB, Banded Carbonatite; TCB, Transgressive Carbonatite; FEN, Fenite; FOS, Phoscorite; FPY, Feldspathic Pyroxenite; MPY, Micaceous Pyroxenite; CPIO melts, Carbonate-phosphate/iron-oxide-rich melts; C/SR, carbonatite/silicate rock ratio; ΔS-E, source-emplacement distance.

* Corresponding author.
E-mail address: r.j.giebel@gmx.de (R.J. Giebel).

https://doi.org/10.1016/j.lithos.2018.10.030
0024-4937/

Table 1
Ideal end-member compositions and substitutiton trends of Palabora micas.

Endmember name	Ideal end-member comp.	Substitution trend	Abbr.	Max. end-member composition at Palabora*
Phlogopite	$KMg_3AlSi_3O_{10}(OH)_2$	–	"Common" phl	$K(Mg_{2.7}Fe_{0.3})(AlSi_3)O_{10}(OH_{1.7}F_{0.3})$
Annite	$KFe^{2+}_3AlSi_3O_{10}(OH)_2$	$3Mg^{2+} \leftrightarrow 3Fe^{2+}$	*Biotite*	$K(Mg_{1.8}Fe_{1.2})(AlSi_3)O_{10}(OH_{1.9}F_{0.1})$
Eastonite	$KMg_2AlAl_2Si_2O_{10}(OH)_2$	$Mg^{2+} + Si^{4+} \leftrightarrow {}^{VI}Al^{3+} + {}^{IV}Al^{3+}$	^{IV}Al-rich phl	$K(Mg_{2.6}Fe_{0.1}Al_{0.3})(Al_{1.3}Si_{2.7})O_{10}(OH_{1.8}F_{0.2})$
Siderophyllite	$KFe^{2+}_2AlAl_2Si_2O_{10}(OH)_2$	$3Mg^{2+} + Si^{4+} \leftrightarrow {}^{VI}Al^{3+} + {}^{IV}Al^{3+} + 2Fe^{2+}$		
Kinoshitalite	$BaMg_3Al_2Si_2O_{10}(OH)_2$	$K^+ + Si^{4+} \leftrightarrow Ba^{2+} + {}^{IV}Al^{3+}$	Ba-bearing phl	$K_{0.7}Ba_{0.3}(Mg_{2.8}Fe_{0.2})(Al_{1.3}Si_{2.7})O_{10}(OH_{1.3}F_{0.7})$
Ferrokinoshitalite	$BaFe^{2+}_3Al_2Si_2O_{10}(OH)_2$	$3Mg^{2+} + K^+ + Si^{4+} \leftrightarrow Ba^{2+} + {}^{IV}Al^{3+} + 3Fe^{2+}$		
Tetraferriphlogopite	$KMg_3Fe^{3+}Si_3O_{10}(OH)_2$	$^{IV}Al^{3+} \leftrightarrow {}^{IV}Fe^{3+}$	Tetraferri-phlogopite	$K(Mg_{2.5}Fe_{0.5})(Fe^{3+}_{0.77}\square_{0.03}Al_{0.1}Si_{3.1})O_{10}(OH_{1.9}F_{0.1})$
Tetraferriannite	$KFe^{2+}_3Fe^{3+}Si_3O_{10}(OH)_2$	$3Mg^{2+} + {}^{IV}Al^{3+} \leftrightarrow {}^{IV}Fe^{3+} + 3Fe^{2+}$		

Note: Mineral names are in accordance with the nomenclature of the International Mineralogical Association (IMA). *Solid solution formular based on max. deviation from ideal phlogopite (phl) composition. Mica type in italics displays biotite from associated silicate rocks (micaceous pyroxenite and fenite).

Brod et al., 2001; Gaspar and Wyllie, 1987; Lee et al., 2003; McCormick and Le Bas, 1996; Seifert et al., 2000), where they are commonly restricted to carbonatites and phoscorites (e.g., Kovdor and Sokli; Krasnova et al., 2004a; Lee et al., 2003) or silicate rocks that reflect a strong metasomatic overprint induced by carbonatites (e.g., Catalao-I; Brod et al., 2001). The crystallization of tetraferriphlogopite is generally considered to be caused by the low availability of Al combined with high fO_2 (Brigatti et al., 1996b; Lee et al., 2003; McCormick and Le Bas, 1996).

Some carbonatites are spatially and temporally associated and genetically related to phoscorites, which are defined as carbonate-bearing ultramafic rocks that mainly consist of magnetite, apatite and forsterite, diopside or phlogopite (Krasnova et al., 2004b). The 21 phoscorite occurrences described world-wide (with Palabora being the type locality) are almost exclusively represented by multiphase phoscorite-carbonatite complexes, with phoscorite situated around or in carbonatite cores. Numerous phoscoritic small scale structures are common in most calcite and dolomite carbonatites (Krasnova et al., 2004b), but many of such occurrences have been insufficiently described. Certainly, there are much more unrecognized phoscorite-carbonatite associations. The genetic relation between carbonatites and associated phoscorites has been the subject of discussions among petrologists for many years and three potential processes have been suggested for the generation of phoscorites: (1) crystallization from an individual magma, (2) fractionation from a carbonatitic magma or (3) separation from an immiscible carbonatitic melt (Krasnova et al., 2004b).

The present investigation provides systematic data on the compositional variation of micas and apatites from the three major rock types (banded carbonatite, transgressive carbonatite and phoscorite), of the Palabora Carbonatite Complex and assesses their petrogenetic and evolutionary significance. Based on these data, the relationship between the two carbonatite types and phoscorite are discussed and a model for explaining similar carbonatite-phoscorite-silicate rock associations is proposed.

2. Geological setting

The Palabora Carbonatite Complex depicts a tripartite, pipe-like intrusion comprising an area of about 18 km^2, which is dominated by various types of clinopyroxenite (Fig. 1). The complex is located next to the city of Phalaborwa in the Limpopo province (South Africa) and was intruded at 2060 Ma into Archean granite-gneiss basement of the north-eastern Kaapvaal craton (Wu et al., 2011). According to gravity data, the complex continues to a depth of at least 5 km (Eriksson, 1982) while 2 km are verified by drilling data (Giebel et al., 2017).

The complex is divided into a northern and southern pyroxenite and the central Loolekop pipe, which comprises a 1.3 × 0.8 km sized carbonatite-phoscorite assemblage, where phoscorite (FOS) is associated with Banded Carbonatite (BCB); both are cut by Transgressive Carbonatite (TCB). This so-called Loolekop deposit is the focus of the present study and represents the only carbonatite world-wide primarily mined for Cu. The Loolekop deposit experienced a multi-stage mineralization, which can be divided into an orthomagmatic, late-magmatic, sulphide and post-magmatic stage (Giebel et al., 2017). The majority of the complex is bordered by a feldspathic pyroxenite (FPY), which represents an interaction of the intruding pyroxenite (micaceous pyroxenite, MPY) with the basement. The surrounding basement was fenitized and late syenite satellite bodies formed in the direct vicinity of the complex. Dolerite dykes of mostly Proterozoic age (Wu et al., 2011) finally crosscut the entire complex. The primary magma forming the carbonatite complex has been identified as being derived from an enriched mantle source and was proposed to have been triggered by the same mantle plume activity which initiated the intrusion of the Bushveld Complex (Wu et al., 2011).

3. Previous work on Palabora apatites and phlogopites

Systematic mineral chemical studies to assess the multi-stage evolution of the carbonatite-phoscorite assemblage of the Palabora Carbonatite Complex have been lacking so far. Apatite is abundant in all rock types with quantities decreasing from FOS > BCB > TCB (Hanekom et al., 1965; Palabora Mining Company, 1976). Aldous (1980) identified apatite as the major REE carrier at Palabora, and later parenthetic studies (using only one sample each of BCB, FOS and MPY) focused on the REE distribution between apatite and carbonates (Dawson and Hinton, 2003), without presenting any genetic implications. Only Wu et al. (2011) and Milani et al. (2017) drew petrogenetic conclusions based on isotope and trace element analyses of apatite and carbonates, and suggested a cogenetic origin for most of their samples (4 FOS, 3 BCB, 2 TCB). Milani et al. (2017) finally pointed out the compositionally "ordinary" nature of Palabora apatite without significant differences between FOS, BCB and TCB.

Few phlogopite data for carbonatites and phoscorites have been presented by Eriksson (1982), who focussed his studies on pyroxenites and noticed that the majority of micas from Palabora range from Mg-rich phlogopites (carbonatites and phoscorites) to Mg-rich biotites (pyroxenites), while phlogopites often show a deficiency in Al (compared to ideal phlogopite) with low concentrations of Ti (compared to other ultrabasic rocks). Fenites (FEN) show very similar mica compositions as pyroxenites and although micas in carbonatites and phoscorites have lower Fe/(Fe + Mg) ratios compared to pyroxenites, they mostly overlap in composition, which lead Eriksson (1982) to conclude that the formation of the carbonatite-phoscorite assemblage was not caused by differentiation of the magma that produced pyroxenites. Although Suwa and Aoki (1975) described rims of tetraferriphlogopite surrounding phlogopites in pyroxenites, these features were not observed in the much more detailed study of Eriksson (1982). Other studies only described the presence of "common" phlogopite (e.g., Aldous, 1980; Hanekom et al., 1965; Lombaard et al., 1964; Palabora Mining Company, 1976). Milani et al. (2017) presented trace element data for micas from a very limited number of samples (3 FOS and 2 BCB, no TCB).

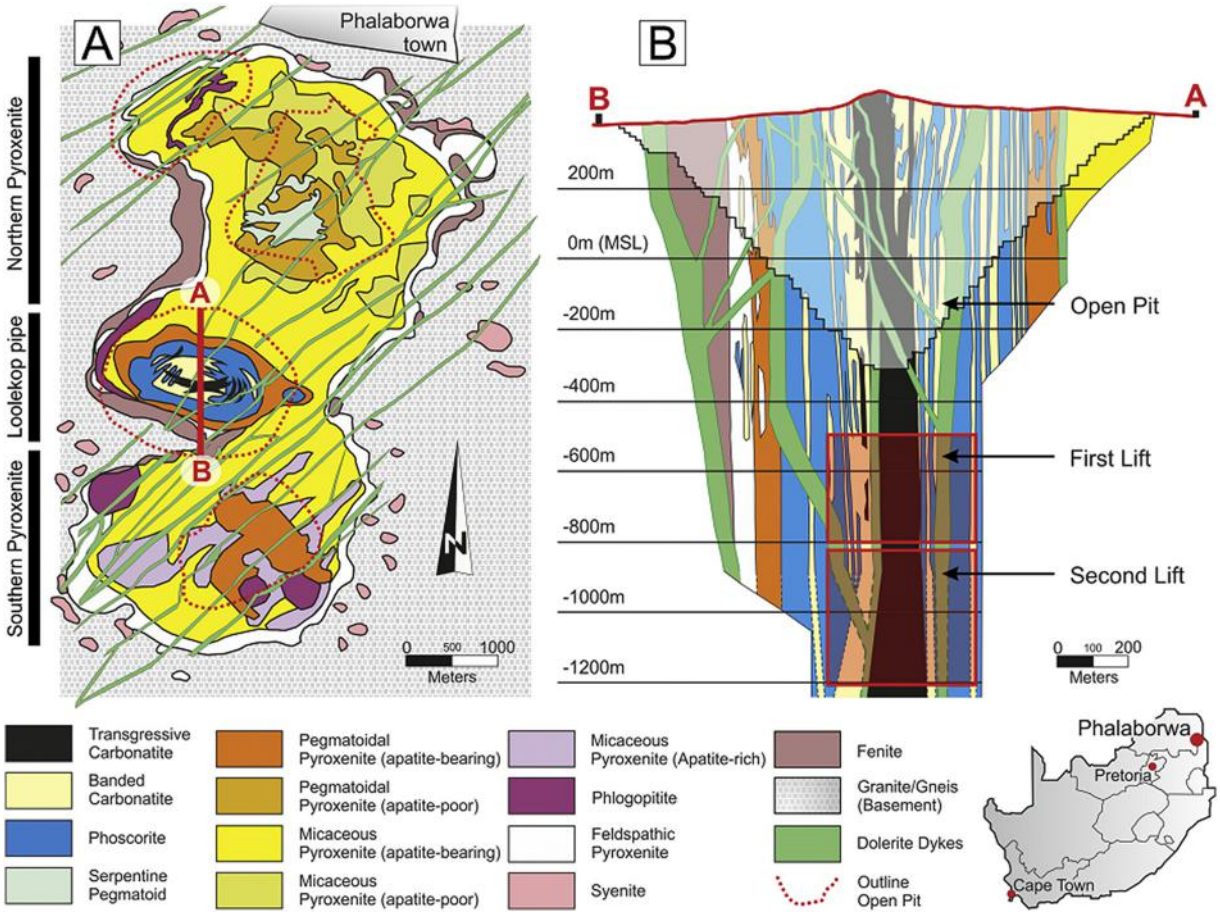

Fig. 1. Generalized geological map of the Palabora Complex (modified after Fourie and Jager, 1986; Hanekom et al., 1965; Wilson, 1998) and cross section of the Loolekop pipe in N-S direction showing the irregular ring structure of the pipe (modified and extended after Wilson, 1998).

4. Sample material, analytical methods, and recalculation procedures

This study is based on 45 representative samples (20 TCB, 15 BCB and 10 FOS) that have been chosen from a collection of about 400 drill core samples from 6 drill holes that combine to a vertical profile of about 2000 m. The composition of micas (452 analyses) and apatite (554 analyses) was acquired using a Jeol JXA 8900 Superprobe at the Department of Geoscience of the Eberhard Karls University, Tübingen (Germany) using four wavelength-dispersive spectrometers (WDS). For standardization, albite (Na), plagioclase (Si, Al and Ca), diopside (Mg), hematite (Fe), topaz (F), tugtupite (Cl), baryte (Ba), rhodonite (Mn), $SrTiO_3$ (Ti), and Cr metal (Cr) where used for micas; for apatites, we used albite (Na), sanidine (K), diopside (Si), apatite (Ca, P and F), hematite (Fe), tugtupite (Cl), baryte (S), rhodonite (Mn), $SrTiO_3$ (Sr), GaAs (As) and REE 1–4 glasses (La, Ce, Pr and Nd; Drake and Weill, 1972). The ZAF matrix correction method (Armstrong, 1988; Bence and Albee, 1968) was employed for quantification. The microprobe was operated at 15 kV accelerating voltage, 12 nA (mica) and 10 nA (apatite) beam current and a defocused beam of 2 μm (mica) and 10 μm (apatite) diameter was used. Overlap corrections for Ti-Ba (in mica) and for Fe-Ce and Pr-La (in apatite) where applied. Further details of the WDS configuration are given in the electronic supplement.

Structural formulae of micas were calculated based on an ideal trioctahedral mica formula ($XY_3[Z_4O_{10}][OH,F,Cl]_2$) and the data were normalized to seven (tetrahedral [Z] plus octahedral [Y]) cations. OH was calculated by assuming (F + Cl + OH) = 2. Earlier studies have shown that Fe^{2+}/Fe^{3+} calculations from EMPA data are reliable and not unrealistically different from Mössbauer data, if appropriate recalculation methods are used (e.g., Brod et al., 2001). We recalculated our EPMA data using the method by Dymek (1983) for Al-bearing phlogopites and the method by Araújo (1996) for Al-deficient tetraferriphlogopites (explained/translated by Brod et al., 2001). For the different substitution trends in mica the following cations are considered to occupy the related sites: (1) Tetrahedral site: Si^{4+}-Al^{3+}-Fe^{3+}, (2) octahedral site: Mg^{2+}-Mn^{2+}-Fe^{2+}-Fe^{3+}-Al^{3+}-Ti^{4+} and (3) interlayer site: K^{+}-Na^{+}-Ba^{2+}-Ca^{2+}.

Structural formulae of apatite were normalized to eight cations and OH was calculated assuming (F + Cl + OH) = 1. For the different substitution trends in apatite the following preferred site occupancies are assumed: (1) A site: Si^{4+}-P^{5+}-S^{6+}-As^{5+} and (2) B site: Na^{+}-Ca^{2+}-Sr^{2+}-REE^{3+}-Fe^{2+}-Mn^{2+}.

5. Textural appearance of mica and apatite

Micas in pyroxenites occur as small (<1 mm) to large (>5 cm) laths interstitial to clinopyroxenes (cpx) with rare inclusions of small cpx, or as small euhedral inclusions (poikilitically) in cpx. They record a magmatic origin. Micas in fenite occur as laths filling veinlets together with calcite.

Micas and apatite are the most abundant orthomagmatic non-carbonates in the carbonatite-phoscorite assemblage at Palabora, together with olivine and magnetite (Giebel et al., 2017). Phlogopites are mainly enclosed by carbonate phases (Fig. 2A) or included in magnetite (Fig. 2C). They often contain inclusions of apatite and vary from up to cm-sized euhedral grains (Fig. 2A) to much smaller anhedral crystals (Fig. 2B). These textural features apply to FOS, BCB and TCB samples, but TCB phlogopites tend to form large euhedral crystals. Phlogopites

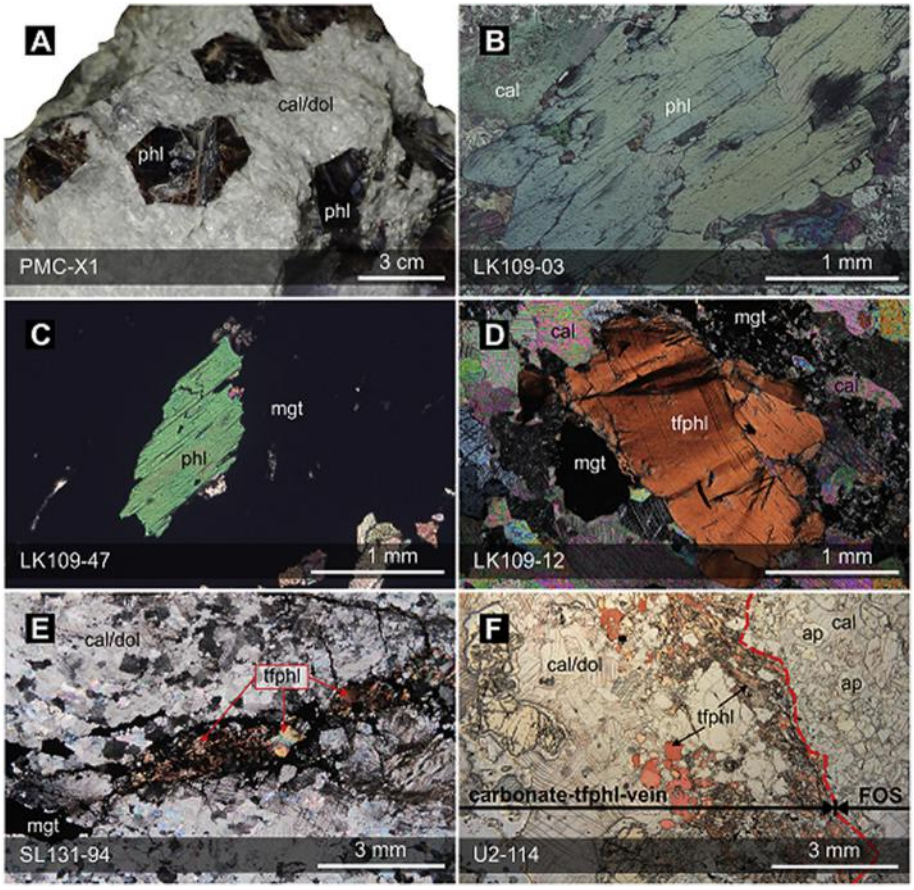

Fig. 2. Mica textures from carbonatites and phoscorites of the Loolekop deposit, Palabora Carbonatite Complex (South Africa). (A) Euhedral phlogopite enclosed by calcite/dolomite (in TCB), (Photo from Mine Mineral Collection PMC). (B) Anhedral phlogopite enclosed by calcite (crossed nicols). (C) Phlogopite enclosed by magnetite (crossed nicols). (D) Foxy-orange tetraferriphlogopite (crossed nicols). (E) Vein-like occurrence of tetraferriphlogopite in TCB with later magnetite mineralization (crossed nicols). (F) Tetraferriphlogopite occurring at the outer rim of a carbonate-dominated vein trough phoscorite. Red dashed line marks the contact between vein and host rock (FOS). Mineral abbreviations: ap – apatite, cal – calcite, dol – dolomite, mgt – magnetite, phl – phlogopite, tfphl – tetraferriphlogopite. (For interpretation of the references to colour in this figure legend, the reader is referred to the web version of this article.)

are generally optically unzoned and undeformed, occasionally altered to chlorite or vermiculite. They typically show pale to bright blueish-greenish (Fig. 2C) to pinkish-violet interference colours and have a nearly colourless to light brownish appearance in bright field.

Tetraferriphlogopites, however, show light red-orange to brown interference colours (Fig. 2D). They appear intense brownish in bright field and show a reverse pleochroism. The reverse pleochroism in tetraferriphlogopite is caused by a related tetrahedral Fe^{3+}-Al substitution and requires an occupancy of $^{IV}Fe^{3+}$ of >0.25 apfu with ^{IV}Al <0.75 apfu at about 3 apfu ^{IV}Si (e.g., Brod et al., 2001). This proposition can be confirmed by our observations and supports the reversed pleochroism in phlogopite with $^{IV}Al/^{IV}Fe^{3+} \leq 3$. Tetraferriphlogopite in both carbonatite types (BCB and TCB) is mostly associated with veins of magnetite (±Fe-Cu-sulphides; Fig. 2E), which show an orientation parallel to that of the tetraferriphlogopites. Occasionally magnetites also form small clusters around tetraferriphlogopite. In some samples, late-stage magnetite forms a distinctive meshwork of veins. In these veins magnetite (±Fe-Cu-sulphides) partly dissolves the pre-existent tetraferriphlogopite assemblage (Fig. 2E & 3B). Tetraferriphlogopite-bearing assemblages in FOS occur as larger, isolated veins (Fig. 2F). Orthomagmatic magnetite in tetraferriphlogopite-rich samples (Fig. 3A) shows directional dissolution fronts, which are highlighted by the residue of exsolved ilmenite lamellae (Fig. 3C). Occasionally, tetraferriphlogopite is associated with aggregates of (rarely euhedral) britholite (Fig. 3D) and apatite-monazite dissolution structures (Fig. 3E; e.g., Giebel et al., 2017) that are both aligned parallel to the vein-like orientation of tetraferriphlogopites (Fig. 3A). In cases, bead-like pellets of graphite occur as string-like (moniliform) appositions (Fig. 3F.1) or more frequently as single beads attached to tetraferriphlogopite. This graphite variety is occasionally associated with magnesite (Fig. 3F.2).

Apatites from carbonatites (BCB and TCB) range from small grains (<100 μm) with a prismatic but mostly rounded habit, to cm-scale elongated euhedral to subhedral crystals, occasionally strongly fractured and rarely with inclusions of thorianite and baddeleyite. Most apatites show variable dissolution features, characterized by reaction rims of monazite around apatite (Fig. 3E; see details in Giebel et al., 2017). Apatites are optically unzoned, but cathodoluminescence images show a sporadic faint zoning often based on fractures and crystal irregularities, which indicate a weak interaction with a pervasive fluid. Apatites in FOS form up to some cm sized irregular masses that are mostly interstitial to olivine, with minor inclusions of small apatite in olivine and magnetite. This apatite variety shows only minor association with monazite.

6. Compositional variation of micas and apatite

Both phlogopite and apatite show no compositional depth-dependent changes for the entire sample profile covering >2000 m. This confirms the absence of a vertical zonation, as has been demonstrated for a profile down to −1550 m for Kovdor (Russia) by Krasnova et al. (2004a).

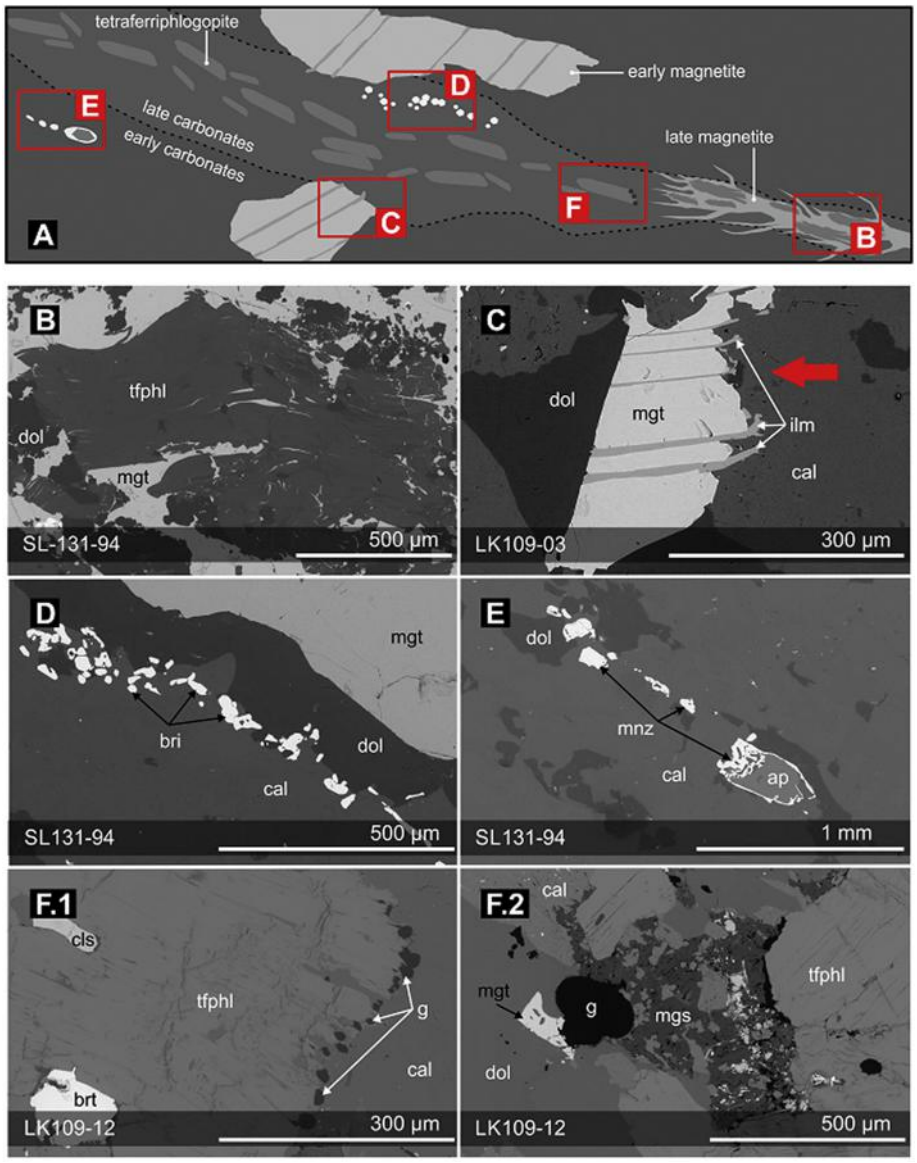

Fig. 3. Schematic illustration and Back Scatter Electron (BSE) images of characteristic textures associated with late-stage tetraferriphlogopite-bearing veins in carbonatites and phoscorites of Palabora. (A) Sketch comprising the local orientation of characteristic textures B to F. (B) Late magnetite dissolving pre-existent tetraferriphlogopite. (C) Primary magmatic magnetite with dissolution front (red arrow) and residual ilmenite lamellae adjacent to immaculate magnetite-ilmenite exsolutions. (D) Aggregate of britholite crystals orientated parallel to vein-like tetraferriphlogopite assemblages. (E) Orientated dissolution structure of apatite-monazite reaction-assemblage. (F.1) Tetraferriphlogopite associated with bead-like graphite pellets, and (F.2) graphite associated with magnesite. For mineral abbreviations see Fig. 2 and bri – fluorbritholite-(Ce), brt – baryte, cls – celestine, g – graphite, mgs – magnesite, mnz - monazite. (For interpretation of the references to colour in this figure legend, the reader is referred to the web version of this article.)

6.1. Mica

Selected electron microprobe analyses of representative micas from the Loolekop deposit (TCB, BCB, FOS, MPY, FEN) are listed in Table 2 (phlogopites) and Table 3 (tetraferriphlogopite and biotite). Core-rim variations in micas are only very minor, usually not exceeding the inter-sample composition range.

The Mg# (100xMg/(Mg + Fe)) of mica from pyroxenites (60–62) and fenites (70–72) is much lower than in carbonatites and phoscorites (81–98) and in the latter rocks, phlogopites (#Mg = 86–98) are distinguished from tetraferriphlogopites (#Mg = 81–93) based on a significant Al-deficiency of the latter (Foster, 1960; Fig. 4). The chemical evolution of phlogopites shows an increase of Al with Mg# (Fig. 4) and a negative correlation between Fe_{Total} and Mg (Fig. 5). Tetraferriphlogopites, however, show a virtually constant Mg content with increasing Fe_{Total}, which mirrors the substitution of $^{IV}Fe^{3+}$ for ^{IV}Al and indicates that the $^{VI}Fe^{2+}$-Mg substitution during their formation is less important. Only when Fe_{Total} reaches a concentration of 1 apfu, $^{VI}Fe^{2+}$ starts to substitute for Mg (Fig. 5C). Thus, in contrast to phlogopites (Fe < 0.4), which show a decrease of Fe^{2+} with differentiation (red arrow in Fig. 5C), tetraferriphlogopites (Fe > 1) show an increase of Fe^{2+} (Fig. 5C).

Enrichment of Ba is an exclusive feature of some phlogopites from TCB samples (Fig. 6A), coupled with an enrichment of ^{IV}Al and following the substitution mechanism $K^{+} + Si^{4+} \leftrightarrow Ba^{2+} + {}^{IV}Al^{3+}$ (expressed as $Al^{3+} + Si^{4+} = 4$ apfu in Fig. 6B) towards kinoshitalite-rich compositions (Table 1). Although some phlogopites from BCB and FOS show enrichment of Al, they follow a different trend (Fig. 4A), implying the substitution of $Mg^{2+} + Si^{4+} \leftrightarrow {}^{IV}Al^{3+} + {}^{VI}Al^{3+}$ (Fig. 6B). The contents of Ti and Na are low, with phlogopites in BCB and FOS reaching higher values than other phlogopites and tetraferriphlogopites (Fig. 7A & B).

Fluorine contents are variable (Fig. 8), with phlogopites in TCB reaching much higher values (up to 0.75 apfu) than in BCB and FOS (up to 0.55 apfu). The typical feature of F depletion in Fe-rich micas

Table 2
Representative major-element composition of phlogopite from FOS, BCB and TCB.

in wt%	"Common" phlogopite						^{IV}Al-rich phlogopite						Ba-bearing phlogopite		
	1	2	3	4	5	6	7	8	9	10	11	12	13	14	15
Na_2O	0.14	0.08	–	0.05	0.25	0.07	0.15	0.05	0.04	0.03	0.12	0.12	0.02	0.08	0.05
K_2O	10.6	10.98	11.05	10.82	10.22	10.32	10.38	10.85	10.62	11.13	11.25	10.6	10.81	10.4	8.31
CaO	0.01	–	0.06	0.04	0.02	0.03	0.04	0.02	0.05	0.01	0.02	0.01	–	0.06	–
BaO	0.06	0.06	0.15	0.38	0.36	0.31	0.53	1	0.97	0.88	0.17	0.38	0.98	2.55	7.13
MgO	25.93	26.61	27.93	25.46	26.96	27.13	25.44	27.18	26.69	25.77	27.82	26.5	27.45	27.49	26.41
MnO	0.02	–	0.01	0.01	–	–	0.03	–	0.04	0.03	0.02	0.03	–	–	0.01
FeO^S	4.25	3.42	1.54	4.73	3.29	2.25	1.55	2.38	2.71	1.5	1.34	3.79	2.17	2.3	1.4
$Fe_2O_3^S$	1.89	1.14	0.95	1.44	1.53	1.92	–	–	–	0.65	–	–	1.48	–	–
Al_2O_3	10.25	10.74	11.67	10.63	10.21	10.77	18.19	12.74	12.97	18.13	12.85	12.61	11.04	12.4	16.62
TiO_2	0.26	0.26	0.62	0.35	0.06	0.15	–	0.03	0.04	0.18	0.18	0.1	0.03	0.06	0.09
Cr_2O_3	–	–	–	–	–	–	–	–	–	–	–	–	–	–	–
SiO_2	42.92	43.57	43.03	42.97	43.58	42.28	39.25	42.49	41.88	39.48	43.31	42.37	42.98	42.32	37.17
Cl	0.02	0.07	–	0.03	0.04	0.03	0.02	0.01	0.02	–	–	0.02	0.01	0.06	0.04
F	1.92	1.12	1.45	1.26	0.95	0.68	0.12	2.5	1.4	0.87	1.68	1.14	3.05	1.52	1.31
$-O = (F,Cl)_2$	0.82	0.49	0.61	0.54	0.41	0.29	0.05	1.06	0.59	0.36	0.71	0.48	1.29	0.65	0.56
TOTAL	97.45	97.56	97.85	97.63	97.06	95.65	95.65	98.19	96.84	98.3	98.05	97.19	98.73	98.59	97.98
H_2O^*	3.3	3.73	3.63	3.61	3.79	3.88	4.2	3.1	3.58	3.93	3.54	3.73	2.83	3.55	3.52
in apfu	Structural formulae calculated for 7 cations (tetrahedral [Z] plus octahedral [Y] cations)														
Na	0.02	0.01	–	0.01	0.03	0.01	0.02	0.01	0.01	–	0.01	0.02	–	0.01	0.01
K	0.96	0.98	0.98	0.98	0.92	0.94	0.93	0.97	0.96	0.98	0.99	0.95	0.97	0.93	0.77
Ca	–	–	0.01	–	–	–	–	–	–	–	–	–	–	–	–
Ba	–	0.02	–	0.01	0.01	0.01	0.01	0.03	0.03	0.02	–	0.01	0.03	0.07	0.2
Mg	2.74	2.78	2.88	2.7	2.82	2.87	2.66	2.83	2.81	2.65	2.86	2.77	2.87	2.87	2.84
Mn	–	–	–	–	–	–	–	–	–	–	–	–	–	–	–
Fe^{2+}	0.25	0.21	0.09	0.29	0.19	0.13	0.09	0.14	0.16	0.09	0.08	0.21	0.13	0.13	0.08
Fe^{3+}	0.1	0.06	0.05	0.08	0.08	0.09	–	–	–	0.03	–	–	0.08	–	–
Al	0.86	0.89	0.96	0.89	0.85	0.89	1.49	1.06	1.08	1.48	1.05	1.04	0.91	1.02	1.41
Ti	0.01	0.01	0.03	0.02	–	0.01	–	–	–	0.01	0.01	0.01	–	–	–
Cr	–	–	–	–	–	–	–	–	–	–	–	–	–	–	–
Si	3.04	3.05	2.99	3.02	3.06	3.01	2.76	2.97	2.96	2.73	2.99	2.98	3.01	2.97	2.68
Cl	–	0.01	–	–	–	–	–	–	–	–	–	–	–	0.01	0.01
F	0.43	0.25	0.32	0.28	0.21	0.15	0.02	0.55	0.31	0.19	0.37	0.25	0.68	0.37	0.3

(1–3) „Common "phlogopite in FOS, (4–6) in BCB; (7–9) ^{IV}Al-rich phlogopite in FOS, (10—12) in BCB; (13–15) Ba-bearing phlogopite in TCB. H_2O^* - calculated from OH (F + Cl + OH = 2). ^{S} - Fe^{2+}/Fe^{3+} ratios calculated from stoichiometry. Dashes indicate that the analyzed element is not present in detectable quantities.

(known as "Fe-F avoidance"; Fleet, 2003, and references therein) is observed in tetraferriphlogopites only, which display a much larger range in total Fe (Fig. 8). Increasing F in phlogopites from BCB/FOS to the later TCB is consistent with observations from carbonatites and phoscorites of the Sokli complex (Finland) where F in F-bearing phases typically increases from early to late stage rocks of the complex (Lee et al., 2003). Consistent with phlogopite data from other carbonatite complexes, the Cl content of phlogopites from Palabora is generally low (<0.01 apfu).

6.2. Apatite

Selected electron microprobe analyses of representative apatites from the Loolekop deposit are listed in Table 4. Apatite is generally fluorapatite (0.6–0.8 apfu F; 0.2–0.4 apfu OH, calculated) with very low concentrations of Cl (≤ 0.025 apfu), as is typical of carbonatites (Hogarth, 1989; Klemme and Dalpé, 2003; Teiber et al., 2015 and references therein). While the bulk of the apatites (in FOS, BCB and TCB), which are interpreted as orthomagmatic phases, shows a large compositional overlap, there are few outliers, which are considered to represent late apatites (Fig. 9). Orthomagmatic apatites contain low REE (~0.01 to 0.05 apfu; Fig. 9), low Si (< 0.04 apfu; Fig. 9A), low Sr (< 0.05 apfu; Fig. 9B) and low Na concentrations (< 0.05 apfu; Fig. 9C). In contrast, late apatites exhibit higher REE concentrations reaching 0.15 apfu (Fig. 9). Conspicuously, these outliers show two distinguishable trends, which behave differently in different rock types. (1) Enrichment of REE with increasing Si (Fig. 9A), but constantly low Sr (Fig. 9B) and Na (Fig. 9C) is identified in FOS according to the britholite substitution ($P^{5+} + Ca^{2+} \leftrightarrow Si^{4+} + REE^{3+}$), while (2) enrichment of REE with constantly low Si (Fig. 9A) but increasing Sr (Fig. 9B) and Na (Fig. 9C) is seen in TCB and is assigned to the belovite substitution ($5Ca^{2+} \leftrightarrow Na^{+} + 3Sr^{2+} + REE^{3+}$). Samples of BCB show features of both trends (Fig. 9).

7. Discussion

7.1. Petrogenetic evolution of micas in the Palabora carbonatites and phoscorites

Besides Mg-rich biotite in pyroxenites and fenites, several phlogopite types in BCB, TCB and FOS can be distinguished based on the data presented above (Figs. 4-8):

(i) Common phlogopite is restricted to BCB and FOS, characterized by the highest Na and Ti contents with no large deviation from the ideal phlogopite formula, with the exception of Fe-enrichment (0.15–0.55 apfu).
(ii) Barium-bearing phlogopite is characterized by an enrichment of Ba and Al (at the expense of K + Si). This type of phlogopite is Fe-poor, shows the widest range in F contents and only occurs in TCB.
(iii) Some phlogopite analyses in BCB and FOS show high Al (up to 1.5 apfu) and Si (up to 3.0 apfu) comparable to phlogopite in TCB, but are relatively low in Ba (< 0.05 apfu; Fig. 6).
(iv) Tetraferriphlogopites occur in BCB, FOS and TCB and are characterized by variable and relatively high Fe, but low Al contents, suggesting the substitution of $^{IV}Fe^{3+}$ for ^{IV}Al (Fig. 7).

Based on their textural appearance, common phlogopite, Ba-enriched phlogopite and Al-rich, but Ba-poor phlogopite are interpreted as orthomagmatic crystallization products, whereas

Table 3
Representative major-element composition of tetraferriphlogopite from FOS, BCB, TCB and biotite from MPY and FEN.

in wt%	Tetraferriphlogopite									Biotite				
	1	2	3	4	5	6	7	8	9	10	11	12	13	14
Na_2O	0.03	0.05	0.05	0.05	0.03	0.01	0.03	–	0.01	0.06	0.07	0.12	0.09	0.06
K_2O	10.85	10.27	10.27	10.60	10.97	10.30	10.75	10.58	10.47	10.32	10.16	9.92	10.43	10.28
CaO	0.05	0.06	0.15	0.05	0.03	0.01	–	0.03	0.01	0.05	0.07	0.02	0.01	0.04
BaO	0.06	0.07	0.06	0.79	0.40	0.07	0.36	0.12	0.05	0.32	0.20	0.26	0.26	0.12
MgO	25.56	25.18	25.02	26.88	26.82	22.74	26.77	25.86	24.73	16.00	15.52	16.27	19.70	18.76
MnO	0.04	0.03	0.02	–	–	0.14	0.04	0.08	0.11	0.19	0.18	0.19	0.18	0.15
FeO^S	4.11	4.29	4.83	2.70	3.05	7.00	4.68	5.62	6.57	18.10	18.35	17.98	13.85	14.34
$Fe_2O_3^S$	5.85	8.44	10.01	4.88	5.09	14.68	1.93	6.60	13.80	–	–	–	–	–
Al_2O_3	7.15	5.93	4.54	8.46	8.02	0.96	8.94	5.49	0.93	11.73	11.99	11.97	11.81	12.56
TiO_2	0.04	0.06	0.05	0.06	–	0.08	0.02	0.05	0.04	0.90	0.94	0.93	0.21	0.26
Cr_2O_3	–	–	–	–	–	–	–	–	–	–	–	–	–	–
SiO_2	42.62	41.88	42.44	42.84	43.21	41.22	43.27	42.60	41.89	39.97	40.01	40.24	41.31	40.22
Cl	0.02	0.03	0.03	0.02	0.04	–	0.02	0.01	0.01	0.22	0.21	0.23	0.05	0.06
F	1.45	1.18	1.15	1.41	1.12	0.46	1.77	0.84	0.36	0.56	0.51	0.51	1.21	0.98
$-O = (F,Cl)_2$	0.62	0.50	0.49	0.59	0.48	0.19	0.75	0.35	0.16	0.29	0.26	0.27	0.52	0.42
TOTAL	97.21	96.97	98.13	98.15	98.30	97.48	97.83	97.53	98.82	98.13	97.95	98.37	98.59	97.41
H_2O^*	3.47	3.55	3.58	3.56	3.71	3.78	3.39	3.76	3.92	3.69	3.71	3.73	3.54	3.59
in apfu	Structural formulae calculated for 7 cations (tetrahedral [Z] plus octahedral [Y] cations)													
Na	0.01	0.01	0.01	0.01	–	–	–	–	–	0.01	0.01	0.02	0.01	0.01
K	0.99	0.96	0.96	0.96	0.99	0.99	0.98	0.98	0.98	0.98	0.97	0.95	0.97	0.98
Ca	–	0.01	0.01	–	–	–	–	–	–	–	0.01	–	–	–
Ba	–	–	–	0.02	0.01	–	0.01	–	–	0.01	0.01	0.01	0.01	–
Mg	2.75	2.74	2.71	2.84	2.82	2.55	2.82	2.78	2.69	1.79	1.74	1.8	2.13	2.05
Mn	–	–	–	–	–	0.01	–	0.01	0.01	0.01	0.01	0.01	0.01	0.01
Fe^{2+}	0.25	0.26	0.29	0.16	0.18	0.44	0.17	0.22	0.3	1.14	1.16	1.12	0.84	0.88
Fe^{3+}	0.32	0.46	0.54	0.26	0.27	0.82	0.21	0.47	0.85	–	–	–	–	–
Al	0.61	0.51	0.38	0.7	0.67	0.09	0.74	0.46	0.08	1.02	1.06	1.05	1.01	1.09
Ti	–	–	–	–	–	0.01	–	–	–	0.05	0.05	0.05	0.01	0.01
Cr	–	–	–	–	–	–	–	–	–	–	–	–	–	–
Si	3.07	3.04	3.08	3.04	3.05	3.08	3.06	3.07	3.06	2.98	2.97	2.98	3	2.96
Cl	–	–	–	–	–	–	–		–	0.03	0.03	0.03	0.01	0.01
F	0.33	0.27	0.26	0.31	0.25	0.11	0.4	0.19	0.09	0.13	0.12	0.12	0.28	0.23

(1–3) Tetraferriphlogopite in FOS, (4–6) in BCB, (7–9) in TCB; (10–12) Biotite in MPY, (13–14) in Fen. H_2O^* - calculated from OH (F + Cl + OH = 2). ^{S} - Fe^{2+}/Fe^{3+} ratios calculated from stoichiometry. Dashes indicate that the analyzed element is not present in detectable quantities.

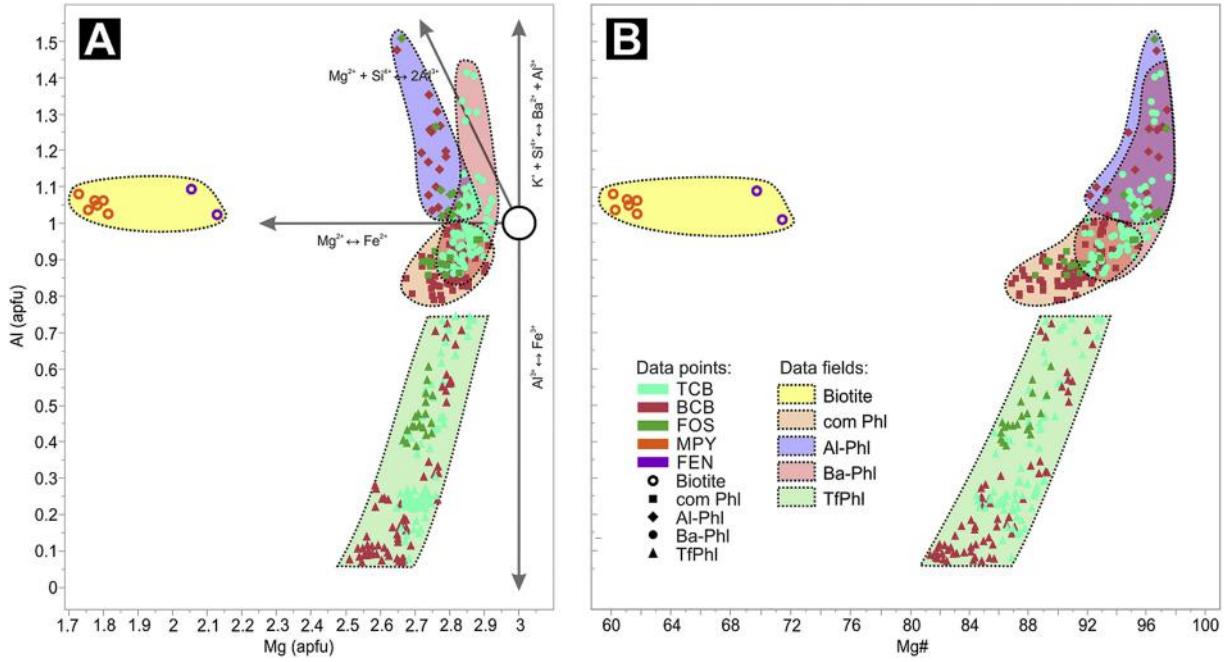

Fig. 4. Compositional variation of mica from Palabora. (A) Mg versus Al. (B) Mg# versus Al. Abbreviations: TCB – Transgressive Carbonatite; BCB – Banded Carbonatite; FOS – Phoscorite; com Phl – "common" phlogopite; Al-Phl – ^{IV}Al-rich phlogopite; Ba-Phl – Ba-bearing phlogopite; TfPhl – Tetraferriphlogopite; Analyses are visually membered in data points and data fields of related data points. For all binary diagrams: Where detection limits are not displayed no analyses plot below D.L.

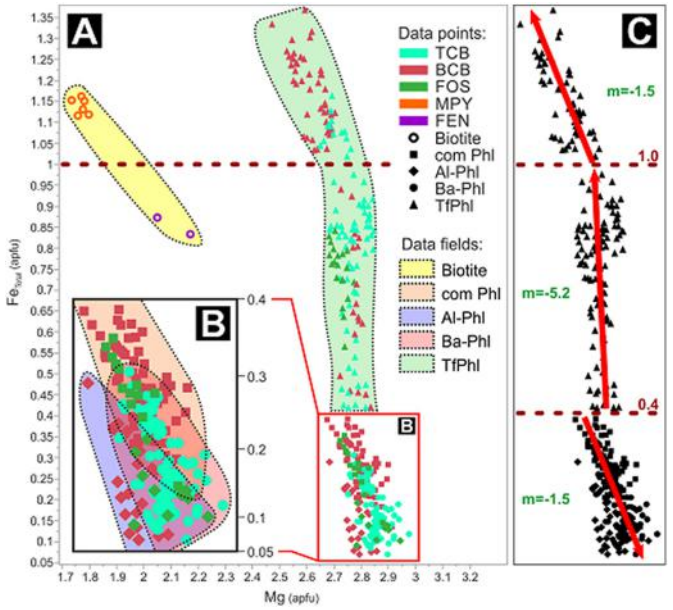

Fig. 5. Variation of Mg (apfu) versus Fe_{Total} (apfu) for micas from Palabora.

tetraferriphlogopites formed during a late-magmatic to hydrothermal stage.

7.1.1. Magmatic crystallization of phlogopite-annite, —kinoshitalite and -eastonite series

Micas of the phlogopite-annite series (common phlogopite) are limited to BCB and FOS, and represent the compositionally most primitive phlogopite type. Usually an increase of $^{VI}Fe^{2+}$ in phlogopites correlates with magma evolution and can be used to assess the differentiation of the igneous system (Brod et al., 2001). However, co-precipitation of larger amounts of magnetite (as is the case in many carbonatites) can cause an increase of Mg# in phlogopites, due to the consumption of Fe (e.g., McCormick and Le Bas, 1996). In this regard, an increasing Mg# is distinctive for the evolution of orthomagmatic mica at Palabora (Fig. 4B). Although Ti concentrations in micas from Palabora are generally low, common phlogopite reaches the highest Ti contents of phlogopites from carbonatites and phoscorites. This may reflect a relatively early formation of this type of phlogopite (e.g., Mitchell and Bergman, 1991), or may be influenced by coexisting mineral phases (e.g., Lee et al., 2003) and physicochemical conditions. Experimental studies have shown that dependencies on melt/liquid composition (e.g., fO_2 and P content) exert only minor effects on the substitution mechanisms for Ti in phlogopite, whereas a temperature decrease or pressure increase (especially in high-K rocks) cause a much stronger decrease of Ti solubility (Arima and Edgar, 1981). Furthermore, the crystallization of Ti-bearing phases (ilmenite and titanomagnetite), in combination with a decrease of temperature, inhibits the incorporation of Ti into mica, forming Ti-depleted phlogopites during the evolution of the magma (e.g., Edgar and Arima, 1983; Tronnes et al., 1985).

Ba-bearing phlogopite (max. kinoshitalite content of 30%) only occurs in TCB, whereas common phlogopite (BCB and FOS) is absent in this rock type. We therefore conclude that the magma crystallizing TCB was specifically enriched in Ba (and Al) compared to the magma crystallizing BCB and FOS, which is further suggested by the common appearance of barytocalcite in TCB. Enrichment of Ba in carbonatitic magmas may be caused by magma differentiation when incompatible elements accumulate in larger amounts in the residual liquid (e.g., Kogarko et al., 2012; McCormick and Heathcote, 1987; McCormick and Le Bas, 1996). Furthermore, Ba-bearing phlogopites show the highest F concentrations. Experimental studies found that F in phlogopite increases with decreasing temperature, which is linked to an increasing crystal/liquid ratio, and is not distinctly affected by pressure (e.g., Edgar and Arima, 1985). While geological observations provide clear evidence that Ba-phlogopite-bearing TCB represents the latest magma/melt, as it intrudes the BCB/FOS assemblage, geochemical data on micas support that TCB represents the most evolved rock type. Since ^{IV}Al-rich phlogopite is limited to BCB and FOS samples that are in contact or close to the contact to TCB, we suggest that this mica type formed by interaction of intruding TCB melt with pre-existing BCB magma (crystal mush, not consolidated). This implies that the TCB magma may have acted as an Al source for contacting BCB/FOS sections and is further affirmed by the occasional slight enrichment of Ba in ^{IV}Al-rich phlogopite and the enrichment of Al in subsequent magnetite

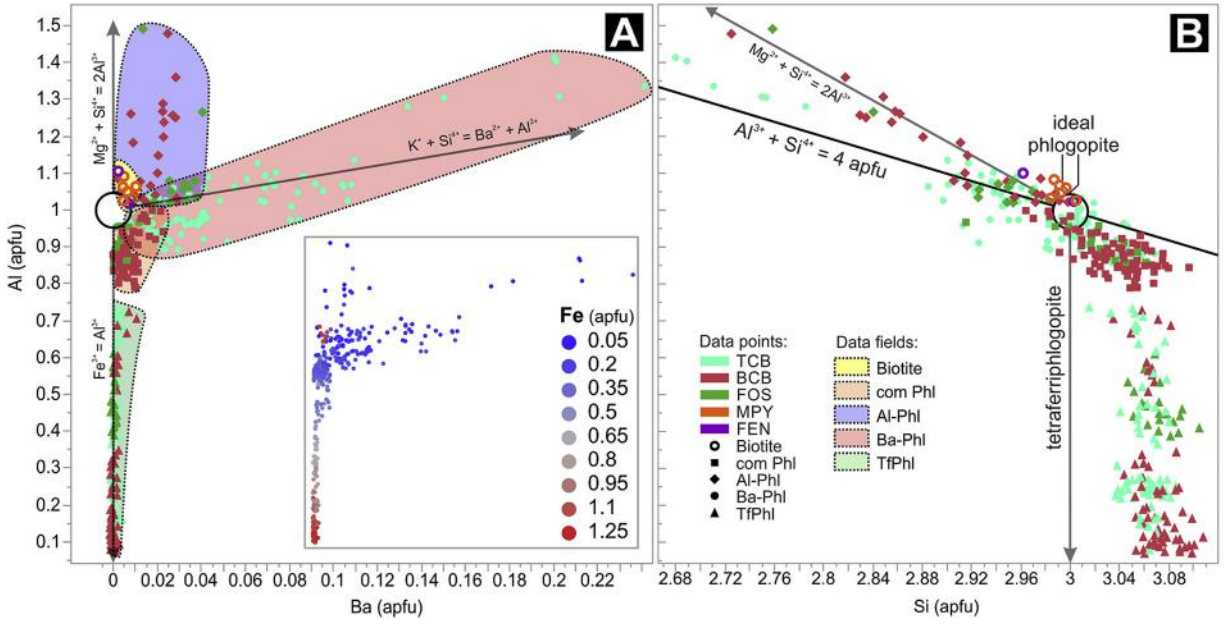

Fig. 6. Compositional variation of mica from Palabora. (A) Ba versus Al. Separated plot reflects Fe enrichment according to the main diagram. Red dots (high Fe) at high Al (1–1.1 apfu) represent biotites from pyroxenites with high Fe^{2+} (octahedral site). (B) Si versus Al. (For interpretation of the references to colour in this figure legend, the reader is referred to the web version of this article.)

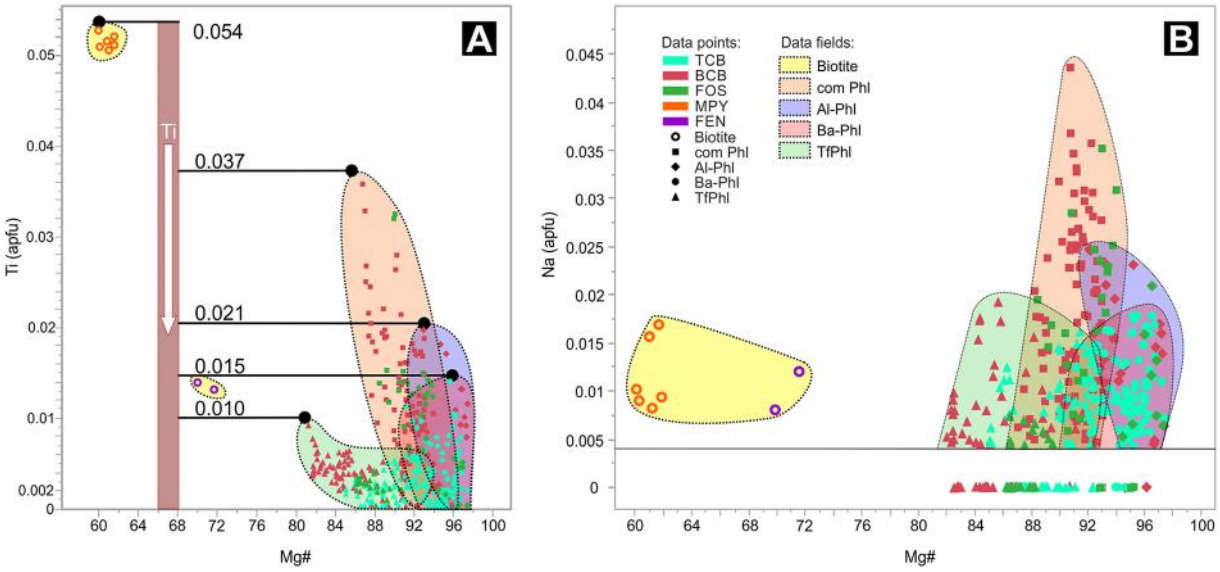

Fig. 7. Compositional variation of mica from Palabora. (A) Mg# versus Ti. (B) Mg# versus Na. For analyses below the detection limit (black horizontal line) the data points were set to zero to illustrate the amount of data below D.L.

in such samples (expressed as abundant exsolved spinel in magnetite from such samples; Giebel et al., 2017). Because early mica crystallization should lead to Al-depletion in evolving carbonatitic magmas, assuming an excess of Al in higher evolved carbonatites (TCB) seems contradicting. However, similar evolutionary trends in micas from carbonatite complexes in the Transvaal/South Africa, Arkansas/USA and Uganda (Clarke et al., 1993; Heathcote and McCormick, 1989; McCormick and Le Bas, 1996) have been observed and were interpreted to result from contamination by country rock material (McCormick and Le Bas, 1996).

The content of Na in phlogopites is assumed to reflect the degree of melt evolution. While early crystallized phlogopites in carbonatites generally show a depletion of sodium, late-stage phlogopites may contain significant amounts of Na (e.g., Sokli carbonatite, Lee et al., 2003).

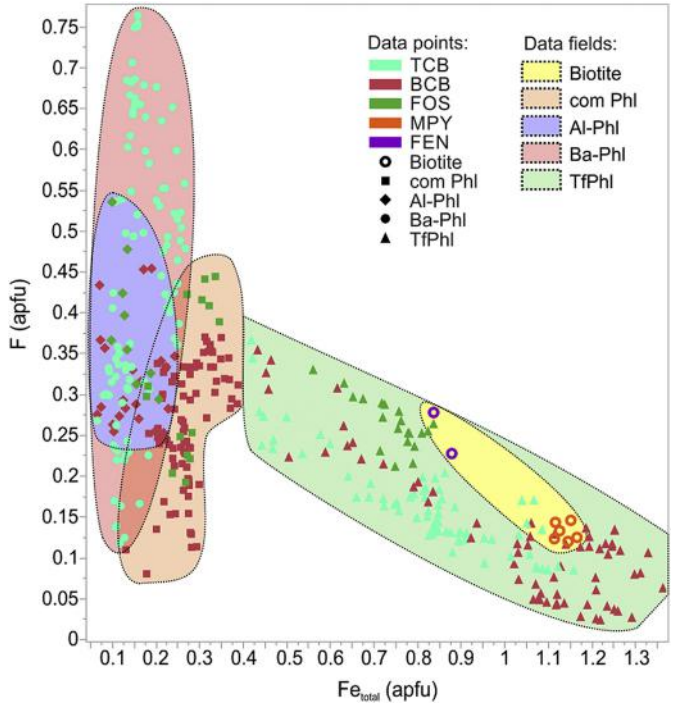

Fig. 8. Variation of Fe_{Total} (apfu) versus F (apfu) for micas from Palabora.

Phlogopites from Palabora, however, show a quite controversial dichotomy: although the Na content is generally low (< 0.045 apfu) and BCB and FOS show an internal increase of Na, which mirrors an evolutionary trend (Fig. 7B), some BCB and FOS (more primitive) show a much higher substitution of Na for K than TCB (more evolved), where a decrease of K is mainly linked to an increase of Ba. This apparent discrepancy arises from the instance that BCB/FOS and TCB do probably not represent a continuous differentiation sequence, but may show basically different evolutionary levels, at which TCB is characterized by a more advanced development of coexisting fluids. Generally, Na shows a high affinity for fluid phases, which migrate to higher levels and surrounding rock sequences, leading to a depletion of Na in the (typically almost Na-free) carbonatite bodies (Veksler and Keppler, 2000). These Na-rich fluids cause metasomatism (fenitization; often characterized by sodium enrichment) of surrounding silicate rocks (Bühn and Rankin, 1999), which is prominent at Palabora (Verwoerd, 1966).

7.1.2. Late-stage formation of tetraferriphlogopite

In general, tetraferriphlogopite crystallizes as a magmatic phase or from late-stage fluids. It typically occurs in late-stage rocks, crystallizing at low temperatures (Fleet, 2003; Lee et al., 2003). In other carbonatite occurrences, presumably magmatic tetraferriphlogopite essentially shows phlogopite cores with normal pleochroism with a continuous enrichment of $^{IV}Fe^{3+}$ due to the formation of nearly ideal tetraferriphlogopite (e.g., Lee et al., 2003; Puustinen, 1973), while tetraferriphlogopites interpreted as precipitated from late-stage fluids rather replace earlier phlogopites, form overgrowth zones and rims with sharp compositional changes to mainly preserved pre-existing phlogopite cores (e.g., Brod et al., 2001) or completely new individual crystals (e.g., Lee et al., 2003).

Tetraferriphlogopites from Palabora crystallized as new individual crystals in veins (see above) probably at a late-magmatic stage (characterized after Giebel et al., 2017), decoupled from the orthomagmatic phlogopite formation. The mineral associations described above indicate a locally controlled contemporaneous mineralization of tetraferriphlogopite and late-magmatic REE phases from the same fluid. This Al-poor fluid was locally enriched in Fe by the dissolution of pre-existing (primary magmatic) magnetite (Fig. 3B), which is confirmed by the small-scale heterogeneous dispersal of tetraferriphlogopites with different Fe/Al ratios depending on the availability of Fe within the fluid. The following schematic reaction is suggested to describe this:

Table 4
Representative major-element composition of apatite from FOS, BCB and TCB.

in wt%	1	2	3	4	5	6	7	8	9	10	11	12	13	14
Na_2O	0.08	0.06	0.08	0.09	0.16	0.12	0.11	0.19	0.16	0.2	1	0.76	0.47	0.45
CaO	54.75	54.69	54.75	54.89	53.84	54.88	51.55	52.5	53.32	53.51	48.59	49.35	52.24	52.52
SrO	0.51	0.61	0.55	0.42	0.82	0.67	0.82	0.8	0.62	0.36	2.57	2.63	1.41	1.5
La_2O_3	–	0.09	0.14	0.16	0.22	0.11	0.74	0.74	0.43	0.21	1.14	0.91	0.56	0.37
Ce_2O_3	0.27	0.24	0.5	0.23	0.45	0.27	1.88	1.61	1.06	0.9	2.25	2.15	1.34	1.17
Pr_2O_3	0.08	0.02	0.07	0.09	0.03	0.2	0.3	0.32	0.14	0.16	0.43	0.25	0.16	0.18
Nd_2O_3	0.16	0.2	0.29	0.18	0.32	0.18	0.99	0.9	0.55	0.69	1.11	0.82	0.57	0.58
FeO	0.04	–	0.01	–	0.04	0.05	0.1	0.03	–	0.01	0.01	0.05	–	0.01
P_2O_5	42.18	42.12	41.52	41.87	41.34	41.63	39.45	39.82	40.44	40.87	40.62	40.62	41.42	41.44
SiO_2	0.11	0.08	0.14	0.09	0.12	0.08	1.45	1.08	0.71	0.54	0.13	0.05	0.1	0.05
SO_3	–	–	0.03	–	0.04	0.03	0.02	–	0.07	0.03	–	0.03	0.02	–
As_2O_5	–	–	–	–	–	–	–	–	–	–	–	–	–	–
MnO	0.03	–	–	–	0.02	–	–	–	–	–	–	–	–	–
Cl	0.07	0.05	0.04	0.08	0.03	0.05	0.02	0.03	0.07	0.05	0.01	0.02	0.02	0.02
F	2.53	2.54	2.75	2.5	2.87	2.56	2.72	2.76	2.5	2.6	2.24	2.35	2.69	2.74
$-O = (F,Cl)_2$	1.06	1.07	1.15	1.05	1.2	1.07	1.14	1.16	1.05	1.09	0.94	0.99	1.13	1.15
TOTAL	99.75	99.63	99.72	99.55	99.10	99.76	99.01	99.62	99.02	99.04	99.16	99.00	99.87	99.88
H_2O^*	0.57	0.56	0.46	0.58	0.4	0.55	0.44	0.43	0.55	0.51	0.65	0.59	0.49	0.47
in apfu	Structural formulae calculated for 8 cations													
Na	0.01	0.01	0.01	0.01	0.03	0.02	0.02	0.03	0.03	0.03	0.17	0.13	0.08	0.07
Ca	4.94	4.93	4.94	4.95	4.91	4.95	4.79	4.83	4.88	4.89	4.54	4.6	4.76	4.79
Sr	0.02	0.03	0.03	0.02	0.04	0.03	0.04	0.04	0.03	0.02	0.13	0.13	0.07	0.07
La	–	–	–	–	0.01	–	0.02	0.02	0.01	0.01	0.04	0.03	0.02	0.01
Ce	0.01	0.01	0.02	0.01	0.01	0.01	0.06	0.05	0.03	0.03	0.07	0.07	0.04	0.04
Pr	–	–	–	–	–	–	0.01	0.01	0.01	0.01	0.01	0.01	0.01	0.01
Nd	–	–	0.01	0.01	0.01	0.01	0.03	0.03	0.01	0.02	0.03	0.03	0.02	0.02
Fe	–	–	–	–	–	–	0.01	–	–	–	–	–	–	–
P	3	3	2.98	2.99	2.98	2.97	2.89	2.89	2.93	2.95	2.99	3.01	2.98	2.98
Si	0.01	0.01	0.01	0.01	0.01	0.01	0.13	0.1	0.06	0.05	0.01	–	0.01	0.01
S	–	–	–	–	–	–	–	–	–	–	–	–	–	–
As	–	–	–	–	–	–	–	–	–	–	–	–	–	–
Mn	–	–	–	–	–	–	–	–	–	–	–	–	–	–
Cl	–	0.01	0.01	0.01	–	0.01	–	–	0.01	0.01	–	–	–	–
F	0.67	0.68	0.73	0.66	0.77	0.68	0.75	0.75	0.68	0.7	0.62	0.65	0.72	0.73

(1–2) Apatite in FOS; (3–4) in BCB, (5–6) in TCB; (7–8) High REE apatite in FOS, (9–12) in BCB, (13–14) in TCB. H2O* - calculated from OH (F + Cl + OH = 1). Dashes indicate that the analyzed element is not present in detectable quantities.

[1] Magnetite + Fluid (late-magmatic) = Tetraferriphlogopite + Fluid'(late-magmatic)

$$0.5Fe^{2+}Fe^{3+}{}_2O_4 + K^+ + 3Si^{4+}\ 2.5Mg^{2+} + 10OH^- = KMg_{2.5}Fe^{2+}{}_{0.5}Fe^{3+}Si_3O_{10}(OH)_2 + 8H^+$$

In contrast to phlogopites, tetraferriphlogopite shows a decrease of Mg#, probably reflected by the evolution of tetraferriphlogopite mineralization without simultaneous magnetite precipitation. Tetraferriphlogopites and the late-stage generation of magnetites, which occur together in veins (described above), are in textural disequilibrium (Fig. 2E).

7.1.3. Changing oxygen fugacity during phlogopite and tetraferriphlogopite formation?

The incorporation of Fe^{2+} and Fe^{3+} into mica provides insights into the fO_2 conditions prevailing during mica crystallization (e.g., Brod et al., 2001) and may be identified by the use of the ternary diagram Fe^{2+}-Fe^{3+}-Mg^{2+} including fO_2 buffer limits after Wones and Eugster (1965) as has been done before (e.g., Brigatti et al., 1996b; Brod et al., 2001), although these buffer limits were originally prepared to characterize biotites of silicate rocks, therefore may only be used with caution in carbonatitic systems (Fig. 10). Phlogopites at Palabora plot below the NNO (nickel-nickel oxide) buffer, most tetraferriphlogopites in FOS and TCB (few BCB) between NNO and HM (hematite-magnetite buffer)

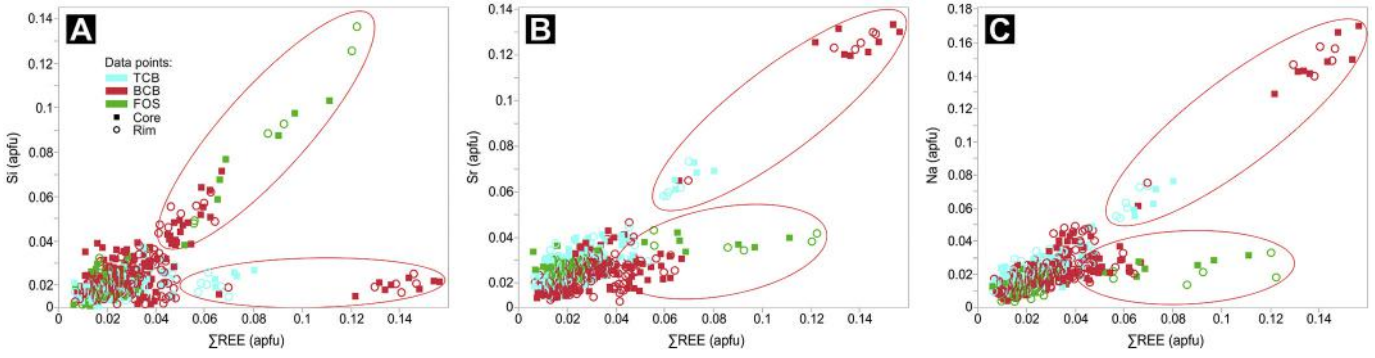

Fig. 9. Compositional variation of Palabora apatites. Diagram of (A) REE_{Total} versus Si, (B) REE_{Total} versus Sr and (C) REE_{Total} versus Na. Red circles mark sections enriched in tetraferriphlogopites. (For interpretation of the references to colour in this figure legend, the reader is referred to the web version of this article.)

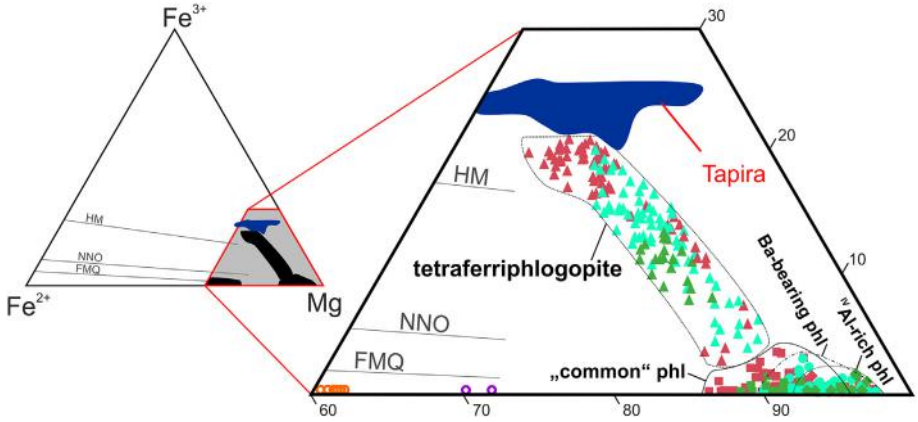

Fig. 10. Palabora phlogopite composition plotted in the ternary Fe^{2+}-Fe^{3+}-Mg with fO_2 buffer after Wones and Eugster (1965). Blue field represents tetraferriphlogopite in carbonatites from Tapira after Brod et al. (2001). (For interpretation of the references to colour in this figure legend, the reader is referred to the web version of this article.)

and tetraferriphlogopites in most BCB (and few TCB) plot above the HM buffer (Fig. 10). These trends clearly confirm the characteristic formation of tetraferriphlogopites at fO_2 above the NNO buffer (Brigatti et al., 1996b). Ideal tetraferriphlogopites would plot along the 25% Fe^{3+}-line (completely substitution of $^{IV}Fe^{3+}$ for ^{IV}Al; e.g., Tapira, Brazil; Fig. 10). The evolution of tetraferriphlogopites almost parallel to the Fe^{3+}-Mg axis reflects a nearly constant Fe^{2+}/Mg ratio with increasing Fe^{3+} and depicts an increase in fO_2 during the evolution of the late-magmatic fluid. However, tetraferriphlogopites from Palabora show prominent positive Eu anomalies (Milani et al., 2017), which suggests reducing conditions. Therefore, we assume that tetraferriphlogopites have been modified by interaction with a rather reduced post-magmatic fluid, as will be described in more detail below. Giebel et al. (2017) showed that this post-magmatic fluid caused an important re-distribution of REE in the carbonatites and phoscorites from Palabora.

In cases, rounded aggregates of graphite occur around tetraferriphlogopite. This feature is often associated with magnesite. This graphite variety is related to the post-magmatic stage and therefore not cogenetic with the tetraferriphlogopite, but the REE budget of tetraferriphlogopites was probably affected by the fluid that precipitated graphite. Based on similar textures, Gellatly (1966) and reference therein, explained the formation of drop-like graphite by the decomposition of carbonates in carbonatites ($T = 455–745$ °C; $P = .05–1$ GPa) related to hydrothermal alteration. The potential for graphite formation increases with cooling of a carbon-saturated C-O-H fluid (most favourable conditions in H_2O-rich fluids with X_O ($O/(O + H)$) = 0.33) due to the shift of the carbon saturation surface and results in an increase of the fO_2^{fluid} (Huizenga, 2011). The typical co-precipitation of graphite with magnetite under such conditions was confirmed by Kogarko et al. (2010). In contrast, very reduced fluid (C—H) conditions rather cause consumption of graphite at lower temperatures (Huizenga, 2011), whilst fluids exceeding the graphite-CO buffer (CCO), may cause carbonate precipitation (Frost and Wood, 1997). Precipitation of graphite in carbonatites at Palabora is suggested according to the following schematic reaction:

[2] Fluid (post-magmatic) = Graphite + Magnesite + Magnetite + Fluid' (post-magmatic)

$CH_4 + 2½CO_2 + 8OH^- + 3Fe^{2+} + Mg^{2+} = 2½C + MgCO_3 + Fe^{2+}Fe^{3+}{}_2O_4 + 6H_2O$.

The enrichment of C-species in the post-magmatic fluid arises from the dissolution of carbonates (calcite, dolomite), which also caused the enrichment of Mg (leading to the formation of magnesite). The possible co-existence of magnesite and graphite lies approximately on the CCO buffer (e.g., Doroshkevich et al., 2010). The mentioned relations favour the presence of an initially rather reduced hydrothermal fluid which evolved into a rather oxidized "post-magmatic" fluid during cooling.

7.2. Comparison of micas from Palabora with other carbonatite/phoscorite complexes

Similar to Palabora, Jacupiranga/Brazil and Kaiserstuhl/Germany show a distinct mica mineralogy among carbonatites/phoscorites and associated silicate rocks (Figs. 11A-C). Jacupiranga phlogopites (in carbonatites and phoscorites) comprise Ba-, ^{IV}Al- and ^{VI}Al-enriched micas. These belong to a mixture of phlogopite-eastonite and phlogopite-kinoshitalite series micas following the trends of ^{IV}Al-rich phlogopite from Palabora, but contain significant higher Ba concentrations (up to 0.6 apfu; Brod et al., 2001) compared to Palabora phlogopites (up to 0.24 apfu Ba; Fig. 6). At Kaiserstuhl, micas of the phlogopite-kinoshitalite series with a strongly variable eastonite component dominate the mica mineralogy in carbonatites, with up to 0.55 Ba apfu (Giebel, unpubl. data). In contrast to Jacupiranga, where phlogopites show a depletion of Al during their evolution (black arrow in Fig. 11B), phlogopites from the Kaiserstuhl Volcanic Complex evolve towards higher concentrations of Al (black arrow in Fig. 11C). Although both types of Ba-bearing phlogopite can occur in carbonatite complexes, the latter trend, which is also reflected by Palabora phlogopites (black arrow in Fig. 11A), appears to be much more common. However, both Jacupiranga and Kaiserstuhl lack tetraferriphlogopite. In contrast, Sokli/Finland comprises mica of the phlogopite-tetraferriphlogopite and phlogopite-eastonite series, but lacks Ba-enriched mica (Fig. 11D; Lee et al., 2003). Kovdor/Russia contains common phlogopites in early-stage phoscorites, whereas late-stage micas are tetraferriphlogopites (Fig. 11E; Krasnova et al., 2004a; Krasnova et al., 2004b). While Sokli and Kovdor display a successive evolution from phlogopites to tetraferriphlogopites (continuous decrease of Al), Palabora shows an evolutionary increase of Al in phlogopites and a separate evolution of tetraferriphlogopite following an Al depletion (Fig. 11A).

Although the mentioned mica types are typical constituents in carbonatites, in most complexes they usually do not occur together and at least one of them is typically lacking (e.g., McCormick and Le Bas, 1996). In that sense, carbonatites and phoscorites of Palabora represent a rare case with a multi-stage and multi-type mica mineralogy combining the whole set of typical micas, namely common phlogopite and members of the phlogopite-eastonite, phlogopite-kinoshitalite, and phlogopite-tetraferriphlogopite series.

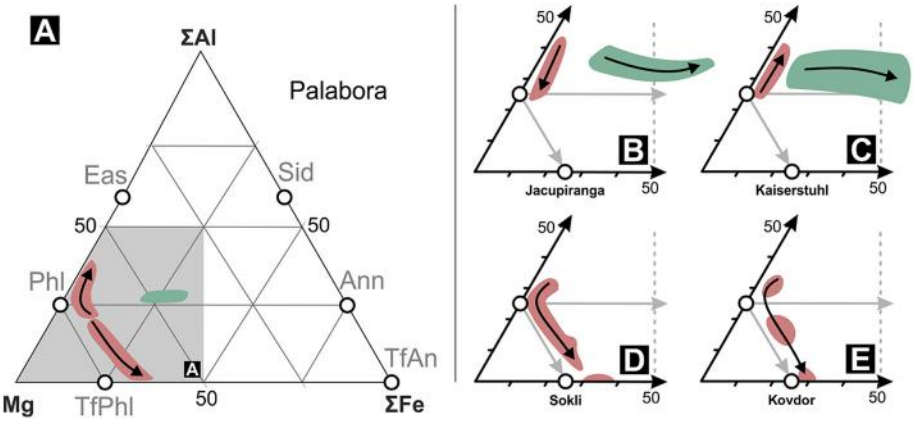

Fig. 11. Compositional trends of mica from Palabora (A) and other carbonatite complexes (B-E). Sokli (Lee et al., 2003), Kovdor (Krasnova et al., 2004a), Jacupiranga (Brod et al., 2001), Kaiserstuhl (Braunger et al., 2018; Giebel, unpubl. data). Green field – micas from associated silicate rocks, red field – micas from carbonatites and phoscorites. Ann - annite, Eas - eastonite, Phl - phlogopite, Sid - siderophyllite, TfAn - tetraferriannite, TfPhl - tetraferriphlogopite. According to the absence of Ba in plots of Fig. 12, a differentiation between phlogopites of the phlogopite-kinoshitalite and phlogopite-eastonite series is not possible in this plots but explained in the text. (For interpretation of the references to colour in this figure legend, the reader is referred to the web version of this article.)

7.3. Tetraferriphlogopite versus Apatite

Although apatite data show no large compositional variations between FOS, BCB and TCB, the few exceptional analyses (circles in Fig. 9) provide information about late-magmatic processes. These outliers depict enrichment of REE and derive from samples that show a strong overprint by late-magmatic fluid characterized by the abundant tetraferriphlogopite precipitation. This confirms the assumption that significant amounts of REE were introduced by late-magmatic fluids, which caused the extensive formation of monazite and britholite (for more detail in respect to the late-magmatic stage and the related REE mineralization the reader is referred to Giebel et al., 2017). The kinds of REE enrichment (with increasing Si or Sr; see above) are certainly controlled by the local enrichment of Si or Sr in the late-magmatic fluid which is connected to the remobilization of the elements from pre-existing mineral phases (Sr-bearing carbonates, silicates). This in turn depends on their availability (proportion) in the related rock types. The preferred incorporation of Si into tetraferriphlogopite requires an excess of Si for a substitution into apatite.

7.4. Genesis of the carbonatite-phoscorite association of Palabora

Our data has shown that banded carbonatites and phoscorites reflect almost identical mica compositions, while transgressive carbonatites as well as associated silicate rocks depict a completely different mica composition. An analogous compositional development of mica has also been described from other carbonatite-phoscorite associations (e.g., Catalão I + II, Sokli; Brod et al., 2001; Lee et al., 2003). This may indicate the genetic relationship between phoscorite and carbonatite, which certainly belong to a common parental magma. While the formation of phoscorite as an individual magma is specified as unrealistic because of the instability at plausible temperatures (Lindsley and Epler, 2017), crystal fractionation or separation from an immiscible carbonatite melt are used to explain the observed geometric relations between the mentioned rock types (see discussion in Krasnova et al., 2004b). The very similar mineral associations in BCB and FOS at Palabora with only differences in modal compositions (Giebel et al., 2017) provide further evidence that these rock types were formed from a common parental magma. The analogous compositional development of mica from BCB and FOS cannot be easily explained by crystal fractionation. We therefore suggest that FOS and BCB formed by exsolution of a parental magma into two immiscible melts. Further observations of orbicular and spherulitic phoscorite fractions in carbonatites and vice versa in several carbonatite complexes (e.g., Krasnova et al., 2004b; Lapin and Vartiainen, 1983), studies of mineral inclusions in olivine and apatite (Mikhailova et al., 2002) as well as individual mineral chemistry (e.g., Lee et al., 2006) argue for the importance of liquid immiscibility as the source of phoscorite formation for most carbonatite-phoscorite associations. Furthermore, melt inclusions show that the parental magma of some carbonatites was enriched in Fe and/or P (e.g., Chen et al., 2013; Guzmics et al., 2008; Krasnova et al., 2004a), while phoscorites contain melt inclusions dominated by different carbonates (e.g., Veksler et al., 1998a; Zaitsev and Kamenetsky, 2013). However, both crystal fractionation and liquid immiscibility seem to be eligible to cause the generation of phoscorites (e.g., Rimskaya-Korsakova and Krasnova, 2002). Therefore, the results of our study have to be seen as an example of phoscorite formation but not as a unique mechanism. Other complexes (Guli, Russia; Kogarko et al., 1997) may form phoscorites by crystal fractionation, or a combination of both crystal fractionation and liquid immiscibility. The deviant phlogopite composition in TCB compared to mica from BCB and FOS implies that TCB represents a higher evolved magma, which experienced a separate evolution.

7.5. Emplacement of Palabora-like carbonatite complexes

Besides the general demand for a model illustrating the related emplacement of carbonatites and phoscorites, an equally highly debated issue is the sequence of magma emplacement in relation to associated silicate rocks. This study has shown that the mica mineralogy of pyroxenites at Palabora (Eriksson, 1982, and this study) completely differs from the mica mineralogy of the carbonatite-phoscorite assemblage, which may indicate that both rocks have experienced an independent development. This furthermore is indicated by previous isotope studies that point out that fractional crystallization and liquid immiscibility are not viable mechanisms to relate silicate rocks and carbonatites/phoscorites from Palabora (Eriksson, 1982). Therefore, we suggest a contemporaneous emplacement of both lithologies but no genetic link between them. Especially Gittins and Harmer (2001) emphasise the independence of spatially associated carbonatites and alkali silicate rocks in igneous complexes. A compilation of worldwide carbonatite complexes for which the emplacement depth is known reveals a relation of emplacement depth and rock type association. Already Frolov (1971) stated that the ratio of carbonatites to associated silicate rocks in many carbonatite-bearing complexes increases with decreasing emplacement depth. Arzamastsev et al. (2000) have shown that the dominance of carbonatites or associated silicate rocks within a Kola peninsula complex seems to be controlled by the depth of the ore body. While short vertical ore bodies show a very low carbonatite/

silicate rock ratio (C/SR), high, vertically extensive ore bodies exhibit a relatively high C/SR ratio. To understand this phenomenon, it is important to recognize that ore bodies with a short vertical extension may represent a deep emplacement within the continental crust and a deep erosion level in relation to the paleo surface (low source-emplacement distance → low ΔS-E). In contrast, complexes with a deep-reaching ore body may display a shallower emplacement with a high ΔS-E and a shallow erosion level in relation to the paleo surface. Volcanic carbonatite complexes often show a significant silicate rock domination (lower C/SR ratio), which apparently displays a contradiction to the previously introduced assumption. This is probably simply linked to a lower ΔS-E because of crustal thinning, as their occurrence is largely restricted to continental rifting zones. Furthermore, deep-level carbonatitic intrusions show a significant higher amount of associated phoscorite than shallow level ones. This would imply that a possible phoscorite-carbonatite separation takes place at deeper crustal levels and the phoscorite proportion decreases with distance to the source.

The following model attempts to explain and combine the approach of magma genesis, evolution and the emplacement of carbonatites and phoscorites in association with mafic to ultramafic silicate rocks (e.g., pyroxenites and olivinites) according to data and observations made in this study as well as from the related literature. This model is only valid for the genesis of carbonatite complexes derived by mantle plume activity which has been confirmed by several studies (e.g., Gibson et al., 1995; Huang et al., 1995; Natali et al., 2018; Wu et al., 2011; Zaitsev and Bell, 1995). It is supposed that mantle plume-derived partial melting displays the most important process causing the formation of carbonatite/phoscorite assemblages, which will be typified by the following model. Our model is driven by three major questions: (1) Why are carbonatite-phoscorite assemblages emplaced late within silicate rock-dominated complexes? (2) How are phoscorites formed and why do they show an almost exclusive association with carbonatites? (3) Why do some carbonatite complexes not show any associated silicate rocks?

7.6. A genetic model for the formation of carbonatite-phoscorite associations

The formation of phoscorite rocks requires a parental magma of carbonatitic composition (see above). Such magmas possibly form below cratonic crust (>86% of all known carbonatitic rocks occur in Precambrian cratons, mostly close to continental margins; Woolley and Kjarsgaard, 2008), where these melts experienced an enrichment in Fe, Ti and P, forming carbonate-phosphate/iron-oxide-rich (CPIO) melts. These may represent magmas parental to carbonatite-phoscorite associations. Primary carbonatitic melts are generated in the lithospheric metasomatized mantle at depths >70 km (Wyllie and Lee, 1998). They probably formed by low degree partial melting (<5%; e.g., Dalton and Presnall, 1998; Dasgupta et al., 2007; Gudfinnsson and Presnall, 2005) at the marginal zones of mantle plumes (Bell and Simonetti, 2010), while more central areas are characterized by the generation of silicate melts, according to a higher degree of melting (Fig. 12A). These primary carbonatitic melts are typically Mg-rich (Harmer and Gittins, 1998; Lee and Wyllie, 1998; Sweeney, 1994) because of their pressure-dependent partitioning of Mg (Lee and Wyllie, 1997) into carbonate liquid at high pressures (>10 kbar; Brooker, 1998) and into silicate melts at lower pressure (Veksler et al., 1998b). Liquid immiscibility of silicate and carbonatitic melts prohibits a re-mixing in the upper mantle and supports the separation of these two melts. During this process, Fe and especially P partition into the carbonatitic melt (Jones et al., 1995; Lindsley and Epler, 2017; Naslund, 1983), which evolves into a CPIO melt. Smaller amounts of carbonatitic/CPIO melt penetrate the lower crust along zones of weakness, but major portions of the CPIO melts remain below the crust becoming denser by the enrichment of Fe and P until equilibration with the silicate melt is reached. A comparison of the density of associated silicate rocks (e.g., pyroxenites Ø 3.3 g/cm^3, melteigites/ijolites Ø 3.0 g/cm^3), carbonatites (Ø 2.9 g/cm^3) and phoscorites (Ø 3.8 g/cm^3; Arzamastsev et al., 2000) shows that a CPIO melt, comprising a carbonatite-phoscorite ratio of <50/50, has a density very close to that of associated silicate rocks. This implies that with increasing enrichment of Fe and P, immiscible CPIO melts lose their high buoyancy and achieve a state of levitation within the much more voluminous silicate melt accumulation.

Processes that activate weakness zones may then allow for channelized magma ascent and according to the state of levitation, CPIO magmas may be dragged into these zones because of depressurization (Fig. 12B) together with already introduced silicate magmas (Fig. 12C). The higher the distance between an ascending channel and the CPIO magma body the longer the melt needs to reach the channel. Hence the feasibility of an introduction of CPIO melt into this channel and the timing of this process highly depends on the distance between both. This condition certainly further defines the degree of Fe-P enrichment. The longer the CPIO melt remains within the high volume of silicate magma, the more it gets enriched in Fe and P. Early opened ascending channels directly above the carbonatitic magma body will be accompanied by less Fe-P enriched carbonatitic melts, while ascending channels in broader vicinity of the carbonatitic body will be accompanied by rather higher Fe-P enriched CPIO melts.

Due to the decrease in temperature and/or pressure of the ascending CPIO melt, unmixing of a phoscoritic and carbonatitic magma may then occur (Fig. 12D). Hou et al. (2018) have shown that an increase of aH_2O and fO_2 enlarges the two-liquid field, which allows for the separation of a silica-free or -poor Fe-Ca-P melt and a silicic magma. Although such a system, which includes a silicic magma, is genetically different, the experimental study of Hou et al. (2018) reflect a very similar mechanism to generate Fe-Ca-P melts such as phoscorites. Furthermore, Hou et al. (2018) demonstrate the preferred portioning of F into the Fe-rich melt, whereat Hou et al. (2017) point out that an enrichment of F favours the development of liquid immiscibility by the complexation of Mg (and Ca) and increasing activity of Fe. While an increase of F promotes the enrichment of Ca in a Fe-P-rich melt, a decrease in fO_2 promotes the partition of silica into this melt (Hou et al., 2018). These variations may be responsible for the variable mineralogy of phoscorites.

Although Fe-Ti oxide melts cannot be stabilized even by P, F and/or C below temperatures of 1300 °C, the presence of these fluxes, with C being the most important one, can stabilize Ti-poor iron oxide melts (common phoscorites) to temperatures below 1000 °C (Lindsley and Epler, 2017). However, the removal of C from exsolved phoscorite melt will initiate crystallization immediately after separation, because P alone is not effective enough to stabilize Fe oxide-dominated magmas. Precipitation of apatite will trigger the formation of Fe (Ti) oxide, and vice versa, which explains the common association of apatite and Fe (Ti) oxides (Lindsley and Epler, 2017). This segregation process further induces a significant density contrast between carbonatite (low density) and phoscorite (high density) melts. This may lead to a slightly descending phoscorite accumulation at the outer zones of the magma channel, caused by the continuously ascending magma flow through the centre of the conduit (Fig. 12D). The adjacent crystallization of carbonatite induces the strong association between phoscorites and early carbonatites. Furthermore, fractionation generates higher differentiated carbonatite magmas, which emplace into higher levels of the crust. The separation of phoscorite, and the related strong density decrease of the evolving carbonatite melt, causes a significant density difference between the silicate and carbonatite magma. This may promote enhanced, jet-like ascent of the carbonatite melt through the ascending silicate magma. Passing through the intruding silicate magma front (Fig. 12E), the carbonatite magma may rapidly ascend to higher crustal levels, because of its extremely low viscosity (Treiman and Schedl, 1983), while silicate magma activity already ceased (based on higher

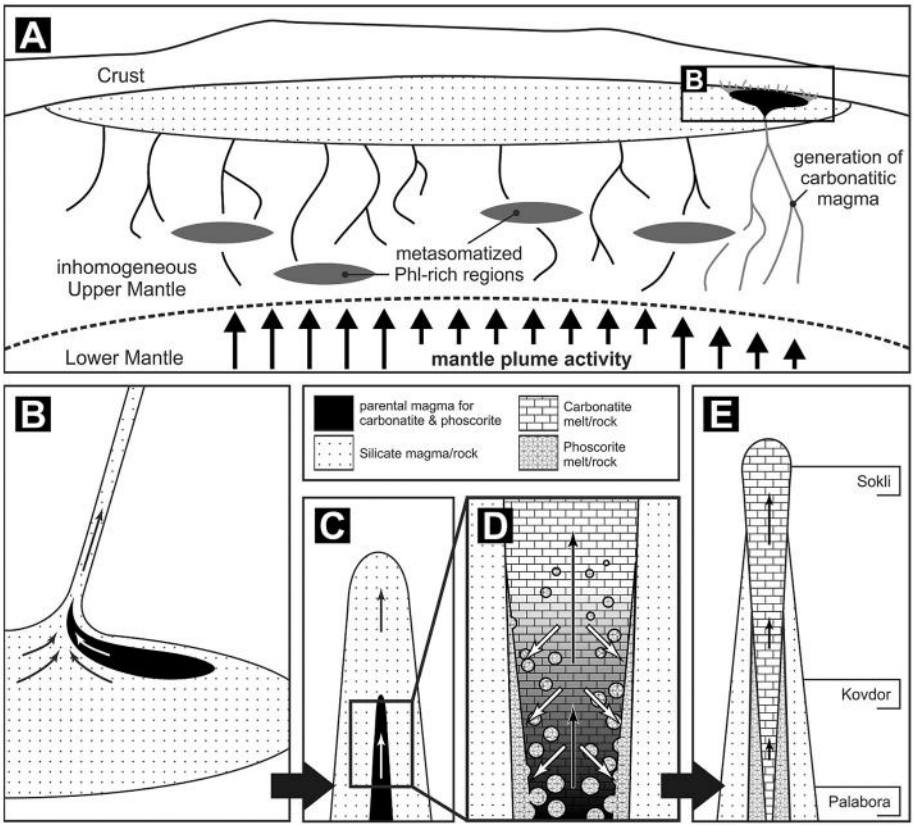

Fig. 12. Conceptual model for the formation of mixed carbonatite-phoscorite-silicate rock associations. (A) Generation of carbonate-rich magma (light grey) associated with silicate magma (dotted pattern) by mantle plume-derived partial melting. Enrichment of Fe and P in the carbonatitic magma may result in a carbonate-phosphate/iron-oxide-rich magma (CPIO; black). (B) According to the state of levitation the CPIO magma will be dragged into an ascending channel and will (C) ascend into the crust while silicate magma was already introduced. (D) Separation of immiscible phoscoritic and carbonatitic melt which causes a strong density difference between carbonatitic and silicate melt. (E) According to the rapid ascending of extreme viscose carbonatitic melt and occasionally ebbed activity of silicate melt, the carbonatitic melt passes through the ascending front of silicate melt und intrudes into higher levels forming insular carbonatite complexes. For details see text.

viscosity and higher solidus temperatures). This may explain some of the carbonatite complexes apparently lacking associated silicate rocks (20% of carbonatites show no silicate rock association; Woolley and Kjarsgaard, 2008; e.g., Sokli), as these would resemble cases with a very high source-emplacement-distance (ΔS-E) that reflect a very high carbonatite/silicate rock ratio and high carbonatite/phoscorite ratio. The latter is further supported by the lack of any extrusive phoscorites (Krasnova et al., 2004b). Geophysical investigations at Sokli (high ΔS-E, high C/SR ratio) furthermore suggest that foiditic rocks are present at much greater depth (Arzamastsev et al., 2000). On the other hand, mixed pyroxenite-carbonatite-phoscorite assemblages as being typical for e.g., Kovdor and Palabora may indicate relatively intermediate to short source-emplacement distances (Fig. 12E), in line with depth estimates of approximately 4 km and 15 km, respectively (Epshteyn and Kaban'kov, 1984; Eriksson, 1982). A final caveat: the appearance of carbonatite complexes is highly variable and the achievement of a certain evolutionary stage of our model may be limited by the formation of extensive magma chambers in the continental (cratonic) crust.

8. Conclusions

Our results have shown, that in the case of Palabora, the compositional variation of apatite is not helpful for reconstructing magmatic differentiation processes, which is in contrast to mica composition. Late-stage apatite textures and compositions, however, confirm the results of earlier assumptions, that additional REE where introduced by late-magmatic fluids (Giebel et al., 2017). The strong variation of mica composition in rocks of Palabora provides evidence for a multi-episodic crystallization history, characterized by the formation of (1) biotites in pyroxenites and fenites, (2) "common" phlogopites in BCB and FOS, (3) Ba-bearing phlogopites in TCB. (4) ^{IV}Al-rich phlogopites in BCB and FOS by interaction with TCB, and (5) the late-magmatic precipitation of tetraferriphlogopites by fluid interaction, where the availability of Al is a prominent factor controlling mica composition.

Analogous trends in the chemical composition and mutual evolution of mica in BCB and FOS argue for the existence of a common parental magma, which probably segregated into two immiscible melts. This emphasizes the potential importance of liquid immiscibility for generating phoscorites, with a carbonate-rich parental magma (developed within the upper lithospheric mantle) being essential to enable such processes. This in turn may explain the exclusive occurrence of phoscorite in association with carbonatite. Distinguished by their mica chemistry, the associated silicate rocks followed a completely separate evolution.

Our generalized model assumes that at deeper crustal levels, more proximal to the melt source, volumetrically higher proportions of ultramafic silicate rocks and lower proportions of carbonatitic rocks are present. Higher crustal levels (i. e., increasing distance to the source) show a volumetrically higher proportion of alkaline silicate rocks with an increasing percentage of carbonatitic rocks. Passing a distinct source-emplacement distance, the carbonatite proportion of a complex can exceed the silicate rock proportion of this complex. Furthermore, a relative volumetric increase of phoscorites with depth is supposed.

Acknowledgements

We thank Glen Taylor (Director of Research UFS) for providing funds for the visits in RSA as well as the stays at Phalaborwa and the DFG for

general funding of this project (MA 2563/10-1). This study was supported by the European Union's Horizon 2020 research and innovation program (grant agreement No 689909). The Department of Geology at the University of the Free State is acknowledged to continuously facilitate contact to PMC (operating company at Palabora) and for several discussions. Furthermore, we want to thank PMC (in particular Thabitha Moyana, Paulien Lourens, Hans-Dieter Paetzold, Pontsho Tyira, Nyiko Makhubele, Bongani Mabunda, Tshepang Molloane) for providing core material, technical assistance during our different sampling campaigns as well as discussions during our field work. Thomas Wenzel is gratefully acknowledged for his continuous support during the EMPA sessions in Tübingen. Eventually we want to thank two anonymous reviewers as well as Editor-in-Chief Nelson Eby for their attentive reviews which improve the manuscript.

Appendix A. Supplementary data

Supplementary data to this article can be found online at https://doi.org/10.1016/j.lithos.2018.10.030.

References

Aldous, R.T.H., 1980. Ore Genesis in Copper Bearing Carbonatites: A Geochemical, Fluid Inclusion and Mineralogical Study. Imperial College London. University of London, London, p. 365.

Araújo, D.P., 1996. Metassomatismo no complexo carbonatítico Catalão-I: implicações para a composição do magma carbonatítico e para o metassomatismo carbonatítico no manto superior. University of Brasilia, Brasilia, Brazil.

Arima, M., Edgar, A., 1981. Substitution mechanisms and solubility of titanium in phlogopites from rocks of probable mantle origin. Contrib. Mineral. Petrol. 77, 288–295.

Armstrong, J.T., 1988. Bence-Albee after 20 years: review of the accuracy of a-factor correction procedures for oxide and silicate minerals. Microbeam Analysis. Appl. Geol. 469–476.

Arzamastsev, A., Glaznev, V., Raevsky, A., Arzamastseva, L., 2000. Morphology and internal structure of the Kola Alkaline intrusions, NE Fennoscandian Shield: 3D density modelling and geological implications. J. Asian Earth Sci. 18, 213–228.

Bell, K., Simonetti, A., 2010. Source of parental melts to carbonatites–critical isotopic constraints. Mineral. Petrol. 98, 77–89.

Bence, A.E., Albee, A.L., 1968. Empirical correction factors for the electron microanalysis of silicates and oxides. J. Geol. 76, 382–403.

Braunger, S., Marks, M., Walter, B.F., Neubauer, R., Reich, R., Wenzel, T., Parsapoor, A., Markl, G., 2018. The Petrology of the Kaiserstuhl Volcanic complex, SW Germany: the Importance of Oxidized Lithosphere for Carbonatite Generation. J. Petrol. https://doi.org/10.1093/petrology/egy078.

Brigatti, M.F., Medici, L., Poppi, L., 1996a. Refinement of the structure of natural ferriphlogopite. Clay Clay Miner. 44, 540–545.

Brigatti, M.F., Medici, L., Saccani, E., Vaccaro, C., 1996b. Crystal chemistry and petrologic significance of Fe^{3+}-rich phlogopite from the Tapira carbonatite complex, Brazil. Am. Mineral. 81, 913–927.

Brod, J., Gaspar, J., De Araújo, D., Gibson, S., Thompson, R., Junqueira-Brod, T., 2001. Phlogopite and tetra-ferriphlogopite from Brazilian carbonatite complexes: petrogenetic constraints and implications for mineral-chemistry systematics. J. Asian Earth Sci. 19, 265–296.

Brooker, R., 1998. The effect of CO_2 saturation on immiscibility between silicate and carbonate liquids: an experimental study. J. Petrol. 39, 1905–1915.

Bühn, B., Rankin, A.H., 1999. Composition of natural, volatile-rich Na–Ca–REE— Sr carbonatitic fluids trapped in fluid inclusions. Geochim. Cosmochim. Acta 63, 3781–3797.

Chakhmouradian, A.R., Reguir, E.P., Zaitsev, A.N., Couëslan, C., Xu, C., Kynický, J., Mumin, A.H., Yang, P., 2017. Apatite in carbonatitic rocks: Compositional variation, zoning, element partitioning and petrogenetic significance. Lithos 274, 188–213.

Chen, W., Kamenetsky, V.S., Simonetti, A., 2013. Evidence for the alkaline nature of parental carbonatite melts at Oka complex in Canada. Nat. Commun. 4, 2687.

Clarke, L., Le Bas, M., Spiro, B., 1993. Rare Earth, Trace Element and Stable Isotope Fractionation of Carbonatites at Kruidfontein, Transvaal, South Africa, 5th International Kimberlite Conference: Extended Abstracts, Brazilia, Brazil. pp. 236–251.

Dalton, J.A., Presnall, D.C., 1998. The continuum of primary carbonatitic–kimberlitic melt compositions in equilibrium with lherzolite: data from the system CaO–MgO–Al_2O_3–SiO_2–CO_2 at 6 GPa. J. Petrol. 39, 1953–1964.

Dasgupta, R., Hirschmann, M.M., Smith, N.D., 2007. Partial melting experiments of peridotite + CO_2 at 3 GPa and genesis of alkalic ocean island basalts. J. Petrol. 48, 2093–2124.

Dawson, J.B., Hinton, R.W., 2003. Trace-element content and partitioning in calcite, dolomite and apatite in carbonatite, Phalaborwa, South Africa. Mineral. Mag. 67, 921–930.

Doroshkevich, A.G.e., Ripp, G., Viladkar, S., 2010. Newania carbonatites, Western India: example of mantle derived magnesium carbonatites. Mineral. Petrol. 98, 283–295.

Drake, M.J., Weill, D.F., 1972. New rare earth element standards for electron microprobe analysis. Chem. Geol. 10, 179–181.

Dymek, R.F., 1983. Titanium, aluminum and interlayer cation substitutions in biotite from high-grade gneisses, West Greenland. Am. Mineral. 68, 880–899.

Edgar, A., Arima, M., 1983. Conditions of phlogopite crystallization in ultrapotassic volcanic rocks. Mineral. Mag. 47, 11–19.

Edgar, A.D., Arima, M., 1985. Fluorine and chlorine contents of phlogopites crystallized from ultrapotassic rock compositions in high pressure experiments; implication for halogen reservoirs in source regions. Am. Mineral. 70, 529–536.

Epshteyn, Y.M., Kaban'kov, V.Y., 1984. The depth of emplacement and mineral potential of ultramafic, ijolite, and carbonatite plutons. Int. Geol. Rev. 26, 1402–1415.

Eriksson, S.C., 1982. Aspects of the Petrochemistry of the Phalaborwa Complex, Northeastern Transvaal, South Africa. University of the Witwatersrand, Johannesburg, p. 496.

Fleet, M.E., 2003. Sheet silicates: Micas. In: Deer, W.A., Howie, R.A., Zussman, J. (Eds.), Rock-Forming Minerals. Geological Society of London, p. 765.

Foster, M.D., 1960. Interpretation of the Composition of Trioctahedral Micas. U.S. Geological Survey Professional Paper, p. 49.

Fourie, P.J., De Jager, D.H., 1986. Phosphate in the Phalaborwa Complex. In: Anhaeusser, C.R., Maske, S. (Eds.), Mineral Deposits of Southern Africa. The Geological Society of South Africa, Johannesburg, pp. 2239–2253.

Frolov, A.A., 1971. Vertical zonations in deposition of ore as in ultrabasic-alkaline rocks and carbonatites. Int. Geol. Rev. 13, 685–695.

Frost, D.J., Wood, B.J., 1997. Experimental measurements of the fugacity of CO_2 and graphite/diamond stability from 35 to 77 kbar at 925 to 1650°C. Geochim. Cosmochim. Acta 61, 1565–1574.

Gaspar, J.C., Wyllie, P.J., 1987. The phlogopites from the Jacupiranga carbonatite intrusions. Mineral. Petrol. 36, 121–134.

Gellatly, D., 1966. Graphite in natural and experimental carbonate systems. Mineral. Mag. 35, 963–970.

Gibson, S., Thompson, R., Leonardos, O., Dickin, A., Mitchell, J., 1995. The Late Cretaceous impact of the Trindade mantle plume: evidence from large-volume, mafic, potassic magmatism in SE Brazil. J. Petrol. 36, 189–229.

Giebel, R.J., Gauert, C.D.K., Marks, M.A.W., Costin, G., Markl, G., 2017. Multi-Stage formation of REE Minerals in the Palabora Carbonatite complex, South Africa. Am. Mineral. 102 (6), 1218–1233.

Gittins, J., Harmer, R., 2001. The carbonatite-alkalic silicate igneous rock 'association': an unfortunate and misleading assumption. J. Afr. Earth Sci. (and the Middle East) 32, A16.

Gudfinnsson, G.H., Presnall, D.C., 2005. Continuous gradations among primary carbonatitic, kimberlitic, melilititic, basaltic, picritic, and komatiitic melts in equilibrium with garnet lherzolite at 3–8 GPa. J. Petrol. 46, 1645–1659.

Guzmics, T., Zajacz, Z., Kodolányi, J., Halter, W., Szabó, C., 2008. LA-ICP-MS study of apatite-and K feldspar-hosted primary carbonatite melt inclusions in clinopyroxenite xenoliths from lamprophyres, Hungary: Implications for significance of carbonatite melts in the Earth's mantle. Geochim. Cosmochim. Acta 72, 1864–1886.

Hanekom, H.J., van Staden, C.M.v.H., Smit, P.J., Pike, D.R., 1965. The geology of the Palabora igneous complex. S. Afr. Geol. Surv. Handb. 54, 185 Memoir.

Harmer, R., Gittins, J., 1998. The case for primary, mantle-derived carbonatite magma. J. Petrol. 39, 1895–1903.

Heathcote, R.C., McCormick, G.R., 1989. Major-cation substitution in phlogopite and evolution of carbonatite in the Potash Sulphur Springs complex, Garland County, Arkansas. Am. Mineral. 74, 132–140.

Hogarth, D., 1989. Pyrocholre, apatite and amphibole: distinctive minerals in carbonatite. In: Bell, K. (Ed.), Carbonatites: Genesis and Evolution. Unwin Hyman, London, pp. 105–148.

Hou, T., Charlier, B., Namur, O., Schütte, P., Schwarz-Schampera, U., Zhang, Z., Holtz, F., 2017. Experimental study of liquid immiscibility in the Kiruna-type Vergenoeg iron–fluorine deposit, South Africa. Geochim. Cosmochim. Acta 203, 303–322.

Hou, T., Charlier, B., Holtz, F., Veksler, I., Zhang, Z., Thomas, R., Namur, O., 2018. Immiscible hydrous Fe–Ca–P melt and the origin of iron oxide-apatite ore deposits. Nat. Commun. 9, 1415.

Huang, Y.-M., Hawkesworth, C., Van Calsteren, P., McDermott, F., 1995. Geochemical characteristics and origin of the Jacupiranga carbonatites, Brazil. Chem. Geol. 119, 79–99.

Huizenga, J.-M., 2011. Thermodynamic modelling of a cooling C–O–H fluid–graphite system: implications for hydrothermal graphite precipitation. Mineral. Deposita 46, 23–33.

Jones, J.H., Walker, D., Pickett, D.A., Murrell, M.T., Beattie, P., 1995. Experimental investigations of the partitioning of Nb, Mo, Ba, Ce, Pb, Ra, Th, Pa, and U between immiscible carbonate and silicate liquids. Geochim. Cosmochim. Acta 59, 1307–1320.

Klemme, S., Dalpé, C., 2003. Trace-element partitioning between apatite and carbonatite melt. Am. Mineral. 88, 639–646.

Kogarko, L., Suddaby, P., Watkins, P., 1997. Geochemical evolution of carbonatite melts in Polar Siberia. Geochem. Int. 35, 113–118.

Kogarko, L., Ryabchikov, I., Divaev, F., Wall, F., 2010. Regime of carbon compounds in carbonatites in Uzbekistan: evidence from carbon isotopic composition and thermodynamic simulations. Geochem. Int. 48, 1055–1063.

Kogarko, L.N., Ryabchikov, I.D., Kuzmin, D.V., 2012. High-Ba mica in olivinites of the Guli massif (Maimecha–Kotui province, Siberia). Russ. Geol. Geophys. 53, 1209–1215.

Krasnova, N., Balaganskaya, E., Garcia, D., 2004a. Kovdor - classic phoscorites and carbonatites. In: Wall, F., Zaitev, A.N. (Eds.), Phoscorites and Carbonatites from Mantle to Mine: the Key Example of the Kola Alkaline Province. Mineralogical Society of Great Britain and Ireland, London, GB, pp. 99–132.

Krasnova, N., Petrov, T., Balaganskaya, E., Garcia, D., Moutte, J., Zaitsev, A., Wall, F., 2004b. Introduction to phoscorites: occurrence, composition, nomenclature and petrogenesis. In: Wall, F., Zaitev, A.N. (Eds.), Phoscorites and Carbonatites from Mantle to Mine: the Key Example of the Kola Alkaline Province. The Mineralogical Society of Great Britain and Ireland, London, GB, pp. 45–74.

Lapin, A., Vartiainen, H., 1983. Orbicular and spherulitic carbonatites from Sokli and Vuorijärvi. Lithos 16, 53–60.
Lee, M.J., Garcia, D., Moutte, J., Lee, J.I., 2003. Phlogopite and tetraferriphlogopite from phoscorite and carbonatite associations in the Sokli massif, Northern Finland. Geosci. J. 7, 9–20.
Lee, M.J., Lee, J.I., Garcia, D., Moutte, J., Williams, C.T., Wall, F., Kim, Y., 2006. Pyrochlore chemistry from the Sokli phoscorite-carbonatite complex, Finland: implications for the genesis of phoscorite and carbonatite association. Geochem. J. 40, 1–13.
Lee, W.-j., Wyllie, P.J., 1997. Liquid immiscibility between nephelinite and carbonatite from 1.0 to 2.5 GPa compared with mantle melt compositions. Contrib. Mineral. Petrol. 127, 1–16.
Lee, W.-J., Wyllie, P.J., 1998. Petrogenesis of carbonatite magmas from mantle to crust, constrained by the system CaO-(MgO+FeO*)-(Na_2O+K_2O)-(SiO_2+Al_2O_3+TiO_2)-CO_2. J. Petrol. 39, 495–517.
Lindsley, D.H., Epler, N., 2017. Do Fe–Ti oxide magmas exist? Probably not! Am. Mineral. 102, 2157–2169.
Lombaard, A.F., Ward-Able, N.M., Bruce, R.W., 1964. The exploration and main geological features of the copper deposit in carbonatite at Loolekop, Palabora complex. In: Haughton, S.H. (Ed.), The Geology of some Ore Deposits in Southern Africa. Geological Society of South Africa, Johannesburg, pp. 315–337.
McCormick, G.R., Heathcote, R.C., 1987. Mineral chemistry and petrogenesis of carbonatite intrusions, Perry and Conway Counties, Arkansas. Am. Mineral. 72.
McCormick, G.R., Le Bas, M.J., 1996. Phlogopite crystallization in carbonatitic magmas from Uganda. Can. Mineral. 34, 469–478.
Mikhailova, Y.A., Krasnova, N., Kretser, Y.L., Wall, F., Pakhomovsky, Y.A., 2002. Inclusions in minerals of the Kovdor intrusion of ultrabasic, alkaline rocks and carbonatites as indicators of the endogenic evolution processes. In: Vladykin, N.V. (Ed.), Deep-seated Magmatism, Magmatic Sources and the Problem of Plumes. Siberian Branch of the Russian Academy of Sciences, Irkutsk–Vladivostok, Russia, pp. 296–320.
Milani, L., Bolhar, R., Frei, D., Harlov, D.E., Samuel, V.O., 2017. Light rare earth element systematics as a tool for investigating the petrogenesis of phoscorite-carbonatite associations, as exemplified by the Phalaborwa Complex, South Africa. Mineral. Deposita 1–21.
Mitchell, R.H., Bergman, S.C., 1991. Petrology of Lamproites. Springer Science & Business Media.
Naslund, H., 1983. The effect of oxygen fugacity on liquid immiscibility in iron-bearing silicate melts. Am. J. Sci. 283, 1034–1059.
Natali, C., Beccaluva, L., Bianchini, G., Siena, F., 2018. Coexistence of alkaline-carbonatite complexes and high-MgO CFB in the Paranà-Etendeka province: Insights on plume-lithosphere interactions in the Gondwana realm. Lithos 296-299, 54–66.
Palabora Mining Company, L.a.G.a.M.S., 1976. The geology and economic deposits of copper, iron and vermiculite in the Palabora Igneous complex: a brief review. Econ. Geol. 71, 177–192.
Puustinen, K., 1973. Tetraferriphlogopite from the Siilinjärvi carbonatite complex, Finland. Bull. Geol. Soc. Finl. 45, 35–42.
Reguir, E., Chakhmouradian, A., Halden, N., Malkovets, V., Yang, P., 2009. Major-andtrace-element compositional variation of phlogopite from kimberlites and carbonatites as a petrogenetic indicator. Lithos 112, 372–384.
Rimskaya-Korsakova, O., Krasnova, N., 2002. Geology of the Deposits of Kovdor Massif. St. Petersburg State University, St. Petersburg, Russia.
Rimskaya-Korsakova, O., Sokolova, E., 1964. About the iron-magnesium micas with the reverse scheme of absorption. Zapiski Vsesoyuznogo Mineralogicheskogo Obshchestva 93, 411–423.
Seifert, W., Kämpf, H., Wasternack, J., 2000. Compositional variation in apatite, phlogopite and other accessory minerals of the ultramafic Delitzsch complex, Germany: implication for cooling history of carbonatites. Lithos 53, 81–100.
Suwa, K., Aoki, K., 1975. Reverse Pleochroism of Phlogopites in Kimberlites and their Related Rocks from South Africa. 1st Prelim. Rept. African Studies. Nagoya University, pp. 60–64.
Sweeney, R.J., 1994. Carbonatite melt compositions in the Earth's mantle. Earth Planet. Sci. Lett. 128, 259–270.
Teiber, H., Marks, M.A., Arzamastsev, A.A., Wenzel, T., Markl, G., 2015. Compositional variation in apatite from various host rocks: clues with regards to source composition and crystallization conditions. Neues Jahrbuch für Mineralogie-Abhandlungen: Journal of Mineralogy and Geochemistry 192, 151–167.
Treiman, A.H., Schedl, A., 1983. Properties of carbonatite magma and processes in carbonatite magma chambers. The Journal of Geology 91, 437–447.
Tronnes, R., Edgar, A., Arima, M., 1985. A high pressure-high temperature study of TiO_2 solubility in Mg-rich phlogopite: implications to phlogopite chemistry. Geochim. Cosmochim. Acta 49, 2323–2329.
Veksler, I., Nielsen, T., Sokolov, S., 1998a. Mineralogy of crystallized melt inclusions from Gardiner and Kovdor ultramafic alkaline complexes: implications for carbonatite genesis. J. Petrol. 39, 2015–2031.
Veksler, I., Petibon, C., Jenner, G., Dorfman, A., Dingwell, D., 1998b. Trace element partitioning in immiscible silicate–carbonate liquid systems: an initial experimental study using a centrifuge autoclave. J. Petrol. 39, 2095–2104.
Veksler, I.V., Keppler, H., 2000. Partitioning of Mg, Ca, and Na between carbonatite melt and hydrous fluid at 0.1–0.2 GPa. Contrib. Mineral. Petrol. 138, 27–34.
Verwoerd, W.J., 1966. South African carbonatites and their probable mode of origin. Annals of the University of Stellenbosch, 41(A2). Stellenbosch University, Stellenbosch.
Wilson, M.G.C., 1998. Copper. In: Wilson, M.G.C., Anhaeusser, C.R. (Eds.), The Mineral Resources of South Africa. Council for Geoscience, Pretoria, pp. 209–217.
Wones, D.R., Eugster, H.P., 1965. Stability of biotite: experiments, theory, and application. Am. Mineral. 50, 1228–1272.
Woolley, A.R., Kjarsgaard, B.A., 2008. Carbonatite Occurrences of the World: Map and Database. Geological Survey of Canada.
Wu, F.-Y., Yang, Y.-H., Li, Q.-L., Mitchell, R.H., Dawson, J.B., Brandl, G., Yuhara, M., 2011. In situ determination of U–Pb ages and Sr–Nd–Hf isotopic constraints on the petrogenesis of the Phalaborwa carbonatite complex, South Africa. Lithos 127, 309–322.
Wyllie, P.J., Lee, W.-J., 1998. Model system controls on conditions for formation of magnesiocarbonatite and calciocarbonatite magmas from the mantle. J. Petrol. 39, 1885–1893.
Zaitsev, A.N., Bell, K., 1995. Sr and Nd isotope data of apatite, calcite and dolomite as indicators of source, and the relationships of phoscorites and carbonatites from the Kovdor massif, Kola peninsula, Russia. Contrib. Mineral. Petrol. 121, 324–335.
Zaitsev, A.N., Kamenetsky, V., 2013. Magnetite-Hosted Melt Inclusions from Phoscorites and Carbonatites (Kovdor, Kola): Ahydrous Analog of Oldoinyo Lengai Natrocarbonatites?, Goldschmidt. Florence, Italy, p. 2576.

Appendix III

Accepted publication

Study C

Giebel, R.J., Parsapoor, A., Walter, B.F., Braunger, S., Marks, M.A.W., Wenzel, T. and Markl, G. (2019b): Evidence for magma – wall rock interaction in carbonatites from the Kaiserstuhl Volcanic Complex (Southwest Germany). *Journal of Petrology.*

JOURNAL OF PETROLOGY

Journal of Petrology, 2019, 1–31
doi: 10.1093/petrology/egz028
Advance Access Publication Date: 14 May 2019
Original Article

OXFORD

Evidence for Magma–Wall Rock Interaction in Carbonatites from the Kaiserstuhl Volcanic Complex (Southwest Germany)

R. J. Giebel [1,2,*], A. Parsapoor[1,†], B. F. Walter[1,3], S. Braunger[1], M. A. W. Marks[1], T. Wenzel[1] and G. Markl[1]

[1]Department of Geosciences, Eberhard Karls Universität Tübingen, Wilhelmstr. 56, 72074 Tübingen, Germany; [2]Department of Geology, University of the Free State, 250 Nelson-Mandela-Drive, Bloemfontein 9300, South Africa; [3]Institute for Applied Geosciences, Karlsruhe Institute of Technology, Adenauerring 20b, Karlsruhe 76131, Germany

*Corresponding author. Department of Geosciences, Eberhard Karls Universität Tübingen, Wilhelmstr. 56, 72074 Tübingen, Germany. Telephone: +49-(0)7071-29-73155. Fax: +49-(0)7071-29-3060. E-mail: r.j.giebel@gmx.de
[†]Joint first authorship.

Received June 6, 2018; and in revised form April 27, 2019; Accepted May 3, 2019

ABSTRACT

The mineralogy and mineral chemistry of the four major sövite bodies (Badberg, Degenmatt, Haselschacher Buck and Orberg), calcite foidolite/nosean syenite xenoliths (enclosed in the Badberg sövite only) and rare extrusive carbonatites of the Kaiserstuhl Volcanic Complex in Southern Germany provide evidence for contamination processes in the carbonatitic magma system of the Kaiserstuhl. Based on textures and composition, garnet and clinopyroxene in extrusive carbonatites represent xenocrysts entrained from the associated silicate rocks. In contrast, forsterite, monticellite and mica in sövites from Degenmatt, Haselschacher Buck and Orberg probably crystallized from the carbonatitic magma. Clinopyroxene and abundant mica crystallization in the Badberg sövite, however, was induced by the interaction between calcite foidolite xenoliths and the carbonatite melt. Apatite and micas in the various sövite bodies reveal clear compositional differences: apatite from Badberg is higher in REE, Si and Sr than apatite from the other sövite bodies. Mica from Badberg is biotite- and comparatively Fe^{2+}-rich (Mg# = 72–88). Mica from the other sövites, however, is phlogopite (Mg# up to 97), as is typical of carbonatites in general. The typical enrichment of Ba due to the kinoshitalite substitution is observed in all sövites, although it is subordinate in the Badberg samples. Instead, Badberg biotites are strongly enriched in ^{IV}Al (eastonite substitution) which is less important in the other sövites. The compositional variations of apatite and mica within and between the different sövite bodies reflect the combined effects of fractional crystallization and carbonatite-wall rock interaction during emplacement. The latter process is especially important for the Badberg sövites, where metasomatic interaction released significant amounts of K, Fe, Ti, Al and Si from earlier crystallized nosean syenites. This resulted in a number of mineral reactions that transformed these rocks into calcite foidolites. Moreover, this triggered the crystallization of compositionally distinct mica and clinopyroxene crystals around the xenoliths and within the Badberg sövite itself. Thus, the presence and composition of clinopyroxene and mica in carbonatites may be useful indicators for contamination processes during their emplacement. Moreover, the local increase of silica activity during contamination enabled strong REE enrichment in apatite via a coupled substitution involving Si, which demonstrates the influence of contamination on REE mineralization in carbonatites.

Key words: contamination; carbonatite; Kaiserstuhl; mineral chemistry; calcite foidolite; REE mineralization; silicates in carbonatites

INTRODUCTION

Carbonatites are mantle-derived magmatic rocks with more than 30% primary igneous carbonate minerals (Mitchell, 2005; Woolley & Kjarsgaard, 2008). In most of the ~ 550 known occurrences they form intrusive bodies (e.g. plugs, pipes, dykes, sills), whereas extrusive equivalents, such as lavas and tuffs are notably scarce, with only about 50 known occurrences (Woolley & Church, 2005). Depending on their predominant carbonate mineral, carbonatites are subdivided into calcite- (sövites and alvikites), dolomite- (beforsites), ferro- and natro-carbonatites (Le Maitre *et al.*, 2002). Calcite is the most common magmatic carbonate (sometimes with exsolution of dolomite), magmatic dolomite and ankerite are less common and other carbonates (e.g. strontianite, barytocalcite) and REE-carbonates (e.g. burbankite, bastnäsite) are generally minor constituents (e.g. Zaitsev *et al.*, 1998; Moore *et al.*, 2015; Giebel *et al.*, 2017).

In addition to carbonate minerals, most carbonatites contain variable amounts of apatite, magnetite (spinel group minerals) and phlogopite and a number of additional silicate minerals (e.g. forsterite, monticellite, melilite, clinopyroxene, amphibole, garnet, feldspathoids, alkali feldspar) have been reported, although it may be difficult to distinguish primary carbonatitic crystals from xenocrysts (e.g. Andersen, 1988; Hogarth, 1989; Barker, 2001; Brod *et al.*, 2001; Chakrabarty *et al.*, 2009; Reguir *et al.*, 2012; Chakhmouradian *et al.*, 2017). In addition, various sulfides (pyrrhotite, pyrite, chalcopyrite, galena, sphalerite) and HFSE- and REE-rich minerals (e.g. baddeleyite/zircon, perovskite/titanite, pyrochlore, zirconolite, calzirtite) are typically present (e.g. Chakhmouradian, 2006; Farrell *et al.*, 2010; Gomide *et al.*, 2013; Bell *et al.*, 2015). Due to the high abundance of apatite and some of the above-mentioned REE- and HFSE-rich minerals, carbonatites are of general economic interest and several occurrences are currently mined (e.g. Araxa, Bayan Obo, Catalao, Kovdor, Mount Weld, Niobec; Gendron *et al.*, 1984; de Oliveira & Imbernon, 1998; Ivanyuk et al., 2002; Krasnova *et al.*, 2004; Kanazawa & Kamitani, 2006; Yang *et al.*, 2011; Neumann & Medeiros, 2015).

Contamination by crustal or cogenetic intrusive rocks is generally not considered to play an important role during carbonatite magmatism, because carbonatitic melts have low densities and extremely low viscosities, enabling them to ascend rapidly (Treiman & Schedl, 1983; Jones *et al.*, 2013 and references therein). High-silica carbonatitic rocks in alkaline silicate–carbonatite complexes, which probably preserve the evidence of contamination of the parental magma, have often been ignored in previous studies, although there is evidence for the interaction between carbonatites and silicate rocks (Andrade *et al.*, 1999). However, potential contamination by silicate rocks in carbonatites cannot easily be detected by means of radiogenic isotope data (such as Sr, Nd and Pb isotope data) as carbonatites often have high concentrations of these elements and their isotope systems are thereby 'buffered' against contamination with silicate rocks, which normally have much lower concentrations of these elements (e.g. Bell & Tilton, 2002 and references therein). The composition of silicate minerals in carbonatites and their comparison with country rocks, mantle rocks and associated ultramafic cumulates and alkaline rocks, however, may allow for their identification as true primary carbonatitic crystals or xenocrysts, but such studies are very rare (e.g. Vuorinen & Skelton, 2004).

Carbonatites from the Kaiserstuhl Volcanic Complex (South Germany) have been investigated previously (e.g. Keller, 1981; Hay & O'Neil, 1983, Hubberten *et al.*, 1988; Wimmenauer, 2003; Wang *et al.*, 2014; Teiber *et al.*, 2015; Braunger *et al.*, 2018; Walter *et al.*, 2018) but no systematic study of their mineralogy and mineral chemistry is available to date. We provide a comprehensive data set for the mineralogical inventory and the compositional variations of the major minerals in sövites and extrusive carbonatites, namely calcite, apatite, spinel group minerals (magnetite-magnesioferrite) and silicate minerals (mica, forsterite, monticellite, clinopyroxene, garnet). Based on the compositional variation of these phases, we tested the suitability of apatite and mica to assess the extent of carbonatite–wall rock interaction (contamination) in one of the sövite bodies of the Kaiserstuhl Volcanic Complex.

GEOLOCICAL SETTING AND OCCURENCE OF CARBONATITES IN THE KAISERSTUHL

The Kaiserstuhl Volcanic Complex (KVC) is situated in the Upper Rhine Graben (Fig. 1a), which is part of a larger extensional zone throughout central Europe that was established in a stress regime caused by Alpine orogenic processes in Tertiary times (e.g., Ziegler, 1982; Wilson & Downes, 1991). The emplacement of the KVC rocks along deep-reaching zones of weakness was enabled by lithospheric thinning (Hüttner, 1996; Edel *et al.*, 2006; Bourgeois *et al.*, 2007). The Upper Rhine Graben is characterized by numerous listric and mostly steep fault sets that are partly subparallel to the graben geometry. These faults and associated structures cause a horst and graben structure and a complex system of variably sized tectonic blocks (e.g. Beccaletto *et al.*, 2010).

The rocks of the KVC are of Miocene age (18–15 Ma; e.g. Kraml *et al.*, 2006 and references therein) and mainly consist of a tephritic to phonolitic rock series, accompanied by minor nephelinitic to limburgitic, and melilititic to haüynitic lithologies and carbonatites (e.g. Baranyi *et al.*, 1976; Keller *et al.*, 1990; Wimmenauer, 2003; Braunger *et al.*, 2018). The KVC rocks probably derive from several magma sources, with carbonatites being genetically related to the melilititic to haüynitic rocks (e.g. Schleicher *et al.*, 1990; Wang *et al.*, 2014).

The four major sövite bodies (Badberg, Degenmatt, Haselschacher Buck, Orberg) are spatially associated

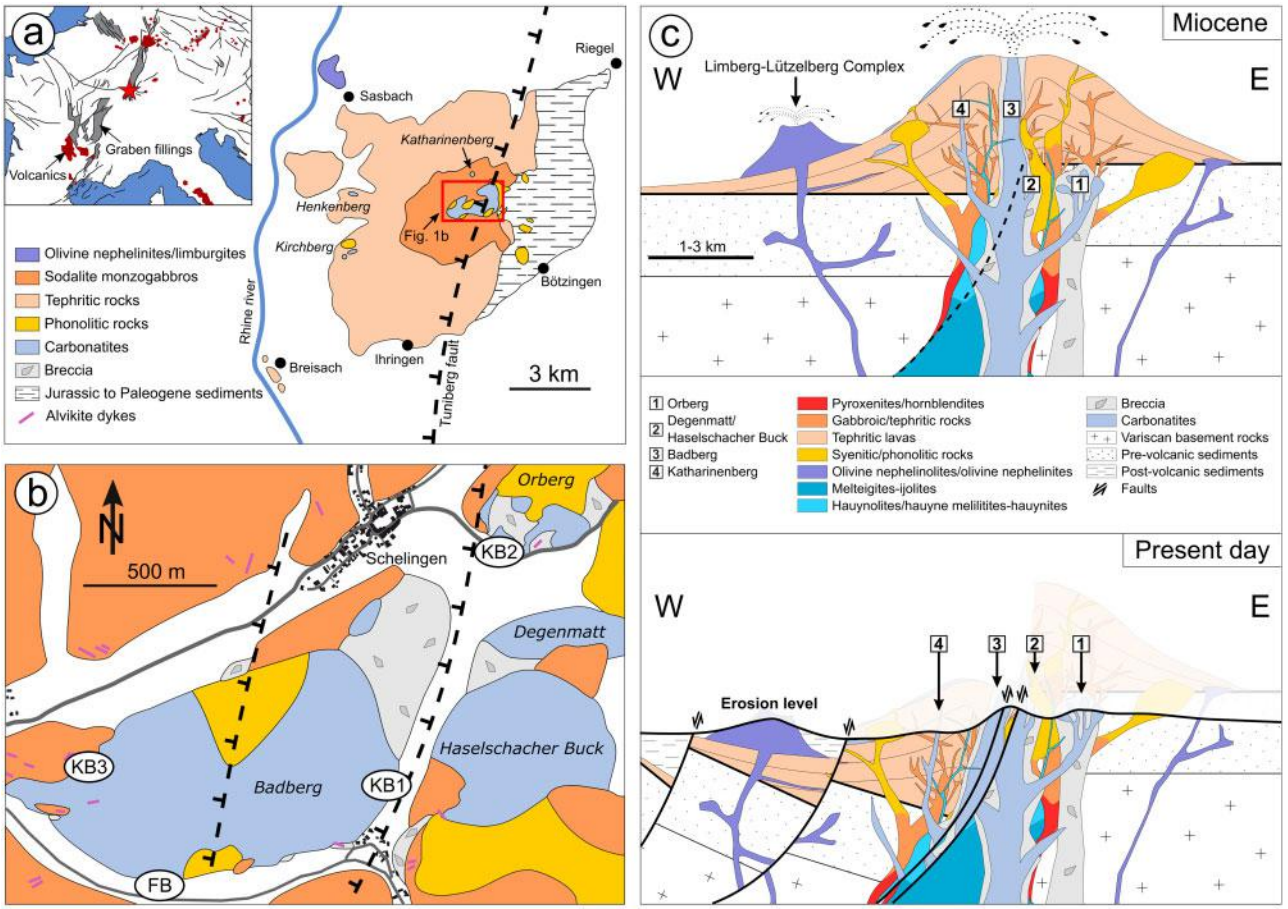

Fig. 1. Geology of the Kaiserstuhl Volcanic Complex (KVC). (a) Simplified geological map of the KVC (modified after Keller *et al.*, 1990) including an overview map of the European Cenozoic Volcanic Province (modified after Dèzes *et al.*, 2004), where the position of the KVC is indicated by a red star. (b) Detailed geological map of the central part of the KVC, which depicts several sövite bodies and the location of the four historic drill holes KB1, KB2, KB3 and FB. The schematic fault system is represented by a duplication of the Tuniberg normal fault. (c) Schematic cross section of the structural development of the carbonatites at the KVC.

with polygenetic breccias in the central area of the KVC and two small sövite occurrences (<10 m in diameter) are exposed at Katharinenberg and Kirchberg (Fig. 1a). The KVC is intersected by the regional Tuniberg Fault (Fig. 1), which causes a vertical displacement of ~1000 m north and ~3000 m south of the KVC, with a westwards down-throw towards the Rhine graben centre (Groschopf *et al.*, 1996; Beccaletto *et al.*, 2010). Geophysical evidence (seismic surveys; e.g. Brauch *et al.*, 2018 and references therein) suggests at least one sub-parallel structure further W that intersects the Badberg sövite body (Fig. 1b), but the vertical displacement of this structure is unknown.

The about 400 m thick, pipe-like Badberg body is banded and inclined at about 60° towards the northwest. It intrudes sodalite monzogabbros and phonolites and is partly underlain by foid syenites and phonolites as indicated by the scientific KB3 and FB drillings (Kirchheimer, 1973; Blust, 1993). Mineral banding in the sövite is subparallel to its contacts towards the country rocks and numerous cm- to m-sized rafts of calcite foidolites occur aligned parallel to the banding. The relative abundance of these xenoliths decreases from the top of the tilted Badberg body towards its deeper parts. The sövite bodies at Degenmatt and Haselschacher Buck probably reflect similar pipe-like geometries but are not exposed well enough to constrain this. However, geophysical data (gravimetric and magnetic) indicate a continuous pipe-like body below the Degenmatt/Haselschacher Buck bodies, whereas there is no evidence that the Badberg body continues to greater depth (Brauch *et al.*, 2018).

Sövites at Orberg are exposed in five quarries (designated as I–V) and display variable geometries. Sövite sills dipping by 25° towards the northeast are exposed in quarries I and II, quarry III exposes a 10 m thick sheet-like body with a dip of 70° towards the northwest , and quarries IV and V show irregular geometries implying a cauliflower-like structure. The emplacement of the Orberg sövites was probably promoted by distinct zones of weakness, reflected by pre-existing polygenic breccias (proved by KB2 scientific drilling in 1991 in quarry II; Hubaux, 1964).

Dolomite-bearing alvikites (still calcite-dominated, though) occur as fine- to medium-grained subvertical dykes, crosscutting all rock types and rare dolomite-

dominated varieties (beforsites) are known (e.g. Van Wambeke, 1964; Sigmund, 1996). Alvikites show variable thicknesses (cm- to m scale) and textures. They have been described in great detail previously (e.g. Katz & Keller, 1981; Sommerauer & Katz-Lehnert, 1985; Katz-Lehnert, 1989) and are not subject to the present study.

At Henkenberg and Kirchberg (Fig. 1a), three layers (each 1 to 1·5 m thick) of extrusive carbonatite, represented as alternating sequences of carbonatitic crystal tuff, lapillistones and lavas and interbedded with tephritic and basanitic pyroclastics, are preserved (Keller, 1978; Keller, 1981, Keller, 1989; Woolley & Kjarsgaard, 2008). The distance between these two localities is about 1·5 km, but the original extent of these deposits is unknown, due to intense anthropogenic land transformations in the 1970s.

SAMPLE MATERIAL AND ANALYTICAL METHODS

The material investigated for this study is part of the sample set (N ≈ 400) of Walter *et al.* (2018) and includes 46 carefully selected samples from surface outcrops and from the scientific KB2 and KB3 drillings, covering the major sövite bodies and the two known occurrences of extrusive carbonatites in the KVC. A complete sample list is given in Table 1, along with locations, GPS coordinates and petrographic details.

Mineral compositions were acquired using a JEOL 8900 electron microprobe at the Institute of Geosciences, Universität Tübingen, Germany. Acceleration voltage was 15 kV (for apatite, phlogopite, clinopyroxene and carbonate) and 20 kV (for garnet and spinel group minerals) using a beam current of 10 nA (for apatite) and 20 nA (for other minerals). Depending on the mineral, the beam diameters varied from a focused beam (for olivine, spinel group minerals, pyroxene and zirconolite), 2 μm (mica), 5 μm (carbonates and garnet) to 10 μm (apatite). Natural and synthetic standards were used for calibration (see ES1, Supplementary Data; supplementary data are available for downloading at http://www.petrology.oxfordjournals.org). Data reduction was performed using the internal ZAF and φρz matrix correction software of JEOL (Armstrong, 1991). Details on the WDS configuration used and typical detection limits for the individual elements of various minerals are given in the Supplementary Data; supplementary data are available for downloading at http://www.petrology.oxfordjournals.org (ES1).

PETROGRAPHY

Sövites

Besides calcite, the most abundant minerals in the different sövites are apatite, mica, spinel group minerals and pyrochlore, with highly variable modal amounts (Table 1; Fig. 2) on a dm- to m-scale. Occasionally, mineral banding represented by alternating coarse-grained and finer grained layers of non-carbonate minerals occurs in some areas. Rarely, thin olivine-rich layers (Orberg) and in one case, a perovskite-rich layer (Badberg, see below) have been exposed. However, the major mineralogical differences between the sövite bodies are reflected by the presence/absence of clinopyroxene, olivine and monticellite.

Olivine is present in two samples from Haselschacher Buck and Katharinenberg and occurs as up to 500 μm large euhedral to subhedral grains, which are often serpentinized along cracks and grain boundaries and are occasionally replaced by calcite (Fig. 3a). Subhedral to anhedral monticellite occurs in one sample from Orberg V (Fig. 3b).

Apatite is the most abundant non-carbonate mineral and occurs in all investigated sövites. Textures range from large radial crystal aggregates (Fig. 3c), medium-sized prismatic grains to anhedral patches mostly enclosed by calcite and less commonly by phlogopite and spinel group minerals. Most apatites show variable zoning patterns, ranging from oscillatory zonation (Fig. 3d; with occasional resorbed cores) to patchy zonation.

Clinopyroxene was only observed in some of the Badberg samples, where it is mostly euhedral but typically cracked and altered along cleavages. In some cases it shows rounded grain boundaries towards calcite (Fig. 3e).

The abundance and general appearance of mica (Figs 3e and 4) differs between samples from Badberg (commonly very mica-rich) and the other localities (generally mica-poor). With the exception of the Badberg samples, mica occurs as <2 mm large euhedral to subhedral laths to stubby grains, mostly enclosed by calcite (Fig. 4a). It is almost colourless under plane-polarized light and is occasionally altered to chlorite. Mica from Orberg III and Katharinenberg is typically oscillatory zoned (Fig. 4b), while mica from the Degenmatt samples is less so, and mica from other localities lacks any visible zonation. Mica from the Badberg samples is much larger (up to 2 cm), exhibiting an olive-green to khaki appearance under plane-polarized light. Two different modes of occurrence in the Badberg samples are distinguished: (1) blocky crystals accumulated at the contact towards the calcite foidolites (Fig. 4c; see below) are classified as 'black-wall mica', whereas (2) bundles of large mica laths occur dispersed in the Badberg samples and are seemingly independent of the presence of calcite foidolite relicts (Fig. 4d).

Spinel group minerals are very common and generally occur as several mm-sized disseminated subhedral to euhedral grains (occasionally very porous; Fig. 3f). They are mostly enclosed by calcite and occasionally contain inclusions of apatite. In very few samples, however, they are overgrown by apatite. Abundant pyrochlore (see details in Walter *et al.*, 2018) and rare zirconolite (Van Wambeke, 1964; Sinclair & Eggleton, 1982; Keller, 1984) crystallized more or less simultaneously with spinel group minerals. Zirconolite was only found in a sample from Haselschacher Buck, where it

Table 1: List of samples investigated in this study along with their major mineralogy

Locality	Rock type	Sample #	Depth	UTM coordinates	Ap	Phl	Mgt	Pcl	Cpx	Grt	Ol/ Mtc	Cal	Dol
Badberg	Calcite foidolite	HTAC 260	Surface	32 U 401310 5327748	x	x	–	(tr)	X*	X	–	x	–
Badberg	Sövite	HTAC 1136	KB3 (267 m)	32 U 400940 5327843	X	X	X*	–	X*	–	–	X	–
Badberg	Calcite foidolite	HTAC 1139	KB3 (254 m)	32 U 400940 5327843	x*	x	–	–	X	X*	–	x	–
Badberg	Calcite foidolite	HTAC 1147	KB3 (241 m)	33 U 400940 5327844	x*	x	–	–	X	X*	–	x	–
Badberg	Calcite foidolite	HTAC 1148	KB3 (240 m)	32 U 400940 5327843	x	x*	–	(tr)	X	X	–	x	–
Badberg	Sövite	HTAC 1151	KB3 (227m)	32 U 400940 5327843	X	X	x	x	x*	–	–	X*	–
Badberg	Sövite	HTAC 1156	KB3 (215 m)	32 U 400940 5327843	X	X*	x	x	–	–	–	X	–
Badberg	Calcite foidolite	HTAC 1158	KB3 (204 m)	32 U 400940 5327843	x	X	–	(tr)	X	X*	–	X	–
Badberg	Calcite foidolite	HTAC 1168	KB3 (177 m)	32 U 400940 5327843	x	x	–	(tr)	X	X*	–	x	–
Badberg	Calcite foidolite	HTAC 1173	KB3 (165 m)	32 U 400940 5327843	x	X	x	–	X	X*	–	x	–
Badberg	Calcite foidolite	HTAC 1178	KB3 (150 m)	32 U 400940 5327843	x*	–	–	(tr)	X*	X	–	X	–
Badberg	Calcite foidolite	HTAC 1197	KB3 (100 m)	32 U 400940 5327843	x	x	–	(tr)	X*	X	–	x	–
Badberg	Sövite	HTAC 1200	KB3 (93m)	32 U 400940 5327843	X	X*	x	(tr)	–	–	–	X	–
Badberg	Calcite foidolite	HTAC 1200	KB3 (93 m)	32 U 400940 5327843	x	X*	x	–	X	X*	–	x	–
Badberg	Sövite	HTAC 1215	KB3 (35 m)	32 U 400940 5327843	X	x	X	x	x*	–	–	X	–
Badberg	Sövite	HTAC 1229	KB3 (-10 m)	32 U 400940 5327843	X*	X	X	x	X*	–	–	X*	–
Badberg	Sövite	HTAC 1237	KB3 (-48 m)	32 U 400940 5327843	X	X*	X	(tr)	x*	–	–	X*	–
Badberg	Sövite	HTAC 1245	KB3 (-66 m)	32 U 400940 5327843	x	X*	X	(tr)	x	–	–	X	–
Badberg	Sövite	HTAC 1362	Surface	32 U 400763 5327907	X	x	X	(tr)	x	–	–	X*	–
Orberg II	Sövite	HTAC 1253	KB2 (4 m)	32 U 402477 5328680	x*	x	X	x	–	–	–	X*	x
Orberg II	Sövite	HTAC 1267	KB2 (271 m)	32 U 402477 5328680	x	x	x	–	–	–	–	X*	x
Orberg II	Sövite	HTAC 1318	KB2 (191.7 m)	32 U 402477 5328680	x	x*	x	–	–	–	–	X	x
Orberg II	Sövite	HTAC 1282	KB2 (242 m)	32 U 402477 5328680	x	x	x	–	–	–	–	X*	x
Orberg II	Sövite	HTAC 1294	KB2 (323 m)	32 U 402477 5328680	x	x	X	x	–	–	–	X*	–
Orberg III	Sövite	HTAC 1410	Surface	32 U 402555 5328668	x*	x*	x*	x	–	–	–	X*	–
Orberg III	Sövite	HTAC 1413	Surface	32 U 402555 5328668	x*	x*	x*	x	–	–	–	X	–
Orberg IV	Sövite	HTAC 0237	Surface	32 U 402691 5328724	X*	x*	X*	x	–	–	–	X*	–
Orberg IV	Sövite	HTAC 0239	Surface	32 U 402691 5328724	X*	–	x	x	–	–	–	X*	–
Orberg IV	Sövite	HTAC-1353	Surface	33 U 402691 5328724	x*	x	x*	x	–	–	–	X	–
Orberg V	Sövite	HTAC 0222	Surface	32 U 402640 5328781	x*	x*	–	x	–	–	–	X	X
Orberg V	Sövite	HTAC 0224	Surface	32 U 402640 5328781	X	–	X*	X	–	–	–	X	–
Orberg V	Sövite	HTAC 0225	Surface	32 U 402640 5328781	x*	x*	x*	X	–	–	–	X*	–
Orberg V	Sövite	HTAC 1356	Surface	32 U 402640 5328781	x*	–	x	–	–	–	–/ X*	X*	–
Orberg V	Sövite	HTAC 1366	Surface	32 U 402620 5328185	x*	x*	–	x	–	–	–	X*	–
Degenmatt	Sövite	HTAC 1399	Surface	32 U 403779 5326957	X*	x*	–	x	–	–	–	X*	–
Haselschacher Buck	Sövite	HTAC 0284	Surface	32 U 402668 5327797	X*	x*	x*	x	–	–	–	X*	–
Haselschacher Buck	Sövite	HTAC 1354	Surface	32 U 402668 5327797	x*	x*	x*	–	–	–	x*/-	X*	–
Katharinenberg	Sövite	HTAC 1415b	Surface	32 U 402288 5329644	X	x*	X*	x	–	–	–	X*	–
Katharinenberg	Sövite	HTAC 1415c	Surface	32 U 402288 5329644	X*	x*	x*	x	–	–	X*/-	X*	–
Henkenberg	Crystal tuff	GM1	Surface	32 U 396571 5327645	x	–	–	–	x*	x*	–	X*	–
Henkenberg	Crystal tuff	GM2	Surface	32 U 396571 5327645	x	–	x*	(tr)	X*	x*	–	X*	–
Henkenberg	Crystal tuff	GM3	Surface	32 U 396570 5327645	x*	x	x*	–	X	x*	–	X	–
Henkenberg	Crystal tuff	HTAC 1369	Surface	32 U 396571 5327640	x	–	x	–	–	x*	–	X	–
Henkenberg	Crystal tuff	HTAC 1371	Surface	32 U 396571 5327640	x	–	x*	–	–	x	–	X	–
Henkenberg	Lapilli stone	GM4	Surface	32 U 396570 5327647	x	–	x*	–	x*	x*	–	X*	–
Kirchberg	Lava	HTAC 1337	Surface	32 U 396571 5327640	–	–	x*	–	–	x*	–	X*	–

X, major component; x, minor component; (tr), trace component.
*, EPMA data available.

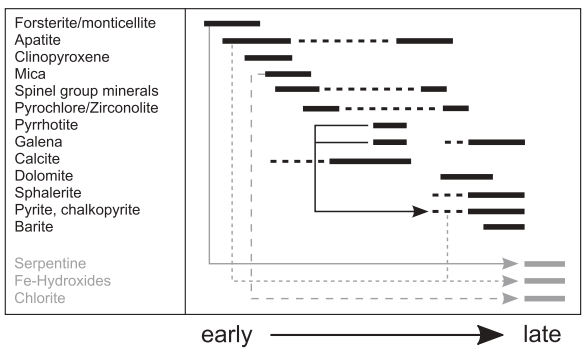

Fig. 2. Paragenetic scheme for sövites of the KVC including major alteration phases (in grey).

occurs as up to 30 μm large and occasionally zoned crystals (Fig. 4g). Perovskite (in the old literature called 'dysanalyte') was reported from a thin horizon at the Badloch quarry (southern Badberg; Wimmenauer, 1963; Hornig-Kjarsgaard, 1998). This outcrop is, however, lost and none of the investigated samples contains perovskite.

The main phase of calcite formation occurred relatively late, only rarely calcite occurs as small inclusions in apatite. Calcite exhibits equigranular and subhedral textures, with grain sizes varying from 100 μm up to several cm. Late-stage dolomitization of calcite is occasionally observed (Fig. 4h).

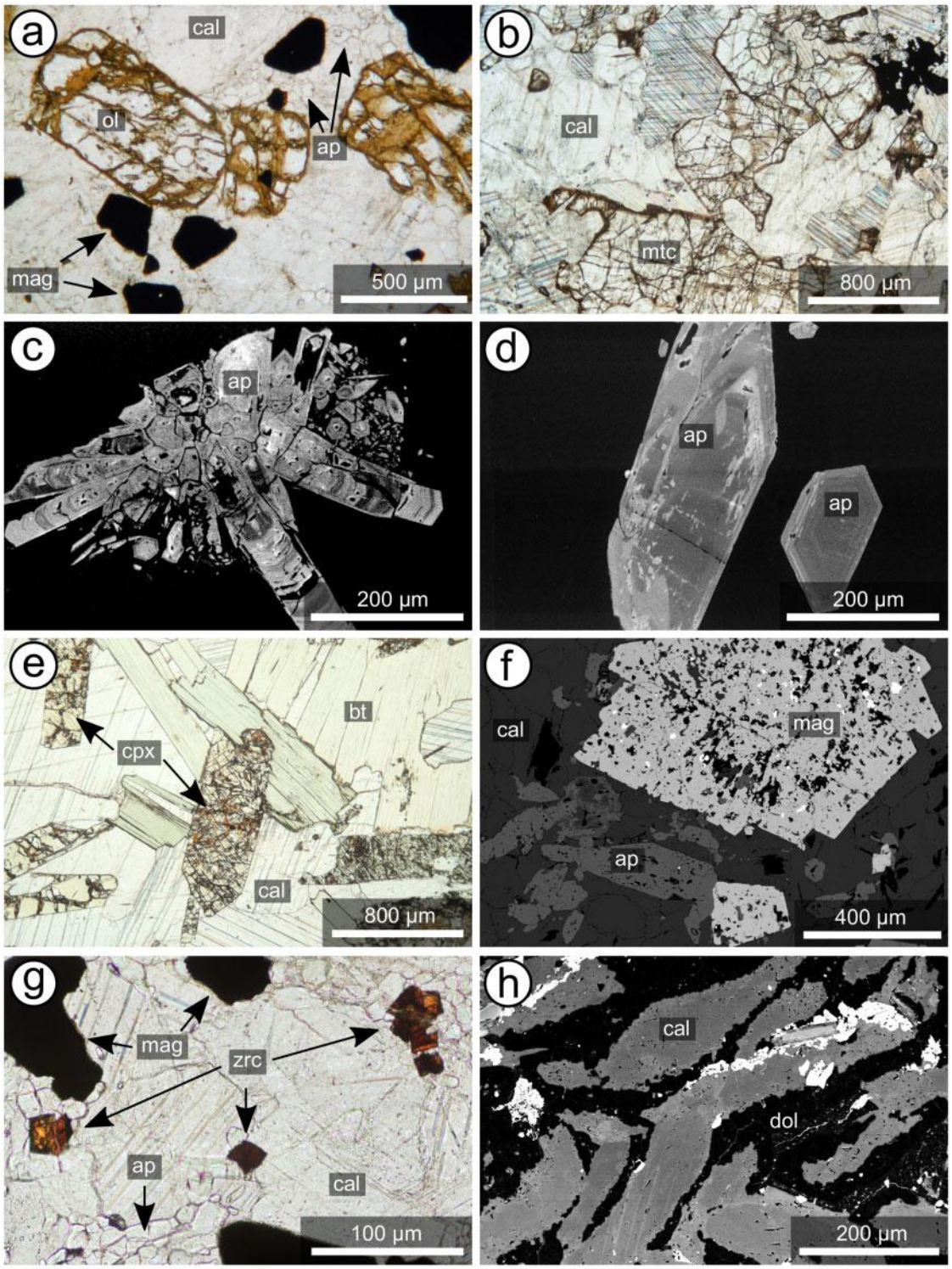

Fig 3. Photomicrographs (plane polarized light) and backscattered electron (BSE) images of the mineral assemblage of sövites from the KVC. (a) Coarse-grained olivine altered to serpentine (Haselschacher Buck). (b) Subhedral to anhedral monticellite (Orberg V). (c) Stellar aggregates of apatite (Orberg V). (d) REE- and Si-rich rims with REE- and Si-poor cores in apatite (Badberg). (e). Partly resorbed and altered clinopyroxene associated with biotite (Badberg). (f) Porous spinel group mineral (magnetite-magnesioferrite) associated with apatite and calcite (Orberg III). (g) Zirconolite (zrc) in olivine-bearing sövite (Haselschacher Buck). (h) Subhedral calcite surrounded and partly replaced by late-stage dolomite (Orberg II).

Abbreviations: ap, apatite; bt, biotite; cal, calcite; cpx, clinopyroxene; dol, dolomite; mag, spinel group mineral (magnetite–magnesioferrite); mtc, monticellite; ol, olivine; zrc, zircon.

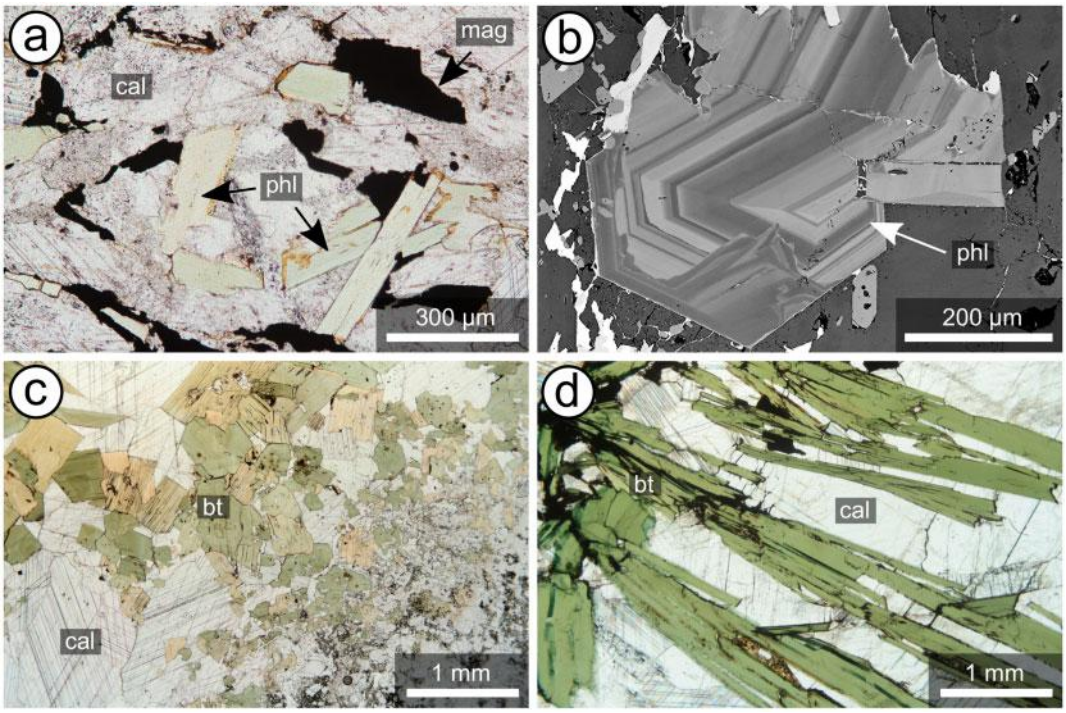

Fig. 4. Photomicrographs (plane polarized light) and backscattered electron (BSE) images of the different appearances of mica in sövites from the KVC. (a) Euhedral to subhedral laths of phlogopite enclosed by calcite and spinel group minerals (magnetite-magnesioferrite; Orberg V). (b) Oscillatory zoned Ba-rich phlogopite (Orberg III). (c) Coarse-grained 'black-wall' biotite (Badberg). (d) Coarse-grained bundles of biotite laths independent of the presence of calcite foidolite (Badberg). Abbreviations (see Fig. 3): bt, biotite; phl, phlogopite.

Rare pyrrhotite crystallized before calcite, but other sulphides (mainly pyrite, with minor galena and sphalerite) are of late-stage/hydrothermal origin and are often associated with fine-grained and interstitial barite.

Extrusive carbonatites

Carbonatite lavas have only been observed at the Kirchberg (Fig. 1). They consist of up to 0·6 mm large oscillatory zoned calcite laths and up to 150 μm large euhedral spinel group mineral grains, set in a fine-grained groundmass of calcite, apatite and spinel group minerals (Fig. 5a). In some cases, the spinel group minerals show thin rims, which are BSE-dark (Fig. 5b). Occasional xenocrysts of nepheline (300 μm; Fig. 5a) and garnet (200 μm) have been observed.

Carbonatite lapillistones and crystal tuffs from the Henkenberg were described in detail by Keller (1981, 1989). Lapillistones consist of calcite laths and sub-rounded lapilli cemented by fine-grained secondary calcite. The 0·5 to 10 mm large lapilli contain, in addition to calcite, larger amounts of spinel group minerals and prismatic apatite, and rare grains of clinopyroxene and garnet (Fig. 5c). Crystal tuffs are mainly composed of fragments of calcite (showing mosaic textures), spinel group minerals, garnet and pyroxene, with rare apatite and pyrochlore, set in a groundmass of calcite (Fig. 5d). Occasionally intercalated clasts of calcite foidolite and sövite can be recognized.

Calcite foidolites

Xenoliths of calcite foidolite (cm- to m-sized) occur only in the Badberg sövite (and rarely in carbonatitic tuff layers of the Henkenberg). Their abundance decreases towards the centre of the Badberg body, where they are strongly disaggregated compared to those in marginal zones. Sövite that contains strongly disaggregated xenoliths is exceptionally mica-rich (Fig. 6). Based on drill core loggings (Blust, 1993), the average carbonatite/xenolith ratio is about 5:1, but varies strongly from about 2:1 (marginal areas) to about 50:1 (central areas) over a range of tens of metres.

The contact between calcite foidolites and the surrounding sövite is characterized by coarse-grained seams of olive-green to khaki mica (see above) and an occasional transition zone consisting of strongly altered garnet and clinopyroxene, frequently intruded by carbonatitic veins (Fig. 7a). The central parts of these xenoliths consist of variable amounts of altered foid minerals (see below) and relict feldspar, with variable amounts of clinopyroxene, garnet and interstitial calcite (Fig. 7b–d).

Former nosean or haüyne (now decomposed to various zeolite minerals and calcite) is the most common phase. It mostly forms rounded grains of variable sizes and only rarely, euhedral grains containing small Fe-sulfide/oxide micro-inclusions are present (Fig. 7c). Rare relics of alkali feldspar are variably replaced by zeolites, calcite, mica and other minerals (Fig. 7d).

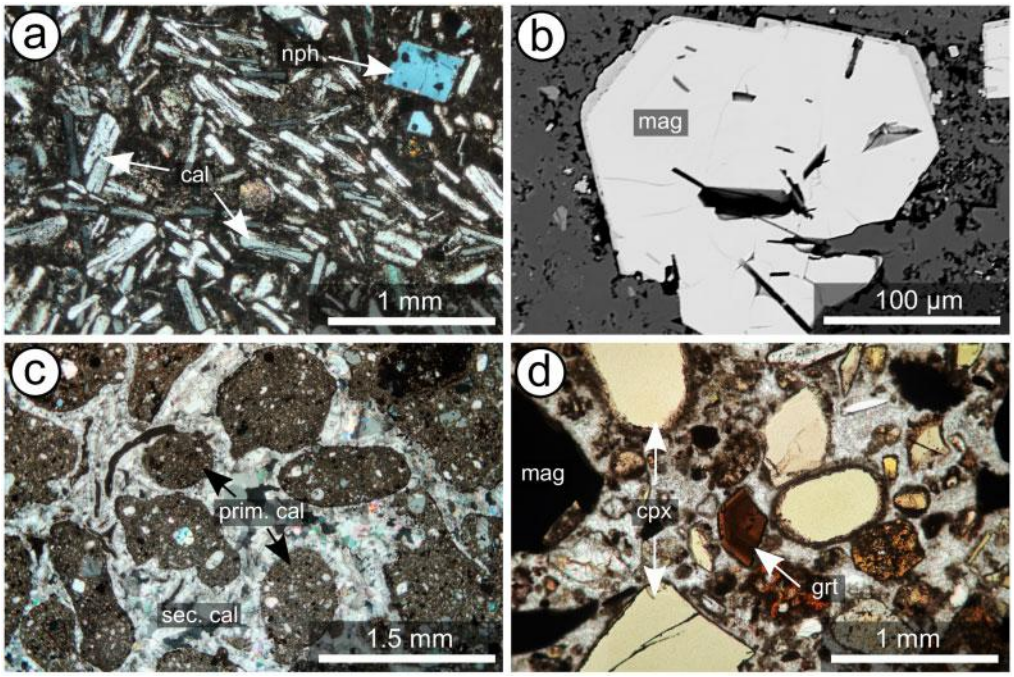

Fig. 5. Photomicrographs (plane and crossed polarized light) and backscattered electron (BSE) images of textural features of extrusive carbonatites from the KVC. (a) Carbonatite lava with calcite laths in a matrix of fine-grained calcite, apatite and spinel group minerals (magnetite–magnesioferrite). (b) Euhedral spinel group minerals with darker rims (enriched in Al) in carbonatite lava. (c) Lapillistone porphyritic lapilli in a fine-grained groundmass of calcite, spinel group minerals and apatite, cemented by secondary calcite. (d) Crystal tuff with fragments of clinopyroxene, garnet (grt) and spinel group minerals in groundmass of calcite.

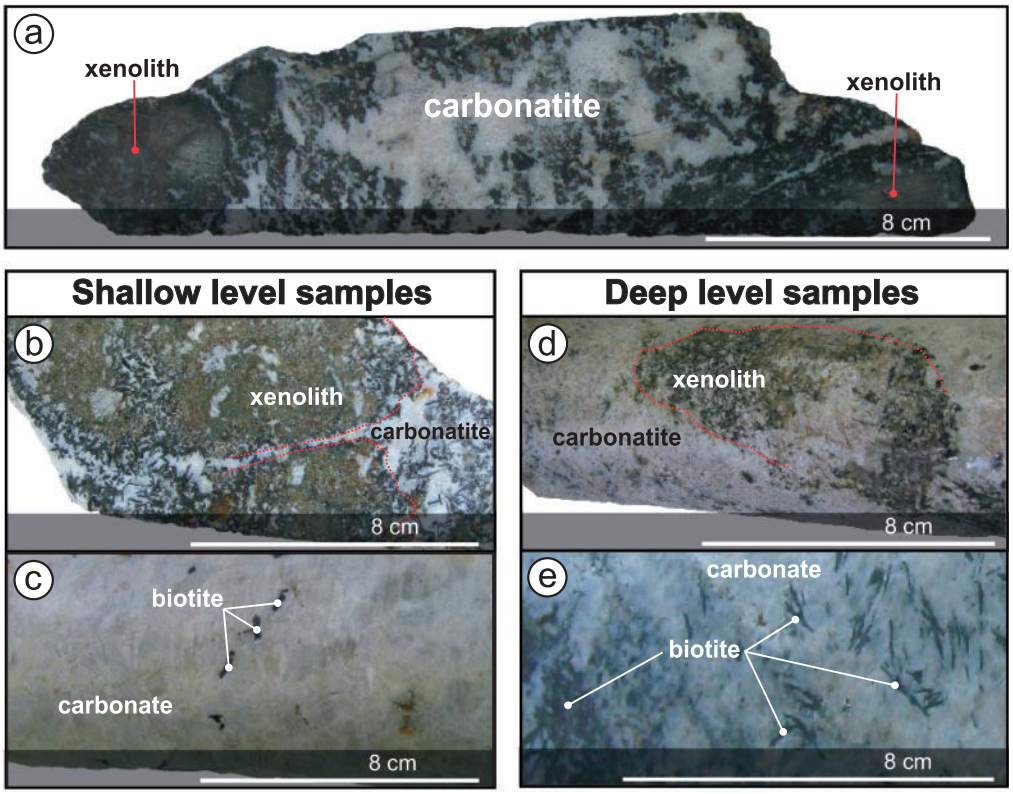

Fig. 6. Xenoliths in the Badberg carbonatites. (a) Carbonatite with a high xenolith proportion and strong proximal (to the xenolith) mica formation. (b) Xenolith from a 'shallow' drill core level (reflecting the marginal zone of the carbonatite pipe) showing significant mica formation around (black-wall mica) and in direct vicinity of the xenoliths. (c) Sections distal to a xenolith within a 'shallow' drill core level showing low mica formation. (d) Xenolith from a 'deep' drill core level (reflecting the central zone of the carbonatite pipe) showing strong disaggregation. The xenolith is nearly almost replaced by calcite. (e) Sections distal to xenolith within a 'deep' drill core level showing significant mica formation. The correlation between stronger disaggregated/resorbed xenoliths and the increased formation of mica shows a clear dependency.

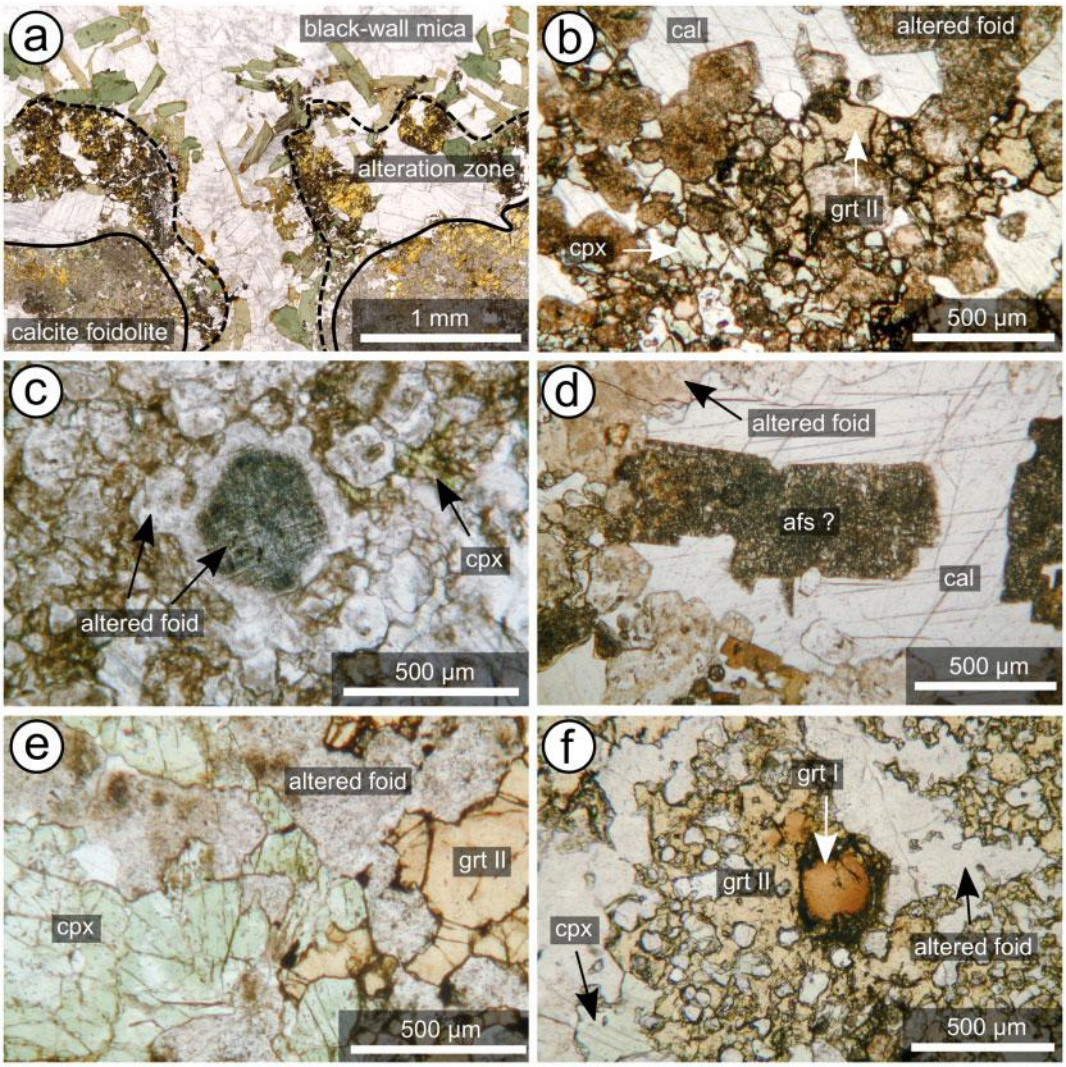

Fig. 7. Photomicrographs (plane polarized light) of the mineral assemblage and textural appearance of calcite foidolites from the KVC. (a) Coarse-grained biotite-rich 'black-wall' at the contact between carbonatite and calcite foidolite. (b) Recrystallized garnet (II) associated with recrystallized clinopyroxene (II), calcite and foid minerals (mostly altered to zeolites). (c) Euhedral nosean (or haüyne) decomposed to zeolite and calcite. (d) Alkali feldspar (afs) replaced by a mixture of zeolite, calcite, biotite, minor clinopyroxene (II) and garnet (II). (e) Clinopyroxene (II), garnet (II) and interstitial calcite in a calcite foidolite. (f) Dark brown and rounded (relict) garnet (I) overgrown by anhedral garnet (II).

Clinopyroxene occurs mostly as pale green, sometimes patchy-coloured subhedral and interstitial grains (Fig. 7e). If present, dark brown garnet I (relict cores) is overgrown by a reddish-brownish garnet II (recrystallized anhedral grains or masses; Fig. 7f). Garnet II is commonly zoned and occasionally forms poikilitic aggregates that enclose former foid minerals (Fig. 7f). Ubiquitous accessory minerals are apatite and titanite, only one sample contains primary spinel group minerals.

MINERAL COMPOSITIONS

Carbonates

Representative analyses are given in Table 2; formula calculations are based on one cation with CO_2 being calculated. Calcite in sövites contains variable, but generally minor amounts of Sr (<2 wt % SrO), Fe (<0·4 wt % FeO), Mg (<1·5 wt % MgO) and Mn (<1·5 wt %). Mean REE contents are generally <0·2 wt % Ce_2O_3 (similar to earlier data; Hornig-Kjarsgaard, 1998), but may occasionally reach higher values; however, the presence of REE-rich micro inclusions cannot be excluded. Calcite from Badberg samples is relatively Sr-rich but Mg-poor compared to calcite from other sövites (Fig. 8). Calcite in extrusive carbonatites is highly variable in composition. In the crystal tuff and lapillistone samples from Henkenberg, primary calcite is Sr-rich but Mg-poor compared to secondary calcite cement (Fig. 8).

Apatite

Representative analyses are given in Table 3 and formula calculations were done using the method of Ketcham (2015). As typical of carbonatites

Table 2: Representative EPMA analyses of carbonates from the Kaiserstuhl Volcanic Complex

Sample #	1229	1237	1362	1267	1294	1267	1318	1316b	1410	237	239	225	1356	1366
Locality	Badberg			Orberg II					Orberg III	Orberg IV		Orberg V		
Mineral	Calcite					Dolomite		Ankerite	Calcite					
Rock type	Sövite													
wt.%														
CaO	55·18	55·45	55·09	55·79	54·74	30·96	28·89	28·88	53·15	54·88	54·67	54·39	56·22	55·63
MgO	0·08	0·04	0·03	0·40	0·12	15·51	18·57	8·88	1·26	0·50	0·58	0·55	0·05	0·36
FeO	bdl	0·04	bdl	0·04	0·16	3·37	0·53	15·15	bdl	0·11	bdl	0·22	0·14	0·26
MnO	0·10	0·24	0·03	bdl	0·38	2·91	2·38	3·21	0·50	0·04	0·19	bdl	bdl	bdl
SrO	1·62	1·55	1·36	1·18	1·40	0·61	1·37	0·27	1·46	1·16	1·07	1·18	0·84	0·00
Ce_2O_3	0·07	0·89	0·07	0·21	0·11	0·03	0·04	bdl	bdl	0·64	0·06	bdl	0·06	bdl
CO_2 (calc.)	44·17	44·75	43·89	44·83	44·07	45·38	45·35	43·75	44·01	44·46	44·13	43·92	44·64	44·21
Total	101·22	102·95	100·46	102·44	100·98	98·77	97·13	100·14	100·38	101·78	100·70	100·25	101·95	100·46
Formula based on 1 cation														
Ca	0·98	0·97	0·99	0·98	0·97	0·54	0·50	0·52	0·95	0·97	0·97	0·97	0·99	0·99
Mg	0·002	0·001	0·001	0·01	0·003	0·37	0·45	0·22	0·03	0·01	0·01	0·01	0·001	0·01
Fe	bdl	0·00	bdl	0·00	0·002	0·05	0·01	0·21	bdl	0·002	bdl	0·003	0·002	0·004
Mn	0·001	0·003	0·00	bdl	0·01	0·04	0·03	0·05	0·01	0·001	0·003	bdl	bdl	bdl
Sr	0·02	0·01	0·01	0·01	0·01	0·01	0·01	0·00	0·01	0·01	0·01	0·01	0·01	0·00
Ce	0·001	0·008	0·001	0·002	0·001	0·0003	0·0003	bdl	bdl	0·01	0·001	bdl	0·001	bdl
Total cations	1·00	1·00	1·00	1·00	1·00	1·00	1·00	1·00	1·00	1·00	1·00	1·00	1·00	1·00

Sample #	284	1354	1399	1415b	1415c	GM1	GM2	GM4	GM4	1337	1337
Locality	Haselschacher Buck		Degenmatt	Katharinenberg		Henkenberg				Kirchberg	
Mineral	Calcite								Sec. Calcite	Calcite	
Rock type	Sövite					Crystal tuff		Lapilli stone		Lava	
Wt %											
CaO	54·86	54·93	51·87	55·31	53·13	56·44	55·03	56·35	56·14	54·82	55·65
MgO	0·31	0·18	0·48	0·53	1·19	0·43	0·05	0·08	0·82	0·03	0·04
FeO	0·29	bdl	0·13	0·09	0·07	bdl	bdl	0·06	bdl	0·40	bdl
MnO	bdl	0·13	1·17	0·14	0·46	bdl	0·15	0·02	bdl	bdl	bdl
SrO	0·87	0·72	0·26	0·38	1·12	0·00	1·48	1·00	bdl	1·36	1·15
Ce2O3	bdl	bdl	0·06	0·17	0·09	bdl	0·09	0·08	0·05	bdl	bdl
CO2 (calc.)	43·94	43·69	42·18	44·36	43·83	44·76	44·00	44·82	44·97	43·88	44·21
Total	100·28	99·65	96·14	100·99	99·87	101·63	100·80	102·41	101·98	100·49	101·04
Formula based on 1 cation											
Ca	0·98	0·99	0·97	0·98	0·95	0·99	0·98	0·99	0·98	0·98	0·99
Mg	0·01	0·004	0·01	0·01	0·03	0·01	0·001	0·002	0·02	0·001	0·001
Fe	0·004	bdl	0·002	0·001	0·001	bdl	bdl	0·001	bdl	0·01	bdl
Mn	bdl	0·002	0·02	0·002	0·01	bdl	0·002	0·00	bdl	bdl	bdl
Sr	0·01	0·01	0·00	0·00	0·01	0·00	0·01	0·01	bdl	0·01	0·01
Ce	bdl	bdl	0·001	0·002	0·001	bdl	0·001	0·001	0·000	bdl	bdl
Total cations	1·00	1·00	1·00	1·00	1·00	1·00	1·00	1·00	1·00	1·00	1·00

bdl, below detection limit.

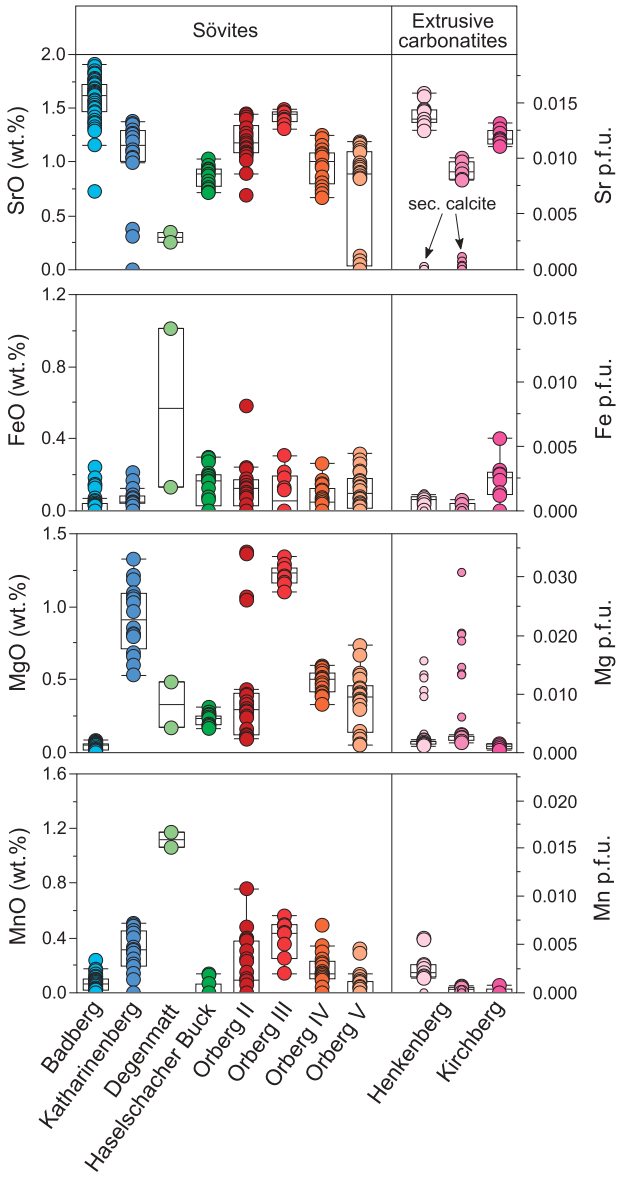

Fig. 8. Composition of calcite in sövites and extrusive carbonatites from the KVC shown as box plot diagrams.

(Chakhmouradian *et al.*, 2017), apatite from the KVC is fluorapatite to hydroxyapatite with variable F (1–2·8 wt %) and very low Cl contents (below 0·02 wt %; Table 4). Most data closely follow a substitution mechanism according to the apatite-britholite series ($Ca^{2+} + P^{5+} \leftrightarrow REE^{3+} + Si^{4+}$; Fig. 9a). Apatites from the Badberg sövites and calcite foidolites reach the highest levels of REE_2O_3 (up to 6·5 wt %), SrO (up to 4 wt %) and SiO_2 (up to 3·6 wt %), but are relatively low in Na_2O (below 0·5 wt %) compared to other locations (Fig. 9). In contrast, apatites from Orberg are low in REE_2O_3 (<3 wt %), SiO_2 (<1·8 wt %) and SrO (<1·5 wt %), but in some cases show elevated Na_2O (up to 1·2 wt %), following the coupled substitution mechanism $2Ca^{2+} + (3Ca^{2+}) \leftrightarrow REE^{3+} + Na^{+} + (3Sr^{2+})$ (apatite-belovite series). Most apatites are compositionally zoned with variable enrichments of REE and Si towards the rim of the crystals. In particular, apatites from the Badberg sövite show a distinct and sharp enrichment of a britholite component (Figs 3d and 9a) and commonly a slight decrease of Sr in their rims (Fig. 9c). Apatite data from samples of the KB3 drill hole (Badberg) show greater scatter in the upper parts of the drill hole than in the lower parts, with higher REE and Si but lower F and slightly lower Sr in the deeper parts of the drill hole (Fig. 10).

Mica

Representative analyses are given in Table 4; formula calculations are based on an ideal trioctahedral mica formula ($XY_3[Z_4O_{10}][OH, F, Cl]_2$) and the data were normalized to 7 (tetrahedral [Z] plus octahedral [Y]) cations. Micas from the KVC are Mg-rich and show variable enrichment of Ba (Fig. 11a), with those from Badberg having lower Ba (<0·07 apfu) and Mg# (72–88) compared to micas from the other localities (up to 0·5 Ba pfu and Mg# 91–97), while tetrahedral Fe^{3+} is similarly low at all localities (<0·05 and <0·07 Fe^{3+} pfu, respectively). Accordingly, mica from Badberg is classified as biotite (after Foster, 1960), whereas mica from all other localities is phlogopite. A continuous 1:1 increase of Al with Ba is caused by the phlogopite-kinoshitalite substitution ($K^{+} + Si^{4+} \leftrightarrow Ba^{2+} + {}^{IV}Al^{3+}$). Deviations from the 1:1 slope towards higher Al indicate an additional effect of the phlogopite–eastonite substitution ($Mg^{2+} + Si^{4+} \leftrightarrow {}^{IV}Al^{3+} + {}^{VI}Al^{3+}$; Fig. 11b) with a shift from the ideal 1:1 line reflecting constant eastonite substitution with increasing kinoshitalite substitution. The distinct oscillatory zonation in phlogopites from Orberg III and Katharinenberg (Fig. 4b) exclusively reflects a variable kinoshitalite substitution. Based on specific chemical characteristics, three mica groups are distinguished:

1. Phlogopites from Degenmatt, Katharinenberg and Orberg III and V are characterized by a large spread in Ba and Al contents (Fig. 11b). Orberg III micas follow a nearly ideal kinoshitalite substitution, whereas for micas from Degenmatt, Katharinenberg and Orberg V the additional importance of the eastonite substitution is obvious (Fig. 11a). Phlogopites of this group are further characterized by intermediate Na and F (Na up to 0·09 apfu, F up to 0·4 apfu; Fig. 11c and d) and the lowest Ti and Mn contents (<0·02 and <0·03 apfu, respectively; Fig. 11e and f).
2. Phlogopites from Orberg II and IV and from Haselschacher Buck show a constant eastonite substitution with increasing kinoshitalite substitution (Ba <0·3 apfu; Fig. 11b) and are further characterized by the highest Na (up to 0·11 apfu), intermediate Ti, (up to 0·03 apfu) and low Mn (<0·03 apfu) and F (<0·15 apfu; Fig. 11c–f) contents.
3. Biotite from the Badberg shows the lowest Mg# (72–88) and although their Ba content is low (<0·07 apfu), they show strong Al enrichment during evolution suggesting the importance of the eastonite substitution (Fig. 11a and b). They are further characterized by the highest Mn (up to 0·1 apfu), low

Table 3: Representative EPMA analyses of apatite from the Kaiserstuhl Volcanic Complex

Sample #	1229	1139	1147	1178	1253	1413	1410	1353	239	237	222	222	225	1356	1399	284	1354	1415c	GM3
Locality	Badberg				Orberg II	Orberg III		Orberg IV			Orberg V				Degen-matt	Haselschacher Buck		Katha-rinenberg	Henken-berg
Rock type	Calcite Foidolite		Sövite																Crystal tuff
wt %																			
Na_2O	0·08	0·10	0·06	0·09	0·22	0·25	0·25	0·21	0·31	0·17	1·06	0·69	0·29	0·04	0·51	0·13	0·12	0·18	0·14
CaO	52·25	52·04	51·00	51·98	54·13	54·31	54·39	54·10	54·00	53·46	52·47	52·38	53·55	52·72	51·31	53·88	53·06	54·82	52·79
SrO	0·90	1·48	1·94	1·25	0·62	0·85	0·81	0·76	0·61	0·67	1·41	1·40	0·68	0·53	1·47	0·49	0·46	0·56	0·51
La_2O_3	1·31	0·60	1·41	0·92	0·57	0·24	0·28	0·25	0·41	0·25	0·40	0·42	0·31	0·79	0·37	0·64	0·66	0·21	0·16
Ce_2O_3	2·07	1·18	1·98	1·49	1·13	0·30	0·43	0·47	0·65	0·50	0·67	0·71	0·57	1·37	0·60	1·10	1·14	0·51	0·37
Pr_2O_3	0·27	0·19	0·25	0·16	0·12	bdl	0·07	0·07	0·13	bdl	0·06	0·16	0·04	0·27	0·03	0·15	0·16	bdl	bdl
Nd_2O_3	0·46	0·24	0·39	0·30	0·47	0·09	0·15	bdl	0·28	0·12	0·24	0·26	0·18	0·42	0·25	0·38	0·39	0·17	0·12
FeO	bdl	0·03	0·04	0·03	bdl	1·07	0·02	bdl	bdl	bdl	0·02	0·07	bdl	bdl	0·04	bdl	0·15	bdl	0·23
P_2O_5	36·62	39·83	36·73	38·86	40·20	39·22	40·72	40·30	40·01	41·19	39·64	39·78	40·26	39·27	40·86	38·48	38·85	40·38	38·77
SiO_2	2·55	0·87	2·50	1·29	0·84	0·21	0·33	0·48	0·52	0·35	0·02	0·17	0·72	1·50	0·04	1·62	1·92	0·53	0·98
SO_3	0·38	0·08	0·34	0·12	0·14	0·17	0·24	0·27	0·22	0·14	0·32	0·24	0·32	0·20	0·12	0·44	0·24	0·23	0·97
As_2O_5	bdl	bdl	bdl	bdl	bdl	bdl	bdl	bdl	0·03	bdl	0·03	bdl	bdl	bdl	bdl	0·04	bdl	bdl	bdl
MnO	bdl	0·04	bdl	bdl	0·02	0·08	0·05	0·02	bdl	0·02	0·12	0·08	0·04	bdl	0·07	bdl	bdl	0·04	0·03
Cl	0·05	0·05	0·02	0·01	0·03	0·03	0·03	0·02	0·05	0·03	0·02	0·04	0·05	0·01	0·01	0·07	0·03	0·04	0·62
F	1·41	2·51	1·09	2·08	1·62	1·70	1·66	1·44	1·42	1·71	1·93	2·08	1·33	1·11	2·73	0·99	1·14	1·45	2·30
−O(F)	0·60	1·06	0·46	0·88	0·68	0·72	0·70	0·61	0·60	0·72	0·81	0·87	0·56	0·47	1·15	0·42	0·48	0·61	0·97
−O(Cl)	0·01	0·01	0·00	0·00	0·01	0·01	0·01	0·00	0·01	0·01	0·00	0·01	0·01	0·00	0·00	0·02	0·01	0·01	0·14
Corrected Total:	97·76	98·17	97·28	97·70	99·42	97·78	98·72	97·79	98·02	97·87	97·56	97·58	97·76	97·75	97·26	97·94	97·81	98·49	96·90
*OH wt.%	1·93	0·99	2·23	1·38	1·83	1·72	1·80	1·99	1·99	1·77	1·52	1·37	2·08	2·27	0·82	2·35	2·24	1·98	0·91
Net Cor. Total:	99·68	99·16	99·51	99·08	101·25	99·50	100·52	99·78	100·01	99·64	99·08	98·95	99·84	100·02	98·08	100·29	100·05	100·47	97·81
Formula calculation based on the method of Ketcham (2015)																			
Na	0·01	0·02	0·01	0·01	0·04	0·04	0·04	0·04	0·05	0·03	0·18	0·12	0·05	0·01	0·09	0·02	0·02	0·03	0·02
Ca	4·92	4·83	4·82	4·86	4·94	5·05	4·96	4·97	4·97	4·89	4·89	4·88	4·91	4·87	4·77	4·97	4·89	5·00	4·92
Sr	0·05	0·07	0·10	0·06	0·03	0·04	0·04	0·04	0·03	0·03	0·07	0·07	0·03	0·03	0·07	0·02	0·02	0·03	0·03
La	0·04	0·02	0·05	0·03	0·02	0·01	0·01	0·01	0·01	0·01	0·01	0·01	0·01	0·02	0·01	0·02	0·02	0·01	0·01
Ce	0·07	0·04	0·06	0·05	0·04	0·01	0·01	0·01	0·02	0·02	0·02	0·02	0·02	0·04	0·02	0·03	0·04	0·02	0·01
Pr	0·01	0·01	0·01	0·01	0·00	bdl	0·00	0·00	0·00	bdl	0·00	0·01	0·00	0·01	0·00	0·00	0·00	bdl	bdl
Nd	0·01	0·01	0·01	0·01	0·01	0·00	0·00	bdl	0·01	0·00	0·01	0·01	0·01	0·01	0·01	0·01	0·01	0·01	0·00
Fe	bdl	0·00	0·00	0·00	bdl	0·08	0·00	bdl	bdl	bdl	0·00	0·00	bdl	bdl	0·00	bdl	0·01	bdl	0·02
P	2·72	2·92	2·75	2·87	2·90	2·88	2·93	2·92	2·91	2·98	2·92	2·93	2·92	2·87	3·00	2·81	2·83	2·91	2·85
Si	0·22	0·08	0·22	0·11	0·07	0·02	0·03	0·04	0·04	0·03	0·00	0·01	0·06	0·13	0·00	0·14	0·16	0·05	0·09
S	0·03	0·00	0·02	0·01	0·01	0·01	0·02	0·02	0·01	0·01	0·02	0·02	0·02	0·01	0·01	0·03	0·02	0·01	0·06
As	bdl	bdl	bdl	bdl	bdl	bdl	bdl	bdl	0·00	bdl	0·00	bdl	bdl	bdl	bdl	0·00	bdl	bdl	bdl
Mn	bdl	0·00	bdl	bdl	0·00	0·01	0·00	0·00	bdl	0·00	0·01	0·01	0·00	bdl	0·01	bdl	bdl	0·00	0·00
Cl	0·01	0·01	0·00	0·00	0·00	0·00	0·00	0·00	0·01	0·00	0·00	0·01	0·01	0·00	0·00	0·01	0·00	0·01	0·09
F	0·39	0·69	0·30	0·57	0·44	0·47	0·45	0·39	0·39	0·46	0·53	0·57	0·36	0·30	0·75	0·27	0·31	0·39	0·63
$OH^{(est.)}$	0·60	0·30	0·69	0·42	0·56	0·53	0·55	0·61	0·61	0·53	0·47	0·42	0·63	0·69	0·25	0·72	0·69	0·60	0·28
Total cations	8·08	8·00	8·06	8·03	8·05	8·15	8·05	8·05	8·07	7·99	8·14	8·09	8·03	8·00	8·00	8·07	8·03	8·06	8·01

*OH wt %, calculated from $OH^{(est.)}$. $OH^{(est.)}$, estimated after calculations of Ketcham (2015).
bdl, below detection limit. Noticeable variation of representative analyses in a single sample has been indicated by the addition of further analyses, reflecting the variation.

Table 4: Representative EPMA analyses of micas from the Kaiserstuhl Volcanic Complex

Sample #	1200	1200	1156	1148	1245	1237	1318	1318	1413	1413	1413	1410	237	222	225	1366	1354	284	1415b	1415c
Locality	Badberg						Orberg II		Orberg III				Orberg IV	Orberg V			Haselschacher Buck		Katharinenberg	
Rock type	Sövite (Black Wall)				Sövite															
wt %																				
Na_2O	0·23	0·23	0·22	0·29	0·36	0·41	0·17	0·13	0·40	0·50	0·58	0·52	0·64	0·29	0·51	0·42	0·66	0·66	0·38	0·48
K_2O	9·69	10·16	9·89	9·26	9·39	9·33	9·81	10·63	4·62	5·25	6·77	7·16	7·33	7·93	6·58	8·90	8·23	6·66	6·33	7·46
CaO	0·02	bdl	0·06	0·03	0·05	0·04	0·18	0·26	0·19	0·01	0·12	0·07	0·05	0·04	0·02	0·04	0·07	0·23	0·04	0·05
BaO	1·74	0·24	0·82	2·42	2·09	2·29	2·56	0·44	14·76	12·57	8·12	8·11	6·81	7·44	10·15	3·21	4·21	8·66	10·83	7·20
MgO	24·02	21·79	20·33	21·40	21·03	22·67	25·62	27·43	23·97	24·42	24·85	24·97	24·06	26·21	25·23	27·02	24·67	24·41	24·82	25·62
MnO	1·03	1·36	1·17	1·08	0·75	0·69	0·36	0·40	0·13	0·17	0·21	0·23	0·35	0·20	0·14	0·26	0·29	0·30	0·11	0·24
FeO^S	5·20	9·25	10·46	7·40	8·82	7·71	2·24	1·89	0·73	1·78	1·86	2·22	4·21	1·60	1·30	1·36	3·72	2·72	1·60	2·26
$Fe_2O_3^S$	0·69	0·01	0·25	0·96	0·18	0·13	0·00	0·00	1·15	0·00	0·40	0·11	0·04	0·05	0·32	1·11	0·00	0·20	0·08	0·16
Al_2O_3	13·74	11·87	13·16	15·39	15·08	14·99	15·06	12·25	20·11	19·29	18·02	18·12	17·07	15·77	18·30	13·87	17·81	18·65	18·87	16·57
TiO_2	0·17	0·76	0·37	0·22	0·55	0·57	1·00	0·18	0·15	0·17	0·29	0·13	0·31	0·22	0·15	0·22	0·39	0·23	0·13	0·11
Cr_2O_3	bdl	0·05	0·02	bdl	bdl	0·01	0·01	bdl	bdl	0·03	0·05	0·03	0·02	0·01	bdl	bdl	0·01	bdl	bdl	0·03
SiO_2	39·51	40·27	39·10	37·38	37·90	38·85	38·70	42·68	29·77	31·95	34·40	35·33	36·01	37·17	34·34	39·20	37·13	34·63	33·40	36·49
Cl	bdl	0·01	0·02	0·01	bdl	0·01	bdl	bdl	0·01	0·02	0·02	bdl	0·02	0·02	0·01	bdl	bdl	bdl	bdl	bdl
F	2·09	1·26	1·32	1·27	0·08	0·19	1·58	3·10	1·14	0·80	0·85	0·93	0·69	1·55	0·88	1·41	0·17	0·15	0·79	0·92
$-O=(F, Cl)_2$	0·88	0·53	0·56	0·54	0·04	0·08	0·67	1·31	0·48	0·34	0·36	0·39	0·30	0·66	0·37	0·59	0·07	0·06	0·33	0·39
Total	98·13	97·26	97·19	97·10	96·28	97·90	97·29	99·39	97·13	96·94	96·54	97·93	97·61	98·50	97·92	97·02	97·36	97·50	97·38	97·57
H_2O^*	3·17	3·51	3·44	3·47	4·05	4·09	3·43	2·82	3·34	3·57	3·64	3·67	3·77	3·39	3·65	3·52	4·12	4·02	3·65	3·68
Formula based on 7 (tetrahedral [Z] plus octahedral [Y]) cations																				
Na	0·03	0·03	0·03	0·04	0·05	0·06	0·02	0·02	0·06	0·07	0·08	0·07	0·09	0·04	0·07	0·06	0·09	0·09	0·05	0·07
K	0·89	0·94	0·93	0·87	0·88	0·85	0·90	0·95	0·46	0·51	0·64	0·67	0·68	0·73	0·62	0·81	0·75	0·62	0·60	0·69
Ca	0·001	bdl	0·005	0·002	0·004	0·003	0·01	0·02	0·02	0·001	0·01	0·01	0·004	0·003	0·001	0·003	0·01	0·02	0·003	0·004
Ba	0·05	0·01	0·02	0·07	0·06	0·06	0·07	0·01	0·45	0·37	0·24	0·23	0·20	0·21	0·29	0·09	0·12	0·25	0·32	0·21
Mg	2·57	2·36	2·23	2·34	2·30	2·42	2·74	2·86	2·75	2·74	2·73	2·71	2·61	2·83	2·77	2·87	2·61	2·66	2·75	2·77
Mn	0·06	0·08	0·07	0·07	0·05	0·04	0·02	0·02	0·01	0·01	0·01	0·01	0·02	0·01	0·01	0·02	0·02	0·02	0·01	0·01
Fe^{2+}	0·31	0·56	0·64	0·45	0·54	0·46	0·13	0·11	0·05	0·11	0·11	0·14	0·26	0·10	0·08	0·08	0·22	0·17	0·10	0·14
Fe^{3+}	0·04	0·00	0·01	0·05	0·01	0·01	0·00	0·00	0·07	0·00	0·02	0·01	0·00	0·00	0·02	0·06	0·00	0·01	0·00	0·01
Al	1·16	1·02	1·14	1·33	1·30	1·26	1·27	1·01	1·83	1·71	1·57	1·55	1·47	1·35	1·59	1·17	1·49	1·61	1·65	1·42
Ti	0·01	0·04	0·02	0·01	0·03	0·03	0·05	0·01	0·01	0·01	0·02	0·01	0·02	0·01	0·01	0·01	0·02	0·01	0·01	0·01
Cr	bdl	0·003	0·001	bdl	bdl	0·001	0·001	bdl	bdl	0·001	0·003	0·002	0·001	0·001	bdl	bdl	0·001	bdl	bdl	0·001
Si	2·84	2·93	2·88	2·74	2·78	2·78	2·78	2·99	2·29	2·41	2·54	2·57	2·62	2·69	2·53	2·79	2·64	2·53	2·48	2·65
Cl	bdl	0·001	0·002	0·002	0·000	0·001	bdl	bdl	0·001	0·002	0·003	bdl	0·002	0·002	0·001	bdl	bdl	bdl	bdl	bdl
F	0·48	0·29	0·31	0·30	0·02	0·04	0·36	0·68	0·28	0·19	0·20	0·21	0·16	0·36	0·21	0·32	0·04	0·04	0·19	0·21
Total cations	7·97	7·98	7·99	7·98	7·99	7·98	8·01	8·00	7·98	7·96	7·97	7·98	7·97	7·99	7·99	7·96	7·96	7·98	7·98	7·97

H_2O^*, calculated from OH (F+Cl+OH = 2). S, Fe^{2+}/Fe^{3+} ratios calculated from stoichiometry.
bdl, below detection limit. Noticeable variation of representative analyses in a single sample has been indicated by the addition of further analyses, reflecting the variation.

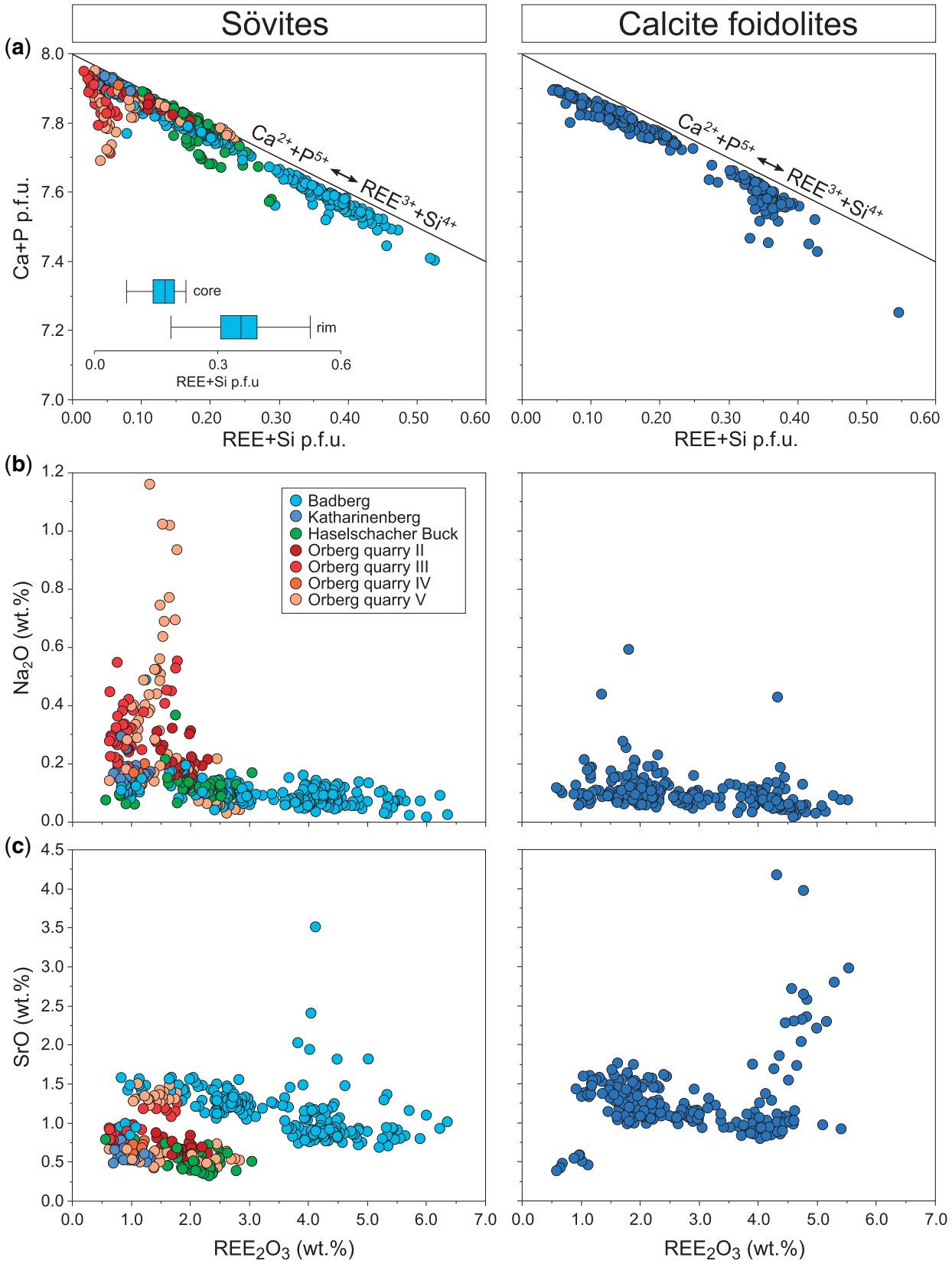

Fig. 9. Chemical variations of apatite in sövites and calcite foidolites from the KVC. (a) Ca+P vs REE+Si representing the apatite-britholite substitution mechanism ($Ca^{2+} + P^{5+} \leftrightarrow REE^{3+} + Si^{4+}$). (b) and (c) Variations of Na_2O and SrO vs REE_2O_3.

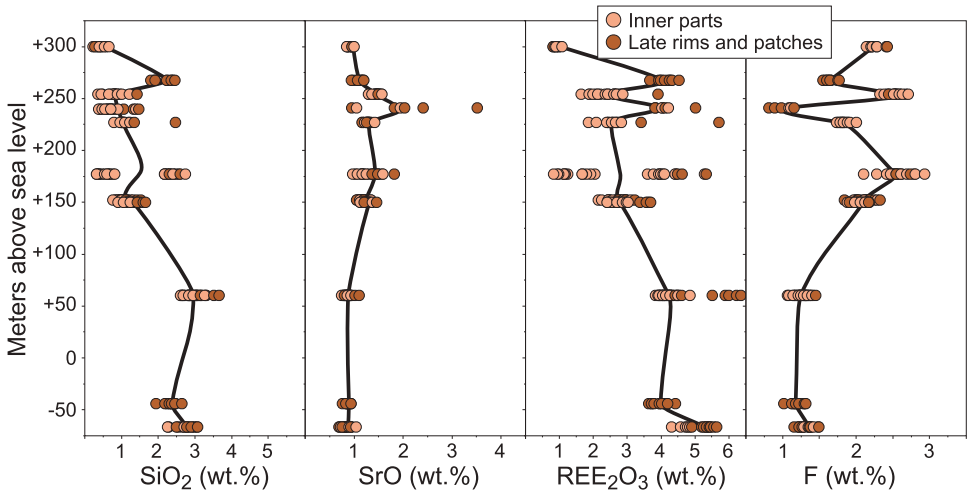

Fig. 10. Compositional variations of apatite with depth (given as m above sea level) in the KB3 drill hole (Badberg). Note: According to the tilting of the Badberg sövite (Fig. 1c), this variation depicts only a restricted depth variation within the sövite pipe, but reflects an additional centre-margin effect.

to intermediate Na (<0·07 apfu) and F (<0·5 apfu) and intermediate to high Ti (<0·06 apfu; Fig. 11c–f). Amongst the Badberg micas, those from black-walls around calcite foidolites (Fig. 7a) show lower Ti and Na, but higher F and Mn contents (Fig. 11c–f), but are otherwise compositionally similar to those formed far away from xenoliths.

Olivine and monticellite

Representative analyses are given in Table 5; formula calculations are based on four oxygens. Olivine in two of the sövites is Mg-rich ($Fo_{96–90}$) but shows a large range in the larnite component, varying from 0·1 to 1·5 mol % (0·06–1·17 wt % CaO; Fig. 12a). The negative correlation between forsterite and larnite components (Fig. 12a) implies a preferred incorporation of Ca with decreasing Mg (Jurewicz & Watson, 1988; Libourel, 1999). The Mn contents (up to 3·0 wt % MnO) are much higher than in the associated silicate rocks of the KVC (grey fields in Fig. 12b), while Ni contents rarely exceed the detection limit (NiO <0·03 wt %). Monticellite (about 75 mol %) is present in one sample (Orberg V) and contains about 20 mol % kirschsteinite ($CaFeSiO_4$) and 5 mol % glaucochroite ($CaMnSiO_4$).

Clinopyroxene

Formula calculations are based on four cations and six oxygens; representative analyses are listed in Table 6. Clinopyroxene in the investigated samples is invariably diopside-rich (Fig. 12c and d). However, clinopyroxene in sövites and calcite foidolites is higher in MnO (up to 1·4 wt %) but lower in TiO_2 (<0·9 wt %) compared to clinopyroxene in extrusive carbonatites (MnO <0·3 wt % and up to 4·1 wt % TiO_2; Fig. 12c and d). The concentration of Cr_2O_3 (up to 0·27 wt %) is only elevated in some extrusive carbonatites (Table 6).

Spinel group minerals

Representative analyses are given in Table 7 and formula calculations are based on three cations and four oxygens. Spinel group minerals in the investigated samples are classified as magnetite–magnesioferrite. In sövites they are poor in Ti (<0·13 apfu) and Al (<0·32 apfu), but relatively rich in Mn (up to 0·22 apfu), compared to those from extrusive carbonatites (Fig. 12e). In extrusive carbonatites, their Mg contents are relatively constant (0·26 to 0·36 apfu) compared to the large range observed in the sövite samples (0·08–0·65 apfu). Amongst the sövites, samples from Orberg reach the highest Mg content, implying a relatively large magnesioferrite component (up to 63 mol %), when considering endmembers magnetite ($Fe^{2+}Fe^{3+}_2O_4$), magnesioferrite ($MgFe^{3+}_2O_4$) and jacobsite ($MnFe^{3+}_2O_4$). Spinel group mineral rims in a carbonatitic lava sample (Fig. 5b) that appear distinctly darker in BSE have high Mg (0·63–0·69 apfu) and Al (0·42–0·56 apfu) concentrations, i.e. are spinel-rich.

Garnet

Representative analyses are listed in Table 8; formula calculations are based on eight cations and twelve oxygens, using the calculation scheme of Locock (2008). Most analyses show a very good 1:1 correlation between Ti + Fe^{3+} and Si + Al (Fig. 13a), indicating solid solution between grossular (0–26%) andradite (47–84%), schorlomite (0–18%) and morimotoite (0–29%) endmembers (Fig. 13b). These garnets are best described as Ti-bearing andradites. They are commonly called 'melanite', but this name is not accepted by the IMA. The contents of Nb, Zr and REE are generally low (<0·02, <0·02 and <0·01 apfu, respectively) but garnet II from the calcite foidolites may reach much higher Nb (up to 0·2 apfu) and Zr (up to 0·2 apfu), whilst REE contents are similarly low (Fig. 13c–e). Such Nb- and Zr-rich

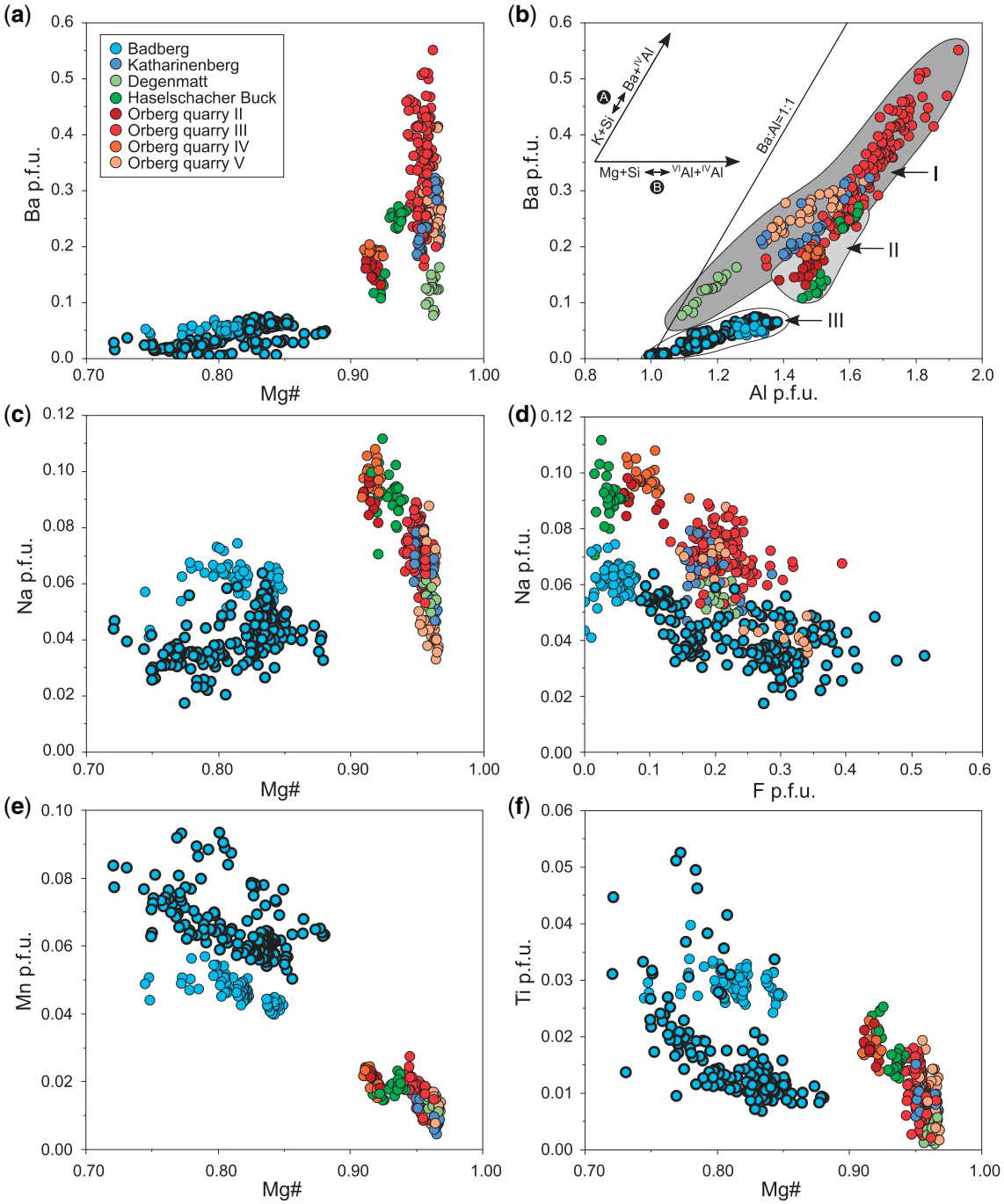

Fig. 11. Compositional variation of mica in sövites from the KVC. (a) Binary diagram of Ba vs Mg#. (b) Binary diagram of Ba versus Al. Inset depicts substitution tendencies: (A) Kinoshitalite substitution, (B) eastonite substitution (for details see text). (c) and (d) Na vs Mg# and F, respectively. (e) and (f) Mn and Ti vs Mg# respectively. Note the separation of biotite from Badberg compared to phlogopite from the other localities, as well as a separation between 'black-wall' mica (marked by heavier outline) and mica which is seemingly 'independent' of the presence of calcite foidolite in the Badberg samples.

analyses show clear deviations from the ideal Ti + Fe^{3+} - Si + Al 1:1 correlation (Fig. 13a). Based on their Mg–Ti characteristics, garnet I and II from the calcite foidolites can be clearly distinguished from each other, with garnet from the extrusive carbonatites plotting in between these two groups (Fig. 13f).

Zirconolite

Representative analyses are given in Table 9; formula calculations are based on four cations. We analysed zirconolite in a sövite from Haselschacher Buck, where it is rich in Nb (up to 21·5 wt % Nb_2O_5) and Ta (up to 4·4 wt % Ta_2O_5) with relatively low amounts of REE+Y (up to

Table 5: Representative EPMA analyses of olivine and monticellite from the Kaiserstuhl Volcanic Complex

Sample #	1415	1415	1354	1354	1356
Locality	Katharinenberg		Haselschacher Buck		Orberg V
Mineral	Forsterite				Monticellite
wt.%					
SiO_2	43·01	42·54	41·64	42·27	38·06
FeO	1·78	4·13	6·29	5·52	8·45
MnO	1·88	2·82	2·97	2·67	2·41
MgO	54·28	50·98	48·77	50·05	18·98
NiO	bdl	bdl	bdl	bdl	bdl
CaO	0·06	0·52	0·86	0·41	32·82
Total	101·03	100·99	100·53	100·92	100·74
Formula based on 4 oxygens					
Si	1·01	1·02	1·01	1·02	1·02
Fe	0·04	0·08	0·13	0·11	0·19
Mn	0·04	0·06	0·06	0·05	0·05
Mg	1·90	1·82	1·77	1·79	0·76
Ni	bdl	bdl	bdl	bdl	bdl
Ca	0·00	0·01	0·02	0·01	0·95
Total cations	2·99	2·98	2·99	2·98	2·98

bdl, below detection limit.

4·5 wt % $REE_2O_3 + Y_2O_3$), U (up to 1·2 wt % UO_2) and Th (up to 1·7 wt % ThO_2), plotting in the Nb+Ta-rich corner of the known compositional range (Fig. 14).

DISCUSSION

Origin of silicate minerals in the Kaiserstuhl carbonatites

Many carbonatites contain minor amounts of silicate minerals (in particular ferromagnesian silicates) with mica being the most common one (Reguir *et al.*, 2012). Their stability largely depends on silica activity, which is generally very low in carbonatites, in addition to temperature and other chemical potentials (Barker, 2001; Massuyeau *et al.*, 2015). Therefore, it is important to distinguish different genetic types of silicate minerals in carbonatites (e.g. Barker, 2001), including:

1. Silicates that crystallized from the carbonatitic magma, either due to a pristine sufficiently high silica activity ('true' primary magmatic silicates; type Ia) or because of a (local) change in silica activity (and the activity of other chemical components), for example by the interaction with wall rocks or xenoliths (type Ib).
2. Entrained crystals from the source rock or from wall rocks encountered during ascent and emplacement of the carbonatitic magma, including crystals from genetically related magmatic silicate rocks (xenocrysts; type II).
3. Subsolidus phases that formed during final cooling due to the interaction with hydrothermal or meteoric fluids (type III).

While a subsolidus origin (type III) can be easily recognized based on characteristic textures (e.g. exsolutions, pseudomorphs, veinlets), it is not easy to distinguish primary (carbonatitic) crystals (type I) from xenocrysts (type II) because there is a broad range of compositional variations of these phases in carbonatites (Chakhmouradian & Zaitsev, 2002; Reguir *et al.*, 2009; Reguir *et al.*, 2012). Also, depending on their composition and reaction kinetics, entrained xenocrysts may or may not be partly resorbed and/or chemically modified by diffusion-controlled reactions with the carbonatite magma. Therefore, only careful textural analyses combined with a detailed comparison between the composition of the mineral in question in the carbonatite with that of mantle rocks (e.g. olivine) and surrounding silicate rocks may provide the opportunity to determine the origin of such silicate minerals. In the following, we discuss the potential origin of the various silicate phases present in the Kaiserstuhl carbonatites.

Mica is the major K-bearing phase in most carbonatites and is typically Fe^{2+}-poor and variably enriched in Ba and Al (Giebel *et al.*, 2019 and references therein). At the KVC, mica in all sövites, except for the Badberg samples, shares these characteristics (Figs 11 and 15) and occurs as a minor phase more or less evenly dispersed in the rocks (Fig. 4a). We suggest that mica in these samples crystallized from the carbonatitic magma itself as a 'true' primary magmatic silicate at sufficiently high silica activities (type Ia). Mica in the Badberg samples, however, is compositionally distinct (Figs 11 and 15), much more abundant compared to the other sövites and partly occurs as seams around xenoliths (Figs 4 and 6). We assume that mica in the Badberg samples formed due to the interaction between entrained xenoliths and the carbonatitic magma (discussed in more detail below) and represents a type Ib phase.

Monticellite is stable at very low silica activities only (Barker, 2001) and is, therefore, commonly found in carbonatites (e.g. Nesbitt & Kelly, 1977; Stoppa & Lupini, 1993; Guzmics *et al.*, 2011), but is exceedingly rare in silicate rocks. None of the silicate lithologies at the KVC contains this phase. Olivine, in contrast, is a typical phase in mantle rocks and in many silicate rocks, including some of the KVC silicate lithologies. However, the high forsterite content, combined with high Mn (Fig. 12b) and very low Ni contents (Braunger *et al.*, 2018) is atypical of xenocrystic or mantle-derived olivine, but is typically observed in carbonatites (e.g. Lee *et al.*, 2004). At the KVC, olivine and monticellite (both Mn-enriched) are fairly rare and only occur in relatively mica-poor samples. Due to their cracked appearance, occasional rounded edges, serpentinization/iddingitization and partial resorption, a xenocrystic origin cannot be excluded. However, the absence of even small-scale compositional modifications (for example compositional zoning as would be expected by diffusional processes) renders this unlikely. Hence, we suggest that monticellite and olivine may represent silicate minerals of type I, probably representing 'true' primary magmatic silicates (type Ia), although it cannot be completely

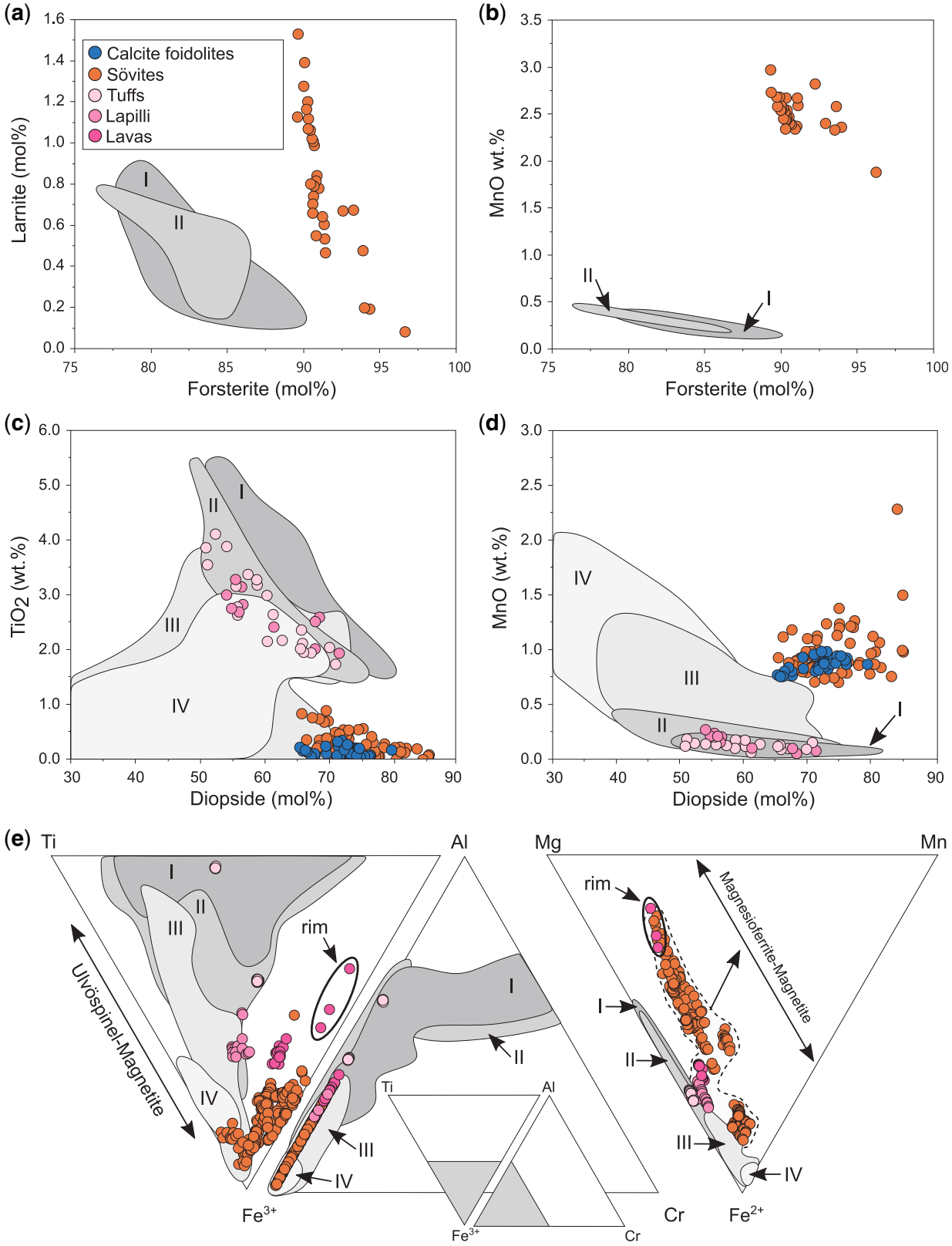

Fig. 12. Composition of olivine, clinopyroxene and spinel group minerals (magnetite-magnesioferrite) from carbonatites and calcite foidolites of the KVC. (a) Larnite vs forsterite components. (b) MnO (wt %) vs forsterite component in olivine. (c) and (d) Concentrations of TiO_2 (wt %) and MnO (wt %) vs diopside component in clinopyroxene. (e) Spinel group mineral compositions from carbonatites of the KVC. Grey fields represent data (olivine, clinopyroxene and spinel group minerals, respectively) for the KVC silicate rocks (Braunger *et al.*, 2018): (I) Olivine nephelinites and limburgites, (II) tephritic rocks, (III) melilititic and haüynitic/haüynolitic rocks, (IV) phonolitic/syenitic rocks, (V) haüynilites and melteigites.

Table 6: Representative EPMA analyses of pyroxene from the Kaiserstuhl Volcanic Complex

Sample #	260	1197	1151	1229	1215	1178	1237	GM1	GM2	GM4
Locality	Badberg							Henkenberg		
Rock type	Calcite foidolite							Crystal tuff		Lapili stone
wt %										
SiO_2	53·44	49·16	49·40	49·20	49·74	51·84	50·74	44·37	45·04	44·89
TiO_2	0·05	0·11	0·21	0·58	0·33	0·10	0·17	3·30	2·30	2·64
Al_2O_3	1·60	3·60	3·61	3·58	3·30	1·08	2·81	9·37	8·52	8·38
Cr_2O_3	bdl	bdl	bdl	bdl	bdl	bdl	bdl	0·04	0·04	0·03
FeO	6·15	8·81	8·61	7·97	7·25	5·96	6·58	7·53	7·35	7·75
MnO	0·94	0·81	0·83	0·95	0·89	1·14	0·99	0·13	0·15	0·15
MgO	13·93	12·52	12·67	12·71	13·22	14·26	13·65	11·53	11·83	11·51
CaO	24·70	23·90	24·35	23·96	24·23	23·90	24·35	22·77	23·65	23·64
Na_2O	0·38	0·47	0·41	0·51	0·40	0·51	0·37	0·53	0·42	0·51
Total	101·19	99·38	100·11	99·47	99·37	98·81	99·67	99·65	99·32	99·56
Formula based on 4 cations and 6 oxygens										
Si	1·96	1·84	1·84	1·84	1·86	1·94	1·88	1·66	1·68	1·68
Ti	0·00	0·003	0·01	0·02	0·01	0·003	0·005	0·09	0·06	0·07
Al	0·07	0·16	0·16	0·16	0·15	0·05	0·12	0·41	0·38	0·37
Cr	bdl	bdl	bdl	bdl	bdl	bdl	bdl	0·001	0·001	0·001
Fe^{3+}	0·04	0·18	0·18	0·17	0·15	0·11	0·12	0·12	0·15	0·16
Fe^{2+}	0·15	0·09	0·08	0·08	0·08	0·08	0·08	0·12	0·08	0·09
Mg	0·76	0·70	0·70	0·71	0·74	0·79	0·76	0·64	0·66	0·64
Mn	0·03	0·03	0·03	0·03	0·03	0·04	0·03	0·004	0·005	0·005
Ca	0·97	0·96	0·97	0·96	0·97	0·96	0·97	0·91	0·95	0·95
Na	0·03	0·03	0·03	0·04	0·03	0·04	0·03	0·04	0·03	0·04
Total cations	4·00	4·00	4·00	4·00	4·00	4·00	4·00	4·00	4·00	4·00
Mg#	0·84	0·88	0·89	0·89	0·91	0·91	0·90	0·85	0·90	0·88

bdl, below detection limit.

excluded that they are the product of small-scale contamination (type Ib).

Clinopyroxene (cpx) and garnet in extrusive carbonatites are broken and partly rounded (Fig. 5d). As they chemically resemble those of the silicate rocks (Figs 12 and 13), both phases are interpreted as being entrained from the KVC silicate rocks during eruption, representing type II silicates. In sövites, cpx only occurs in the Badberg samples, where it is mostly euhedral and compositionally distinct from those found in extrusive carbonatites and the known silicate rocks of the KVC, but very similar to the recrystallized cpx of calcite foidolites (Fig. 12c and d). Therefore, we suggest that cpx in the Badberg sövites formed similarly to mica (see above) by the interaction between xenoliths and carbonatite magma, representing a type Ib silicate. A possible entrainment of recrystallized cpx from calcite foidolites or an entrainment of original cpx (both representing a type II silicate) from the calcite foidolite precursor lithology (before alteration) is considered unlikely, as cpx in sövite is mostly euhedral (Fig. 3e), whereas it is interstitial and completely recrystallized in calcite foidolites (Fig. 7e). Also, a lack of small-scale compositional modifications (zoning) by xenocryst–carbonatite magma interactions render an entrainment of the original cpx improbable.

Mineralogical and mineral chemical differences among the KVC carbonatites

Based on geophysical and structural data (Brauch *et al.*, 2018; see above) we assume that the various sövite bodies of the KVC once belonged to a common subvertical pipe structure that was intersected, displaced and tilted by subsequent tectonic activity within the Rhine Graben system (Fig. 1c). Consequently, sövites at the Badberg may represent a higher emplacement level (shallower level of the pipe) than the Haselschacher Buck and Degenmatt occurrences. Orberg sövites may represent a large apophysis of this structure (e.g. Hubaux, 1964; Katz-Lehnert, 1989) and based on pyrochlore textures and compositions, these rocks experienced an intense hydrothermal overprint (Walter *et al.*, 2018). Although it is assumed that all four carbonatite localities belong to one batch of melt, major mineralogical and mineral chemical differences between the Badberg sövites and the other carbonatite bodies are prominent:

1. only Badberg sövites contain variable amounts of calcite foidolites (Figs 6 and 7);
2. only Badberg sövites are comparatively rich in mica that is texturally and compositionally distinct from mica in the other sövite occurrences (Figs 4c, d and 6);
3. only some Badberg sövites contain clinopyroxene (Fig. 3e);
4. only apatite in Badberg sövites shows exceptionally Si- and REE-rich rims (Fig. 9a).

In the following we discuss the significance of the calcite foidolites and the possible reasons for the presence of compositional distinct mica and apatite in the Badberg sövites, including contamination, magmatic differentiation and hydrothermal overprint.

Table 7: Representative EPMA analyses of magnetite from the Kaiserstuhl Volcanic Complex

Sample	1237	1136	1215	1151	1362	1410	1413	1353	237	225	224	1354	284	1415b	1415c	1371	GM2	GM3	GM4	1337
Locality	Badberg					Orberg III		Orberg IV		Orberg V		Haselschacher Buck		Katharinenberg		Henkenberg				Kirchberg
Rock type	Sövite															Crystal tuff			Lapilli stone	Lava
wt %																				
SiO_2	0·02	0·09	0·12	0·04	0·10	0·04	0·04	0·04	0·02	0·02	0·02	0·03	0·03	0·12	0·05	0·31	0·05	0·15	0·10	0.04
TiO_2	2·81	9·41	3·60	2·07	5·64	1·24	1·91	1·23	1·51	1·29	1·48	1·74	3·04	2·23	2·80	4·04	3·52	7·57	2·34	1.79
Fe_2O_3	62·87	46·64	61·37	65·25	56·20	65·74	64·94	67·16	68·68	66·04	65·35	64·87	64·11	64·51	63·38	57·31	61·56	51·17	62·75	65.90
FeO	17·87	30·68	26·70	25·84	22·13	18·42	25·93	15·82	15·35	18·69	19·99	26·88	22·06	18·84	20·92	24·08	27·20	28·19	18·06	15.54
MnO	3·99	0·65	3·08	3·96	3·46	4·62	3·69	4·76	4·85	4·18	3·72	2·89	5·50	4·29	4·31	2·87	2·69	1·74	3·99	5.02
MgO	8·54	6·73	3·64	2·43	8·08	6·53	2·38	8·18	8·54	6·75	6·36	2·30	4·25	7·25	6·17	6·44	3·36	6·37	8·30	8.55
V_2O_3	0·41	0·15	0·19	0·25	0·22	0·47	0·18	0·38	0·59	0·59	0·31	0·18	0·91	0·31	0·24	0·08	0·20	0·15	0·41	0.52
Al_2O_3	5·51	7·39	2·85	1·57	6·36	4·20	1·79	4·07	2·73	4·21	4·45	2·33	1·18	4·15	4·01	6·77	2·59	6·22	6·16	4.35
Cr_2O_3	0·03	0·04	0·01	0·01	0·03	0·03	0·01	0·02	0·04	0·04	0·02	0·01	0·05	0·02	0·01	0·01	0·01	0·01	0·03	0.03
ZnO	0·29	0·07	0·13	0·20	0·20	0·28	0·16	0·31	0·28	0·29	0·28	0·19	0·30	0·24	0·30	0·14	0·13	0·12	0·28	0.33
Total	102·34	101·85	101·67	101·62	102·43	101·58	101·04	101·97	102·59	102·08	102·00	101·43	101·45	101·95	102·20	102·04	101·31	101·67	102·42	102.09
Formula based on 3 cations and 4 oxygens																				
Si	0·001	0·003	0·004	0·002	0·003	0·001	0·001	0·001	0·000	0·001	0·001	0·001	0·001	0·004	0·002	0·011	0·002	0·005	0·004	0.001
Ti	0·07	0·24	0·10	0·06	0·14	0·03	0·05	0·03	0·04	0·03	0·04	0·05	0·08	0·06	0·07	0·11	0·09	0·20	0·06	0.05
Fe^{3+}	1·62	1·21	1·68	1·81	1·45	1·75	1·81	1·76	1·80	1·75	1·73	1·80	1·76	1·70	1·68	1·49	1·69	1·34	1·62	1.72
Fe^{2+}	0·52	0·88	0·81	0·80	0·63	0·56	0·80	0·47	0·45	0·55	0·60	0·83	0·68	0·56	0·62	0·70	0·83	0·83	0·52	0.45
Mn	0·12	0·02	0·10	0·12	0·10	0·14	0·12	0·14	0·14	0·12	0·11	0·09	0·17	0·13	0·13	0·08	0·08	0·05	0·12	0.15
Mg	0·43	0·34	0·19	0·13	0·41	0·34	0·13	0·42	0·44	0·35	0·32	0·13	0·23	0·37	0·32	0·33	0·18	0·32	0·42	0.44
V	0·01	0·002	0·003	0·004	0·003	0·01	0·003	0·01	0·01	0·01	0·004	0·003	0·01	0·004	0·003	0·001	0·003	0·002	0·01	0.01
Al	0·22	0·30	0·12	0·07	0·25	0·17	0·08	0·16	0·11	0·17	0·18	0·10	0·05	0·17	0·17	0·28	0·11	0·25	0·25	0.18
Cr	0·001	0·001	0·00	0·00	0·001	0·001	0·00	0·001	0·001	0·001	0·001	0·00	0·001	0·00	0·00	0·00	0·00	0·00	0·001	0.001
Zn	0·01	0·002	0·004	0·01	0·01	0·01	0·004	0·01	0·01	0·01	0·01	0·01	0·01	0·01	0·01	0·004	0·004	0·003	0·01	0.01
Total cations	3·00	3·00	3·00	3·00	3·00	3·00	3·00	3·00	3·00	3·00	3·00	3·00	3·00	3·00	3·00	3·00	3·00	3·00	3·00	3.00

Table 8: Representative EPMA analyses of garnet from the Kaiserstuhl Volcanic Complex

Sample #	1158	1158	1168	1168	1147	1147	1173	1173	GM1	GM2	GM2	GM3	1369	1369	GM4	1337	1337
Location	Badberg								Henkenberg							Kirchberg	
Rock type	Calcite foidolite								Crystal tuff						Lapilli stone	Lava	
wt %																	
SiO_2	36·36	33·52	36·67	34·21	35·34	27·57	32·00	34·72	32·88	33·62	30·35	33·55	28·38	31·12	32·29	32·83	34·95
TiO_2	2·08	3·48	0·82	3·11	2·66	8·60	9·34	4·81	7·02	5·55	10·55	5·45	13·52	9·77	7·27	7·10	3·78
ZrO_2	0·17	1·12	0·17	2·67	0·44	3·93	0·12	0·08	0·33	0·17	0·38	bdl	0·55	bdl	0·07	0·19	0·32
Y_2O_3	bdl	bdl	0·07	bdl	bdl	bdl	bdl	bdl	bdl	0·15	0·10	bdl	0·14	bdl	0·17	bdl	bdl
Al_2O_3	5·55	3·91	4·62	2·63	3·03	1·93	1·41	1·17	2·24	2·66	3·34	2·63	4·20	2·22	3·24	1·66	2·77
Fe_2O_3	22·16	22·82	23·98	23·99	24·87	20·56	25·07	26·84	24·40	25·12	22·24	24·76	20·04	22·13	22·81	25·78	25·84
MnO	0·56	0·55	0·58	0·79	0·62	0·73	0·49	0·50	0·78	0·63	0·52	0·76	0·49	0·62	0·62	0·58	0·94
MgO	0·69	0·89	0·55	0·89	0·69	1·25	0·46	0·27	0·62	0·49	0·95	0·46	0·95	0·90	0·88	0·45	0·22
CaO	32·37	33·16	33·11	32·47	31·87	31·59	32·27	32·73	32·50	33·05	32·63	32·19	31·67	31·93	32·82	32·29	32·57
Na_2O	0·01	0·02	0·03	0·07	0·04	0·17	0·26	0·21	0·12	0·06	0·08	0·12	0·11	0·09	0·07	0·14	0·08
ThO_2	bdl	bdl	0·04	bdl	bdl	bdl	bdl	bdl	bdl	bdl	0·04	0·04	bdl	0·06	bdl	bdl	bdl
UO_2	bdl	bdl	bdl	bdl	bdl	bdl	bdl	bdl	bdl	bdl	bdl	bdl	bdl	bdl	bdl	bdl	bdl
Ta_2O_5	bdl	0·17	bdl	bdl	bdl	0·13	bdl	bdl	bdl	0·07	bdl	0·12	0·03	0·06	bdl	bdl	bdl
Nb_2O_5	0·16	1·57	0·49	1·19	0·45	5·19	bdl	0·11	0·13	bdl	0·14	bdl	bdl	0·22	0·27	bdl	0·09
SrO	bdl	bdl	bdl	bdl	bdl	bdl	bdl	bdl	bdl	bdl	bdl	bdl	bdl	bdl	bdl	bdl	bdl
La_2O_3	bdl	bdl	bdl	bdl	bdl	bdl	bdl	bdl	bdl	bdl	bdl	bdl	bdl	bdl	bdl	bdl	bdl
Ce_2O_3	bdl	bdl	0·10	0·12	bdl	0·10	bdl	bdl	bdl	bdl	bdl	bdl	bdl	0·08	bdl	0·07	0·07
Nd_2O_3	bdl	bdl	bdl	0·09	bdl	bdl	bdl	bdl	bdl	bdl	bdl	bdl	bdl	bdl	bdl	0·05	0·07
Pr_2O_3	bdl	0·06	0·05	bdl	bdl	bdl	bdl	bdl	bdl	0·04	bdl	bdl	0·06	bdl	0·07	bdl	0·07
Sm_2O_3	bdl	bdl	bdl	bdl	bdl	bdl	bdl	bdl	bdl	bdl	bdl	bdl	bdl	0·05	0·04	bdl	0·03
F	bdl	bdl	bdl	bdl	bdl	bdl	bdl	bdl	bdl	bdl	bdl	bdl	bdl	bdl	bdl	bdl	bdl
Total	100·11	101·27	101·27	102·23	100·01	101·75	101·43	101·45	101·01	101·62	101·30	100·08	100·13	99·25	100·61	101·13	101·79
Formula based on 8 cations and 12 oxygens																	
Si	2·98	2·78	2·99	2·84	2·95	2·38	2·67	2·88	2·74	2·78	2·52	2·81	2·39	2·64	2·69	2·74	2·88
Ti	0·13	0·22	0·05	0·19	0·17	0·56	0·59	0·30	0·44	0·34	0·66	0·34	0·86	0·62	0·45	0·45	0·23
Zr	0·01	0·05	0·01	0·11	0·02	0·17	0·01	0·00	0·01	0·01	0·02	bdl	0·02	bdl	0·00	0·01	0·01
Y	bdl	bdl	0·003	bdl	bdl	bdl	bdl	bdl	bdl	0·01	0·004	bdl	0·01	bdl	0·01	bdl	bdl
Al	0·54	0·38	0·44	0·26	0·30	0·20	0·14	0·11	0·22	0·26	0·33	0·26	0·42	0·22	0·32	0·16	0·27
Fe^{2+}	0·16	0·06	0·08	0·16	0·18	0·32	0·20	0·15	0·13	0·08	0·12	0·12	0·23	0·20	0·06	0·17	0·14
Fe^{3+}	1·21	1·36	1·40	1·34	1·39	1·01	1·38	1·53	1·40	1·48	1·27	1·44	1·05	1·22	1·36	1·45	1·46
Mn	0·04	0·04	0·04	0·06	0·04	0·05	0·03	0·04	0·05	0·04	0·04	0·05	0·04	0·04	0·04	0·04	0·07
Mg	0·08	0·11	0·07	0·11	0·09	0·16	0·06	0·03	0·08	0·06	0·12	0·06	0·12	0·11	0·11	0·06	0·03
Ca	2·85	2·94	2·90	2·88	2·85	2·92	2·89	2·91	2·90	2·93	2·91	2·89	2·86	2·91	2·93	2·89	2·88
Na	0·002	0·00	0·00	0·01	0·01	0·03	0·04	0·03	0·02	0·01	0·01	0·02	0·02	0·01	0·01	0·02	0·01
Th	bdl	bdl	0·00	bdl	bdl	bdl	bdl	bdl	bdl	bdl	0·00	0·00	bdl	0·00	bdl	bdl	bdl
U	bdl	bdl	bdl	bdl	bdl	bdl	bdl	bdl	bdl	bdl	bdl	bdl	bdl	bdl	bdl	bdl	bdl
Ta	bdl	0·004	bdl	bdl	bdl	0·003	bdl	bdl	bdl	0·001	bdl	0·003	0·001	0·001	bdl	bdl	bdl
Nb	0·01	0·06	0·02	0·04	0·02	0·20	bdl	0·004	0·01	bdl	0·01	bdl	bdl	0·01	0·01	bdl	0·003
Sr	bdl	bdl	bdl	bdl	bdl	bdl	bdl	bdl	bdl	bdl	bdl	bdl	bdl	bdl	bdl	bdl	bdl
REE total	bdl	bdl	0·004	0·006	bdl	0·003	bdl	bdl	bdl	bdl	bdl	bdl	0·002	0·005	0·003	0·004	0·007
F	bdl	bdl	bdl	bdl	bdl	bdl	bdl	bdl	bdl	bdl	bdl	bdl	bdl	bdl	bdl	bdl	bdl
Total cations	8·00	8·00	8·00	8·00	8·00	8·00	8·00	8·00	8·00	8·00	8·00	8·00	8·00	8·00	8·00	8·00	8·00

bdl, below detection limit. Noticeable variation of representative analyses in a single sample has been indicated by the addition of further analyses, reflecting the variation.

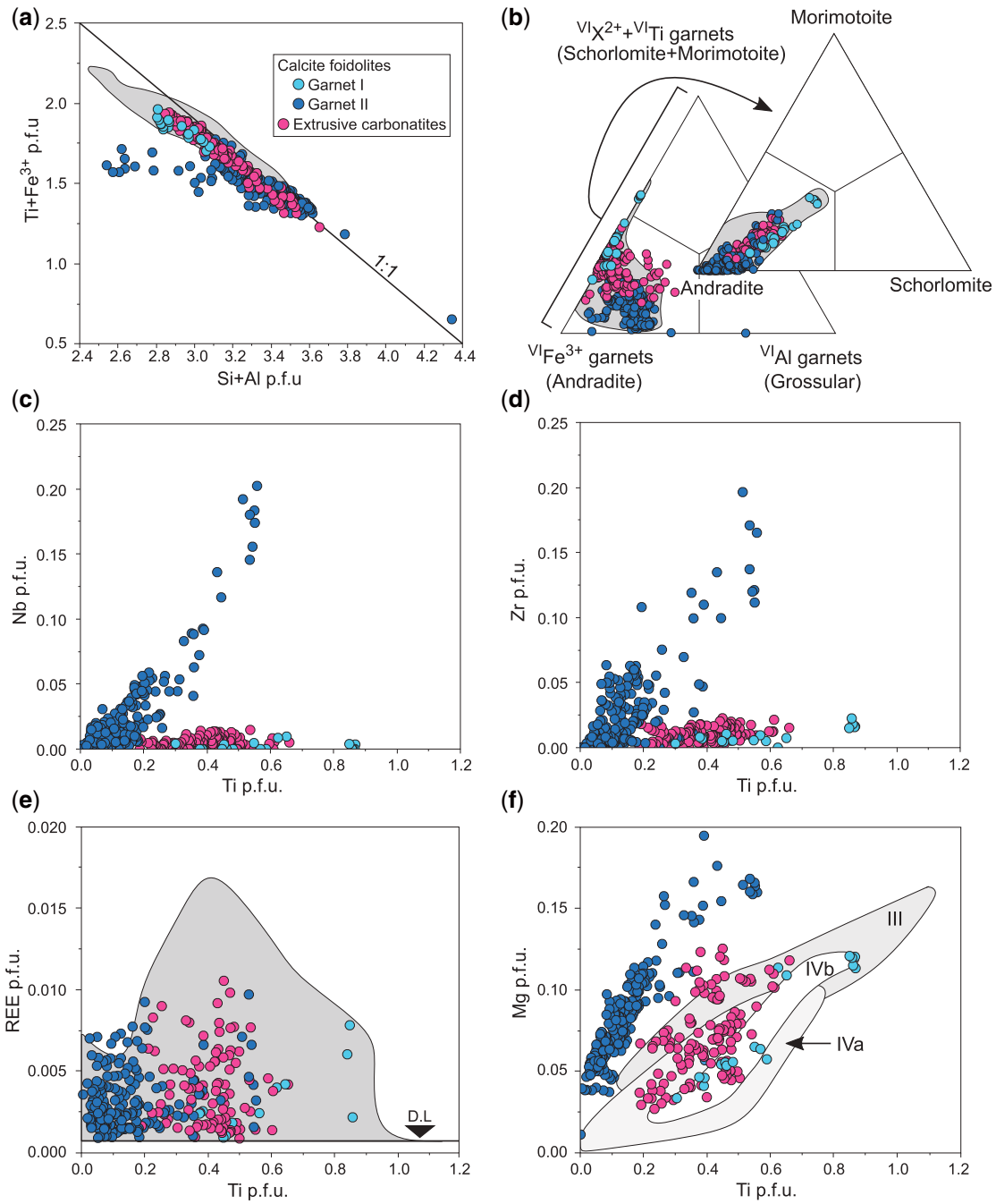

Fig. 13. Compositional variation of garnet from carbonatites and calcite foidolites of the KVC. (a) Ti+Fe^{3+} vs Si+Al. The solid line illustrates the ideal 1:1 substitution. (b) Garnet composition based on the octahedral-site occupations Fe^{3+}, X^{2+}+Ti (X= Mg, Fe^{2+}) and Al and based on the endmembers andradite, morimotoite and schorlomite. (c)–(f) Concentrations of Nb, Zr, REE and Mg vs Ti, with data from the KVC silicate rocks shown as grey fields for comparison (Braunger *et al.*, 2018): (III) melilititic and haüynitic/haüynolitic rocks, melteigites, IVa) nosean syenites (former 'ledmorites'), (IVb) phonolites and nosean syenite inclusions therein.

Significance of calcite foidolites (carbonatite magma–xenolith interaction)

Calcite foidolites in the Badberg sövites (Figs 6 and 7) probably do not represent cumulates of the carbonatite magma itself, since their mineralogy is very different from the sövites and large differences in the modal abundances would be expected. Also, feldspar, which is found as relicts in the calcite foidolites, is generally unstable at the low silica activities expected for carbonatite magmas (Barker, 2001; Massuyeau *et al.*, 2015). Therefore, we assume that these rocks represent equivalents of previously emplaced silicate rocks entrained in and subsequently resorbed and metasomatized by the intruding carbonatitic magma.

Despite their textural resemblance to haüynolites that occur as xenoliths in some phonolitic rocks (Czygan, 1977), the chemical composition of relict garnet (garnet type I) in calcite foidolites suggests that the

Table 9: Representative EPMA analyses of zirconolite from the Kaiserstuhl Volcanic Complex

Sample #	1354	1354	C 71	C 72
Locality	Haselschacher Buck		Kaiserstuhl	
Rock type	Sövite			
wt %				
CaO	12·56	12·52	11·38	12·20
Na_2O	bdl	bdl	n.a.	n.a.
SrO	0·29	bdl	n.a.	n.a.
La_2O_3	0·16	0·30	n.a.	n.a.
Ce_2O_3	1·71	2·02	0·77	0·90
Pr_2O_3	0·37	0·34	n.a.	n.a.
Nd_2O_3	1·03	1·13	1·10	n.a.
Sm_2O_3	0·27	0·19	0·27	n.a.
Y_2O_3	0·48	0·49	n.a.	n.a.
ZrO_2	33·75	32·68	30·51	34·80
UO_2	1·04	1·23	1·22	1·40
ThO_2	1·18	1·65	5·13	4·10
TiO_2	10·81	10·66	13·56	22·70
Nb_2O_5	21·20	21·53	22·07	15·70
Ta_2O_5	4·10	4·45	3·08	n.a.
MgO	n.a.	n.a.	0·85	n.a.
Al_2O_3	0·91	0·82	n.a.	n.a.
FeO	8·00	7·77	7·41	7·60
MnO	0·98	1·03	0·94	0·20
SiO_2	bdl	bdl	n.a.	n.a.
F	bdl	bdl	n.a.	n.a.
Total	98·83	98·80	98·29	99·60
Formula based on 4 cations				
Ca	0·90	0·91	0·84	0·87
Na	bdl	bdl	n.a.	n.a.
Sr	0·01	bdl	n.a.	n.a.
REE+Y	0·10	0·12	0·05	0·02
Zr	1·11	1·07	1·02	1·08
U	0·01	0·02	0·02	0·02
Th	0·02	0·03	0·08	0·06
Ti	0·55	0·54	0·70	1·10
Nb	0·64	0·66	0·67	0·46
Ta	0·07	0·08	0·06	n.a.
Mg	n.a.	n.a.	0·09	n.a.
Al	0·07	0·07	n.a.	n.a.
Fe	0·45	0·44	0·42	0·38
Mn	0·06	0·06	0·05	0·01
Si	bdl	bdl	n.a.	n.a.
F	bdl	bdl	n.a.	n.a.
Total cations	4·00	4·00	4·00	4·00

bdl, below detection limit. n.a., not analysed.
C71: Data from Keller (1984). C72: Data from Sinclair & Eggleton (1982).

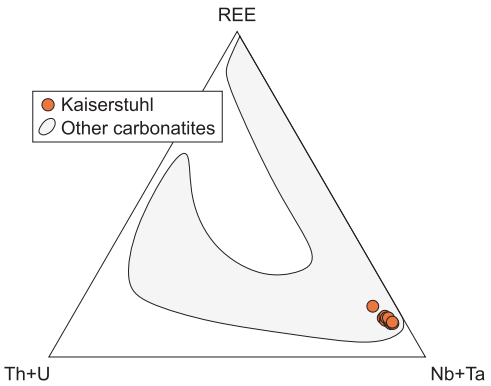

Fig. 14. Compositional variation of zirconolite from the KVC in comparison with other carbonatites (data from Williams & Gieré, 1996; Hurai *et al.*, 2018).

nosean syenites that underlie the Badberg body (as evidenced by the FB drill core; see Walter *et al.*, 2018), are the most likely protolith (Fig. 13). However, in contrast to nosean syenites, calcite foidolites have a higher proportion of sodalite-group minerals, alkali feldspar is almost absent and clinopyroxene and garnet are subhedral to anhedral. We attribute these mineralogical and textural differences to the interaction with the carbonatite magma (Fig. 16).

Carbonatites reach liquidus temperatures above 1000 °C (e.g. Kharlomov, 1981; Panina, 2005; Guzmics *et al.*, 2011) and contain large amounts of volatile phases (e.g. F and H_2O; Treiman & Essene, 1984; Jago & Gittins, 1991). Therefore, they can cause intense metasomatism (Elliot *et al.*, 2018) and may be capable of partly assimilating silicate rocks. Textural evidence for the interaction between the entrained xenoliths and the carbonatite magma includes: (i) the almost complete replacement of precursor alkali feldspar by foids; (ii) the compositional change of nosean to haüyne; (iii) blackwall-like mica seams around the xenoliths; (iv) the occurrence of recrystallized garnet (garnet type II) with relics of original garnet cores (garnet type I); and (v) crosscutting carbonatitic veins (Figs 6 and 7). The modifications in nosean syenites can be expressed by the schematic mineral reactions (1) – (3):

$$\text{alkali feldspar} + \text{nosean (nosean syenite)} \rightarrow \text{haüyne (calcite foidolite)}$$

$$2\ KAlSi_3O_8 + Na_8Al_6Si_6O_{24}SO_4 + CaSO_4(\text{melt}) + CaO\ (\text{melt}) = Ca_2Na_6Al_6Si_6O_{24}(SO_4)_2 + Al_2O_3 + 6\ SiO_2 + K_2O + Na_2O \quad \text{(reaction 1)}$$

$$\text{original cpx (nosean syenite)} \rightarrow \text{recrystallized cpx (calcite foidolite)}$$

$$10\ Ca_{0.8}Na_{0.2}Mg_{0.4}Fe^{2+}{}_{0.3}Fe^{3+}{}_{0.3}Al_{0.1}Si_{1.9}O_6 + 2\ CaO\ (\text{melt}) + 3\ MgO\ (\text{melt}) + 0.5\ Al_2O_3 (\text{reaction 1}) = 10\ CaMg_{0.7}Fe^{2+}{}_{0.1}Fe^{3+}{}_{0.2}Al_{0.2}Si_{1.8}O_6 + 3\ FeO + Na_2O + SiO_2 + 0.25\ O_2 \quad \text{(reaction 2)}$$

$$\text{original garnet I (nosean syenite)} \rightarrow \text{recrystallized garnet II (calcite foidolite)}$$

$$10\ (Ca_{2.9}Mg_{0.1})(Fe^{2+}{}_{0.3}Fe^{3+}{}_{1.2}Ti_{0.5})(Al_{0.2}Si_{2.8})O_{12} + 0.5\ ZrO_2(\text{melt}) + 0,25\ Nb_2O_5(\text{melt}) + 0.5\ Al_2O_3(\text{reaction 1}) + 0.125\ O_2(\text{melt}) = 10\ (Ca_{2.9}Mg_{0.1})(Fe^{2+}{}_{0.2}Fe^{3+}{}_{1.3}Ti_{0.3}[Zr,\ Nb]_{0.1}Al_{0.1})(Al_{0.2}Si_{2.8})O_{12} + 2\ TiO_2 \quad \text{(reaction 3)}$$

Garnet II has relatively high Nb and Zr contents (Fig. 13), reflecting the importance of the carbonatitic magma during metasomatism, as carbonatites are typically enriched in these elements (usually stored in pyrochlore, perovskite, baddeleyite and zirconolite). Similar modifications of silicate rocks by carbonatitic melts have been described as 'antiskarn'

metasomatism (Anenburg & Mavrogenes, 2018) and reflect the mutual interaction during contamination.

Importantly, xenoliths in the lower sections of the KB3 drill hole, which represents the central part of the tilted Badberg body, are much more strongly disaggregated, which may indicate higher degrees of resorption compared to the marginal parts of the body. This may be attributed to a longer lasting heat flow that predominantly occurred in the central area of the carbonatite pipe, while marginal zones experienced an earlier and more rapid cooling. Consequently, this central zone contains more silica that may have induced the observed exceptional mica enrichment in those parts (Fig. 6). In these samples (down-hole below +100 metres above sea level), pyrochlore is enriched in Fe^{2+}, Al and Ti (Walter *et al.*, 2018), which was probably released by the resorption of xenoliths. Note that such enrichment of Fe^{2+} and Al in pyrochlore is confined to the Badberg locality and does not exist at the other carbonatite localities of the KVC.

The significance of mica composition

The enhanced formation of mica (and the formation of diopside instead of monticellite/olivine) in the Badberg samples cannot be ascribed to magmatic differentiation, since silicates in carbonatites crystallize early, which would decrease the SiO_2 concentration and silica activity in the carbonatite magma with fractionation (e.g. Krasnova *et al.*, 2004; Lee *et al.*, 2004). However, strong textural evidence and mineral compositions (see above) suggest a connection between the formation of mica (and cpx) and the entrainment of xenoliths in the sövites from Badberg.

In contrast to mica from the other sövite bodies of the KVC (which are dominated by the kinoshitalite substitution), mica at Badberg is dominated by the eastonite substitution (see above). This indicates that the availability of Al exceeds the availability of Ba, most likely due to the provision of Al by the resorption of feldspar (reaction 1). Furthermore, Badberg mica shows an unusual enrichment in octahedral Fe^{2+}. This is atypical for the other sövites of the KVC and carbonatites in general (e.g. Kovdor, Palabora, Sokli and Jacupiranga; Fig. 15), where the formation of tetraferriphlogopite (incorporation of Fe^{3+}) or Fe-poor phlogopite is preferred over the formation of Fe^{2+}-rich mica (biotite; e.g. Lee *et al.*, 2003; Krasnova *et al.*, 2004; Giebel *et al.*, 2019). While all other localities of the KVC show 'typical carbonatite micas' with respect to their Mg, Al and Fe concentrations, Badberg micas are more similar to micas from silicate rocks (Fig. 15), which we ascribe to the metasomatic interaction with the calcite foidolite clasts and rafts (see above). Alteration reactions (1) – (3) above demonstrate the release of K, Al, Si and Fe^{2+}, which are consumed to form Fe^{2+}-bearing mica (Figs 4c and 7a) according to the schematic reaction:

$$K_2O\ (\text{see reaction 1}) + Al_2O_3(\text{see reaction 1}) + 6\ SiO_2(\text{see reactions 1 and 2}) + FeO\ (\text{see reaction 2}) + 5\ MgO\ (\text{melt}) + 2\ H_2O\ (\text{melt}) = 2\ KMg_{2.5}Fe_{0.5}AlSi_3O_{10}(OH)_2 \quad \text{(reaction 4)}$$

Besides the Fe^{2+}-enrichment, the micas of the Badberg contain elevated amounts of Ti and Mn. While Mn and also F are preferably incorporated into the mica precipitating directly on the resorbed clasts (black-wall

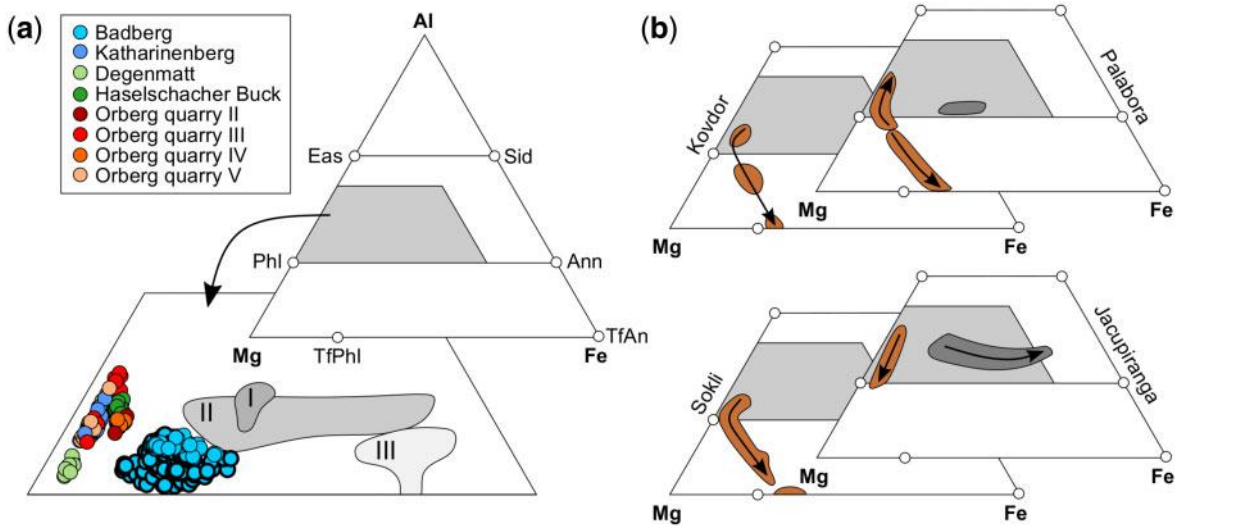

Fig. 15. (a) Ternary diagrams of $Mg–Al_{total}–Fe_{total}$ reflecting the compositional characteristics of mica from the sövites of the KVC, with numbered grey areas representing mica compositions from the silicate rocks of the KVC (Braunger *et al.*, 2018): (I) olivine nephelinites; (II) tephritic rocks; (III) haüyne melilitites. (b) Mica compositions from other carbonatites with brown fields indicating mica compositions in carbonatites and dark grey field mica compositions from associated silicate rocks (Palabora, Kovdor, Sokli and Jacupiranga; Brod *et al.*, 2001; Lee *et al.*, 2003; Krasnova *et al.*, 2004; Giebel *et al.*, 2019). Ann, annite; Eas, eastonite; Sid, siderophyllite; Phl, phlogopite; TfPhl, tetraferriphlogopite; TfAn, tetraferriannite.

mica), Ti, Na and Ba behave mostly conversely and appear to have been enriched in the carbonate melt, further distant from the resorbed clasts (Fig. 11). The enhanced crystallization of mica at Badberg and the related consumption of Mg from the carbonatite melt may also be the reason for the relative depletion of Mg in subsequently crystallized calcite (Fig. 8), due to the generally very rapid diffusion in carbonatite melts and their resulting very fast equilibration (e.g. Anenburg *et al.*, 2018 and references therein). Besides Mg, Ba was also derived from the carbonatite melt itself, while the enrichment of Ti (reaction 3) and additional Mn is probably related to the resorption and recrystallization of clinopyroxene and garnet I. The absence of Fe^{2+}-poor mica cores suggests that the entire mica crystallization in the Badberg sövites took place during nosean syenite–carbonatite magma interaction. Hence, mica composition cannot be easily used to track magmatic differentiation at Badberg, but may still be applicable at the other localities.

Enrichment of Ba in carbonatites is generally ascribed to differentiation because of its incompatible character (e.g. Kogarko *et al.*, 2012; McCormick & Heathcote, 1987; McCormick & Le Bas, 1996). Moreover, Ba is efficiently mobilized in carbonatites, is strongly concentrated in residual liquids and dissolves favourably in aqueous fluids (Anenburg & Mavrogenes, 2018). Thus, the strong enrichment of Ba in the mica from the Orberg sövites (Fig. 11) confirms the assumption of Walter *et al.* (2018) that the Orberg sövites are evolved and hydrothermally overprinted. The high Mg# of Orberg mica is attributed to the relative enrichment of Mg over Fe during differentiation (fractional crystallization) due to the contemporaneous formation of Fe-rich spinel group minerals. This is the reverse of what is typically expected during silicate-magma differentiation (dependent on the redox state of the magma; e.g. Heathcote & McCormick, 1989; Giebel *et al.*, 2019). A comparison between the enrichment of Ba and the increase of the Mg# in these micas suggests a much stronger sensitivity of the former in terms of mica evolution. In conclusion, mica does not only record differentiation, but also contamination processes in carbonatites exceptionally well.

The significance of apatite composition

The local increase in silica activity in the carbonatite melt (reactions 1 & 2) enhanced the incorporation of Si in apatite (Figs 9 and 10) and favoured simultaneous REE incorporation due to the britholite substitution (e.g. Hammouda *et al.*, 2010). In contrast to cores of Badberg apatites, which generally reveal a lower britholite substitution, rims are significantly more strongly affected (Fig. 9a). The sharp contact between the cores and rims suggests an abrupt and strong compositional change of the carbonatite magma during apatite formation, which excludes continuous magma differentiation, although the generally high Sr contents in Badberg apatites (Fig. 9c) indicate a relatively evolved character for the Badberg sövites.

In contrast to a few apatites from the Orberg that occur in strongly hydrothermally altered samples and experienced a belovite substitution (see above; Fig. 9), which is typical for hydrothermal apatite evolution in many carbonatites (e.g. de Toledo *et al.*, 2004; Doroshkevich *et al.*, 2009), a hydrothermal origin of the Badberg apatites in respect of the increased britholite substitution (0·3–0·5 REE+Si pfu) in its rims is also unlikely. This phenomenon is restricted to magmatic temperatures (>600 °C), while hydrothermal conditions (including sufficient SiO_2) promote the formation of REE-poorer apatite and REE-rich silicate minerals (e.g. cerite; Anenburg & Mavrogenes, 2018; Anenburg *et al.*, 2018). In addition, typical hydrothermal interaction textures (reprecipitation/replacement reactions; e.g. Giebel *et al.*, 2017) are typically absent in Badberg sövites.

We assume that the enhanced britholite substitution in apatites is related to the interaction between the carbonatite magma and silicate xenoliths. The core–rim variation records the time-dependent effect of contamination. This is additionally reflected by the increasing Si and REE content in apatite in the deeper sections of drill core KB3 (Fig. 10; central zones of the pipe), where a stronger disaggregation of xenoliths caused an increased release of silica (see above). Experimental data (Klemme & Dalpé, 2003) confirm enhanced partitioning of REE into apatite with increasing SiO_2 content in the melt. This emphasizes the potential importance of contamination of carbonatitic magmas for REE mineralization; the local enrichment of Si favours an early (magmatic) incorporation of REE into apatite, which inhibits the subsequent enrichment of REE in residual liquids/fluids. These late-stage fluids, however, are the most common source for the deposit-quality enrichment of REE-minerals and/or REE-rich minerals in carbonatites (Wall & Mariano, 1996). This connection is convincingly indicated by a comparison of the REE concentrations in apatite and pyrochlore between the Badberg and other carbonatite bodies (Fig. 17). While Badberg apatites are REE-rich (due to contamination; Fig. 9a), the incorporation of REE in Badberg (late-stage) pyrochlore seems to be largely unaffected. In contrast, apatites at other localities are relatively REE-poor, while hydrothermally overprinted pyrochlore at these localities is strongly REE-enriched (see details in Walter *et al.*, 2018). This potentially has economic implications, although it should be noted that calcite (due to its high modal content) further contributes to the REE budget of the rocks.

Mica in carbonatites – a potential clue to wall rock interaction processes?

Many carbonatites contain appreciable amounts of mica (e.g. Brod *et al.*, 2001; Lee *et al.*, 2003; Reguir *et al.*,

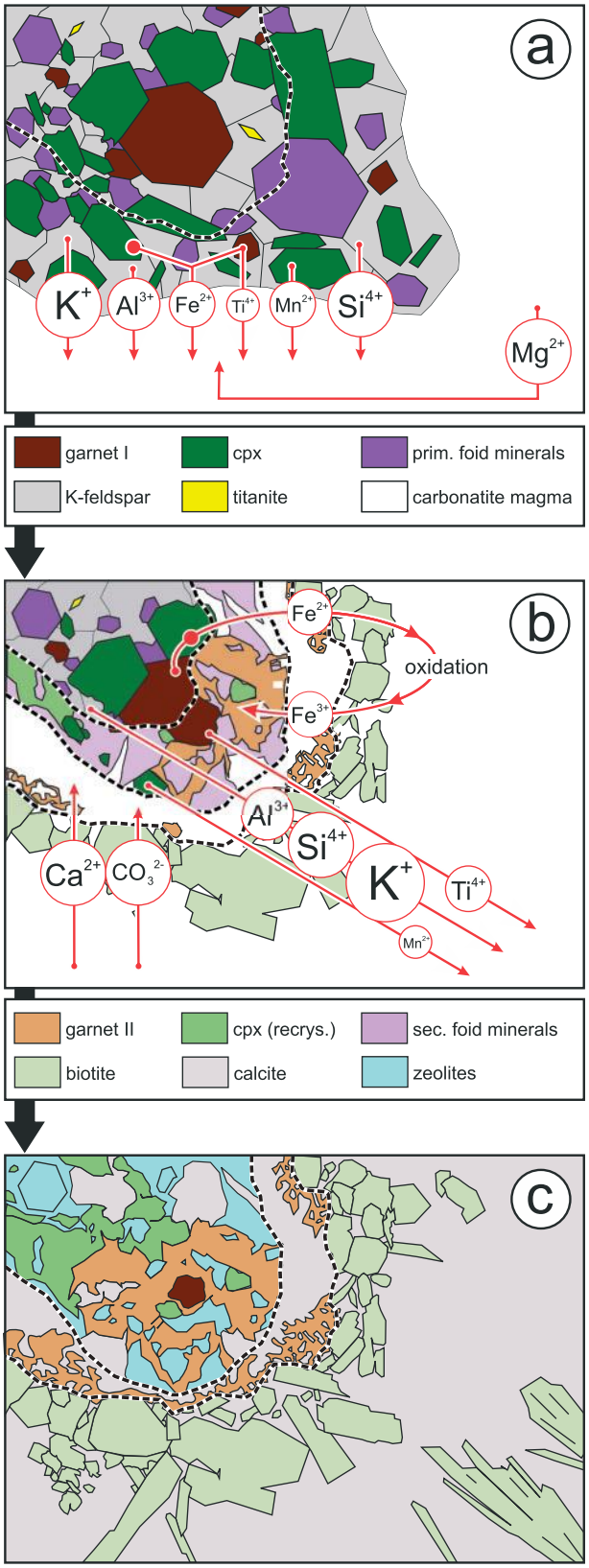

Fig. 16. Schematic diagram illustrating processes during contamination of carbonatitic melt by wall rock. (a) Interaction of carbonatitic melt with xenoliths of nosean syenite leads to resorption of primary minerals in marginal zones and associated release of some elements into the melt. (b) The released elements cause the formation of mica in black-walls, with Mg mostly provided by the carbonatitic melt. Contemporaneously Fe^{3+}, Ca and CO_3^{2-} are incorporated in recrystallized garnet II, diopsidic clinopyroxene II and calcite. (c) Completely resorbed/recrystallized xenolith (now represented as calcite foidolite) with relictic garnet I; primary nosean is completely replaced by zeolite.

2009; Giebel *et al.*, 2019). In many carbonatites mica is more or less equally distributed in the rock, but some carbonatites contain cm- to m-sized mica-rich areas as schlieren and lenses and even mica-dominated rocks (glimmerites) occur in some cases at the contact between carbonatites and the host rocks (glimmeritization; e.g. Gittins *et al.*, 1975; Hoatson *et al.*, 2011).

Our study shows that interaction of carbonatite magma with silicate rocks may induce mica crystallization in carbonatites due to the mobilization and redistribution of K, Si, Al, Mg, Fe and H_2O (reaction 4). Similarly, Vuorinen & Skelton (2004) and Chakhmouradian *et al.* (2008) showed that mica with an unusual Fe^{2+}-rich composition in the Alnö and Eden Lake sövites most probably is the product of the reaction between the carbonatite melt and the silicate host rocks. Thereby, the general question arises whether 'pure' carbonatites are capable of crystallizing mica in larger quantities at all, or whether an additional enrichment of K, Al, Si and Fe by contamination and interaction with silicate wall rocks is critically important. Sufficient Mg occurs in the carbonatite magma itself and experimental studies have shown that carbonate melts are capable of containing relatively high concentrations of H_2O (e.g. 10 wt % at 1 kbar; Keppler, 2003). However, the available experimental data indicate that carbonatites can dissolve only minor amounts of Al (usually $<$1 wt % Al_2O_3; Brooker & Kjarsgaard, 2011) and Si ($<$2·9 wt % SiO_2) at conditions pertinent to the KVC (750–1200 °C, subvolcanic pressures; Weidendorfer *et al.*, 2017).

We performed mass balance calculations based on these experimental constraints, typical Al and Si concentrations in mica from the Badberg (and various other carbonatites) and carbonatite melt densities (2·2–2·6 g/cm^3) estimated for middle to shallow crustal levels at 800–1200 °C (e.g. Wolff, 1994; Genge *et al.*, 1995; Dobson *et al.*, 1996; Kono *et al.*, 2014). These calculations indicate that only minor modal amounts of mica ($<$7%) can form from a carbonatitic melt – assuming that sufficient K, Mg and H_2O are available and no other silicate minerals are present (ES1, Supplementary Data; supplementary data are available for downloading at http://www.petrology.oxfordjournals.org). Consequently, larger amounts of mica in carbonatites would require an additional external introduction of Si and Al. In fact, the enrichment of Al in some carbonatites has been ascribed to the resorption of feldspar from fenitized wall rocks (McCormick & Le Bas, 1996), which obviously also releases alkalis and Si. Further, because of the relatively early fractionation of mica in

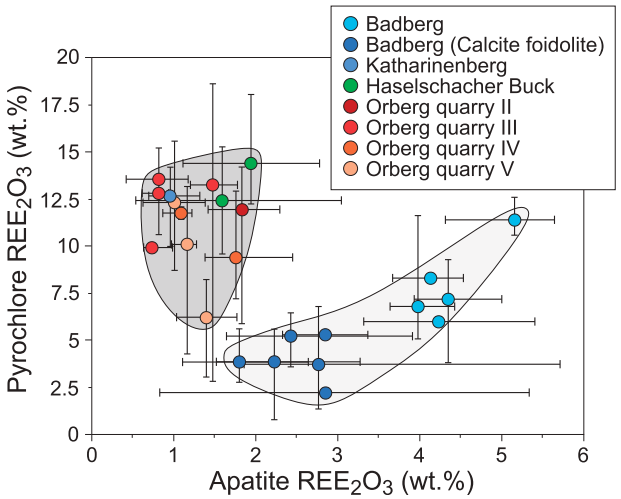

Fig. 17. Comparison of REE concentrations in pyrochlore and apatite in sövites from different localities in the KVC. The error bars represent the maximum or the minimum values, respectively, for pyrochlore/apatite within a sample.

carbonatites, rather mica-poor carbonatites are generally expected at shallow crustal levels. This further excludes the possibility that a compositionally distinct carbonatite magma is responsible for the unusual enrichment of mica in the Badberg sövites. Hence, contamination may play a key-role for enhanced mica formation in evolved carbonatitic systems, such as the KVC. This notion is most likely also applicable for the formation of other silicate minerals (e.g. Anenburg & Mavrogenes, 2018). Here, though, different processes have to be distinguished, including: (1) assimilation of wall rocks/crystals (occurrence of xenoliths/xenocrysts); (2) interaction with wall rocks via diffusion along compositional gradients (wall rock modifications); and (3) introduction of alkali-rich fluids (not easily detectable).

CONCLUSIONS AND IMPLICATIONS

It is generally supposed that crustal contamination plays a negligible role during carbonatite intrusion due to the high rate of magma ascent, extremely low viscosity and occasionally extraordinary low temperatures of carbonatitic magmas (Treiman & Schedl, 1983; Jones *et al.*, 2013 and references therein). At the same time, carbonatitic magmas are known to be extremely reactive because of their massive compositional contrast to almost all crustal rock types and cogenetic silicate rocks (the strong geochemical gradients result in intense diffusional processes) and because of their high amounts of fluxing agents such as P, F and other volatiles, causing various types of metasomatic reactions in deep-seated mantle regions as well as at shallow crustal levels.

Especially shallow-level carbonatites in active rift zones, of which the Kaiserstuhl Volcanic Complex (Southwest Germany) is a good example, may be associated with brittle deformation during and after magma emplacement, which may support disaggregation and entrainment of fragments and rafts of country rocks and/or cogenetic intrusive rocks. Sub-surface levels may even promote the fragmentation of wall rocks by explosive eruptions, where fragments of wall rock may be partly resorbed by carbonatite melt prior to consolidation.

Our study presents textural and geochemical evidence that intense interaction between carbonatite magma and fragments of earlier, cogenetic, intrusive silicate rocks at a shallow emplacement level can indeed influence the mineralogy and mineral chemistry of sövites. This contamination process causes a mineralogical and geochemical modification of both carbonatite and silicate rocks.

Mica that crystallized from such locally contaminated carbonatites may incorporate relatively high amounts of octahedral Fe^{2+}, which is atypical of carbonatites in general. Such contamination processes may even influence the timing, type and intensity of REE mineralization and hence may be able to cause a relocation of economic levels in a carbonatitic system. In the Badberg case, wall rock interaction causes preferred incorporation of REE in apatite during the magmatic stage. This resulted in relative REE depletion during the late-magmatic/hydrothermal stages. At Orberg, however, contamination processes probably did not play an important role and indeed, REE enrichment in pyrochlore in these samples is much more intense during the hydrothermal stage. However, the otherwise commonly observed formation of late magmatic and hydrothermal REE-F-carbonate minerals (e.g. bastnäsite, synchysite, parisite) in carbonatites is largely lacking at the KVC.

ACKNOWLEDGEMENTS

We thank Wolfhard Wimmenauer (University of Freiburg) and Manfred Martin (LRGB Freiburg) for providing sample material. Wolfhard Wimmenauer was of invaluable help during field work and we are very grateful that he took the time to show one of us (B.W.) outcrops forgotten for decades. We especially thank Klaus Brauch, Michael Tauchnitz, Claudia Pohl, Dietmar Kopp, Gregory Symons (terratec Geophysical Services), Samuel Weatherley, Graham Banks and Björn Heincke (Geological Survey of Denmark and Greenland), Pete Siegfried (Geo-Africa Prospecting Services cc) and Kathryn Goodenough (British Geological Survey), for insightful discussions on the structural framework of the KVC. Anatoly Zaitsev (University of St. Petersburg), Anton Chakhmouradian (University of Manitoba) and Udo Neumann (University of Tübingen) are gratefully acknowledged for constructive discussions on various topics related to this study. We further thank Rainer Babiel and Stefan Kreissl for their continuous support during analytical sessions and Simone Schafflick for thin section preparation. Finally, we thank Michael Anenburg, Ingrid Hornig-Kjarsgaard, Alasdair Skelton

and an anonymous reviewer, as well as Editor Gerhard Wörner, for their attentive reviews that allowed us to improve this manuscript significantly.

FUNDING

This work was supported by the Alexander von Humboldt Foundation [sponsorship of A. Parsapoor–Georg Forster Research Fellowship] and has further received funding from the European Union's Horizon 2020 research and innovation programme [grant agreement No 689909]. R.J. Giebel and S. Braunger are supported by the Deutsche Forschungsgemeinschaft [grants MA 2563/10 and MA2563/12, respectively].

SUPPLEMENTARY DATA

Supplementary data are available at *Journal of Petrology* online.

REFERENCES

Andersen, T. (1988). Evolution of peralkaline calcite carbonatite magma in the Fen complex, southeast Norway. *Lithos* **22**, 99–112.

Anenburg, M., Burnham, A. D. & Mavrogenes, J. A. (2018). Ree redistribution textures in altered fluorapatite: symplectites, veins, and phosphate-silicate-carbonate assemblages from the Nolans Bore P-REE-Th deposit, Northern Territory, Australia. *The Canadian Mineralogist* **56**, 331–354.

Anenburg, M. & Mavrogenes, J. A. (2018). Carbonatitic versus hydrothermal origin for fluorapatite REE-Th deposits: Experimental study of REE transport and crustal "antiskarn" metasomatism. *American Journal of Science* **318**, 335–366.

Andrade, F., Möller, P., Lüders, V., Dulski, P. & Gilg, H. (1999). Hydrothermal rare earth elements mineralization in the Barra do Itapirapuã carbonatite, southern Brazil: behaviour of selected trace elements and stable isotopes (C, O). *Chemical Geology* **155**, 91–113.

Armstrong, J. T. (1991). Quantitative elemental analysis of individual microparticles with electron beam instruments. In: Heinrich, K. F. J. and Newbury, D. E. (eds) *Electron Probe Quantitation*. New York: Plenum Press, pp. 261–315.

Baranyi, I., Lippolt, H. J. & Todt, W. (1976). K-Ar Altersbestimmungen an tertiaren Vulkaniten des Oberrheingraben-Gebietes: II Die Alterstraverse vom Hegau nach Lothringen. *Oberrheinische Geologische Abhandlungen* **25**, 41–62.

Barker, D. S. (2001). Calculated silica activities in carbonatite liquids. *Contributions to Mineralogy and Petrology* **141**, 704–709.

Beccaletto, L., Capar, L., Cruz-Mermy, D., Rupf, I., Nitsch, E., Oliviero, G., Elsass, P., Perrin, A. & Marc, S. (2010). The GeORG Project - Geological Potential of the Upper Rhine Graben - Situation, goals and first scientific results, 23ème Réunion des Sciences de la Terre (RST2010). BRGM, Bordeaux, France, HAL ID: hal-00642768.

Bell, K. & Tilton, G. R. (2002). Probing the mantle: the story from carbonatites. *Eos, Transactions American Geophysical Union* **83**, 273–277.

Bell, K., Zaitsev, A., Spratt, J., Fröjdö, S. & Rukhlov, A. (2015). Elemental, lead and sulfur isotopic compositions of galena from Kola carbonatites, Russia–implications for melt and mantle evolution. *Mineralogical Magazine* **79**, 219–241.

Blust, G. (1993). Petrographie und Geochemie der silikatischen Ganggesteine der Bohrung KB3 Steinreise. PhD thesis, Albert-Ludwigs University Freiburg, p. 83.

Bourgeois, O., Ford, M., Diraison, M., De Veslud, C. L. C., Gerbault, M., Pik, R., Ruby, N. & Bonnet, S. (2007). Separation of rifting and lithospheric folding signatures in the NW-Alpine foreland. *International Journal of Earth Sciences* **96**, 1003–1031.

Brauch, K. W., Pohl, C. M., Symons, G. & Tauchnitz, M. (2018). *Paper on Instrument Test and Best Practice for Carbonatites and Alkaline Rocks. Horizon2020 Internal Report, HiTechAlkCarb Project No.689909*. Terratec Geoservices. D4.2. p. 78.

Braunger, S., Marks, M., Walter, B. F., Neubauer, R., Reich, R., Wenzel, T., Parsapoor, A. & Markl, G. (2018). The petrology of the Kaiserstuhl Volcanic Complex, SW Germany: the importance of oxidized lithosphere for carbonatite generation. *Journal of Petrology* **59**, 1731–1762.

Brod, J., Gaspar, J., De Araújo, D., Gibson, S., Thompson, R. & Junqueira-Brod, T. (2001). Phlogopite and tetra-ferriphlogopite from Brazilian carbonatite complexes: petrogenetic constraints and implications for mineral-chemistry systematics. *Journal of Asian Earth Sciences* **19**, 265–296.

Brooker, R. & Kjarsgaard, B. (2011). Silicate-carbonate liquid immiscibility and phase relations in the system SiO_2–Na_2O–Al_2O_3–CaO–CO_2 at 0.1-2.5 GPa with applications to carbonatite genesis. *Journal of Petrology* **52**, 1281–1305.

Chakhmouradian, A., Mumin, A., Demény, A. & Elliott, B. (2008). Postorogenic carbonatites at Eden Lake, Trans-Hudson Orogen (northern Manitoba, Canada): geological setting, mineralogy and geochemistry. *Lithos* **103**, 503–526.

Chakhmouradian, A. R. (2006). High-field-strength elements in carbonatitic rocks: geochemistry, crystal chemistry and significance for constraining the sources of carbonatites. *Chemical Geology* **235**, 138–160.

Chakhmouradian, A. R., Reguir, E. P., Zaitsev, A. N., Couëslan, C., Xu, C., Kynický, J., Mumin, A. H. & Yang, P. (2017). Apatite in carbonatitic rocks: compositional variation, zoning, element partitioning and petrogenetic significance. *Lithos* **274**, 188–213.

Chakhmouradian, A. R. & Zaitsev, A. N. (2002). Calcite–amphibole–clinopyroxene rock from the Afrikanda complex, Kola Peninsula, Russia: mineralogy and a possible link to carbonatites. III. Silicate minerals. *The Canadian Mineralogist* **40**, 1347–1374.

Chakrabarty, A., Sen, A. K. & Ghosh, T. K. (2009). Amphibole—a key indicator mineral for petrogenesis of the Purulia carbonatite, West Bengal, India. *Mineralogy and Petrology* **95**, 105–112.

Czygan, W. (1977). Petrographie und Geochemie der Foidsyenit-Einschlusse im Phonolith von Niederrotweil im Kaiserstuhl. *Berichte der Naturforschenden Gesellschaft Freiburg im Breisgau* **67**, 41–52.

de Oliveira, S. M. B. & Imbernon, R. A. L. (1998). Weathering alteration and related REE concentration in the Catalão I carbonatite complex, central Brazil. *Journal of South American Earth Sciences* **11**, 379–388.

de Toledo, M. C. M., Lenharo, S. L., Ferrari, V. C., Fontan, F., de Parseval, P. & Leroy, G. (2004). The compositional evolution of apatite in the weathering profile of the Catalão I alkaline-carbonatitic complex, Goiás, Brazil. *The Canadian Mineralogist* **42**, 1139–1158.

Dèzes, P., Schmid, S. & Ziegler, P. (2004). Evolution of the European Cenozoic Rift System: interaction of the Alpine

and Pyrenean orogens with their foreland lithosphere. *Tectonophysics* **389**, 1–33.

Dobson, D. P., Jones, A. P., Rabe, R., Sekine, T., Kurita, K., Taniguchi, T., Kondo, T., Kato, T., Shimomura, O. & Urakawa, S. (1996). In-situ measurement of viscosity and density of carbonate melts at high pressure. *Earth and Planetary Science Letters* **143**, 207–215.

Doroshkevich, A. G., Viladkar, S. G., Ripp, G. S. & Burtseva, M. V. (2009). Hydrothermal REE mineralization in the Amba Dongar carbonatite complex, Gujarat, India. *The Canadian Mineralogist* **47**, 1105–1116.

Edel, J.-B., Whitechurch, H. & Diraison, M. (2006). Seismicity wedge beneath the Upper Rhine Graben due to backwards Alpine push? *Tectonophysics* **428**, 49–64.

Elliott, H., Wall, F., Chakhmouradian, A., Siegfried, P., Dahlgren, S., Weatherley, S., Finch, A., Marks, M., Dowman, E. & Deady, E. (2018). Fenites associated with carbonatite complexes: a review. *Ore Geology Reviews* **93**, 38–59.

Farrell, S., Bell, K. & Clark, I. (2010). Sulphur isotopes in carbonatites and associated silicate rocks from the Superior Province, Canada. *Mineralogy and Petrology* **98**, 209–226.

Foster, M. D. (1960). Interpretation of the composition of trioctahedral micas. *U.S. Geological Survey Professional Paper*, 49.

Gendron, L., Bis, R. & Rodrigue, M. (1984). Underground mining and pyrochlore ore processing at Niobec Mine, Quebec, Canada. In: Stuart, H. (ed.) *Niobium, Proceedings of the International Symposium of the Metallurgical Society of AIME (American Institute of Mining, Metallurgical and Petroleum Engineers)*. Warrendale, Pennsylvania, pp. 79–96.

Genge, M. J., Price, G. D. & Jones, A. P. (1995). Molecular dynamics simulations of CaCO3 melts to mantle pressures and temperatures: implications for carbonatite magmas. *Earth and Planetary Science Letters* **131**, 225–238.

Giebel, R. J., Gauert, C. D. K., Marks, M. A. W., Costin, G. & Markl, G. (2017). Multi-Stage formation of REE minerals in the Palabora Carbonatite Complex, South Africa. *American Mineralogist* **102**, 1218–1233.

Giebel, R. J., Marks, M. A. W., Gauert, C. D. K. & Markl, G. (2019). A model for the formation of carbonatite-phoscorite assemblages based on the compositional variation of mica and apatite from the Palabora Carbonatite Complex, South Africa. *Lithos* **324–325**, 89–104.

Gittins, J., Allen, C. & Cooper, A. (1975). Phlogopitization of pyroxenite; its bearing on the composition of carbonatite magmas. *Geological Magazine* **112**, 503–507.

Gomide, C. S., Brod, J. A., Junqueira-Brod, T. C., Buhn, B. M., Santos, R. V., Barbosa, E. S. R., Cordeiro, P. F. O., Palmieri, M., Grasso, C. B. & Torres, M. G. (2013). Sulfur isotopes from Brazilian alkaline carbonatite complexes. *Chemical Geology* **341**, 38–49.

Groschopf, R., Kessler, G., Leiber, J., Maus, H., Ohmert, W., Schreiner, A. & Wimmenauer, W. (1996). *Erläuterungen zur Geologischen Karte Von Baden-Württemberg Freiburg i. Br. und Umgebung*. Freiburg: Geologische Landesamt Baden-Würrtemberg.

Guzmics, T., Mitchell, R. H., Szabó, C., Berkesi, M., Milke, R. & Abart, R. (2011). Carbonatite melt inclusions in coexisting magnetite, apatite and monticellite in Kerimasi calciocarbonatite, Tanzania: melt evolution and petrogenesis. *Contributions to Mineralogy and Petrology* **161**, 177–196.

Hammouda, T., Chantel, J. & Devidal, J.-L. (2010). Apatite solubility in carbonatitic liquids and trace element partitioning between apatite and carbonatite at high pressure. *Geochimica et Cosmochimica Acta* **74**, 7220–7235.

Hay, R. & O'Neil, J. (1983). Carbonatite tuffs in the Laetolil Beds of Tanzania and the Kaiserstuhl in Germany. *Contributions to Mineralogy and Petrology* **82**, 403–406.

Heathcote, R. C. & McCormick, G. R. (1989). Major-cation substitution in phlogopite and evolution of carbonatite in the Potash Sulphur Springs complex, Garland County, Arkansas. *American Mineralogist* **74**, 132–140.

Hoatson, D. M., Jaireth, S. & Miezitis, Y. (2011). The major rare-earth-element deposits of Australia: geological setting, exploration and resources. Canberra: Geoscience Australia.

Hogarth, D. (1989). Pyrocholre, apatite and amphibole: distinctive minerals in carbonatite. In: Bell, K. (ed.) *Carbonatites: Genesis and Evolution*. London: Unwin Hyman, pp. 105–148.

Hornig-Kjarsgaard, I. (1998). Rare earth elements in sövitic carbonatites and their mineral phases. *Journal of Petrology* **39**, 2105–2121.

Hubaux, A. (1964). Sructure des carbonatites de Schelingen. In: Van Wambeke, L. (ed.) *Les Roches Alcalines et Les Carbonatites du Kaiserstuhl*. Brussels: European Atomic Energy Community (EURATOM). Mineralogy Geochemistry Section, pp. 31–46.

Hubberten, H.-W., Katz-Lehnert, K. & Keller, J. (1988). Carbon and oxygen isotope investigations in carbonatites and related rocks from the Kaiserstuhl, Germany. *Chemical Geology* **70**, 257–274.

Hurai, V., Huraiová, M., Gajdošová, M., Konečný, P., Slobodník, M. & Siegfried, P. R. (2018). Compositional variations of zirconolite from the Evate apatite deposit (Mozambique) as an indicator of magmatic-hydrothermal conditions during post-orogenic collapse of Gondwana. *Mineralogy and Petrology* **112**, 279–296.

Hüttner, R. (1996). Tektonik im Grundgebirge. In: Groschopf, R., Kessler, G., Leiber, J., Maus, H., Ohmert, A., Schreiner, A. & Wimmenauer, A. (eds) *Geologische Karte Von Baden-Württemberg 1: 50000, Freiburg i.Br. und Umgebung*. Freiburg im Breisgau, Germany: Landesamt für Geologie, Rohstoffe und Bergbau Baden-Württemberg, pp. 119–228.

Ivanyuk, G. Y., Yakovenchuk, V. & Pakhomovsky, Y. A. (2002). *Kovdor*. Apatity, Russia: Laplandia Minerals, p. 326.

Jago, B. C. & Gittins, J. (1991). The role of fluorine in carbonatite magma evolution. *Nature* **349**, 56.

Jones, A. P., Genge, M. & Carmody, L. (2013). Carbonate melts and carbonatites. *Reviews in Mineralogy and Geochemistry* **75**, 289–322.

Jurewicz, A. J. & Watson, E. B. (1988). Cations in olivine, Part 2: diffusion in olivine xenocrysts, with applications to petrology and mineral physics. *Contributions to Mineralogy and Petrology* **99**, 186–201.

Kanazawa, Y. & Kamitani, M. (2006). Rare earth minerals and resources in the world. *Journal of Alloys and Compounds* **408**, 1339–1343.

Katz, K. & Keller, J. (1981). Comb-layering in carbonatite dykes. *Nature* **294**, 350–352.

Katz-Lehnert, K. (1989). Petrologie der Gangkarbonatite im Kaiserstuhl. PhD thesis, Albert-Ludwigs University Freiburg, p. 290.

Keller, J. (1978). Karbonatitische Schmelzen im Oberflächenvulkanismus des Kaiserstuhls. *Fortschritte der Mineralogie* **56**, 1–58.

Keller, J. (1981). Carbonatitic volcanism in the Kaiserstuhl alkaline complex: evidence for highly fluid carbonatitic melts at the earth's surface. *Journal of Volcanology and Geothermal Research* **9**, 423–431.

Keller, J. (1984). Der jungtertiäre Vulkanismus Südwestdeutschlands: Exkursionen im Kaiserstuhl und Hegau. *Fortschritte der Mineralogie* **62**, 2–35.

Keller, J. (1989). Extrusive carbonatites and their significance. In: Bell, K. (ed.) *Carbonatites: genesis and Evolution*. London: Unwin Hyman, pp. 70–88.

Keller, J., Brey, G., Lorenz, V., Sachs, P. & Schleicher, H. (1990). Pre-conference excursion 2A: volcanism and petrology of the Upper Rhinegraben (Urach-Hegau-Kaiserstuhl). *IAVCEI International Volcanic Congress Mainz*, p. 60.

Keppler, H. (2003). Water solubility in carbonatite melts. *American Mineralogist* **88**, 1822–1824.

Ketcham, R. A. (2015). Calculation of stoichiometry from EMP data for apatite and other phases with mixing on monovalent anion sites. *American Mineralogist* **100**, 1620–1623.

Kharlomov, Y. S. (1981). Origin of carbonatites of the Kovdor deposit. *International Geology Review* **23**, 865–880.

Kirchheimer, F. (1973). Weitere Mitteilungen über das Vorkommen radioaktiver Substanzen in Süddeutschland. *Jahresheft des Geologischen Landesamtes Baden-Württemberg* **15**, 33–125.

Klemme, S. & Dalpé, C. (2003). Trace-element partitioning between apatite and carbonatite melt. *American Mineralogist* **88**, 639–646.

Kogarko, L. N., Ryabchikov, I. D. & Kuzmin, D. V. (2012). High-Ba mica in olivinites of the Guli massif (Maimecha–Kotui province, Siberia). *Russian Geology and Geophysics* **53**, 1209–1215.

Kono, Y., Kenney-Benson, C., Hummer, D., Ohfuji, H., Park, C., Shen, G., Wang, Y., Kavner, A. & Manning, C. E. (2014). Ultralow viscosity of carbonate melts at high pressures. *Nature Communications* **5**, 5091.

Kraml, M., Pik, R., Rahn, M., Selbekk, R., Carignan, J. & Keller, J. (2006). A new multi-mineral age reference material for 40Ar/39Ar,(U-Th)/He and fission track dating methods: The Limberg t3 Tuff. *Geostandards and Geoanalytical Research* **30**, 73–86.

Krasnova, N., Balaganskaya, E. & Garcia, D. (2004). Kovdor - classic phoscorites and carbonatites. In: Wall, F. & Zaitev, A. N. (eds) *Phoscorites and Carbonatites from Mantle to Mine: The Key Example of the Kola Alkaline Province.* London, GB: Mineralogical Society of Great Britain and Ireland, pp. 99–132.

Le Maitre, R., Streckeisen, A., Zanettin, B., Le Bas, M., Bonin, B., Bateman, P., Bellieni, G., Dudek, A., Efremova, A. & Keller, J. (2002). Igneous rocks. A classification and glossary of terms. *Recommendations of the IUGS Subcomission on the Systematics of Igneous Rocks.* Cambridge: Cambridge University Press, p. 236.

Lee, M., Garcia, D., Moutte, J., Williams, C. & Wall, F. (2004). Carbonatites and phoscorites from the Sokli Complex, Finland. In: Wall, F. & Zaitev, A. N. (eds) *Phoscorites and Carbonatites from Mantle to Mine: The Key Example of the Kola Alkaline Province.* London, UK: Mineralogical Society, pp. 133–162.

Lee, M. J., Garcia, D., Moutte, J. & Lee, J. I. (2003). Phlogopite and tetraferriphlogopite from phoscorite and carbonatite associations in the Sokli massif, Northern Finland. *Geosciences Journal* **7**, 9–20.

Libourel, G. (1999). Systematics of calcium partitioning between olivine and silicate melt: implications for melt structure and calcium content of magmatic olivines. *Contributions to Mineralogy and Petrology* **136**, 63–80.

Locock, A. J. (2008). An Excel spreadsheet to recast analyses of garnet into end-member components and a synopsis of the crystal chemistry of natural silicate garnets. *Computers & Geosciences* **34**, 1769–1780.

Massuyeau, M., Gardès, E., Morizet, Y. & Gaillard, F. (2015). A model for the activity of silica along the carbonatite–kimberlite–mellilitite–basanite melt compositional joint. *Chemical Geology* **418**, 206–216.

McCormick, G. R. & Heathcote, R. C. (1987). Mineral chemistry and petrogenesis of carbonatite intrusions, Perry and Conway Counties, Arkansas. *American Mineralogist* **72**, 59–66.

McCormick, G. R. & Le Bas, M. J. (1996). Phlogopite crystallization in carbonatitic magmas from Uganda. *The Canadian Mineralogist* **34**, 469–478.

Mitchell, R. H. (2005). Carbonatites and carbonatites and carbonatites. *The Canadian Mineralogist* **43**, 2049–2068.

Moore, M., Chakhmouradian, A. R., Mariano, A. N. & Sidhu, R. (2015). Evolution of rare-earth mineralization in the Bear Lodge carbonatite, Wyoming: Mineralogical and isotopic evidence. *Ore Geology Reviews* **64**, 499–521.

Nesbitt, B. E. & Kelly, W. C. (1977). Magmatic and hydrothermal inclusions in carbonatite of the Magnet Cove Complex, Arkansas. *Contributions to Mineralogy and Petrology* **63**, 271–294.

Neumann, R. & Medeiros, E. B. (2015). Comprehensive mineralogical and technological characterisation of the Araxá (SE Brazil) complex REE (Nb-P) ore and the fate of its processing. *International Journal of Mineral Processing* **144**, 1–10.

Panina, L. I. (2005). Multiphase carbonate-salt immiscibility in carbonatite melts: data on melt inclusions from the Krestovskiy massif minerals (Polar Siberia). *Contributions to Mineralogy and Petrology* **150**, 19–36.

Reguir, E., Chakhmouradian, A., Halden, N., Malkovets, V. & Yang, P. (2009). Major-and trace-element compositional variation of phlogopite from kimberlites and carbonatites as a petrogenetic indicator. *Lithos* **112**, 372–384.

Reguir, E. P., Chakhmouradian, A. R., Pisiak, L., Halden, N. M., Yang, P., Xu, C., Kynický, J. & Couëslan, C. G. (2012). Trace-element composition and zoning in clinopyroxene-and amphibole-group minerals: implications for element partitioning and evolution of carbonatites. *Lithos* **128**, 27–45.

Schleicher, H., Keller, J. & Kramm, U. (1990). Isotope studies on alkaline volcanics and carbonatites from the Kaiserstuhl, Federal Republic of Germany. *Lithos* **26**, 21–35.

Sigmund, J. (1996). Diatrembreccien, Mantelxenolithe und Karbonatite in der Kernbohrung KB 2 im Kaiserstuhl. PhD thesis, Albert-Ludwigs University, Freiburg, p. 154.

Sinclair, W. & Eggleton, R. (1982). Structure refinement of zirkelite from Kaiserstuhl, West Germany. *American Mineralogist* **67**, 615–620.

Sommerauer, J. & Katz-Lehnert, K. (1985). A new partial substitution mechanism of CO_3^{2-}/CO_3OH^{3-} and SiO_4^{4-} for the PO_4^{3-} group in hydroxyapatite from the Kaiserstuhl alkaline complex (SW-Germany). *Contributions to Mineralogy and Petrology* **91**, 360–368.

Stoppa, F. & Lupini, L. (1993). Mineralogy and petrology of the Polino monticellite calciocarbonatite (Central Italy). *Mineralogy and Petrology* **49**, 213–231.

Teiber, H., Marks, M. A., Arzamastsev, A. A., Wenzel, T. & Markl, G. (2015). Compositional variation in apatite from various host rocks: clues with regards to source composition and crystallization conditions. *Neues Jahrbuch für Mineralogie - Abhandlungen* **192**, 151–167.

Treiman, A. H. & Essene, E. J. (1984). A periclase-dolomite-calcite carbonatite from the Oka complex, Quebec and its calculated volatile composition. *Contributions to Mineralogy and Petrology* **85**, 149–157.

Treiman, A. H. & Schedl, A. (1983). Properties of carbonatite magma and processes in carbonatite magma chambers. *The Journal of Geology* **91**, 437–447.

Van Wambeke, L. (1964). Geochemie minerale des carbonatites du Kaiserstuhl. In: Van Wambeke, L. (ed.) *Les Roches Alcalines et Les Carbonatites du Kaiserstuhl*. Brussels: European Atomic Energy Community (EURATOM). Mineralogy Geochemistry Section, pp. 65–92.

Vuorinen, J. H. & Skelton, A. D. (2004). Origin of silicate minerals in carbonatites from Alnö Island, Sweden: magmatic crystallization or wall rock assimilation? *Terra Nova* **16**, 210–215.

Wall, F. & Mariano, A. N. (1996). Rare earth minerals in carbonatites: a discussion centred on the Kangankunde Carbonatite, Malawi. In: Jones, A. P., Wall, F. & Williams, C. T. (eds) *Rare Earth Minerals: Chemestry, Origin and Ore Deposits. Mineralogical Society Series*. London: Chapman and Hall, pp. 193–226.

Walter, B. F., Parsapoor, A., Braunger, S., Marks, M. A. W., Wenzel, T., Martin, M. & Markl, G. (2018). Pyrochlore as a monitor for magmatic and hydrothermal processes in carbonatites from the Kaiserstuhl volcanic complex, SW Germany *Chemical Geology* **498**, 1–16.

Wang, L.-X., Marks, M. A., Wenzel, T., Von Der Handt, A., Keller, J., Teiber, H. & Markl, G. (2014). Apatites from the Kaiserstuhl Volcanic Complex, Germany: new constraints on the relationship between carbonatite and associated silicate rocks. *European Journal of Mineralogy* **26**, 397–414.

Weidendorfer, D., Schmidt, M. W. & Mattsson, H. B. (2017). A common origin of carbonatite magmas. *Geology* **45**, 507–510.

Williams, C. & Gieré, R. (1996). Zirconolite: a review of localities worldwide and a compilation of its chemical compositions. *Bulletin of the Natural History Museum London* **52**, 1.

Wilson, M. & Downes, H. (1991). Tertiary-Quaternary extension-related alkaline magmatism in western and central Europe. *Journal of Petrology* **32**, 811–849.

Wimmenauer, W. (1963). Beiträge zur Petrographie des Kaiserstuhls. *Teil VI: Die Karbonatite; Teil VII: Zur Petrogenese des Kaiserstuhls. Neues Jahrbuch der Mineralogie, Abhandlungen* **99**, 231–276.

Wimmenauer, W. (2003). Kaiserstuhl. In: *Geologische Karte Von Baden-Württemberg 1: 25.000 Mit Erläuterungen*. Freiburg: Landesamt für Geologie, Rohstoffe und Bergbau Baden-Württemberg.

Wolff, J. (1994). Physical properties of carbonatite magmas inferred from molten salt data and application to extraction patterns from carbonatite–silicate magma chambers. *Geological Magazine* **131**, 145–153.

Woolley, A. & Church, A. (2005). Extrusive carbonatites: a brief review. *Lithos* **85**, 1–14.

Woolley, A. R. & Kjarsgaard, B. A. (2008). *Carbonatite Occurrences of the World: Map and Database*. Geological Survey of Canada. Open File 5796.

Yang, K.-F., Fan, H.-R., Santosh, M., Hu, F.-F. & Wang, K.-Y. (2011). Mesoproterozoic carbonatitic magmatism in the Bayan Obo deposit, Inner Mongolia, North China: constraints for the mechanism of super accumulation of rare earth elements. *Ore Geology Reviews* **40**, 122–131.

Zaitsev, A. N., Wall, F. & Le Bas, M. J. (1998). REE-Sr-Ba minerals from the Khibina carbonatites, Kola Peninsula, Russia: their mineralogy, paragenesis and evolution. *Mineralogical Magazine* **62**, 225–250.

Ziegler, P. (1982). Triassic rifts and facies patterns in Western and Central Europe. *Geologische Rundschau* **71**, 747–772.

Appendix IV

Accepted publication

Study D

Dietzel, C.A.F., Kristandt, T., Dahlgren, S., Giebel, R.J., Marks, M.A.W. and Markl, G. (2019): Hydrothermal processes in the Fen carbonatite complex, southern Norway. *Ore Geology Reviews*. Vol. **111**.

Ore Geology Reviews 111 (2019) 102969

Contents lists available at ScienceDirect

Ore Geology Reviews

journal homepage: www.elsevier.com/locate/oregeorev

Hydrothermal processes in the Fen alkaline-carbonatite complex, southern Norway

Christian A.F. Dietzel[a,1], Tim Kristandt[a,1], Sven Dahlgren[b,c], R. Johannes Giebel[a,d], Michael A.W. Marks[a,*], Thomas Wenzel[a], Gregor Markl[a]

[a] Department of Geosciences, Eberhard Karls University, Wilhelmstr. 56, 72076 Tübingen, Germany
[b] Buskerud, Telemark and Vestfold County Councils, Fylkeshuset, Svend Foynsgt. 9, 3110 Tønsberg, Norway
[c] Department of Geociences, University of Oslo, PBox 1047 Blindern, 0316 Oslo, Norway
[d] Department of Geology, University of the Free State, 250 Nelson-Mandela-Drive, Bloemfontein 9300, South Africa

ARTICLE INFO

Keywords:
Monazite
REE-F-carbonates
Samarskite
Aeschynite
Nb-Fe-REE-Th-oxide
Rødberg

ABSTRACT

We present detailed textural and chemical analyses of the hydrothermal sulfide- and REE-Th-Nb-mineralization observed in the Fen complex (southern Norway), which is the biggest carbonatite-related REE and Th deposit in Europe. The alkaline silicate rocks and carbonatites of the Fen complex underwent two hydrothermal alteration events that caused (i) the formation of sulfides and (ii) (re)-mobilization of REE, Fe and Al. This renders the Fen complex an ideal locality to study the genesis of hydrothermal sulfide and REE mineralization in carbonatites. Our observations record a hydrothermal alteration history of the Fen carbonatite complex, which is relevant to many carbonatite complexes worldwide.

The first alteration event (pyrite-stage) caused the crystallization of sulfides (mostly pyrite) in all lithologies and was induced by a sulfide-rich fluid 1 that was probably derived from adjacent mafic alkaline silicate rocks. Veins formed during this hydrothermal event show a typical succession from magnetite via pyrite I + hematite + magnetite to pyrite II.

A subsequent alteration event is characterized by the interaction of two evolving fluids, namely (1) a REE-rich fluid 2 that was probably derived from the carbonatites (autometasomatic fluid) and (2) an oxidizing meteoric fluid 3 that mainly introduced Si and was in equilibrium with the basement host rocks. The interaction of these two fluids with the carbonatitic rocks resulted in various characteristic types of calcite-hematite rocks locally called rødberg. During their late-stage silicification by fluid 3, P was mobilized from magmatic apatite and reprecipitated in close-by rødberg veins as small fluorapatite-monazite veins.

The interaction of the carbonatite-derived fluid 2 and meteoric fluid 3 also resulted in the formation of distinct zones of LREE-phases, notably REE-F-carbonates (bastnäsite, parisite, synchysite), monazite and allanite, and HREE-phases (including samarskite, aeschynite and an unnamed Nb-Fe-REE-Th-oxide. The most pronounced HREE-enrichment occurs in domains of strongest hydrothermal alteration, which was probably caused by preferential precipitation of HREE-rich complexes coupled with later partial leaching of LREE by F-rich fluids during silicification. Thorium-rich minerals were precipitated in close association with HREE-rich minerals implying similar hydrothermal behaviour of Th and HREE.

1. Introduction

The global demand for rare earth elements (REE) is on an all-time high, with products containing REE amounting to roughly 5% of the global Gross National Product (Tukker, 2014). Therefore REE are a resource of growing importance for the industrialized world. When China (the world's main REE supplier) declared in 2009 that it would reduce exports of REE, increased interest in REE deposits and the search and re-evaluation of Europe's REE reserves began (Stone, 2009).

Carbonatite complexes are among the most promising sources of REE, although their frequently complex mineralogy and intergrowth textures pose a crucial problem in the assessment of their economic potential (Mariano and Mariano, 2012). Several studies have shown that primary REE mineralization in carbonatites often involved a multi-

* Corresponding author.
E-mail address: michael.marks@uni-tuebingen.de (M.A.W. Marks).
[1] Joint first authorship.

https://doi.org/10.1016/j.oregeorev.2019.102969
Received 6 March 2019; Received in revised form 3 June 2019; Accepted 7 June 2019
Available online 08 June 2019

stage hydrothermal alteration, which included complex replacement, remobilization and reprecipitation processes (e.g., Giebel et al., 2017; Moore et al., 2015). Since those hydrothermal processes are the main reason for the formation of economic REE deposits (e.g., Bayan Obo, Bachu, Bear Lodge, Cheng et al., 2018; Kanazawa and Kamitani, 2006; Moore et al., 2015), their understanding is of the utmost importance (e.g., Smith et al., 2015).

During hydrothermal processes, REE mainly migrate as F^-, Cl^-, OH^-, CO_3^{2-}, SO_4^{2-} or PO_4^{3-} complexes (e.g., Williams-Jones et al., 2012). Therefore, H_2O-CO_2-Cl-F fluids commonly associated with carbonatite crystallization are important for REE-mineral formation (Bühn and Rankin, 1999). Decreasing complex stability from La to Lu in hydrothermal fluids can lead to a fractionation of REE (Migdisov et al., 2009, 2016).

The biggest carbonatite-related REE resource in continental Europe is the Fen carbonatite complex in southern Norway (Goodenough et al., 2016). The hematitized carbonatites in the Fen complex (locally called rødberg) represent a prime example of highly REE- and Th-enriched rocks related to hydrothermal alteration (Andersen, 1984, 1987; Andersen and Qvale, 1986; Marien et al., 2018). Besides, the Fen complex exhibits hydrothermal sulfides (e.g., Andersen, 1984), which have not yet been thoroughly investigated. The present study combines detailed textural and chemical analyses of the hydrothermal sulfide- and REE-Th-Nb-mineralization observed in the Fen complex. These observations record a hydrothermal alteration history of the Fen carbonatite complex, which is relevant to many carbonatite complexes worldwide.

2. Geological setting

Located 110 km southwest of Oslo (Norway), the Fen complex (Fig. 1) is an Ediacaran (≈580 Ma) alkaline-carbonatite complex, situated about 13 km west of the alkaline syenite plutons of the late Paleozoic Oslo rift. The complex is roughly circular with a diameter of about 3 km and was emplaced into Precambrian Telemark orthogneisses (1190 Ma; Dahlgren et al., 1990). The present level of erosion of the central complex is estimated to be around 1 to 3 km below the Cambrian surface (Sæther, 1957). Gravimetric data suggest mafic silicate rocks extending from a few hundred metres below the present surface down to a depth of about 15 km (Ramberg, 1973).

Rocks of the Fen complex have been exploited for various resources over the last 400 years. Historical mining for hematitic iron ores from the “red-rocks” (rødberg) at the Gruveåsen mining hill took place from the 1650-ies until 1927, and later (1953 to 1965) Nb was mined from søvite in the Søve and Tufte areas (Dahlgren, 2006). The REE mineralizations of the Fen Complex are of two different types, one type highly enriched in Th, in the rødberg, and another type with much less Th in the rauhaugites (Dahlgren, 2015). Recent exploration by *REE Minerals* (www.reeminerals.no) established a REE mineralization with inferred resources of 84 Mt at 1.08 wt% REO, and smaller zones reaching concentrations up to 4.49 wt% REO (Lie and Østergaard, 2014).

The evolution of the Fen complex (very simplified) occurred during two major, magmatic stages. Stage I involved emplacement of the ijolite-melteigite-clinopyroxenite series rocks (including calcite- amphibole-, and biotite-bearing varieties, such as hollaite and vipetoite; Bergstøl and Svinndal, 1960; Brøgger, 1921) and coarse-grained calcite carbonatites (søvite; Brøgger, 1921) and dolomite carbonatites (rauhaugite, Brøgger, 1921; rauhaugite type 1, Sæther, 1957). These magmas released substantial amounts of fluids that produced fenites, i.e. an alkali metasomatism of the country rock Telemark orthogneisses (Brøgger, 1921). Stage II produced calcite-bearing ultramafic lamprophyres, (damtjernites; Brøgger, 1921; Dahlgren, 1994) and further, ferroan dolomite-bearing (rarely ankerite; see below) carbonatites (rauhaugite type 2, Sæther, 1957; ferrocarbonatite, Andersen 1984, 1986; Andersen and Qvale, 1986). During the later parts of this second stage the red hematite-calcite rocks (rødberg) was formed. Rauhaugites type 2 have been interpreted as metasomatized lamprophyres (Sæther, 1957), a cogenetic emplacement of lamprophyres and rauhaugites was suggested by Andersen (1986) and Andersen and Qvale (1986). Age data for the emplacement of the central carbonatites range from 523 to 601 Ma, with the satellitic lamprophyre dikes having an $^{40}Ar/^{39}Ar$ age of 583 ± 15 Ma (Meert et al., 1998).

The rødberg (“red rock” in Norwegian) is a calcite-hematite-rock formed by hydrothermal alteration of rauhaugite (Brøgger, 1921; Sæther, 1957; Vogt, 1910). While søvite and rauhaugite of the first magmatic stage gave $\delta^{18}O$ temperatures of 600 to 700 °C (interpreted to be orthomagmatic), $\delta^{18}O$ data for rødberg indicate a hydrothermal formation at 200–300 °C (Friedrichsen, 1968). The rødberg is mainly located in the eastern part, with small outcrops scattered throughout the complex. According to Andersen (1984) and Andersen and Qvale (1986), it was formed at the end of the rauhaugite intrusion by breakdown of Fe-bearing dolomite, magnetite and pyrite to hematite through reaction with meteoric waters. Parts of the rødberg show hydrothermal enrichment of REE and Th (Andersen, 1987; Marien et al., 2018).

3. Sample locations

Surface outcrops at Fen are scarce or protected, therefore most of the sampling was conducted in the Tufte adit, a 1 km long tunnel leading to the former Tufte Nb mine that was situated in the centre of the Fen complex (Fig. 1).

The Tufte adit (X1 on Fig. 1) crosses cm- to tens of meters thick units of søvites, rauhaugites, hollaites, fenites that are cut by hydrothermal rødberg veins and a particularly rich pyrite-magnetite vein with abundant hematite and REE-F-carbonates further referred to as Tufte adit vein. In the adit, søvites were sampled where aggregates of sulfides were visible (at 103 m, 950 m, 955 m, 957 m, 960 m, and 965 m). From 528 m to 535 m, rauhaugite with inclusions of pyrite and magnetite, as well as the massive two metres wide Tufte adit vein at about 532 m from the entrance were sampled in great detail. The rødberg was sampled at 335 m, 357 m, 403 m, 410 m, 512 m, 955 m and 1000 m. Samples at 512 m compromise rauhaugite and a transect across a 10 cm wide hydrothermal hematite-magnetite-calcite-apatite vein on the western side wall of the mine, which is strongly enriched in monazite and REE-F-carbonates. Fenites were sampled at 103 m, 174 m, 241 m, 278 m and 345 m.

At the Gruveåsen mine dump (X2 on Fig. 1) several loose blocks of silicified rødberg from former mining operations were collected and one large Th-rich rødberg sample was collected at the dump of the Vasker mine (X3 on Fig. 1). A further 13 samples derive from the cores from six drilling sites (X4–X9 on Fig. 1). They comprise søvites and rauhaugites containing mm- to cm-sized pyrite, sometimes containing aggregates of REE minerals. Søvites and rauhaugites are cut by centimetre- to metre-sized veins of differently textured rødberg, associated with centimetre-thick veins of apatite, barite and/or fluorite. Sample site X10 marks an outcrop of a freshly blasted tractor trail near Melteig farm, where fenites were sampled. Site X11 is located on a hillslope behind Melteig farm, where melteigites were collected.

A list of sample sites with lithologies and their mineralogy is given in Table 1. In all, 47 polished thin sections were investigated in detail. Additionally, four whole-rock samples from the rødberg vein and its wall rock at 512 m in the Tufte adit X1, from X2 and X3, were analyzed for their major and minor element compositions and their REE, Th and Nb content.

4. Methods

Textural analysis of polished thin sections involved transmitted and reflected light microscopy as well as backscattered electron (BSE) images of a Hitachi Tabletop SEM at the University of Tübingen using an acceleration voltage of 15 kV.

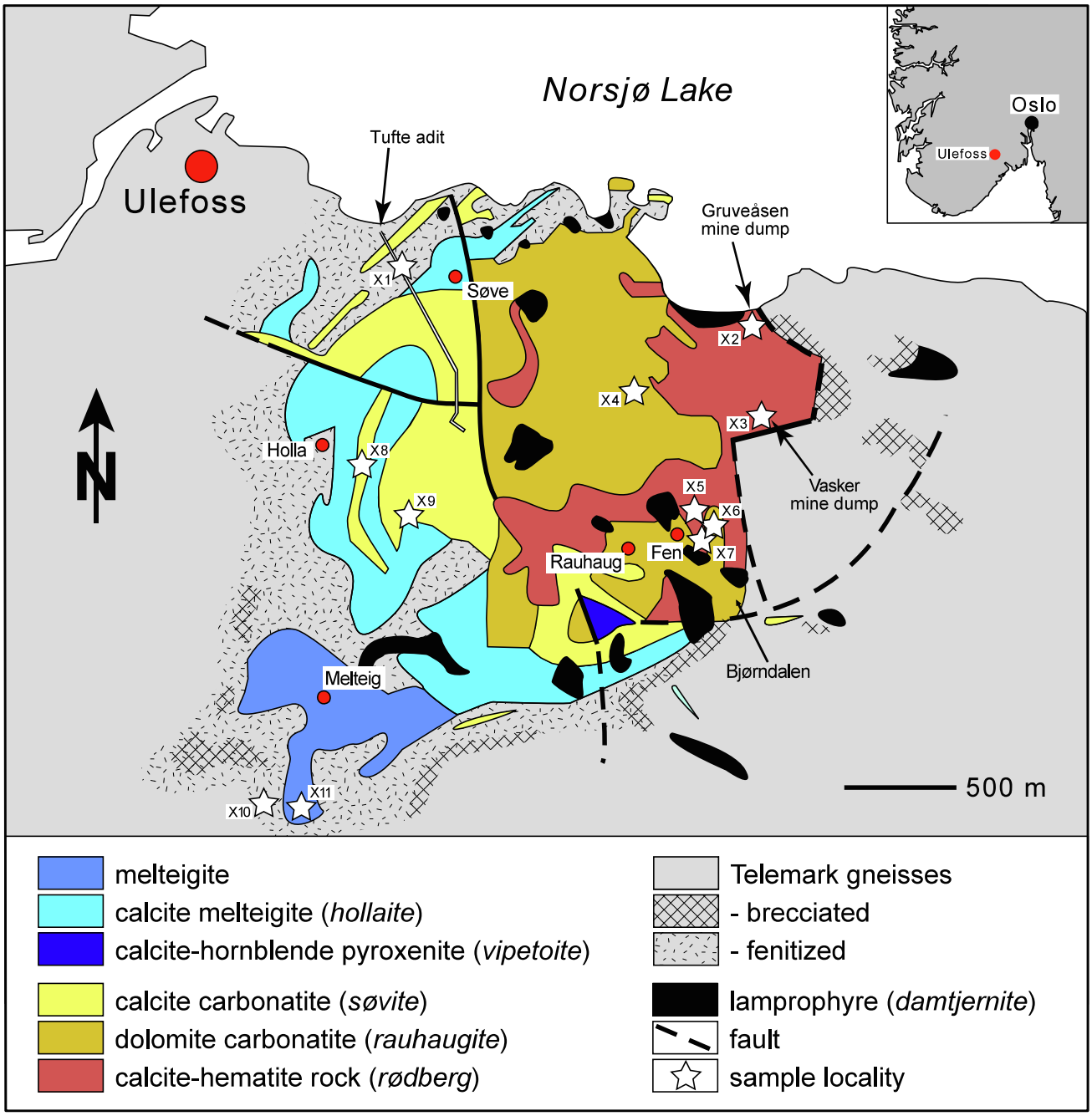

Fig. 1. Simplified geological map of the Fen carbonatite complex in southern Norway (modified after Sæther, 1957) with key localities and sample sites (X1-X11).

Quantitative analysis of minerals was performed using a JEOL JXA 8900 Superprobe at the Department of Geosciences, University of Tübingen, with an acceleration voltage of 15 kV (apatite, REE-F-carbonates, aeschynite, and samarskite), 20 kV (monazite and magnetite) and 25 kV (sulfides) and a beam current of 20 nA (apatite, sulfides, magnetite, REE-F-carbonates, aeschynite, and samarskite) and 100 nA (monazite). The beam diameter was varied from focused beam (sulfides, aeschynite and magnetite), 2 µm (REE-F-carbonates), 5 µm (monazite) to 10 µm (apatite). Standardization was done using natural and synthetic standards, for REE we used REE-bearing glasses (REE16G block, P&H Developments Ltd.), which were regularly analysed during each analytical sequence. Data reduction was performed using the internal ZAF and Φρz matrix correction software of JEOL (Armstrong, 1991). Further details on standard materials, WDS configurations and typical detection limits for the individual elements of the various minerals are given in the electronic supplement.

Four rødberg samples were selected for whole-rock analyses by XRF and LA-ICP-MS. The samples were crushed, ground and turned into tablets using Merck Spectromelt® A 12. XRF analysis of the main elements was done at Tübingen University using a Bruker AXS S4 Pioneer (Rh-tube at 4 kW) with 32 standardised samples (compiled in Govindaraju, 1989). Prior to preparation, the samples were ground with an agate mill for 10 min. For the fused beads 1.5 g of dried sample powder (at 105 °C) was mixed with 7.5 g MERCK spectromelt A12 (mixture of 66% Li-tetraborate and 34% Li-metaborate) and melted at 1200 °C beads using an Oxiflux system from CBR analytical service. Detection limits and analytical errors are sample specific and usually in the range of 0.1% (relative).

Trace elements including REE and Th was done using a LA-ICP-MS with an AGILENT 7700 spectrometer after laser ablation with a CETAC

Table 1
List of sample locations (X1-X11) with lithologies including their main mineralogy.

Sample location	Location name		Lithology	Main minerals
X1	Tufte adit		Fenite (N = 5)	Ab, pl, cpx, ap, ep, amp, py, mt, ilm, sp, gn, po, ccp
			Rauhaugite (N = 5)	Dol, cal, rfc, mca, chl, mt, hem, py, thr, ap, po, ccp, gn, brt
			Rødberg (N = 8)	Cal, dol, hem, mt, ap, chl, brt, py, mnz, rfc, thr
			Søvite (N = 7)	Cal, dol, ap, mt, clf, mca, py, pcl
			Tufte adit vein (N = 9)	Mt, py, hem, rfc, chl, gp, sp, mnz, ccp, gn
X2	Gruveåsen mine dump		Rødberg (N = 4)	Hem, mt, qz, cal, py, mnz, aln, clf, rfc, thr
X3	Vasker mine dump		Rødberg (N = 1)	Hem, mt, qz, cal, ap, chl, py, mnz, rfc, aes, sam, um, thr
X4	Drill core	FEN TEIG 3	Rødberg (N = 1)	Cal, dol, hem, ap, rfc, py
X5		FEN DDH-16	Rauhaugite (N = 3)	Dol, cal, rfc, mca, chl, mt, hem, py, thr, ap, po, ccp, gn, brt
			Rødberg (N = 3)	Cal, dol, ap, hem, py, rfc, mnz, brt, fl, thr
X6		FEN DDH-18	Rauhaugite (N = 1)	Dol, cal, rfc, mca, chl, mt, hem, py, thr, ap, po, ccp, gn, brt
X7		FEN DDH-11	Rødberg (N = 3)	Cal, dol, hem, chl, fl, py, rfc, brt, qz, thr
X8		FEN HLA-1	Søvite (N = 1)	Cal, dol, ap, mt, clf, mca, py, pcl
X9		FEN TH-19	Søvite (N = 1)	Cal, dol, ap, mt, clf, mca, py, pcl
X10	Melteig farm		Fenite (N = 1)	Ab, pl, cpx, ap, ep, amp, py, mt, ilm, sp, gn, po, ccp
X11			Melteigite (N = 2)	Cpx, ne, ttn, mt, ap, po, ccp, py, gn

Abbreviations: Ab = albite, aln = allanite, amp = amphibole, ap = apatite, brt = barite, cal = calcite, ccp = chalcopyrite, chl = chlorite, clf = columbite-(Fe), cpx = clinopyroxene, dol = dolomite, ep = epidote, fl = fluorite, gn = galena, hem = hematite, ilm = ilmenite, mca = mica, mnz = monazite, mt = magnetite, ne = nepheline, pcl = pyrochlore, pl = plagioclase, po = pyrrhotite, py = pyrite, qz = quartz, rfc = REE-F-carbonates, sam = samarskite, sp = sphalerite, thr = thorite, ttn = titanite.

LSX-213 laser system at the Dept. of Mineralogy, University of Stuttgart, Germany. The raw data were calibrated against NIST612, NIST610, DLH7 and DLH8 glasses using Ca (based on XRF) as internal standard. The REE data were normalized to chondrite data (Anders and Grevesse, 1989).

5. Petrography

5.1. Fenite

Fenites contain mm- to cm-thick veins of coarse-grained albite (rarely overgrown by K-feldspar), green clinopyroxene, greenish to brownish amphiboles, epidote and rounded apatite. Pyrite and calcite fill fractures that crosscut any other textures. Pyrite appears to have been partially replaced by calcite. Most pyrites show round inclusions of pyrrhotite and chalcopyrite; sphalerite replaces pyrite, galena grows in fractures within pyrite.

5.2. Melteigite

Melteigites consist of grass to olive green needles of clinopyroxene, magnetite, titanite and apatite with interstitial nepheline. Pyrrhotite and chalcopyrite are usually found as inclusions in pyrite and most notable are birds-eye textures, in which pyrrhotite is almost completely replaced by pyrite in a grid-like manner (Fig. 2a). Later-stage (probably hydrothermal) magnetite often replaces and overgrows pyrite

5.3. Søvite

Søvites are rich in coarse-grained calcite with variable amounts of dolomite, euhedral apatite, brown to green mica and magnetite. Magnetite may show strong dissolution and exsolution (ilmenite, rarely rutile) textures. Mostly euhedral pyrite contains inclusions of calcite, apatite, mica, magnetite, pyrrhotite, and chalcopyrite (Fig. 2b). Galena fills fractures within pyrite and sphalerite may form seams around pyrite. In some cases, pyrite occurs as subparallel trails of grains in the carbonates. Further accessory minerals are pyrochlore, columbite and zircon; a paragenetic sequence for søvites is illustrated in Fig. 2c.

5.4. Rauhaugite

Rauhaugite is generally a dolomite carbonatite, in which dolomite contains variable amounts of Fe (ferroan dolomite), rarely reaching ankerite composition. This rock type is equivalent to rauhaugite type 2 of Sæther (1957), and ferrocarbonatite of Andersen (1984, 1987). Samples of rauhaugite 1 (Brøgger, 1921; Sæther, 1957) have not been included in this study.

The studied samples are rich in mm-sized ferroan dolomite (rarely ankerite) and sometimes apatite (Fig. 3a). It is often replaced by probably hydrothermal calcite in proximity to pyrite and/or magnetite. Three secondary mineral associations can be distinguished, which may overlap with each other: (a) Millimetre- to centimetre-sized clusters of pyrite with rounded inclusions of pyrrhotite and chalcopyrite, REE-F-carbonates, scarce dolomite and very rarely hessite (Ag_2Te). Fractures in pyrite are commonly filled with galena, barite, chlorite and REE-F-carbonates (Fig. 3b). Seams of calcite typically enclose the pyrite. Mineral associations (b) and (c) consist of calcite, pyrite, hematite, chlorite, REE-F-carbonates (Fig. 3c) and small amounts of monazite and thorite. Wherever hematite occurs finely disseminated between the calcite, chlorite is absent (b), while hematite is rare in chlorite-rich associations (c). Thorite often forms needles around pyrite and is generally more common in hematite-rich portions of the samples (Fig. 3d). Pyrite in associations (b) and (c) seems to be replaced by calcite, chlorite and the REE-F-carbonates (bastnäsite, synchysite and parisite) which are often syntactically intergrown. Rare magnetite is commonly associated with REE-F-carbonate-rich and hematite-rich assemblages. Late-stage quartz, replacing any association, is most commonly observed wherever hematite is finely disseminated between calcite II grains. A paragenetic sequence for rauhaugites is given in Fig. 2e.

5.5. The Tufte adit vein

The Tufte adit vein mainly consists of pyrite and magnetite with subordinate hematite and REE-F-carbonates. Sub- to euhedral magnetite contains interstitial pyrite and may be altered and rounded close to pyrite or REE-F-carbonates, including martitization (Fig. 4a, b). Early pyrite I contains euhedral hematite and wormlike magnetite inclusions (Fig. 4c, d) and is overgrown by inclusion-free pyrite II (Fig. 4c). Pyrite II may also form interstitial aggregates between magnetite and is in some cases overgrown by later magnetite II. REE-F-carbonates reach diameters of up to one millimetre, the biggest grains growing in cavities (Fig. 4e) on top of magnetite or pyrite. Smaller grains are often located in pores of magnetite II or in zones of dissolved pyrite and magnetite II. Some crystals occur at the margins of pyrite crystals or occur as small rounded inclusions within them. Some of the REE-F-carbonate grains are zoned and some show syntaxial intergrowth of bastnäsite,

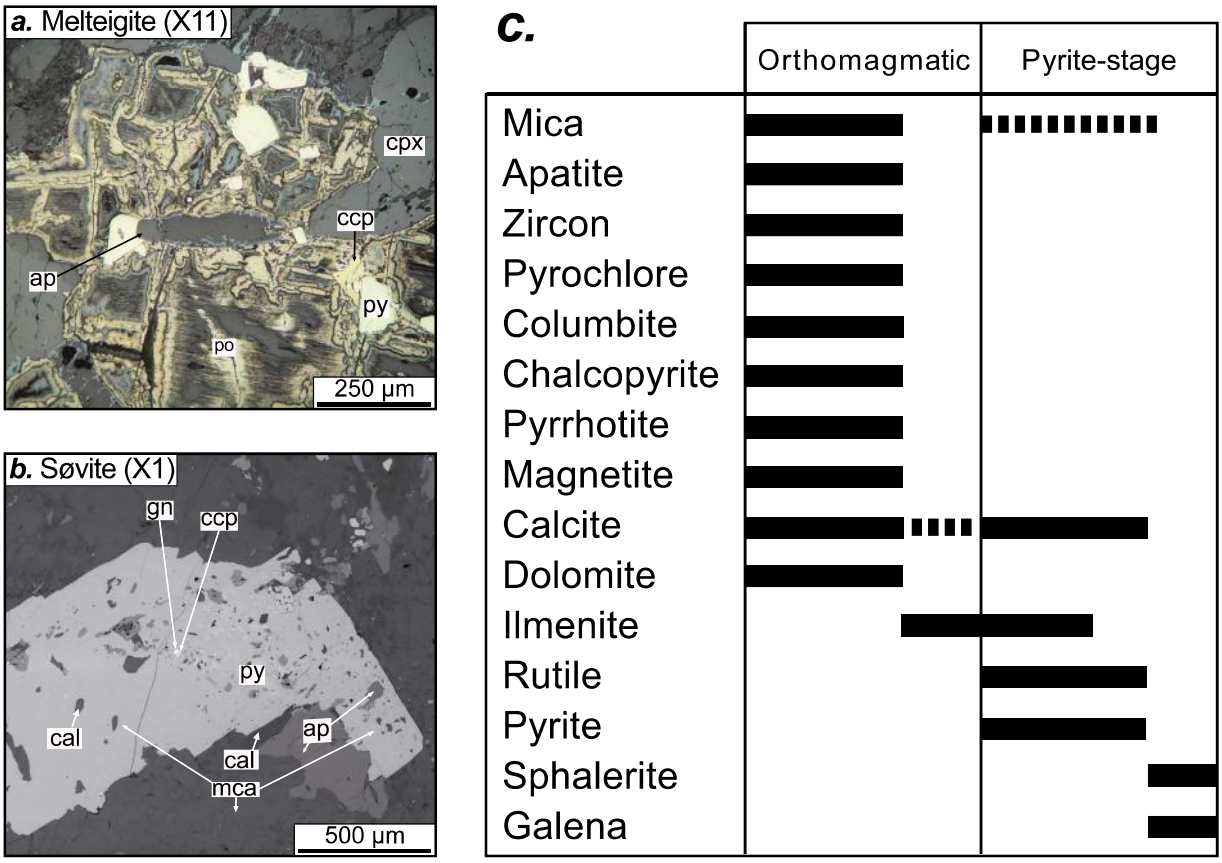

Fig. 2. (a) Birds-eye texture in melteigite with pyrite replacing pyrrhotite (reflected light microscopy). (b) Pyrite in søvite contains inclusions of magmatic calcite, apatite and mica (BSE image). (c) Paragenetic sequence for søvites. Abbreviations as given in Table 1.

synchysite and parisite (Fig. 4e).

Accessory minerals are monazite, apatite, barite, sphalerite, chalcopyrite, galena, chlorite and gypsum. Rare monazite between REE-F-carbonate grains overgrows magnetite and pyrite. Anhedral apatite II occurs together with barite in cracks in magnetite II and pyrite. Rare sphalerite intergrown with chalcopyrite overgrows REE-F-carbonates in cavities and contains some galena in small cracks (also in magnetite II and pyrite). Chlorite and gypsum overgrow the REE-F-carbonates in cavities. See Fig. 4g for paragenetic sequence.

5.6. Rødberg

Rødberg samples invariably consist of fine-grained calcite and hematite with variable amounts of quartz (Fig. 5). In coarse-grained and relatively Fe-rich samples, magnetite occurs densely intergrown with hematite. Pyrite relics are common, but may be replaced by hematite and magnetite. Rødberg veins cutting across unaltered carbonatites (søvite and rauhaugite) may contain distinct apatite-veins (Fig. 5a). Apatite-veins that occur at the boundary between søvite and rauhaugite contain minor quartz, chlorite and monazite and replace only calcite in sövite, while ferroan dolomite and apatite I are left unaltered.

In some samples, coarse-grained calcite I and aggregates of synchysite and parisite are replaced by veins of anhedral apatite with fine-grained hematite and calcite (Fig. 5d and e). Anhedral monazite, metamict thorite needles and minute hematite occur around partially dissolved calcite or large hematite grains (Fig. 5d and f). In a rødberg vein in the Tufte adit (512 m) apatite-veins contain patches of monazite, synchysite, hematite and porous magnetite (Fig. 5a–c). A vein of porous magnetite is cut by later non-porous magnetite (Fig. 5b). Monazite may be replaced by REE-F-carbonates and chlorite (Fig. 6a), the chlorite being associated with barite and columbite cutting magnetite (Fig. 6b). Barite is commonly found around partially replaced pyrite grains.

In rødberg from the Gruveåsen mining hill (X2) carbonate and pyrite are largely replaced by hematite and magnetite. The REE-bearing minerals in this sample are monazite, allanite and relics of anhedral REE-F-carbonates interstitially enclosed in a dense matrix of tabular hematite (Fig. 6c and d) with accessory columbite and thorite. Abundant quartz aggregates (Fig. 6e) presumably resemble magmatic apatite of former rauhaugite (compare Fig. 3a). Hematite is not replaced, but is cut by late quartz veins.

A very quartz-rich sample from the Vasker mine (X3) contains aeschynite, samarskite and an unnamed Ti-Nb-Fe-Th-oxide (in the following named UM for simplicity). The latter is best described by the formula $(Y,Er,U,Th,Fe^{3+})_3(Ti,Nb,Ta)_{10}O_{26}$ of the unnamed mineral UM1926-01-O:HNbTaTiU (Smith and Nickel, 2007). Aeschynite and UM are accompanied by rounded monazite aggregates (Fig. 6f) and minor synchysite, while UM forms partial pseudomorphs after aeschynite. Where UM is overgrown by apatite II and quartz, the replacement of aeschynite appears to be more complete (Fig. 7a). Based on textures and composition three types of samarskite can be distinguished: samarskite I and II are enclosed in monazite intergrown with hematite (Fig. 7b). Anhedral samarskite III is intergrown with hematite, chlorite and quartz and is often associated with aeschynite and UM (Fig. 7a). In drill cores X5 and X7, rødberg is associated with large veins of purple fluorite that are often intergrown with apatite II and chlorite. A complete paragenetic sequence that includes observations from all rødberg samples is given in Fig. 7c.

6. Whole-rock compositions

The rødberg vein from the Tufte adit has very similar REE

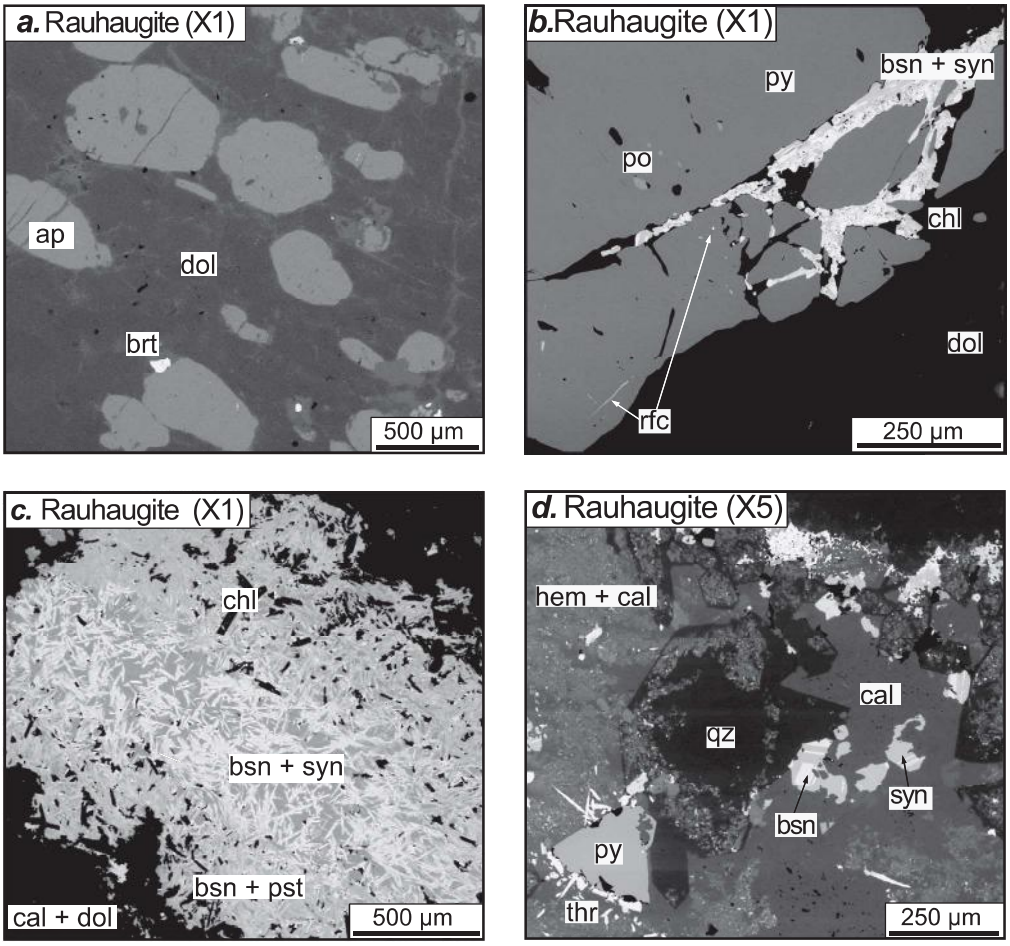

Fig. 3. Mineral textures and paragenetic scheme for rauhaugites of the Fen complex (Norway). (a) Coarse-grained apatite in a dolomite-dominated matrix with accessory barite. (b) Fractures in pyrite filled with chlorite and syntactically intergrown REE-F-carbonates (here bastnäsite and synchysite). Fe-bearing dolomite surrounds the pyrite (BSE image). (c) Aggregate of REE-F-carbonates with a bastnäsite- and synchysite-rich inner part surrounded by intergrown bastnäsite, parisite and chlorite. (d) Pyrite surrounded by thorite needles and REE-F-carbonates (here bastnäsite and synchysite) in a matrix of secondary calcite, hematite and quartz. (e) Paragenetic sequence for rauhaugites. Abbreviations as given in Table 1.

concentrations to the brecciated rauhaugite host and a similar pattern (but much higher concentrations) than the rødberg ore from Gruveåsen mining hill (Table 2; Fig. 8). The rødberg sample from the Vasker mine, however, shows a much flatter REE pattern and a strong enrichment of HREE and Th compared to the other samples (Table 2; Fig. 8)

7. Mineral compositions

Representative mineral analyses are given in Tables 3 and 4 and the full data set is given in the electronic supplement. In the following we focus on REE contents of the major REE phases and on trace element

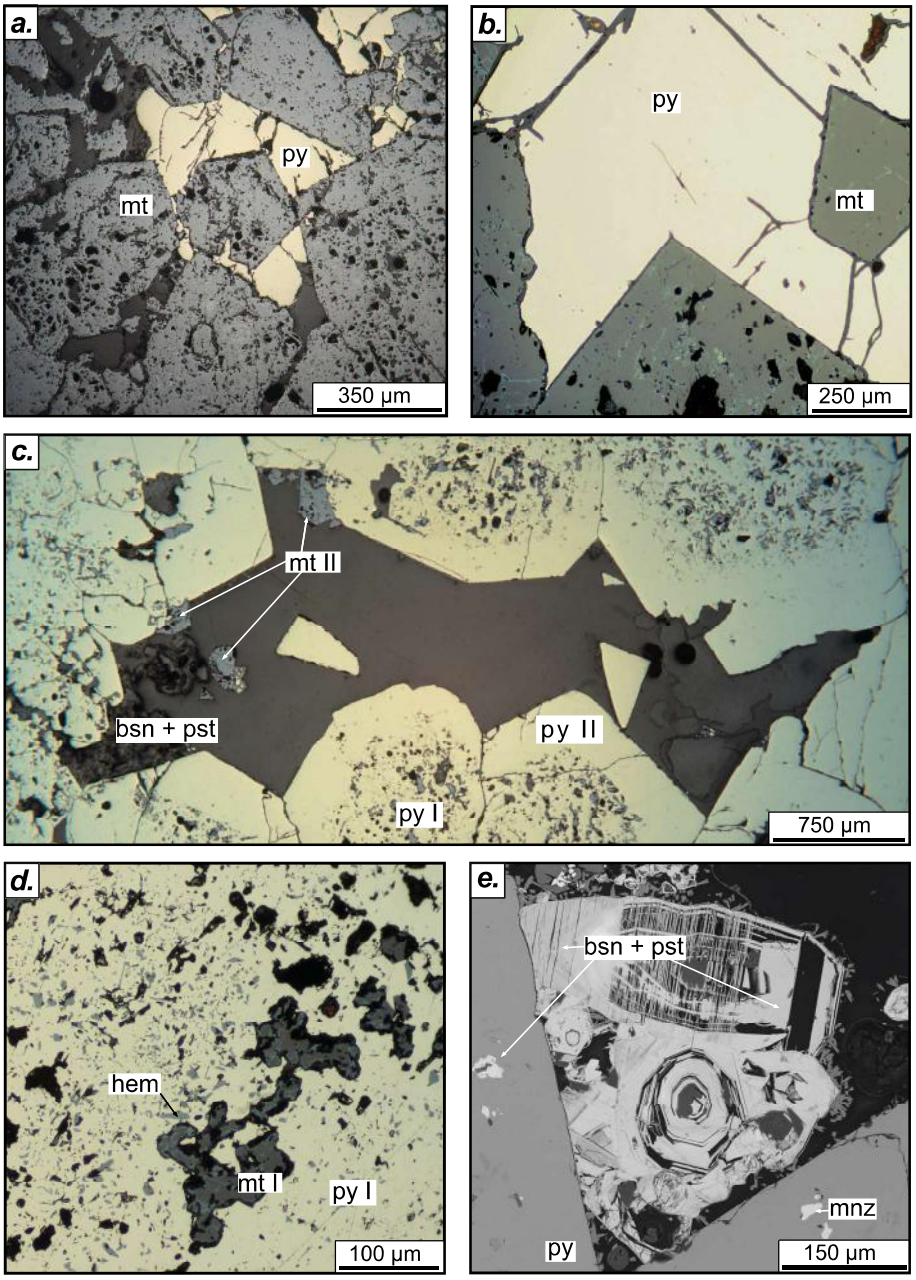

Fig. 4. Mineral textures and paragenetic scheme for the Tufte adit vein. (a) Interlaced magnetite with interstitial pyrite (reflected light image). (b) Magnetite with partial martitisation overgrown by pyrite. (c) A cavity with euhedral pyrite growing into it. Early pyrite I contains inclusions of magnetite and hematite and is overgrown by inclusion-free pyrite II. Even later magnetite II grows on top of pyrites II and REE-F-carbonates (here bastnäsite and parisite). (d) Close up of euhedral hematite and wormlike magnetite inclusions in pyrite I (e) REE-F-carbonates (here bastnäsite and parisite) growing into a cavity (BSE image). (f) Paragenetic sequence for the vein. Abbreviations as given in Table 1.

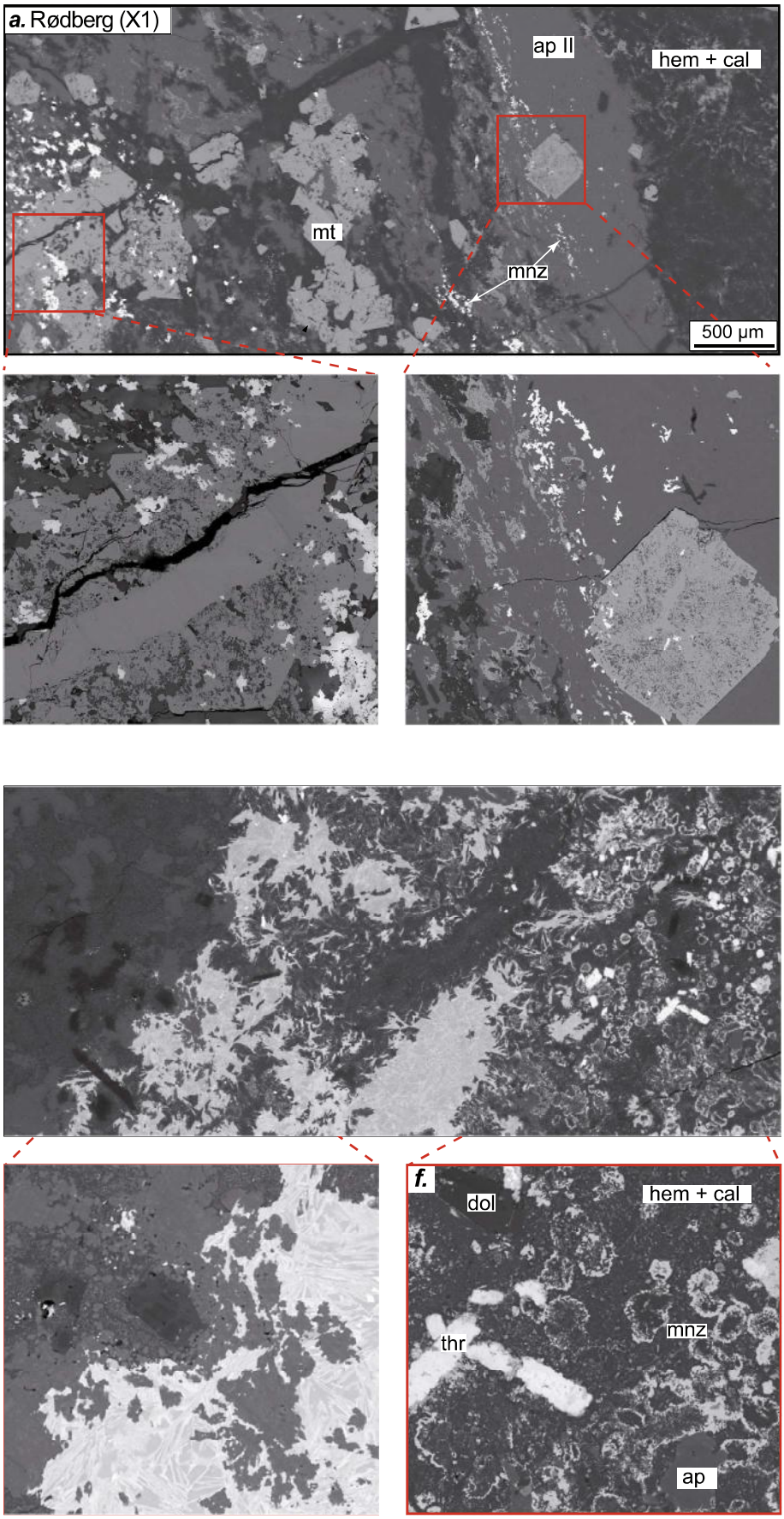

Fig. 5. Microtextures in rødberg samples (BSE images). (a) Apatite-vein with porous magnetite and monazite aggregates cutting a fine-grained hematite-calcite matrix with coarse magnetite and monazite. (b) Close-up of (a) with porous magnetite vein intergrown with apatite and monazite cut by late-stage magnetite and calcite. (c) Close-up of (a) with porous magnetite in apatite-vein and "flow-bands" of hematite and monazite. (d) Area of fine-grained hematite-calcite matrix with aggregates of parisite and synchysite, thorite and monazite. (e) + (f) are close-ups showing intergrowth of parisite and synchysite (e) and replacement of calcite by atoll-shaped monazite associated with porous thorite. Abbreviations as given in Table 1.

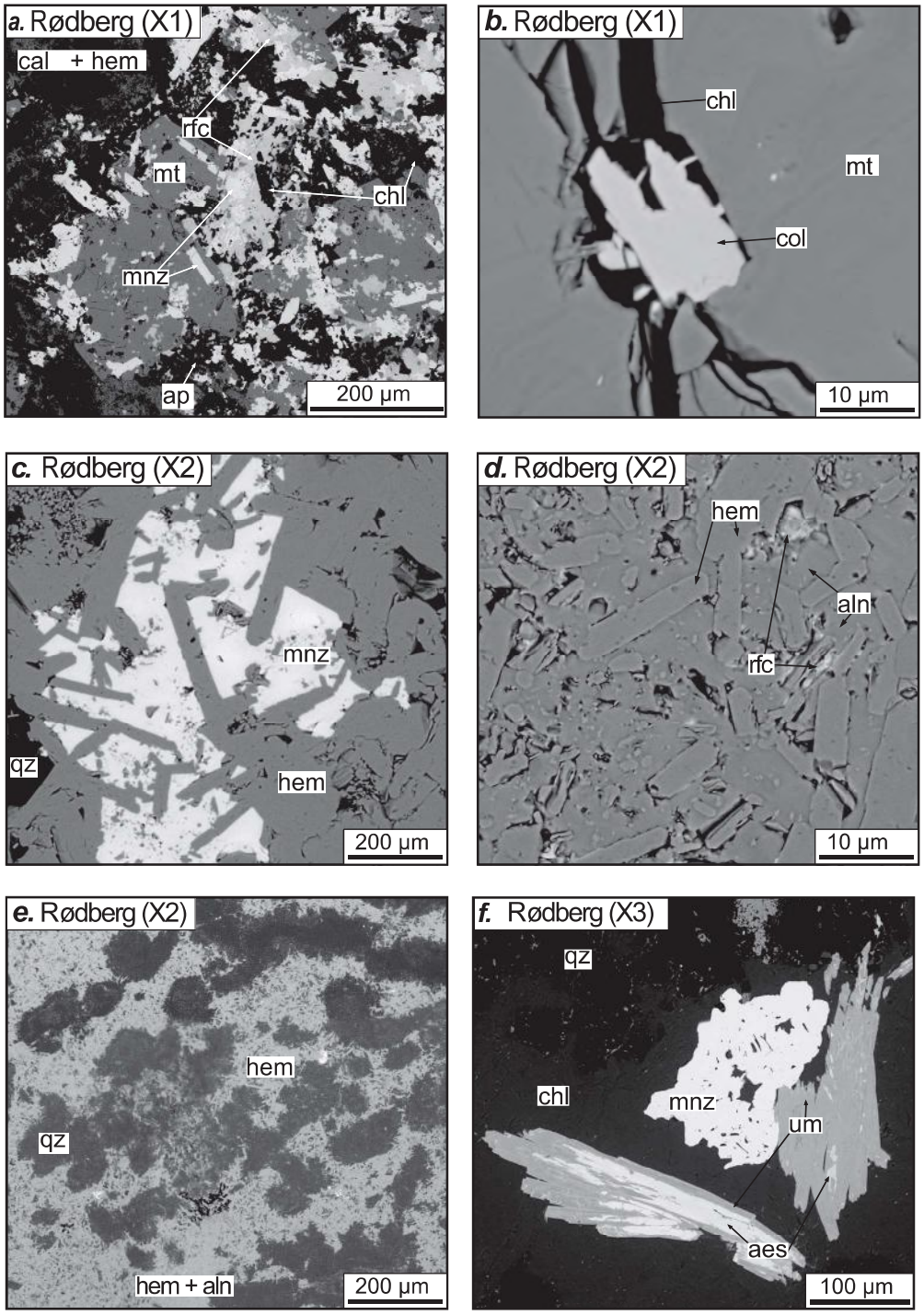

Fig. 6. Microtextures in rødberg samples (BSE images). (a) Aggregate of porous magnetite intergrown with monazite and REE-fluorocarbonates with later replacement of monazite by REE-fluorocarbonates and chlorite. (b) Columbite in a chlorite vein cutting across magnetite vein (c) Interstitial monazite growing onto euhedral hematite. (d) Tabular hematite with interstitial allanite and minor REE-fluorocarbonates. (e) Carbonate replaced by hematite and minor allanite in interstitial space, with quartz aggregates probably replacing primary apatite (compare Fig. 3a). (f) Monazite associated with aeschynite, which is marginally replaced by Ti-Nb-Fe-Th-oxide (UM) inside of chlorite vein partially replaced by quartz. Abbreviations as given in Table 1.

contents in pyrite and magnetite. All monazites and REE-F-carbonates from the Fen are strongly LREE-enriched (Table 3) and typically represent Ce-dominated members. In contrast samarskite and UM are strongly HREE-enriched and typically represent Y-dominated members, while aeschynite is MREE-enriched with Nd-dominated members (Table 4). These endmembers are displayed by the suffix -(Ce), -(Y) and –(Nd), respectively, as recommended by the Commission on New Minerals, Nomenclature and Classification (CNMNC) of the International Mineralogical Association (IMA).

7.1. Apatite

Both magmatic apatites (from søvites and rauhaugites) and hydrothermal apatites (from rødberg samples) are LREE-dominated (Table 3). However, magmatic apatites reach higher REE and Na concentrations (> 1.66 wt% REE_2O_3; 0.39 wt% Na_2O) compared to hydrothermal apatite (about 0.58 wt% REE_2O_3; 0.29 wt% Na_2O), while contents of Si are generally below the detection limit. The positive correlation between Na and REE indicates that REE are incorporated by the coupled substitution 2 $Ca^{2+} \leftrightarrow Na^{+} + REE^{3+}$ as has been observed before in apatite from other carbonatites (Fig. 9a; e.g., Giebel et al., 2019a,b). In the case for Fen, however, this substitution meachanism is less important for hydrothermal apatites than for magmatic ones (Fig. 9a), which is opposite to what was observed at Palabora (RSA) and Kaiserstuhl (Germany). In contrast, average F and Fe contents in magmatic apatites (2.66 wt% F, 0.74F pfu; 0.02 wt% FeO) are lower than in

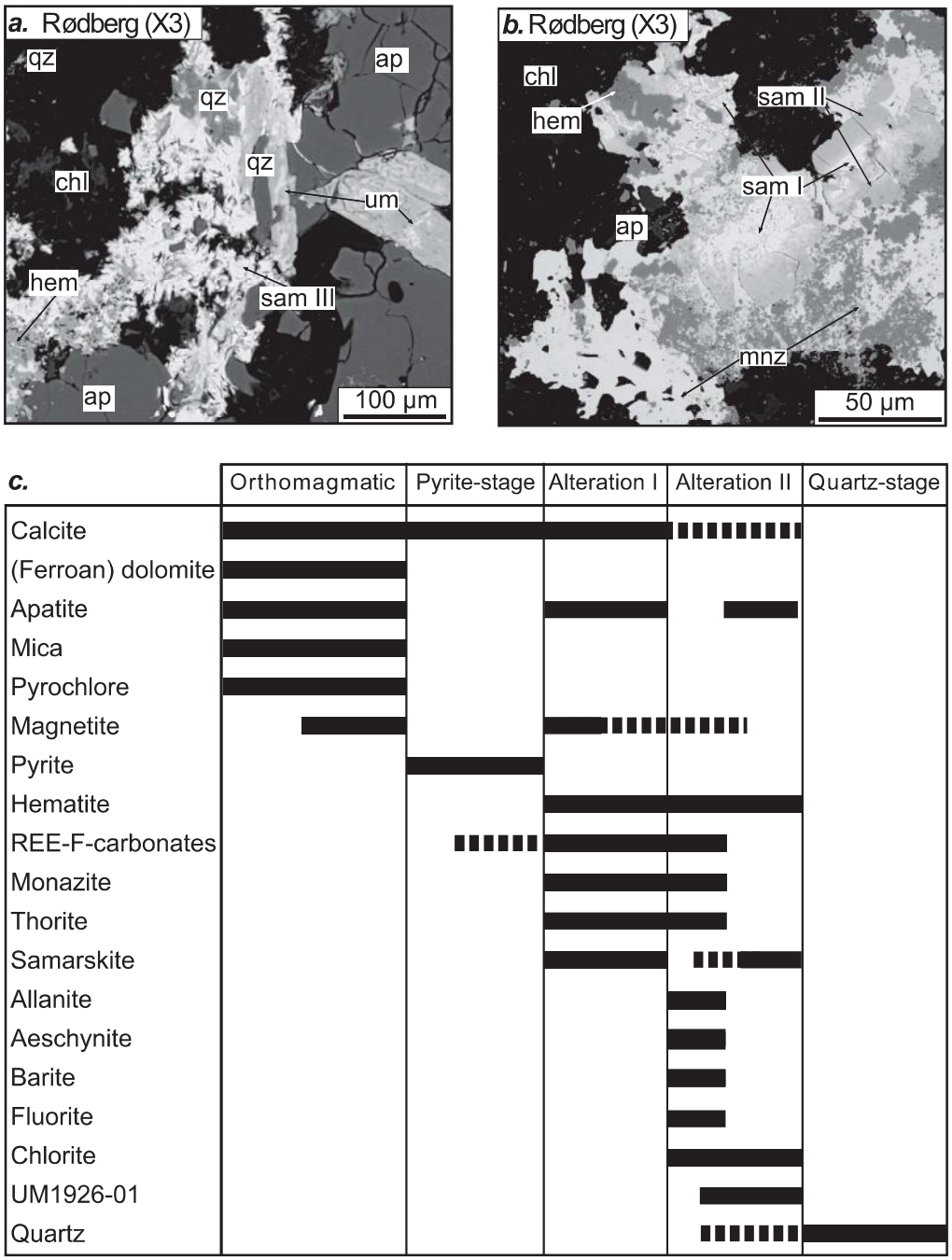

Fig. 7. Samarskite microtextures in rødberg samples (BSE images). (a) UM pseudomorph after aeschynite overgrown by apatite and samarskite III. Note intergrowth of samarskite III with anhedral chlorite, hematite and quartz as partial replacement of UM. (b) Samarskite I and II overgrown by hematite and monazite with partial replacement by quartz. (c) Paragenetic sequence for rødberg samples. Abbreviations as given in Table 1.

hydrothermal apatite (3.58 wt% F, 0.96F pfu; 0.1 wt% FeO; Fig. 9b). This might reflect for examples changes in crystallization conditions (e.g. temperature, oxygen fugacity) and crystallization media (melt versus fluid), which causes different partitioning behavior of these elements. However, the slightly higher Fe content in apatite from rødberg samples could also reflect abundant and very fine-grained hematite inclusions in these commonly reddish apatites as this may cause mixed analyses during microprobe analyses (probe diameter of 10 µm).

7.2. Monazite

In general, monazite-(Ce) from rauhaugite and rødberg is compositionally similar (Table 3). However, most REE (exclusive La and Ce) tend to increase in rødberg from Gruveåsen < Tufte adit < Vasker Grube (Fig. 9c), Rauhaugites overlap those pattern (especially for HREE) but show the lowest Pr, Nd, Sm and Eu contents. La in contrast, tends to decrease from Tufte adit rauhaugite ≥ Gruveåsen rødberg = Tufte adit rødberg > Vasker Grube rødberg (hematite ore), whereas Ce marks the pivot at which these REE trends change (Fig. 9c).

7.3. REE-F-carbonates

The chondrite-normalized REE patterns for REE-F-carbonates show similarly strong LREE enrichment with very minor tendentious differences in MREE between analyses from rauhaugite ≤ Tufte adit vein ≤ rødberg (Fig. 9d). In contrast, highest La concentrations occur in

Table 2
Major and trace element composition of four whole-rock samples of the Fen complex (Norway).

	Tufte adit (rødberg vein)	Tufte adit (rauhaugite)	Gruveåsen mining hill (rødberg ore)	Vasker mine (rødberg ore)
Major elements based on XRF (wt.%)				
SiO_2	1.2	0.4	60.9	16.5
TiO_2	0.1	0.0	1.4	0.3
Al_2O_3	0.9	0.0	5.7	0.6
Fe_2O_3	48.3	2.2	21.7	80.0
MnO	0.3	0.7	0.1	0.0
MgO	1.6	2.0	3.5	0.5
CaO	24.7	50.3	1.5	0.3
Na_2O	0.1	0.0	0.1	0.0
K_2O	0.0	0.0	0.0	0.0
P_2O_5	2.0	0.5	0.7	0.0
LOI	18.8	41.7	3.5	1.5
Sum	98.0	97.9	98.9	99.7
Trace elements based on LA-ICP-MS (µg/g)				
Sc	31	22	77	29
V	123	14	80	160
Cr	17	10	302	44
Ni	9	5	60	22
Rb	3	1	1	1
Cs	B.d.l.	B.d.l.	B.d.l.	B.d.l.
Sr	1107	460	54	20
Ba	2582	113	156	36
La	4219	5269	696	455
Ce	6931	9064	1564	679
Pr	760	1003	228	92
Nd	3006	3953	1171	368
Sm	396	481	326	45
Eu	64	64	77	7
Gd	119	105	196	11
Tb	6	5	27	1
Dy	17	16	155	3
Ho	2	2	28	B.d.l.
Er	5	5	78	1
Tm	1	1	12	B.d.l.
Yb	5	4	72	1
Lu	1	1	8	B.d.l.
Y	65	48	522	14
Zr	337	47	532	8
Hf	4	1	12	B.d.l.
Nb	815	540	2568	618
Ta	2	1	12	2
Th	326	352	1339	93
U	13	37	17	1

LOI = loss on ignition; B.d.l. = below detection limit.

rauhaugite and the lowest in rødberg and again, Ce marks a pivot for the patterns.

7.4. Samarskite

The exact stoichiometry of samarskite is still controversial (Capitani et al., 2016) and reported to vary between ABO_4 and AB_2O_6 (Lumpkin et al., 1988). While samarskite-(Y) I in the Vasker mine sample shows a good match for a stoichiometry of ABO_4, an aggregate of samarskite-(Y) II and anhedral aggregates of samarskite-(Y) III fit with a stoichiometry of AB_2O_6. Analysis of samarskite, in particular samarskite-(Y) II and III, was difficult due to its small-scale intergrowth with chlorite and high microporosity. Therefore, analytical totals are rather low, although the calculated cation sites fit the anticipated stoichiometric formulas (Table 4, electronic supplement). While samarskite-(Y) I is poor in Fe_2O_3 (0.3 wt%) and ThO_2 (0.1 wt%), it is strongly enriched in HREE (about 40 wt% Y_2O_3). Samarskite-(Y) II is comparatively poor in REE (on average about 3 wt% Y_2O_3), but has higher concentrations of Fe_2O_3 (on average 26 wt%) and ThO_2 (1.5 wt%) than samarskite-(Y) I. Analyses of samarskite-(Y) III aggregates fall inbetween samarskite I and II (Table 4; on average Fe_2O_3 ~ 8.7 wt%, ThO_2 ~ 1.3 wt%, REE_2O_3 ~ 24.9 wt% and ~ 13.5 wt% Y_2O_3). The chondrite-normalized REE patterns show similar tendencies for samarskite-(Y) I and III (with exception of Y), while samarskite-(Y) II tends to be lower in MREE and HREE (Fig. 9e).

7.5. Aeschynite

Analysis of aeschynite was difficult due to high microporosity and partial and very fine-grained replacement by UM (Fig. 7a). Accordingly, some calculated formulae show an over-occupancy of around 10% for the A-site and of 1% for the B-site (Table 4, electronic supplement). Chondrite-normalized REE patterns for aeschynite-(Nd) show relative enrichment of MREE and depletion of LREE and HREE, which results in concave REE patterns with a maximum at Nd (Fig. 9f). Aeschynite-(Nd) contains on average 0.6 wt% ThO_2 (Table 4).

7.6. Unnamed mineral (UM1926-01-O:HNbTaTiU)

The unnamed Ti-Nb-Fe-Th-oxide (UM) in a sample from the Vasker mine is best expressed as $(Fe^{3+}_{2.5}Ca_{0.2}Th_{0.2}Y_{0.1})(Ti_7Nb_3)O_{26}$ and most closely matches the mineral formula (Y, Er, U, Th, Fe^{3+})$_3$(Ti, Nb, Ta)$_{10}O_{26}$ as described by Smith and Nickel (2007; see above). The mineral grains show, however, a high degree of metamictization and microporosity, which causes low analytical totals. Additionally, high Y contents (relative to LREE) indicate slightly higher HREE than LREE. However, HREE were not analyzed, further adding to low analytical totals. Nevertheless, UM is poor in REE (on average 1.2 wt%, Table 4), but high in ThO_2 (up to 5 wt%). Incomplete chondrite-normalized REE patterns for UM indicate a maximum at Gd and relative depletion of LREE and HREE (Fig. 9f). In comparison aeschynite, which is replaced by UM, LREE are stronger depleted than HREE.

7.7. Pyrite

Many of the analyzed trace elements in pyrite are below or close to the detection limit with no systematic differences between the investigated lithologies (electronic supplement). Only As (1.2 wt%), Bi (0.2 wt%), Sb (0.08 wt%) and Ag (0.13 wt%) reach higher contents (electronic supplement).

7.8. Magnetite

Magnetite at the Fen complex is relatively poor in minor elements (electronic supplement). Still, magnetite in søvites and especially in melteigites reaches higher contents of TiO_2 (up to 3 wt%), V_2O_5 (up to 0.5 wt%), MnO (up to 1 wt%) and Cr_2O_3 (up to 0.05 wt%) compared to hydrothermal magnetite in fenites, rauhaugites and samples of the Tufte adit vein. However, Al is enriched in magnetites of the Tufte adit vein (up to 0.8 wt% Al_2O_3), rauhaugite (up to 0.6 wt% Al_2O_3) and in some magnetites from melteigite (up to 0.4 wt% Al_2O_3). Magnesium behaves unsystematically and is generally < 0.5 wt% MgO.

8. Discussion

8.1. Previous models of rødberg formation

On the basis of Sr, O and C isotopic data and textural observations, Andersen (1984) argued that rødberg was formed by the dissolution and oxidation of ferroan dolomite, ankerite and pyrite leading to the local enrichment of ferric iron and to hematite precipitation. He suggested that this was caused by oxidizing hydrothermal fluids derived from basement host rocks that were mobilized by the cooling carbonatite intrusion. The massive iron ores were considered to be the result of oxidation of pre-existing magnetite-pyrite ores (Andersen, 1983).

The local HREE-enrichment was explained by selective dissolution of carbonate, leading to a volume reduction of up to 70 vol% in rødberg

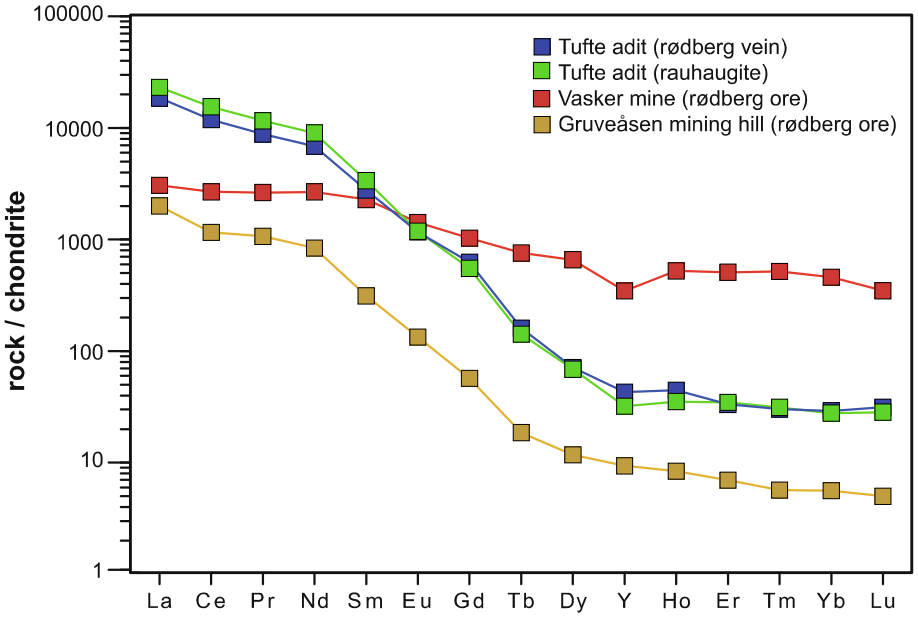

Fig. 8. Chondrite-normalized REE diagrams for whole-rock samples of the Fen complex (Norway).

and thus to a subsequent enrichment of relatively immobile HREE-minerals, followed by a leaching of LREE by F-rich fluids (Andersen, 1987). In contrast, Marien et al. (2018) argued, based on whole-rock data and textural observations, for an enrichment of HREE-minerals by fractional precipitation from a F- and Cl-rich fluid. According to this model, HREE-minerals precipitated first upon cooling or contact with carbonate rock due to the lower stability of HREE-complexes in aqueous solutions relative to LREE-complexes (Williams-Jones et al., 2012). Marien et al. (2018) furthermore suggested that in rødberg of the Bjørndalen district, primary magmatic apatite I was an important source of phosphate for the formation of monazite veinlets and primary apatite grains acted as a trap for REE-rich fluids forming monazite due to the relative immobility of P.

8.2. Proposed hydrothermal evolution at Fen

The observed mineral textures are best explained by interaction of three different fluids responsible for large-scale element remobilization (Fig. 10). Fluid 1 was a S-rich fluid leading to the precipitation of sulfides (I in Fig. 10). Fluid 2 can be subdivided into fluids 2a – 2c: Fluid 2a was rich in REE^{3+}, 2b was rich in REE^{3+} and Fe^{2+}, and Fluid 2c was rich in REE^{3+}, Fe^{2+} and Al^{3+}. Fluid 3, finally, was an oxidizing fluid, which can be subdivided into fluid 3a and 3b. Fluid 3a was rich in silica, while fluid 3b was rich in phosphate. The evolution of these fluids is recorded by the different textures in the rauhaugites, the Tufte adit vein and in the rødberg samples.

Pyrite is widespread in all major lithologies and, in some cases replacing presumably magmatic sulphides, such as pyrhotite (Fig. 2a). We suggest that sulfide-rich fluids (fluid 1) may have unmixed from mafic silicate rocks, which, due to gravity modeling (Ramberg, 1973) has been proposed to be more common at depth and it appears reasonable to us to relate the hydrothermal sulfides in carbonatites, fenites and rødberg rocks to a common source. Sulfide-rich fluids are well known from many mafic rock suites (Métrich and Mandeville, 2010; Naldrett, 2013).

The details of the textures in the Tufte adit vein (inclusions of REE minerals in pyrite and pyrite in REE minerals) prove that contemporaneous with the sulfide mineralization, REE-rich fluids (fluid 2) percolated through the same rocks. Given the typical connection of REE-rich fluids with carbonatite complexes, these fluids are believed to have evolved from the crystallization of the carbonatites. It is however unclear, if they relate to søvites or rauhaugites exposed at the surface today, or if they unmixed from a deep, hidden carbonatite body.

Wherever the pyrite is overgrown by later, generally hematite-bearing REE-rich associations, pyrite is rounded and anhedral. In fractures of pyrite, REE-F-carbonates, hematite and chlorite crystallized (Fig. 3b) forming REE-rich, REE- and Fe-rich or REE-, Fe- and Al-rich mineral associations, respectively. These associations occur in both rauhaugites and in the Tufte adit vein. The associations all contain ubiquitous REE-F-carbonates, calcite and minor monazite and probably precipitated from a fluid 2 evolving from fluid 2a (precipitating only REE-F-carbonates and monazite) via fluid 2b (precipitating REE-minerals and hematite) to fluid 2c (precipitating REE-minerals, hematite and chlorite). The evolution of this fluid is believed to be related to the breakdown of ferroan dolomite and the dissolution of mica, leading to enrichment of Fe and Al. Such hematite-rich associations occur throughout the Fen Complex. The oxidized fluid 3 derived from the surrounding gneissic basement was already proposed by Andersen (1984).

The massive silicified hematite ore veins at the Gruveåsen mining hill reach thicknesses up to 8 m and lengths up to 100 m (Vogt, 1910). They are considered to be a result of large scale carbonate replacement by fluid 2b and fluid 3a, the latter also adding SiO_2 to the rock. Quartz pseudomorphs after apatite (Fig. 6e) found in these ore veins imply a mobilization of phosphate from magmatic apatite I (II in Fig. 10) during this process. This lead to a phosphate-enriched fluid 3b which precipitated (after reaction with calcite) reddish apatite II in thin and hydraulically connected rødberg veins (IV in Fig. 10) as witnessed at 512 m and 1000 m in the Tufte adit and in drill cores X4 and X5 (Figs. 5 and IV in 10). The generally higher F and lower REE and Na contents in hydrothermal apatite II compared to magmatic apatite I has been observed in other carbonatites as well, but is not universal, as hydrothermal apatite from some carbonatites (e.g., Kaiserstuhl, Palabora; Fig. 9b) is REE- and Na-rich compared to magmatic apatite of the same body (Chakhmouradian et al., 2017; Giebel et al., 2019a,b).

8.3. Fluid interaction and REE enrichment in rødberg

The association of REE-F-carbonates with small inclusions of thorite probably reflects the fact that hydrothermal REE-minerals can incorporate less Th than magmatic ones. Accordingly, some Th from fluid 2a could not be incorporated into REE-F-carbonates, but crystallized as

Table 3
Representative electron microprobe analyses of apatite, monazite and REE-F-carbonates from the Fen complex (Norway).

Sample location	X1	X1	X1	X1	X4	X5	X1	X1	X2	X3	X1	X1	X5	X5	X1	X1	X1
Mineral	Apatite I			Apatite II			Monazite				Bastnäsite		Synchysite		Parisite		
Rock type	Rauhaugite		Søvite	Rødberg			Rauhaugite	Rødberg			Rauhaugite	Vein	Rauhaugite	Rødberg	Rauhaugite	Vein	Rødberg
wt.%																	
Na_2O	0.23	0.38	0.35	bdl	0.11	0.09	–	–	–	–	0.03	0.01	0.02	bdl	bdl	0.01	0.01
CaO	53.94	53.40	53.04	54.96	54.12	54.17	0.16	0.32	0.05	0.19	2.54	0.42	17.50	18.14	10.29	10.42	9.90
SrO	0.61	0.65	0.66	bdl	0.68	0.56	–	–	–	–	bdl	0.30	0.33	0.35	0.65	bdl	0.13
BaO	–	–	–	–	–	–	–	–	–	–	bdl	0.09	0.08	bdl	bdl	bdl	0.12
La_2O_3	0.09	0.41	0.27	0.11	0.05	bdl	19.75	18.87	18.83	14.45	20.75	24.49	10.78	11.63	19.73	20.92	17.69
Ce_2O_3	0.25	0.81	0.64	bdl	0.16	bdl	35.80	31.98	33.30	31.91	32.83	33.40	22.83	23.88	28.64	28.56	26.06
Pr_2O_3	bdl	bdl	0.19	bdl	bdl	bdl	3.20	3.35	3.48	3.97	3.95	4.33	2.81	3.78	2.78	3.01	3.64
Nd_2O_3	bdl	0.26	0.41	0.23	0.23	0.05	10.03	12.87	13.04	16.52	10.90	9.59	9.87	10.21	7.18	7.42	11.64
Sm_2O_3	–	–	–	–	–	–	0.58	1.41	0.89	1.81	0.98	0.71	1.25	0.97	0.59	0.61	1.20
Eu_2O_3	–	–	–	–	–	–	0.18	0.25	0.17	0.33	0.35	0.23	0.47	0.27	0.07	0.14	0.30
Gd_2O_3	–	–	–	–	–	–	0.28	0.35	0.18	0.43	bdl	bdl	bdl	0.42	0.57	0.23	bdl
Tb_2O_3	–	–	–	–	–	–	bdl	bdl	bdl	bdl	–	–	–	–	–	–	–
Dy_2O_3	–	–	–	–	–	–	bdl	0.08	0.04	0.09	–	–	–	–	–	–	–
Er_2O_3	–	–	–	–	–	–	bdl	bdl	bdl	bdl	–	–	–	–	–	–	–
Yb_2O_3	–	–	–	–	–	–	bdl	0.03	bdl	bdl	–	–	–	–	–	–	–
Y_2O_3	–	–	–	–	–	–	0.23	0.14	0.04	0.31	bdl	bdl	bdl	bdl	bdl	bdl	0.42
ThO_2	–	–	–	–	–	–	0.81	0.96	0.27	0.22	0.53	1.19	2.53	bdl	1.34	bdl	1.26
MnO	0.07	bdl	bdl	bdl	bdl	bdl	–	–	–	–	–	–	–	–	–	–	–
FeO	0.05	bdl	bdl	0.13	0.05	0.10	–	–	–	–	–	–	–	–	–	–	–
P_2O_5	41.86	41.70	41.36	41.91	41.63	41.53	29.85	29.57	28.97	29.32	–	–	–	–	–	–	–
SiO_2	bdl	bdl	bdl	bdl	bdl	bdl	0.27	0.16	0.20	0.13	–	–	–	–	–	–	–
CO_2 (calc.)	–	–	–	–	–	–	–	–	–	–	20.77	20.19	27.14	28.03	24.52	24.50	24.42
Cl	0,01	0,01	bdl	0.01	0.04	bdl	–	–	–	–	–	–	–	–	–	–	–
F	2.65	3.25	2.21	3.64	3.61	3.31	–	–	–	–	6.81	8.16	5.35	4.48	6.85	6.09	5.49
$-O=(F,Cl)_2$	1.12	1.37	0.93	1.53	1.53	1.39	–	–	–	–	2.87	3.43	2.25	1.89	2.88	2.56	2.31
Total	98.64	99.50	98.20	99.46	99.45	98.42	101.14	100.23	99.42	99.59	97.57	99.68	98.71	100.27	100.33	99.35	99.97
H_2O*	0.95	0.41	1.32	0.08	0.08	0.35	–	–	–	–	1.02	0.26	0.24	0.74	0.09	0.46	0.72
apfu	the method of Ketcham (2015)						Formula calculation based on 2 cations				$1(CO_3)^{2-}$		$2(CO_3)^{2-}$		$3(CO_3)^2$		
Na	0.08	0.13	0.12	bdl	0.04	0.03	–	–	–	–	0.00	0.00	0.00	bdl	bdl	0.00	0.00
Ca	9.81	9.72	9.74	9.96	9.87	9.91	0.01	0.01	0.00	0.01	0.10	0.02	1.01	1.01	0.99	1.00	0.96
Sr	0.06	0.06	0.07	bdl	0.07	0.05	–	–	–	–	0.00	0.01	0.01	0.01	0.03	0.00	0.01
Ba					–	–	–	–	–	–	bdl	0.00	0.00	bdl	bdl		0.00
La	0.01	0.03	0.02	0.01	0.00	bdl	0.28	0.27	0.28	0.21	0.27	0.33	0.21	0.22	0.65	0.69	0.59
Ce	0.02	0.05	0.04	bdl	0.01	bdl	0.51	0.46	0.49	0.46	0.42	0.44	0.45	0.46	0.94	0.94	0.86
Pr	bdl	bdl	0.01	bdl	bdl	bdl	0.05	0.05	0.05	0.06	0.05	0.06	0.06	0.07	0.09	0.10	0.12
Nd	bdl	0.02	0.03	0.01	0.01	0.00	0.14	0.18	0.19	0.23	0.14	0.12	0.19	0.19	0.23	0.24	0.37
Sm	–	–	–	–	–	–	0.01	0.02	0.01	0.02	0.01	0.01	0.02	0.02	0.02	0.02	0.04
Eu	–	–	–	–	–	–	0.00	0.00	0.00	0.00	0.00	0.00	0.01	0.00	0.00	0.00	0.01
Gd	–	–	–	–	–	–	0.00	0.00	0.00	0.00	bdl	bdl	bdl	0.01	0.02	0.01	bdl
Tb	–	–	–	–	–	–	bdl	bdl	bdl	bdl	–	–	–	–	–	–	–
Dy	–	–	–	–	–	–	bdl	0.00	0.00	0.00	–	–	–	–	–	–	–
Er	–	–	–	–	–	–	bdl	bdl	bdl	bdl	–	–	–	–	–	–	–
Yb	–	–	–	–	–	–	bdl	0.00	bdl	bdl	–	–	–	–	–	–	–
Y	–	–	–	–	–	–	0.00	0.00	0.00	0.01	0.00	bdl	0.00	bdl	bdl	0.00	0.02
Th	–	–	–	–	–	–	0.00	0.01	0.00	0.00	0.00	0.01	0.03	bdl	0.03	0.00	0.03
Mn	0.01	bdl	bdl	bdl	bdl	bdl	–	–	–	–	–	–	–	–	–	–	–
Fe	0.01	bdl	bdl	0.02	0.01	0.01	–	–	–	–	–	–	–	–	–	–	–
P	6.01	6.00	5.99	6.00	5.99	6.00	0.98	0.99	0.98	0.99	–	–	–	–	–	–	–
Si	bdl	bdl	bdl	bdl	bdl	bdl	0.01	0.01	0.01	0.01	–	–	–	–	–	–	–

(*continued on next page*)

Table 3 (*continued*)

Sample location	X1	X1	X1	X4	X5	X1		X1	X2	X3	X1		X1	X5	X5	X1		X1	X1
Mineral	Apatite I			Apatite II		Monazite					Bastnäsite		Synchysite			Parisite			
Rock type	Rauhaugite		Søvite	Rødberg			Rauhaugite	Rødberg			Rauhaugite	Vein	Rauhaugite	Rødberg	Rauhaugite	Rauhaugite	Vein	Vein	Rødberg
Cl	bdl	bdl	bdl	0.00	0.01	bdl	–	–	–	–	–	–	–	–	–	–	–	–	–
F	1.42	1.75	1.20	1.95	1.94	1.79	–	–	–	–	0.76	0.94	0.91	0.74	1.94	1.94	1.73	1.73	1.56
Total cations	16.01	16.01	16.02	16.00	16.00	16.00	1.99	2.00	2.01	2.00	0.99	1.00	1.99	1.99	3.00	3.00	3.00	3.00	3.01

H_2O^* - calculated from OH pfu (F + Cl + OH = Z). Apatite, Bastnäsite, Synchysite: Z = 1; Parisite Z = 2
bdl: bellow detection limit

discrete Th minerals (Budzyń et al., 2011; Doroshkevich et al., 2008; Giebel et al., 2017; Harlov et al., 2011; Read et al., 2002).

Later, monazite and apatite crystallized a few hundred micrometres away from partially dissolved aggregates of REE-F-carbonate (Fig. 5), probably due to the limited mobility of phosphorus and the high availability of Ca^{2+} released from dissolved calcite. Porous thorite needles associated with the monazite again suggest that the Th mobilized from dissolved REE-F-carbonates (which contain up to 1.3% ThO_2) could not be completely incorporated into monazite.

As the whole-rock REE patterns of the rødberg vein at 512 m inside the Tufte adit and of the rauhaugite next to it are very similar (Fig. 8), it is likely, that fluids 2b and 2c permeated both rauhaugite and rødberg. This lead to the formation of aggregates of REE-F-carbonates and sometimes chlorite (Fig. 5d) in rauhaugite, while apatite II, monazite and hematite only formed in the rødberg vein upon contact with fluid 3b. This together with the very low enrichment of REE in the Gruverasen (X2) ore sample indicates, that the degree of hematitization is not necessarily correlated to the enrichment of both REE and Th. This renders hematite a potentially misleading indicator of REE-enrichment. The commonly observed enrichment of REE in rødberg probably simply reflects the increased permeability of a brecciated rock for both fluids 2 and 3.

8.4. Enrichment of HREE and Th-Fe ores from the Vasker mine

Textural observations in the sample from the Vasker mine support the model for primary HREE-enrichment proposed by Marien et al. (2018) and contradict the model involving reduction of rock volume proposed by Andersen (1987). The additional leaching of LREE by F-rich fluids also proposed by Andersen (1987) is however confirmed by this study as happening during silicification

Our observations are as follows: initially HREE-rich samarskite I was followed by Fe- and Th-rich samarskite II which in turn was overgrown by LREE-rich monazite and hematite (Fig. 7a and b). This texture is interpreted to be related to a mixing of fluid 2b and 3b. Later, MREE-rich aeschynite and LREE-rich monazite precipitated in chlorite-rich veins as a result of mixing of more evolved (Al-rich) fluid 2c with fluid 3b (Fig. 6f). Still later, the Nb-Ti-Fe-Th-oxide (UM) partially replaced aeschynite during the silicification process, which was caused by a renewed influx of fluid 3a (V in Fig. 10). The replacement of aeschynite by UM released REE resulting in the precipitation of HREE in samarskite III close to UM, while the LREE were transported further away (Fig. 7a). Also, some monazite aggregates indicate LREE mobilisation, as they are overgrown and marginally replaced by fluorapatite (Fig. 7c), which was in turn replaced by quartz.

The association of aeschynite and monazite in chlorite veins at Vasker mine demonstrates that at this location, the hydrothermal fluid 2c mobilized Fe, Ti and Al, as well as Th and Nb in addition to REE. Similar processes have been observed at other sites, e.g. at Olserum in Sweden (Andersson et al., 2018).

In general in the Fen rocks, Th is incorporated in thorites (61.6 wt% ThO_2), REE-F-carbonates (0.7 wt% ThO_2) and monazites (0.7 wt% ThO_2) both in rødberg and rauhaugite. At the Vasker mine, Th is additionally contained in UM (4.6 wt% ThO_2) and samarskite II (2.6 wt% ThO_2) suggesting a hydrothermal mobility of Th similar to that of HREE rather than to LREE.

The rocks at the Vasker mine are more enriched in HREE and HFSE compared to the rock from the Tufte adit. We suggest that this may reflect a shorter distance to the source of the REE-rich fluid 2 and/or higher temperatures at the Vasker mine compared to the Tufte adit, in accordance with the preferred precipitation of HREE in hydrothermal fluids upon contact with carbonate rocks (e.g., Williams-Jones et al., 2012). As REE-patterns of carbonatites are usually LREE-rich (Möller et al., 1980), comparatively high amounts of fluid must have passed through the Vasker mine sample to deliver the high total HREE concentration observed. This process was probably followed by leaching of

Table 4
Representative electron microprobe analyses of samarskite, aeschynite and UM from the Fen complex (Norway).

Sample location	X3	X3	X3	X3	X3	X3	X3
Mineral	Samarskite I	Samarskite II	Samarskite III	Aeschynite		UM	
Rock type	Rødberg						
wt.%							
CaO	0.09	1.06	3.36	1.34	1.50	1.00	0.87
La_2O_3	bdl	0.10	bdl	0.71	0.79	bdl	bdl
Ce_2O_3	0.21	0.61	0.26	8.61	9.24	0.08	bdl
Pr_2O_3	0.17	0.16	0.12	2.91	2.99	bdl	bdl
Nd_2O_3	1.97	0.72	1.58	18.52	17.19	0.20	0.12
Sm_2O_3	2.36	bdl	2.68	5.31	4.86	bdl	bdl
Gd_2O_4	5.09	0.69	4.70	2.27	2.01	0.13	0.11
Eu_2O_3	0.99	bdl	1.14	1.16	1.04	bdl	bdl
Y_2O_3	36.92	2.85	14.19	3.07	3.11	1.10	0.85
ThO_2	0.09	1.34	1.25	0.46	0.77	4.32	2.98
TiO_2	0.28	1.03	0.27	28.50	27.34	39.88	41.37
Fe_2O_3	0.33	26.66	11.18	1.10	0.66	14.21	14.71
Nb_2O_5	52.70	56.67	55.91	24.92	26.52	31.69	32.16
Ta_2O_5	bdl	bdl	bdl	0.18	0.13	0.22	0.13
Total	101.20	91.89	96.64	99.06	98.15	92.83	93.30
	Formula calculation based on						
apfu	4 oxygen	6 oxygen		6 oxygen		26 oxygen	
Ca	0.00	0.07	0.22	0.09	0.09	0.24	0.20
La	bdl	0.00	bdl	0.02	0.02	bdl	bdl
Ce	0.00	0.01	0.01	0.19	0.21	0.01	bdl
Pr	0.00	0.00	0.00	0.06	0.07	bdl	bdl
Nd	0.03	0.01	0.03	0.39	0.36	0.02	0.01
Sm	0.03	bdl	0.06	0.11	0.10	bdl	bdl
Gd	0.07	0.01	0.10	0.04	0.04	0.01	0.01
Eu	0.01	bdl	0.02	0.02	0.02	bdl	bdl
Y	0.86	0.09	0.47	0.10	0.10	0.13	0.10
Th	0.00	0.02	0.02	0.01	0.01	0.22	0.15
Ti	0.01	0.05	0.01	1.28	1.21	6.72	6.84
Fe^{3+}	0.01	1.20	0.52	0.05	0.03	2.39	2.43
Nb	0.97	1.53	1.56	0.67	0.71	3.21	3.19
Ta	bdl	bdl	bdl	0.00	0.00	0.01	0.01
Total cations	1.99	2.99	3.02	3.03	2.97	12.96	12.94
OH*	–	–	–	0.37	0.72	–	–

OH* - calculated from the total difference to 100 wt%.
bdl: bellow detection limit.

LREE during silicification- similar to the process proposed by Andersen (1987). As regional airborne gamma-ray maps by Heincke et al. (2008) show local hotspots of Th close to the Vasker mine, and as high Th contents appear to be linked to the HREE mineralisation, this area probably represents an important source area for fluid 2.

8.5. The significance of hydrothermal processes in carbonatite complexes

Late- and post-magmatic hydrothermal processes such as those depicted at Fen play an important role in carbonatite-related REE mineralizations worldwide. While late-magmatic hydrothermal fluids often form a discrete REE mineralization by adding REE to an existing rock (e.g., Giebel et al., 2017), post-magmatic hydrothermal processes are responsible for element remobilization and redistribution, mineral replacement and reprecipitation rather than for new addition of REE (e.g., Moore et al., 2015)

At Fen, late- and post-magmatic fluids are often not clearly distinguishable. Rødberg and iron ores show a cogenetic hydrothermal replacement of carbonate minerals by hematite, magnetite, monazite, apatite, barite or columbite, demonstrating large scale elemental remobilization by fluids interpreted to be both late- and post-magmatic (REE-rich fluids and oxidized basement fluids). Like at Fen, large parts of the REE-Nb mineralization in Bayan Obo are associated with hematite/magnetite iron ores. However, their origin is still considered to be of either magmatic (Sun et al., 2013) or sedimentary and magmatic-hydrothermal origin (e.g., Fan et al., 2016). It has been suggested that the Bayan Obo deposit originally formed by metasomatism accompanying the intrusion of carbonatites into marbles followed by later deformation, metamorphic and hydrothermal overprint (e.g., Smith et al., 2015 and references therein). This and later hydrothermal overprints probably resulted in a remobilization of the original Fe and REE mineralization (e.g., Smith et al., 2015).

Apatite and REE-rich veins similar to the ones found at Fen have been reported from other carbonatites such as Bachu in NW China (e.g., Cheng et al., 2018) where hydrothermal processes lead to local enrichment of REE in veins of barite, celestine, fluorapatite and monazite-(Ce) with REE concentrations of up to 20 wt% (Cheng et al., 2018). The origin of the REE-rich fluids forming these veins has been attributed to fluid exsolution from evolved carbonatites (Cheng et al., 2018). In contrast, the formation of apatite veins at Fen appears to be related to the mobilization of phosphate following the replacement of magmatic apatite by quartz. Silicification is often described as an accompanying process to hydrothermal REE mineralization in carbonatite deposits, where the enrichment of Si in the fluid is attributed to the interaction with the silicate host rock/continental crust (Andrade et al., 1999; Simonetti and Bell, 1995).

9. Conclusions

The Fen carbonatite complex was subject to intense late- and post-magmatic hydrothermal alteration by at least three different fluids resulting in two distinct phases of mineralization. The first alteration was

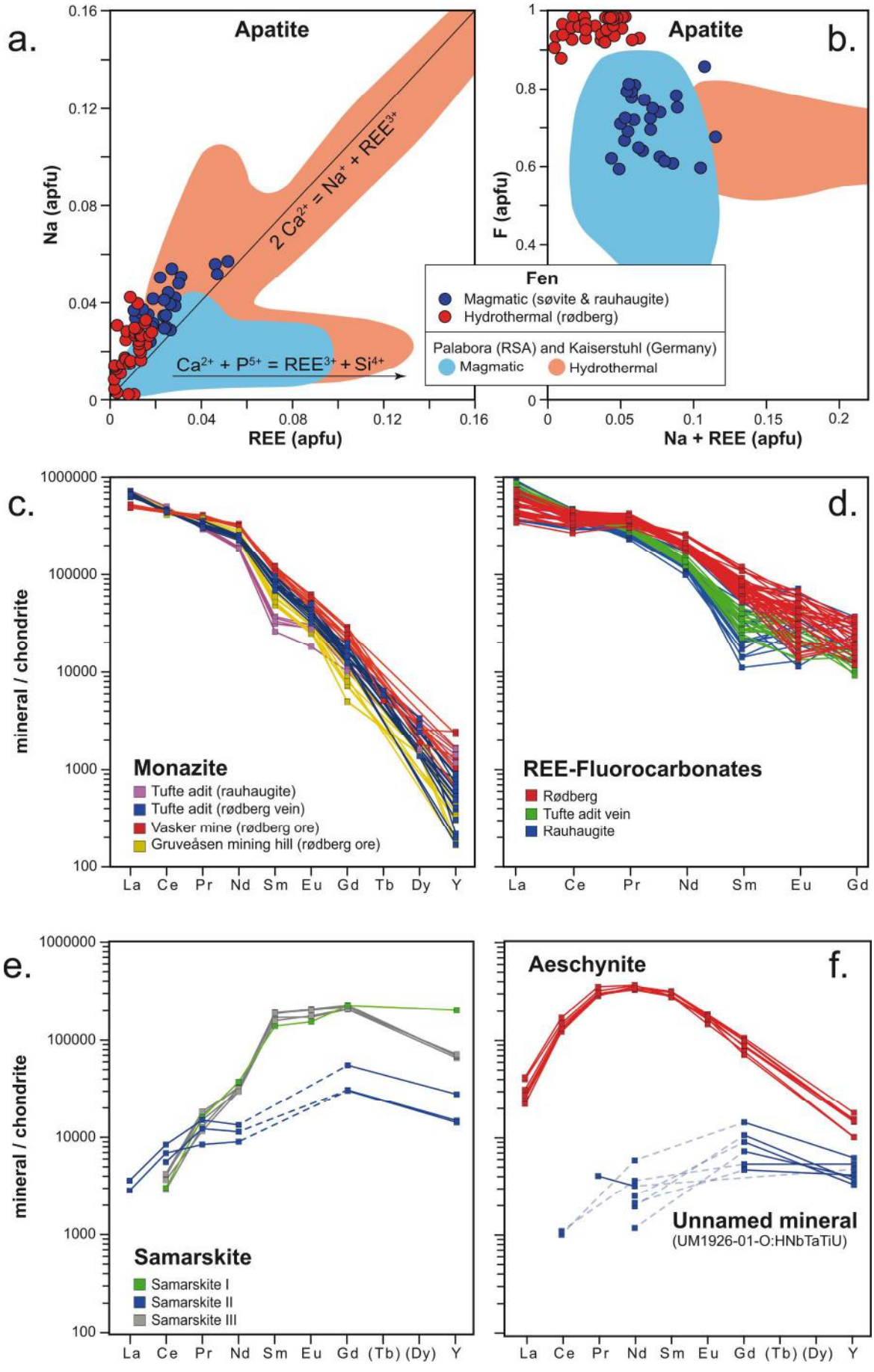

(caption on next page)

Fig. 9. (a) and (b) Apatite compositions (magmatic and hydrothermal) from Fen (this study) compared to literature data from Palabora (RSA; Giebel et al., 2019a) and Kaiserstuhl (Germany; Giebel et al., 2019b). Chondrite-normalized REE diagrams for (c) Monazite (d) REE-F-carbonates (e) Samarskite (f) Aeschynite and an unnamed Nb-Ti-Fe-Th-Oxide (UM).

characterized by a sulfide-rich fluid that led to widespread pyrite formation in all lithologies at Fen. This fluid is most likely related to mafic silicate rocks at depth. During a second (pene-contemporaneous) alteration phase, a REE-rich fluid led to remobilization and redistribution of Fe and Al and to the formation of REE-F-carbonates in carbonatites. This fluid is believed to have unmixed from a late-stage carbonatitic melt. At the same time, a third SiO_2-rich oxidized (meteoric) fluid, most probably derived from the gneissic basement, produced the rødberg rocks by both in-situ oxidation of parts of the original carbonatites and mixing with the carbonatite-derived Fe-rich second fluid.

Replacement of magmatic apatite by quartz in silicified Fe-ores mobilized phosphate, which reprecipitated as apatite II veins in and close to rødberg veins accompanied by the formation of monazite by mixing with REE-rich fluids and replacement of REE-F-carbonates. Hence, the metasomatic silicification at Fen not only redistributed P, but also preferentially remobilized LREE and, hence, resulted in the relative enrichment of HREE in some silicified rocks. The formation of hydrothermal aeschynite in chlorite veins contemporaneous with apatite II veins found in areas of HREE-enrichment implies that evolved carbonatitic fluids are probably able to mobilize REE, Nb and Ti.

The occurrence of Th-rich minerals together with HREE-minerals and the concomitant enrichment of Th and HREE in whole-rocks implies similar behaviour of Th and HREE in hydrothermal systems. The formation of zones of both relative HREE and of absolute total REE enrichment was probably related to large amounts of carbonatite-derived REE-rich fluids penetrating the earlier crystallized carbonatites along brecciated, highly permeable zones.

Acknowledgements

We are grateful to S. Schafflick for preparing the thin sections used in this study and to J.Opitz (Stuttgart) for trace element analysis of whole-rock samples. We thank the exploration company *REE Minerals* for the generous access to some of the drill-core samples studied in this project. The editorial handling of Guest Editor F. Stoppa and the comments of an anonymous reviewer are greatly appreciated.

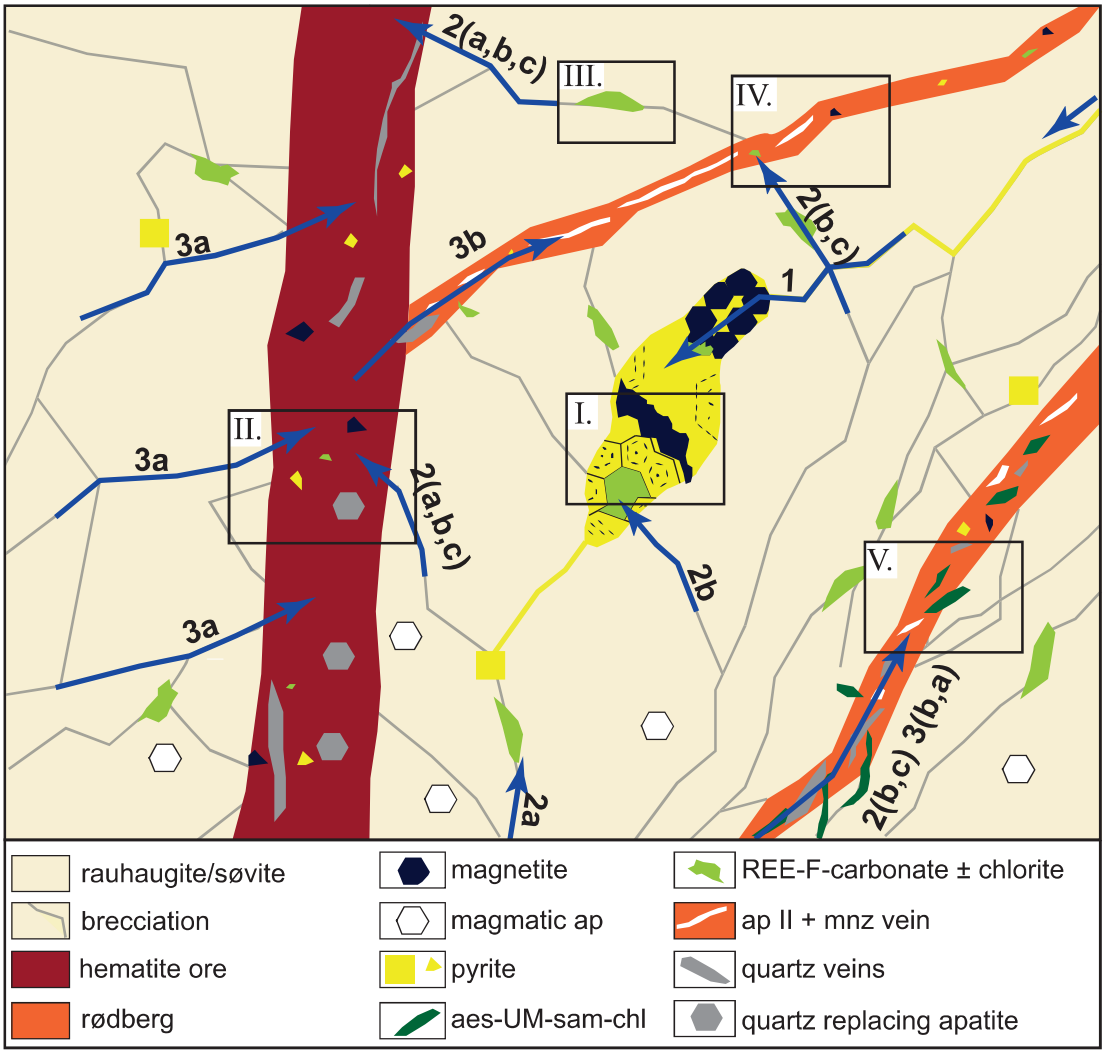

Fig. 10. Schematic diagram illustrating the hydrothermal alteration of carbonatites. An early pyrite-stage (fluid 1) is followed by the formation of red hematite-calcite rocks (rødberg), often silicified hematite ores, REE-mineralizations and apatite veins (fluids 2 and 3). Arrows indicate interaction of fluids, boxes labelled with roman numbers refer to textures observed at different localities (I. Tufte adit vein, II. Gruveåsen mining hill, III. & IV. Tufte adit, V. Vasker mine) as described in the text.

Appendix A. Supplementary data

Supplementary data to this article can be found online at https://doi.org/10.1016/j.oregeorev.2019.102969.

References

Anders, E., Grevesse, N., 1989. Abundances of the elements: meteoritic and solar. Geochim. Cosmochim. Acta 53, 197–214.

Andersen, T., 1983. Iron ores in the Fen central complex, Telemark (S. Norway): petrography, chemical evolution and conditions of equilibrium. Nor. Geol. Tidsskr. 63, 73–82.

Andersen, T., 1984. Secondary processes in carbonatites: petrology of "rødberg"(hematite-calcite-dolomite carbonatite) in the Fen central complex, Telemark (South Norway). Lithos 17, 227–245.

Andersen, T., 1986. Magmatic fluids in the Fen carbonatite complex, SE Norway. Contrib. Miner. Petrol. 93, 491–503.

Andersen, T., 1987. A model for the evolution of hematite carbonatite, based on whole-rock major and trace element data from the Fen complex, southeast Norway. Appl. Geochem. 2, 163–180.

Andersen, T., Qvale, H., 1986. Pyroclastic mechanisms for carbonatite intrusion: evidence from intrusives in the Fen central complex, SE Norway. J. Geol. 94, 762–769.

Andersson, S.S., Wagner, T., Jonsson, E., Michallik, R.M., 2018. Mineralogy, paragenesis, and mineral chemistry of REEs in the Olserum-Djupedal REE-phosphate mineralization, SE Sweden. Am. Mineral. 103, 125–142.

Andrade, F.R.D.d., Möller, P., Lüders, V., Dulski, P., Gilg, H.J.C.G., 1999. Hydrothermal rare earth elements mineralization in the Barra do Itapirapuã carbonatite, southern Brazil: behaviour of selected trace elements and stable isotopes (C, O). 155, 91-113.

Armstrong, J.T., 1991. Quantitative elemental analysis of individual microparticles with electron beam instruments. In: Heinrich, K.F.J., Newbry, D.E. (Eds.), Electron Probe Quantitation. Plenum Press, New York, pp. 261–315.

Bergstøl, S., Svinndal, S., 1960. The carbonatite and per-alkaline rocks of the Fen area—petrology. Nor. Geol. Unders. 208, 99–105.

Brøgger, W.C., 1921. Die Eruptivgesteine des Kristianiagebietes. 4. Das Fengebiet in Telemark, Norwegen. Videnskaps-Selskapets Skrifter 9, 1-402. Academy of Science, Oslo.

Budzyń, B., Harlov, D.E., Williams, M.L., Jercinovic, M.J., 2011. Experimental determination of stability relations between monazite, fluorapatite, allanite, and REE-epidote as a function of pressure, temperature, and fluid composition. Am. Mineral. 96, 1547–1567.

Bühn, B., Rankin, A., 1999. Composition of natural, volatile-rich Na–Ca–REE— Sr carbonatitic fluids trapped in fluid inclusions. Geochim. Cosmochim. Acta 63, 3781–3797.

Capitani, G.C., Mugnaioli, E., Guastoni, A., 2016. What is the actual structure of samarskite-(Y)? A TEM investigation of metamict samarskite from the Garnet Codera dike pegmatite (Central Italian Alps). Am. Mineral. 101, 1679–1690.

Chakhmouradian, A.R., Reguir, E.P., Zaitsev, A.N., Couëslan, C., Xu, C., Kynický, J., Mumin, A.H., Yang, P., 2017. Apatite in carbonatitic rocks: Compositional variation, zoning, element partitioning and petrogenetic significance. Lithos 274, 188–213.

Cheng, Z., Zhang, Z., Aibai, A., Kong, W., Holtz, F., 2018. The role of magmatic and post-magmatic hydrothermal processes on rare-earth element mineralization: a study of the Bachu carbonatites from the Tarim Large Igneous Province, NW China. Lithos 314–315, 71–87.

Dahlgren, S., 1994. Late Proterozoic and Carboniferous ultramafic magmatism of carbonatitic affinity in southern Norway. Lithos 31, 141–154.

Dahlgren, S., 2006. Fenvulkanen. In: Ramberg, I.B., Bryhni, I., Nøttvedt, A. (Eds.), Landet blir til. Norges geologi. Norwegian Geological Society, pp. 146.

Dahlgren, S., 2015. REE and thorium potential of the Fen Complex. Norway –Suppl. Min. J. 12.

Dahlgren, S., Heaman, L., Krogh, T., 1990. Geological evolution and U-Pb geochronology of the Proterozoic central Telemark area Norway. Geonytt 17, 38.

Doroshkevich, A.G., Ripp, G.S., Viladkar, S.G., Vladykin, N.V., 2008. The Arshan REE carbonatites, southwestern Transbaikalia, Russia: mineralogy, paragenesis and evolution. Can. Mineral. 46, 807–823.

Fan, H.-R., Yang, K.-F., Hu, F.-F., Liu, S., Wang, K.-Y., 2016. The giant Bayan Obo REE-Nb-Fe deposit, China: controversy and ore genesis. Geosci. Front. 7, 335–344.

Friedrichsen, H., 1968. Sauerstoffisotopen einiger Minerale der Karbonatite des Fengebietes, Süd Norwegen. Lithos 1, 70–75.

Giebel, R.J., Gauert, C.D., Marks, M.A., Costin, G., Markl, G., 2017. Multi-stage formation of REE minerals in the Palabora Carbonatite Complex, South Africa. Am. Mineral. 102, 1218–1233.

Giebel, R.J., Parsapoor, A., Walter, B.F., Braunger, S., Marks, M.A.W., Wenzel, T., Markl, G., 2019b. Evidence for magma - wall rock interaction in carbonatites from the Kaiserstuhl Volcanic complex (Southwest Germany). J. Petrol.

Giebel, R.J., Marks, M.A.W., Gauert, C.D.K., Markl, G., 2019a. A model for the formation of carbonatite-phoscorite assemblages based on compositional variations in mica and apatite from the Palabora Carbonatite Complex, South Africa. Lithos 324–325, 89–104.

Goodenough, K., Schilling, J., Jonsson, E., Kalvig, P., Charles, N., Tuduri, J., Deady, E., Sadeghi, M., Schiellerup, H., Müller, A., 2016. Europe's rare earth element resource potential: an overview of REE metallogenetic provinces and their geodynamic setting. Ore Geol. Rev. 72, 838–856.

Govindaraju, K., 1989. Compilation of working values and sample description for 272 geostandards. Geostand. Geoanal. Res. 13, 1–113.

Harlov, D.E., Wirth, R., Hetherington, C.J., 2011. Fluid-mediated partial alteration in monazite: the role of coupled dissolution–reprecipitation in element redistribution and mass transfer. Contrib. Miner. Petrol. 162, 329–348.

Heincke, B.H., Smethurst, M.A., Bjørlykke, A., Dahlgren, S., Rønning, J.S., Mogaard, J.O., 2008. Airborne Gamma-Ray Spectrometer Mapping for Relating Indoor Radon Concentrations to Geological Parameters in the Fen Region, Southeast Norway. Geology for Society, Geological Survey of Norway Special Publication, pp. 131–143.

Kanazawa, Y., Kamitani, M., 2006. Rare earth minerals and resources in the world. J. Alloy. Compd. 408–412, 1339–1343.

Lie, A., Østergaard, C., 2014. The Fen Rare Earth Element Deposit, Ulefoss, South Norway. 21th North Mineral Consulting and Exploration, Svendborg.

Lumpkin, G., Ewing, R., Eyal, Y., 1988. Preferential leaching and natural annealing of alpha-recoil tracks in metamict betaflte and samarskite. J. Mater. Res. 3, 357–368.

Mariano, A.N., Mariano Jr., A., 2012. Rare earth mining and exploration in North America. Elements 8, 369–376.

Marien, C., Dijkstra, A.H., Wilkins, C., 2018. The hydrothermal alteration of carbonatite in the Fen Complex, Norway: mineralogy, geochemistry, and impilications for rare earth element resource formation. Mineral. Mag. 82, 115–131.

Meert, J.G., Torsvik, T.H., Eide, E.A., Dahlgren, S., 1998. Tectonic significance of the Fen Province, S. Norway: constraints from geochronology and paleomagnetism. J. Geol. 106, 553–564.

Métrich, N., Mandeville, C.W., 2010. Sulfur in magmas. Elements 6, 81–86.

Migdisov, A.A., Williams-Jones, A.E., Wagner, T., 2009. An experimental study of the solubility and speciation of the Rare Earth Elements (III) in fluoride- and chloride-bearing aqueous solutions at temperatures up to 300°C. Geochim. Cosmochim. Acta 73, 7087–7109.

Migdisov, A., Williams-Jones, A.E., Brugger, J., Caporuscio, F.A., 2016. Hydrothermal transport, deposition, and fractionation of the REE: experimental data and thermodynamic calculations. Chem. Geol. 439, 13–42.

Möller, P., Morteani, G., Schley, F., 1980. Discussion of REE distribution patterns of carbonatites and alkalic rocks. Lithos 13, 171–179.

Moore, M., Chakhmouradian, A.R., Mariano, A.N., Sidhu, R., 2015. Evolution of rare-earth mineralization in the Bear Lodge carbonatite, Wyoming: mineralogical and isotopic evidence. Ore Geol. Rev. 64, 499–521.

Naldrett, A.J., 2013. Magmatic Sulfide Deposits: Geology, Geochemistry and Exploration. Springer Science & Business Media.

Ramberg, I.B., 1973. Gravity studies of the Fen complex, Norway, and their petrological significance. Contrib. Miner. Petrol. 38, 115–134.

Read, D., Andreoli, M.A., Knoper, M., Williams, C.T., Jarvis, N., 2002. The degradation of monazite: Implications for the mobility of rare-earth and actinide elements during low-temperature alteration. Eur. J. Mineral. 14, 487–498.

Sæther, E., 1957. The alkaline rock province of the Fen area in southern Norway. I kommisjon Hos F. Bruns, Bokhandel, Trondheim. Det Konglige Norske Vitensksap-Selskaps Skrifter 1, 1-150. The Royal Academy of Science, Trondheim.

Simonetti, A., Bell, K., 1995. Nd, Pb, and Sr isotope systematics of fluorite at the Amba Dongar carbonatite complex, India; evidence for hydrothermal and crustal fluid mixing. Econ. Geol. 90, 2018–2027.

Smith, M.P., Campbell, L.S., Kynicky, J., 2015. A review of the genesis of the world class Bayan Obo Fe–REE–Nb deposits, Inner Mongolia, China: multistage processes and outstanding questions. Ore Geol. Rev. 64, 459–476.

Smith, D.G., Nickel, E.H., 2007. A system of codification for unnamed minerals: report of the subcommittee for unnamed minerals of the IMA commission on new minerals, nomenclature and classification. Can. Mineral. 45, 983–990.

Stone, R., 2009. As China's rare earth R&D becomes ever more rarefied, others tremble. Science (New York, NY) 325, 1336–1337.

Sun, J., Zhu, X., Chen, Y., Fang, N.J.P.R., 2013. Iron isotopic constraints on the genesis of Bayan Obo ore deposit, Inner Mongolia, China. 235, 88-106.

Tukker, A., 2014. Rare earth elements supply restrictions: market failures, not scarcity, hamper their current use in high-tech applications. Environ. Sci. Technol. 48, 9974.

Vogt, J.H.L., 1910. Norges Jernmalmforekomster. Norges geologiske undersøkelse, Kristiania.

Williams-Jones, A.E., Migdisov, A.A., Samson, I.M., 2012. Hydrothermal mobilisation of the rare earth elements – a tale of "ceria" and "yttria". Elements 8, 355–360.